

Probing cosmology with QUaD:
Scientific optimization of an experiment to measure
the polarization of the Cosmic Microwave
Background.

by
Melanie Bowden

A thesis submitted to the
University of Wales
for the degree of
Doctor of Philosophy

UMI Number: U584672

All rights reserved

INFORMATION TO ALL USERS

The quality of this reproduction is dependent upon the quality of the copy submitted.

In the unlikely event that the author did not send a complete manuscript and there are missing pages, these will be noted. Also, if material had to be removed, a note will indicate the deletion.



UMI U584672

Published by ProQuest LLC 2013. Copyright in the Dissertation held by the Author.
Microform Edition © ProQuest LLC.

All rights reserved. This work is protected against
unauthorized copying under Title 17, United States Code.



ProQuest LLC
789 East Eisenhower Parkway
P.O. Box 1346
Ann Arbor, MI 48106-1346

Acknowledgements

This work has carried as part of the QUaD project and throughout the course of my PhD I have received help and advice from many people within the collaboration. I thank my supervisor Walter Gear for his support, particularly in the initial stages of the work, and for reading through the drafts of this thesis under tight time constraints. This work would not have been possible without the help of Andy Taylor who provided the ideas for the survey area and parameter estimation calculations and has given me numerous crash courses on cosmology, data analysis and statistics and invaluable help with applying for jobs and writing papers. Ken Ganga has given me continual help with the survey design and data simulations and has also been a constant source of moral support.

I thank Mike Zemcov for his help with the data simulations, for letting me use the results of his map-making code and for useful discussions throughout the last year, Simon Melhuish for looking after my computer and for his tips on how to use the English language, Tim Waskett for help with formatting this thesis and Ian Bacchus for bringing me Diet Coke. Phil Mauskopf has provided me with the motivation to still be interested in cosmology when it has started to fade away.

Finally, I would like to thank Douglas for his emotional support throughout the last three years and for explaining to me how instrumentation works.

Contents

1	Introduction	3
1.1	The CMB	4
1.1.1	The CMB in a smooth Universe	4
1.1.2	The CMB temperature anisotropies	10
1.1.3	Observing the CMB	21
1.1.4	Initial conditions - inflation	24
1.1.5	Status of CMB temperature observations	28
1.1.6	Key points	31
1.2	The polarization of the CMB	33
1.2.1	The Stokes parameters	33
1.2.2	E-B decomposition	35
1.2.3	Generation of CMB polarization	40
1.2.4	Calculating the polarization at recombination	43
1.2.5	Secondary polarization anisotropies	43
1.2.6	Degeneracy breaking	48
1.2.7	Key points	50
1.3	Thesis overview	51
2	The QUaD experiment	53
2.1	Measuring CMB polarization with QUaD.	53
2.2	The QUaD instrument	57
2.2.1	Telescope and optics	57
2.2.2	Focal plane and feed horns	58
2.2.3	Cryogenics	59
2.2.4	Detectors	62
2.2.5	Electronics	64
2.3	Other CMB polarization experiments	66
2.3.1	Detections and upper limits	66
2.3.2	Experiments currently in operation	69

CONTENTS

2.3.3	Upcoming experiments	70
2.3.4	Planned next generation experiments	71
3	Astrophysical foregrounds	73
3.1	Dust	76
3.2	Synchrotron	79
3.3	Free-free emission	82
3.4	Point sources	82
3.5	Conclusions and Outlook	84
4	Sensitivity calculation	87
4.1	Formalism for describing random noise	87
4.2	Contribution to the NEP for a bolometric experiment	90
4.3	Derivation of photon noise for a PSB	91
4.4	Calculating QUaD sensitivity	94
4.5	Results	97
5	Forecasting performance of QUaD	101
5.1	Parameter estimation theory	101
5.1.1	The likelihood function	101
5.1.2	Confidence limits and the Fisher matrix	103
5.2	Application to CMB polarization	107
5.3	Multipole coverage	110
5.4	Including foreground models	111
5.5	Determining area of sky to observe	112
5.5.1	Formalism for finding optimal survey area	112
5.5.2	Chile calculation	114
5.5.3	South Pole calculation	121
5.6	Power spectrum predictions	128
5.7	Parameter forecasts	134
5.8	Key points	143
6	Observing strategy	145
6.1	Focal plane layout	145
6.1.1	Factors to consider for focal plane layout	145
6.1.2	Possible designs for the focal plane layout	149
6.1.3	Projection onto the sky	150
6.2	Scanning strategies	154
6.2.1	Scanning speeds	154

CONTENTS

6.2.2	Z-axis rotation	158
6.2.3	Possible scan strategies	159
6.3	QUaD observing strategy	166
7	Data analysis and simulations	169
7.1	Data analysis pipeline	169
7.1.1	Map making	170
7.1.2	Power spectrum estimation	171
7.2	Simulations	171
7.2.1	Simulations of CMB signal	171
7.2.2	Including noise	174
7.2.3	Systematic effects	181
7.2.4	Future work	185
8	Conclusions and future work	187
8.1	Summary of results and future work.	187
8.2	Outlook for CMB polarization measurements	189
A	Fourier transforms of sampled data	191
B	Details of E-B decomposition	195
C	Amplitude modulation	197

CONTENTS

List of Figures

1.1	The frequency spectrum of the CMB	9
1.2	Physical processes occurring in the generation of the CMB anisotropy . . .	17
1.3	Spherical Bessel function used in the projection of spatial perturbations at recombination to angular anisotropies seen today.	23
1.4	Physical effects determining the temperature power spectrum	24
1.5	Parameters used to define completely polarized radiation	33
1.6	E-B decomposition	37
1.7	Polarization power spectra	39
1.8	Generation of polarization from Thomson scattering.	41
1.9	Effect of reionization on E-mode power spectrum	44
1.10	Effect of weak lensing on TT and EE power spectra	45
1.11	Distortion of a pure E-field by a gravitational lens	46
1.12	Effect of weak lensing on BB power spectrum	46
2.1	1/f noise spectrum	55
2.2	Schematic of optics chain.	57
2.3	Ray tracing diagram of QUaD optics	58
2.4	Schematic of cryostat	60
2.5	Helium phase diagram	60
2.6	Schematic of fridge	61
2.7	Bolometer parameters	62
2.8	Bolometer absorber geometries.	63
2.9	Cold electronics circuit	65
2.10	Detections of CMB polarization.	68
3.1	WMAP foregrounds	74
3.2	Estimated levels of polarized dust fluctuations compared to CMB	78
3.3	Estimated levels of polarized synchrotron fluctuations compared to CMB .	82
3.4	Estimated levels of polarized point source fluctuations compared to CMB. .	84

LIST OF FIGURES

3.5	Foreground templates used to predict regions with low foreground contamination.	86
4.1	Atmospheric transmission at different sites	96
4.2	Power from each of the telescope components for two optics models.	99
5.1	$\Delta\chi^2 = 1$ two parameter error ellipse.	106
5.2	Variation in the number of hours of night-time each day for the Chile site.	114
5.3	Region of sky observable from Chile site.	115
5.4	Possible patches of sky to observe from Chile.	116
5.5	Variation of SNR with area for 5 equal size patches for a two year survey in Chile.	118
5.6	Observing times from the South Pole.	122
5.7	Possible patches of sky to observe from South Pole.	123
5.8	Variation of SNR with area for a single patch of sky at the South Pole.	124
5.9	Variation of optimal survey area and SNR as a function of tensor-to-scalar ratio	125
5.10	Power spectrum error bars of QUaD, foreground comparison	128
5.11	EE power spectrum error bars of QUaD using a linear scale	129
5.12	BB power spectrum error bars of QUaD using a linear scale	129
5.13	Power spectrum error bars of QUaD for a single year	130
5.14	Power spectrum error bars of QUaD for a single year	130
5.15	Comparison of power spectrum error bars for QUaD with other ground based experiments	132
5.16	Comparison of power spectrum error bars for QUaD with satellite experiments	132
5.17	Comparison of power spectrum error bars for QUaD with Planck	133
5.18	Parameter derivatives (log axes)	135
5.19	Parameter derivatives (linear axes)	136
5.20	Error ellipses	139
5.21	Error ellipses	141
6.1	Fully sampling sky with array of gaussian beams	147
6.2	SCUBA scanning angle	148
6.3	Best scan angle for creating a fully sampled strip of sky	149
6.4	Focal plane projection onto the sky.	150
6.5	Possible focal plane layouts	151
6.6	Possible focal plane layouts	152
6.7	Possible focal plane layouts	153

LIST OF FIGURES

6.8	Representation of the waveplate on the PSB.	155
6.9	Conversion from angle moved in azimuth to angle moved on celestial sphere.	157
6.10	A spherical triangle	160
6.11	Spherical triangle for coordinate transformations	160
6.12	Spiral scan pattern	162
6.13	Ring scan pattern	162
6.14	Motion in azimuth and elevation for bow tie scan strategy.	163
6.15	Bow tie scan patterns	164
6.16	South Pole scanning strategy	165
6.17	South Pole scan strategy	167
7.1	HEALPix pixelization	172
7.2	Simulated timeline with CMB signal only.	174
7.3	Simulated timestream with white noise.	177
7.4	Simulated timeline with white noise and atmospheric 1/f noise.	178
7.5	Simulated timestream with all 3 noise components.	179
7.6	Output maps from simulation	180
7.7	Model of instrumental polarization	182
7.8	Simulated timeline with instrumental polarization.	183
A.1	Why the maximum measureable frequency in a signal must be less than half the sampling rate.	193
C.1	Modulation of a signal	198

LIST OF FIGURES

List of Tables

1.1	WMAP best fit cosmological parameters	29
2.1	QUaD experimental parameters.	56
3.1	Foreground parameters.	76
4.1	QUaD Telescope parameters.	95
4.2	Atmospheric model parameters	97
4.3	Zenith transmission at the centre of the QUaD bands.	97
4.4	Predicted sensitivity at each site in the 3 QUaD frequency bands.	97
5.1	Observing times per year for 5 possible patches observable from Chile. . . .	116
5.2	Results for a one/two year survey for 5 equal size patches.	117
5.3	Results for a two-scale two-year survey.	120
5.4	Results for a one/two year survey at the South Pole for a single patch of sky. .	123
5.5	CMB experiment parameters.	133
5.6	Fisher matrix estimates if r is not included in analysis (six parameter fit) in the case of no foregrounds.	138
5.7	Fisher matrix estimates for different foreground models for a seven param- eter fit.	138
5.8	Fisher matrix estimates for different values of the minimum observable ℓ .	140
5.9	Fisher matrix estimates used to test which part of the CMB measurement is providing information.	142
7.1	NETs for noise simulations	176

Chapter 1

Introduction

The **Big Bang** theory, in which the Universe began in a hot dense state and gradually expanded and cooled, has now become the standard model of cosmology. The general acceptance of this model is due to three seminal observations.

- The measurement of the Hubble flow, indicating that the Universe is expanding.
- The measurement of light element abundances matching those predicted by Big Bang nucleosynthesis.
- The detection of an isotropic background of radiation (Penzias and Wilson (1965)) at a temperature of 2.7K, the Cosmic Microwave Background (CMB), as predicted by the Big Bang model.

A standard theory of structure formation within this Big Bang model is now also emerging. In this model, tiny inhomogeneities in the primordial Universe provided the seeds through which the large scale structure of galaxies and galaxy clusters could grow through gravitational instability. This is supported observationally by the measurement of tiny fluctuations in the CMB (Smoot et al. (1992)), and also by the filament-like structure observed in high-redshift galaxy cluster surveys (e.g. Colless et al. (2001), Percival et al. (2002)).

There has been a huge increase in the amount of observational data over the past decade. This has meant that the results from a variety of different techniques can be combined to give a set of concurrent values for the key parameters which determine the evolution of the Universe within the standard Big Bang model. This has resulted in an observationally favoured **concordance model**. The key features of this model are that:

- the Universe is flat,
- the expansion of the Universe is accelerating,

- ordinary baryonic matter can only account for about 5% of the total energy density, the main contributions to the total density are dark matter ($\sim 1/3$) and dark energy ($\sim 2/3$).

Dark matter is a material which can only interact gravitationally with the rest of the Universe. Although there are a number of possible candidates from theoretical particle physics, the nature of dark matter is still extremely speculative. Dark energy is a term for a negative pressure which opposes gravity and causes the Universe to accelerate. The simplest form of dark energy is a cosmological constant Λ , but other dynamic forms of dark energy have also been proposed. The evidence for the acceleration of the expansion rate comes from measurements of high-redshift supernovae (Perlmutter et al. (1999)). If these constraints are combined with the CMB measurement of flatness, a Universe with no dark energy is ruled out with high confidence. The concordance model also gives values for the size and spectrum of the initial perturbations in the Universe.

However, although current observations indicate the existence of dark matter, dark energy and primordial inhomogeneities in the Universe, our understanding of these new concepts is still very limited. The current tasks of observational cosmology are to put constraints on the nature of dark energy and dark matter and on the mechanism which generated the initial inhomogeneities. One of the most promising new cosmological probes is the measurement of the polarization of the CMB. This thesis discusses an experiment specifically designed to measure this signal.

In this chapter I provide an overview of CMB polarization. In the first half I review the formation of the CMB anisotropies and current status of CMB temperature measurements. In the second half I then go on to look at how the CMB becomes polarized and how observations of the CMB polarization can be used to probe cosmology.

1.1 The CMB

1.1.1 The CMB in a smooth Universe

The background cosmology

In order to discuss how the CMB can be used to test and constrain the concordance model it is useful to first discuss the tools and parameters needed to describe an expanding Universe. In the simplest case the Universe can be thought of as being perfectly smooth and any perturbations are then added onto this simple model. The dynamics of this smooth Universe can be derived from two initial assumptions:

- the large scale structure of the Universe is determined by gravitational interactions and these effects can be described by Einstein's theory of gravity, General Relativity,

- on a sufficiently large scales the Universe is homogeneous and isotropic.

In General Relativity, a free particle will always travel on the straightest possible path through 4-dimensional space-time. The gravitational effects we observe are due to the curvature of space-time influencing the particle's motion. The way in which the Universe is curved can be expressed in terms of the space-time metric¹, $g_{\mu\nu}$. In four dimensions, instead of thinking in terms of the distance between two points, it is more useful to think in terms of the proper time between two events, τ . This is the time ticked on a clock which passes through both events. A free particle will therefore travel along the path along which the proper time takes it's extremal value. The metric can be used to map the coordinate interval between two events into the proper time using the metric equation:

$$ds^2 = g_{\mu\nu} dx^\mu dx^\nu. \quad (1.1)$$

where the interval, ds , is related to the proper time by $ds^2 = -d\tau^2$. The Einstein equations give the relationship between the space-time curvature and the distribution of mass and energy in the Universe:

$$G^{\mu\nu} + \Lambda g^{\mu\nu} = 8\pi T^{\mu\nu} \quad (1.2)$$

where the components of the Einstein tensor $G^{\mu\nu}$ are obtained from the space-time metric and the components of the stress-energy tensor $T^{\mu\nu}$ from the mass-energy distribution of the Universe. The Λ term gives the contribution to the mass-energy distribution from dark energy. In these equations, the curvature determines the distribution of matter and energy, but then any change to any part of this distribution will alter the metric and so change the overall distribution, which is consistent with the description of gravity as a force between massive objects. The first assumption therefore tells us how to determine the gravitational interactions given the form of the metric and the mass-energy distribution. The background metric can be obtained from the second assumption; homogeneity and isotropy dictate that the space-time metric must be the Friedman-Robertson-Walker (FRW) metric:

$$ds^2 = -dt^2 + a(t)^2 \left[\frac{dr^2}{1 - kr^2} + r^2(d\theta^2 + \sin^2\theta d\phi) \right] \quad (1.3)$$

where (t, r, θ, ϕ) are the coordinates specifying the position of a point in space-time and k is either 0, -1 or 1 depending on the curvature of the Universe. The function $a(t)$, the scale factor, describes the expansion of the Universe.

To determine the form of the stress-energy tensor we assume that the different types of matter and radiation in the Universe can be modelled as a fluid. This means that only

¹Throughout this Chapter we use the notation commonly used in General Relativity in which Greek indices (c.g. ν) denote the four space-time coordinates and Roman indices (c.g. i) denote the three spatial coordinates. In this notation repeated indices imply a summation c.g. for a vector, \mathbf{V} , $g_{ij}V^j = g_{i1}V^1 + g_{i2}V^2 + g_{i3}V^3$. We also set $c = G = 1$.

bulk properties need to be considered, not the motion of individual particles. The equations of motion, the continuity equation (conservation of energy) and the Euler equation (conservation of momentum) can be used to completely describe the evolution of the fluid. As a first approximation the **perfect fluid** model can be used. This means the fluid can be completely described in terms of its pressure and density i.e. there is no vorticity (rotational flows) or shear (velocity gradients) in the fluid. The stress-energy tensor then takes a simple form in which only the diagonal elements are non-zero and are given by:

$$T^{\mu\nu} = \text{diag}(\rho, P, P, P) \quad (1.4)$$

where density, $\rho(t)$, and pressure, $P(t)$, are unknown functions of time. The factor $a(t)$ is found by solving Einstein's equations using the FRW metric (to give $G^{\mu\nu}$) and the diagonal form of $T^{\mu\nu}$. The Einstein equations are a set of 10 equations, however, isotropy and homogeneity reduce this set to just two independent equations: one equation from the time-time component of Einstein's equations and one from the space-space components. The time-time component $G^{00} = 8\pi T^{00}$ gives the Friedman equation:

$$\left(\frac{\dot{a}}{a}\right)^2 = \frac{8\pi}{3}\rho - \frac{k}{a^2} + \frac{\Lambda}{3} \quad (1.5)$$

where the Λ term represents the contribution to the expansion from a cosmological constant. The equations of motion of the fluid (which determine ρ in the above expression) are just expressions for the conservation of energy (continuity equation) and momentum (Euler equation) which are given by the expression:

$$\frac{DT^{\mu\nu}}{Dx^\nu} = 0 \quad (1.6)$$

where D/Dx^ν represents a covariant derivative². The terms in the covariant derivative depend on the metric and so take the expansion and curvature of the Universe into account. Again, due to spatial homogeneity, only the time component of this is non-trivial (i.e. the Euler equation is not needed). This gives the continuity equation:

$$\frac{d}{dt}(\rho a^3) = -P \frac{d}{dt}(a^3) \quad (1.7)$$

It is also possible (but algebraically messy) to obtain the continuity equation (1.7) by combining the time-time (1.5) and space-space field equations. It is therefore possible to

²When we take a derivative, say dS/dx , we are finding the change in a quantity, S , if we change x by a small amount, dx . If the metric is dependent on the value of the coordinates then dx will also depend on the coordinate system being used and on the position at which the derivative is being taken. This can be taken into account by using the **covariant derivative**, DS/Dx , which contains extra terms involving the derivatives of the metric to allow for this coordinate dependence. If the metric has no coordinate dependence, as is the case for Cartesian coordinates in flat space-time, the covariant derivative reduces to dS/dx .

describe all of the background cosmology with just two equations, the Friedman Equation (1.5) and the continuity equation (1.7). However, something extra is needed to solve this set of equations as there are three unknowns, $a(t)$, $\rho(t)$ and $P(t)$ and only two independent equations. To specify a complete solution, more physics is needed to specify the relationship between ρ and P . This is the equation of state which can be written in its simplest form as:

$$P = \omega\rho \quad (1.8)$$

where ω depends on the type of matter/energy. The three main sources contributing to $T^{\mu\nu}$ are non-relativistic matter (e.g. baryons and CDM) with $\omega_m = 0$, relativistic matter (e.g. photons) with $\omega_r = 1/3$ and dark energy with $\omega_{de} < -1/3$. If dark energy does not evolve with time it can be modelled as a cosmological constant, Λ , for which $\omega = -1$. However, in other dark energy models ω_{de} will take different values. One of the most promising ways to determine the nature of dark energy is to put observational constraints on ω_{de} . Once the equation of state is known, the continuity equation can be integrated to find ρ as a function of a , and then the Friedman equation can be used give a as a function of t .

Since the field equations are a set of differential equations, a unique solution also requires the specification of a and \dot{a} at some instant of time. From an observational viewpoint it is convenient to define the Hubble constant, $H = \dot{a}/a$ and to use the present value of H , along with the present value of the density, denoted H_0 and ρ_0 , as the boundary conditions for this problem. ρ_0 is normally stated in terms of the critical density, $\rho_c \equiv 3H_0^2/8\pi$ and is denoted by $\Omega_0 = \rho_0/\rho_c$. In a Universe in which only gravity influences the expansion (i.e. a Universe with no dark energy), if the density of the Universe is lower than ρ_c it will expand forever and if it is higher than ρ_c it will eventually re-collapse. It is likely that the main contributions to Ω_0 do not come from ordinary matter that can be detected in the laboratory. For this reason, Ω_0 is divided into five components, Ω_b , for ordinary baryonic matter³, Ω_{CDM} , for cold dark matter, Ω_r , for radiation, Ω_ν , for hot dark matter (which is thought to consist mainly of neutrinos) and Ω_{de} , for the contribution from dark energy. One of the main missions of observational cosmology is to find these values at the present epoch in order to obtain the boundary conditions needed to solve the equations governing the large-scale evolution of the Universe.

An important effect that can be seen from the continuity equation is that the density of the different components of the Universe will evolve at different rates:

- for CDM, $\rho \propto a^{-3}$
- for radiation, $\rho \propto a^{-4}$

³In cosmology the term baryons is taken to include all non-exotic forms of matter, in particular it includes electrons.

- for dark energy, $\rho \propto a^{-3(1+\omega_{de})}$, (with $\rho \propto \text{constant}$ for a cosmological constant).

The overall expansion rate will therefore change as different components form the dominant contribution to the equation of state. There are three distinct eras in the expansion history of the Universe, the **radiation dominated** (RDE), **matter dominated** (MDE) and **dark energy dominated** (DDE). The Universe will move from one epoch to another as the Universe expands. The CMB was formed slightly after the Universe changed from radiation domination to matter domination. We now go on to explain how the CMB was formed in the expanding homogeneous Universe we have just described.

The formation of the CMB

At very early times, the Universe can be modelled as a plasma of different particles. The density and temperature are so high that all of the reactions occurring in the plasma are in equilibrium, with the rate at which any particle is created equal to the rate at which it is destroyed. The interactions between different particles couple them together so that they evolve as a single plasma. As the Universe cools and its density reduces the reaction rates drop. When the reaction rate of a certain species falls below the expansion rate, the reactions are not rapid enough to keep the particles in equilibrium and this species will evolve separately from that of the rest of the plasma. This process is called **decoupling**.

The CMB is created when the photons decouple from the plasma. At this time, the main components of the plasma are photons, protons and electrons. The electrons couple to the protons through the electrostatic Coulomb interactions. The photons are coupled to the electrons through Thomson scattering. The protons and electrons can combine to form neutral hydrogen, but if enough photons have energies above the hydrogen binding energy (13.6 eV), the hydrogen will be quickly re-ionized so there will be no net hydrogen production. The number of photons in the early Universe is much higher than the number of baryons, so significant hydrogen production does not occur until the peak energy of the photon distribution is about 0.25 eV. The electron density will then drop rapidly, reducing the Thomson scattering rate, and so the photons will decouple from the plasma. This epoch is termed **recombination**.

The photons can be described by their distribution function, $f(t, \mathbf{x}, E, \hat{\mathbf{p}})$. This gives the probability that at time t , a particle will be at position, \mathbf{x} , travelling with momentum of magnitude⁴, E , in a direction defined by the unit vector $\hat{\mathbf{p}}$. For a homogeneous and isotropic Universe, the photon distribution does not depend on position nor direction, and so the distribution only depends on how the magnitude of the momentum varies with time. For an equilibrium distribution of photons, this is given by the Bose-Einstein

⁴Note that as $c=1$, the magnitude of the photons momentum is equal to their energy, so this quantity is given the symbol E .

function:

$$f(t, E) = \frac{1}{e^{E(t)/k_b T(t)} - 1} \quad (1.9)$$

where k_b is the Boltzmann constant. The energy density is given by:

$$\rho(E) = g(E)f(E)EdE \quad (1.10)$$

where $g(E)dE$ is the number of energy states with energy in the interval dE . Re-instating the correct factors of h and c , this gives the familiar black body energy distribution:

$$\rho(\nu) = \frac{8\pi h}{c^3} \frac{\nu^3}{e^{h\nu/k_b T} - 1} \quad (1.11)$$

After recombination, the photons can evolve freely, affected only by the expansion of the Universe. From the continuity equation it can be shown that temperature and frequency of the photons scale as a^{-1} . The CMB frequency spectrum will therefore have a black body spectrum, but with an amplitude much smaller than that of the photons before decoupling due to the expansion of the Universe since that time. The $2.73K$ black body spectrum of the CMB was measured by the FIRAS instrument on the COBE satellite (Mather, J. C. et al. (1994)), as predicted by the Big Bang model. This is shown in Fig 1.1.

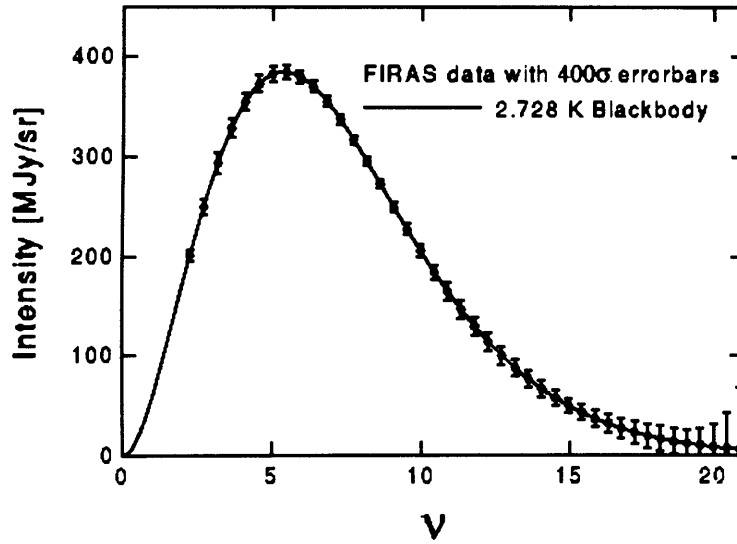


Figure 1.1: The frequency spectrum of the CMB as measured by COBE (Mather, J. C. et al. (1994)). The x-axis has units of cm^{-1} .

In a Universe without any initial inhomogeneities, this black body distribution would completely describe the CMB. However, the fact that galaxies and galaxy clusters exist means that there must have been some density variations in the early Universe to provide

the seeds for this structure. The next Section describes how these inhomogeneities create anisotropies in the CMB temperature distribution.

1.1.2 The CMB temperature anisotropies

Perturbations at decoupling

In the standard Big Bang model, structure is formed out of this homogenous background of particles through the **gravitational instability paradigm**. In this scenario, small deviations from homogeneity in the mass-energy distribution occur due to quantum mechanical fluctuations in the early Universe. These perturbations grow into structure through gravitational instability. Standard physics cannot be used to predict how these fluctuations are produced as if we go far enough back in time conditions become so extreme that current theories of particle physics and gravity will break down. In order to predict the inhomogeneities in the CMB it is therefore necessary to assume that the Universe contains small perturbations to homogeneity after a certain epoch in which General Relativity and standard particle physics can be used. The spectrum of these perturbations can be parameterized, adding a number of new **initial condition parameters** to the list of parameters which need to be determined from observations. Currently the most plausible way in which these perturbations can be generated is called inflation. This is discussed in Section 1.1.4.

To calculate the influence of these inhomogeneities on the CMB, we need to determine their effect on the photon distribution at the time of decoupling. The density perturbations are described by their deviation from the average density:

$$\delta = \frac{\delta\rho}{\rho} \quad (1.12)$$

It is useful to picture these perturbations in terms of waves or fluctuation **modes** in the homogeneous background with different spatial wavelengths λ . The amplitude of each mode, $\delta(k)$, gives the size of the density fluctuation on each scale, where the magnitude the wave vector, k , is $2\pi/\lambda$. The evolution of the different modes will depend on the scale of the perturbation.

There are two events which will affect the amplitude of each mode, **matter-radiation equality** and **decoupling**. The expansion of the Universe will also mean there are two important scales affecting each mode, the **horizon size** (the maximum distance light can travel since the start of the Universe) and the **Jeans length** (the largest scale at which pressure fluctuations will be strong enough to resist gravitational collapse).

Scales bigger than the horizon are not affected by any causal processes and so evolve as if they were in a separate Universe. When a mode is outside the horizon, the density

perturbations for both photons and matter will behave in the same way. This evolution depends on how the perturbations are defined with respect to the unperturbed background, which is determined by the choice of **gauge**. As will be discussed in Section 1.1.2, the two most commonly used gauges are the Newtonian gauge, in which super horizon modes remain constant, and the synchronous gauge in which super horizon modes will grow. When a mode crosses the horizon its subsequent evolution depends on if the horizon crossing occurs in the RDE or the MDE. Small scale modes will enter the horizon in the RDE. In this case, the growth of the CDM matter slows down compared to that before horizon crossing. This is due to the fact that photons can free-stream out of the perturbations. This motion will also inhibit the growth of the metric perturbations since the photons are the dominant component influencing the metric.

After matter-radiation equality, CDM will become the dominant component and so the growth of the metric and CDM perturbations is no longer suppressed. However, for scales which are smaller than the Jeans length, Thomson scattering will create a pressure which opposes the gravitational collapse of the baryons and photons causing the photon-baryon fluid to oscillate. These oscillations will occur up until the photons decouple and so the amplitude of each mode at decoupling will depend on the stage the mode is at in its oscillation. The baryon density will also oscillate with the photons until decoupling, at which point the baryon perturbations on each scale will catch up with those in the CDM. Decoupling occurs just after matter-radiation equality, and so the growth rate of the CDM perturbations will have been suppressed until only slightly before this time. The metric perturbations will therefore still be relatively small. This is the reason that the fluctuations in the CMB are so small compared to perturbations in the matter density seen today. In summary:

- The evolution of super horizon modes is gauge dependent. In the Newtonian gauge super horizon perturbations will remain constant, while in the synchronous gauge they will grow. This is the same in both the RDE and the MDE.
- Sub horizon modes:
 - in RDE
 - * growth of all perturbations is suppressed compared to that before horizon crossing due to the free-streaming of the photons,
 - in MDE before decoupling
 - * growth of CDM (and hence metric) no longer suppressed,
 - * perturbations in photons and baryons for modes smaller than Jeans length will oscillate,

- in MDE after decoupling
 - * photon perturbations are not strongly coupled to the metric (as they are no longer coupled to baryons), so will remain constant,
 - * baryon perturbations can grow as they are no longer coupled to the photons,
 - * CDM perturbations continue to grow.

The next section shows how to extend the formalism set up in the Section 1.1.1 for describing the photon distribution to calculate the amplitude and phase of each of the modes in the photon perturbations at the time of decoupling. In the unperturbed case, the photon distribution can be involved simply by using the fluid equations and the expanding metric of the background space-time. When inhomogeneities are present, we must now include the perturbations these create in both the metric and the photon distribution, which makes the calculation more complicated.

Calculating the perturbations at decoupling

In Section 1.1.1 we saw that if the photons are in equilibrium at decoupling their distribution function will be a Bose-Einstein distribution. This will evolve only due to the effects of expansion on the energy density and temperature of the Universe, which can be calculated using the Einstein equations. However, when we add inhomogeneities this will lead to perturbations in the photon distribution and the equilibrium distribution is no longer correct. The perturbed distribution function is given by (Dodelson (2003)):

$$f(\mathbf{x}, E, \hat{\mathbf{p}}, t) = \left[\exp \left(\frac{E}{k_b T(t) [1 + \Theta((\mathbf{x}, \hat{\mathbf{p}}, t))]} \right) - 1 \right]^{-1} \quad (1.13)$$

where $\Theta(\mathbf{x})$ is the perturbation to the temperature field, $\Theta = \delta T/T$. Θ depends on both the position of the photons, \mathbf{x} , and the direction of the photons, $\hat{\mathbf{p}}$. The fluid picture of the photons is no longer valid as the introduction of perturbations gives the photon distribution a directional dependence and the motion of individual particles becomes important. This can be thought of as treating the photons as a gas instead of as a fluid. It is therefore not enough to calculate just the continuity and Euler equations. Instead, the evolution of the photons can be determined from the Boltzmann equation:

$$\frac{Df}{Dt} = C[f] \quad (1.14)$$

where $C[f]$ are the collision terms. For photons at recombination this term is due to the Compton scattering between photons and electrons and depends on the electron density, the Thomson scattering cross-section, the baryon velocity and the photon distribution. If

there where no collision terms the Boltzmann equation would be equivalent to a **photon geodesic equation** which is just a mathematical statement of the fact that photons will move on the straightest possible path through the perturbed space-time. This incorporates all of the gravitational effects on the photons so is obviously dependent on the form of the perturbed metric. As mentioned before, it is useful to expand the temperature perturbation in terms of its Fourier modes, $\Theta(\mathbf{k}, \hat{\mathbf{p}}, t)$. The directional dependence of each mode will depend only on the angle between the wave vector, \mathbf{k} , and the photon direction. It is therefore convenient to describe the direction in terms of μ the cosine of the angle between these two directions:

$$\mu = \hat{\mathbf{k}} \cdot \hat{\mathbf{p}} \quad (1.15)$$

and the magnitude of the wavevector k . The angular dependence of the photon distribution function can then be expressed more clearly by expanding each Fourier mode in terms of its multipole moments, Θ_ℓ :

$$\Theta_\ell(k, t) \equiv \frac{1}{(-i)^\ell} \int \frac{d\mu}{2} \mathcal{P}_\ell(\mu) \Theta(k, \mu, t) \quad (1.16)$$

In real space, the different multipoles, $\Theta_\ell(\mathbf{x}, \mu, t)$, can be thought of as the size of the temperature difference if an observer is at a point \mathbf{x} , at time t and compares the temperature in different directions. For the monopole, Θ_0 , there will be no difference in the temperature perturbation from any two directions, for the dipole, Θ_1 , the biggest difference will occur if the two directions are separated by 180° , for the quadrupole, Θ_2 , if they are separated by 90° etc. The first two moments are due to the density and velocity perturbations in the photon distribution. Before recombination begins the photons are coupled tightly to the baryons. The mean free path (the distance a photon can travel before it hits an electron) will be very small and so any moments higher than the dipole will be removed by this rapid scattering. This epoch is called the **tight coupling** limit and the photons will behave as a fluid in this case with any directional dependence being lost due to the rapid scattering. The first two multipoles can therefore also be derived from the fluid equations for conservation of energy and momentum. The full Boltzmann treatment only becomes necessary during recombination when higher-order multipoles begin to develop.

The form of the perturbed metric depends on the **gauge** chosen. Einstein's equations are a set of ten equations, but only six of these equations are independent. This is because there are four degrees of freedom in the model, corresponding to a choice in the way the four coordinates used to describe the perturbations are related to the background cosmology. This choice is termed **gauge freedom**. The two main gauges used are the synchronous gauge and the Newtonian gauge. The synchronous gauge defines the perturbations in terms of the rest frame of the CDM. The Newtonian gauge defines the

perturbations with respect to a fixed background into which the Universe is expanding. Defining the metric perturbations in this way means that the equations reduce down into familiar Newtonian equations for a gravitational field in the non-relativistic limit and hence it is easier to interpret the resulting equations in terms of actual physical quantities. This Newtonian gauge will be used throughout this Chapter.

The metric is no longer diagonal and can be written in the form:

$$g_{\mu\nu} = g_{\mu\nu}^{frw} + h_{\mu\nu} \quad (1.17)$$

where $g_{\mu\nu}^{frw}$ is the FRW metric describing the background space-time (Equation 1.3) and $h_{\mu\nu}$ are the perturbations to the metric. For the perturbed metric, $h_{\mu\nu}$ is non-zero and the metric line element takes the form (in the Newtonian gauge):

$$ds^2 = -(1 + 2\Psi)dt^2 + a^2[(1 + 2\Phi)\delta_{ij} + 2H_{ij}]dx^i dx^j + 2aB_i dx^i dt \quad (1.18)$$

This introduces four new terms, Ψ and Φ , the scalar perturbation potentials, B_i , the vector perturbation potential, and H_{ij} , the tensor or gravitational wave potential. It is useful to split the metric into these three components as the effects of scalar, vector and tensor perturbations are decoupled. This means that the fluctuations in the CMB due to scalar metric perturbations can be calculated independently of the fluctuations due to tensor perturbations. This is called the **decomposition theorem**. Vector perturbations create a vorticity or rotational motion which, unlike the perturbations caused by scalars and tensors, will not be enhanced by gravitational collapse. As the Universe expands, any initial vector perturbations will be strongly damped and so are expected to have no effect on the CMB as they are negligible at recombination. The only way vector perturbations could be important is if for some reason perturbations are continually being created up until recombination, however, models in which this occurs are much more exotic than the standard inflationary models (which predict no contribution to the CMB anisotropy from vector perturbations) and so are not part of the current standard cosmological model. Scalar perturbations are represented by two scalar potentials, the Newtonian potential, Ψ , and the curvature potential, Φ . In the non-relativistic limit Ψ is equivalent to the gravitational potential acting in Newtonian physics due to the gravitational effects of the baryons and the CDM. Φ represents changes to the motion of the relativistic particles due to distortions in the metric. The tensor perturbations are represented by two variables, h_+ and h_x . For a perturbation in the positive x -direction the tensor contribution to the metric will be given by:

$$H_{ij} = \begin{pmatrix} h_+ & h_x & 0 \\ h_x & -h_+ & 0 \\ 0 & 0 & 0 \end{pmatrix}. \quad (1.19)$$

The position of the non-zero components will vary depending on the direction of the perturbation. This is equivalent to the standard metric used in the description of a gravitational wave (Schutz (1985)). In fact, tensor perturbations can be thought of a spectrum of very long wavelength primordial gravitational waves.

The perturbed stress-energy tensor for the photons will no longer be diagonal once they have decoupled from the plasma. The photon distribution is now determined by four components, the density, ρ , pressure, P , used in the fluid description, and also velocity, v , and anisotropic stress (which is a tensor with components Π_{ij}) perturbations which are now present due to the directional dependence of the photon distribution. The evolution of the metric perturbations depends not only on the photons, but also on the perturbations to the CDM and baryons. The perfect fluid approximation is valid for these species through recombination and so their evolution can be determined using the continuity and Euler equations. However, the coupling of the baryons to the photons through Thomson scattering must also be taken into account, giving an extra term in the baryon Euler equation.

The evolution of the photon distribution, Θ can therefore be determined by solving the Boltzmann equation, where the coupling of the photons to the baryons depends on the optical depth for Thomson scattering, τ , which will decrease as the electron density reduces during recombination. This is coupled to the metric perturbations, Ψ, Φ, h_+, h_- , through the Einstein equations. The metric perturbations will also be effected by the CDM and baryon density and velocity perturbations, $\delta_{\text{CDM}}, \delta_b, v_{\text{CDM}}, v_b$, which evolve through the baryon and CDM continuity and Euler equations. This is summarised in Fig. 1.2. For completeness these equations in the Newtonian gauge from Seljak and Zaldarriaga (1996) are given on the next below.

photon Boltzmann equation

$$\dot{\Theta} + ik\mu\Theta = \dot{\Phi} - ik\mu\Psi - \dot{\tau} \left[\Theta_0 - \Theta + i\mu v_b + \frac{1}{2}\mathcal{P}_2(\mu)\Theta_2 \right] \quad (1.20)$$

scalar metric perturbations

$$\begin{aligned} k^2\Phi + 3\frac{\dot{a}}{a} \left(\dot{\Phi} + \frac{\dot{a}}{a}\Psi \right) &= -4\pi a^2 \delta\rho \\ k^2 \left(\dot{\Phi} + \frac{\dot{a}}{a}\Psi \right) &= 4\pi a^2 \delta f \end{aligned} \quad (1.21)$$

where $\delta\rho$ is the sum of the average density of each species, $\bar{\rho}_i$, giving $\delta\rho = \sum_i \delta_i \bar{\rho}_i$ and δf is the sum of the average momentum of each species, $\delta f = \sum_i (\bar{\rho}_i + \bar{P}_i)v_i$, where \bar{P}_i is the average pressure of each species.

tensor metric perturbations

$$\ddot{h}_i + 2\frac{\dot{a}}{a}\dot{h}_i + k^2 h_i = 0 \quad (1.22)$$

where i is either $+$ or \times .

CDM fluid equations

$$\begin{aligned} \dot{\delta}_{CDM} &= -kv_{CDM} + 3\dot{\Phi}, \\ \dot{v}_{CDM} &= -\frac{\dot{a}}{a}v_{CDM} + k\Psi \end{aligned} \quad (1.23)$$

baryon fluid equations

$$\begin{aligned} \dot{\delta}_b &= -kv_b + 3\dot{\Phi}, \\ \dot{v}_b &= -\frac{\dot{a}}{a}v_b + k\Psi + c_s^2 k\delta_b + \frac{\dot{\tau}}{R}(3\Theta_1 - v_b) \end{aligned} \quad (1.24)$$

where $R = 4\bar{\rho}_r/3\bar{\rho}_b$ and \mathcal{P}_2 is the second Legendre polynomial.

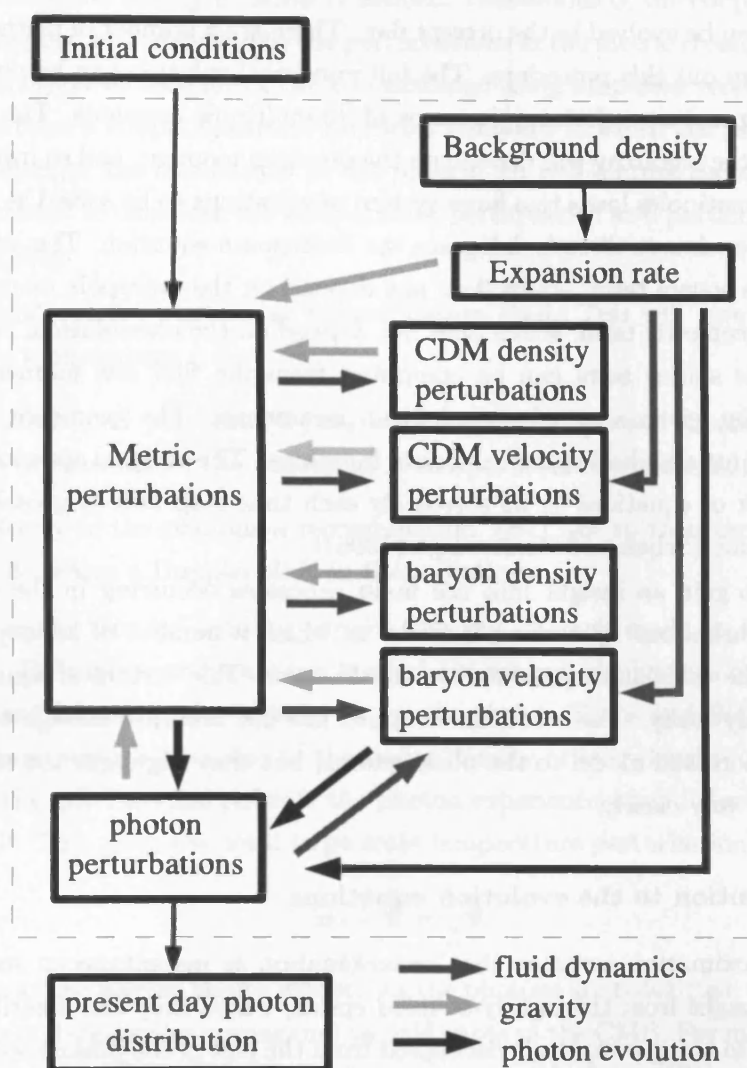


Figure 1.2: An initial spectrum of metric perturbations is set up early on in the RDE of the Universe. The evolution of these perturbations is governed gravitationally through the perturbed Einstein equations, which link the metric to the matter and energy distribution of the Universe, a combination of the effect of photons, baryons and dark matter. Conversely, the evolution of these components is coupled to the metric evolution through the fluid equations for the density and velocity of baryons and dark matter, and through the Boltzmann equation for the evolution of the photons. In addition, there is a coupling of the baryons and photons through Thomson scattering. The average background energy density of the Universe (determined through Friedmann and zero-order Einstein equations by the total matter density and the dark energy) will determine the expansion rate which will influence the evolution of the different perturbations. This set of coupled equations can be evolved from the initial conditions to the present day to determine the photon distribution today.

To find the present day temperature distribution of the CMB, $\Theta(k, \mu, t_0)$, the initial metric fluctuations need to be defined at some epoch before recombination. This system of equations can then be evolved to the present day. There are a number of methods which can be used to carry out this procedure. The full numerical solution can be obtained by expanding the temperature anisotropy in terms of its multipole moments. The evolution of each moment in the hierarchy will depend on the previous moment, and so involving the hierarchy for high multipoles leads to a large system of equations to be solved at each time step. A faster approach is to directly integrate the Boltzmann equation. The integral can be separated into a source term, which does not depend on the multipole moment being calculated, and a geometric term, which does not depend on the cosmological parameters in the model. The source term can be computed from the first few moments of the Boltzmann hierarchy, given a set of cosmological parameters. The geometric terms for each multipole are just standard spherical Bessel functions. The integral approach greatly reduces the number of equations to be solved for each time step and so greatly reduces the computation time (Seljak and Zaldarriaga (1996)).

It is possible to gain an insight into the main processes occurring in the formation of the photon perturbations by making a model in which a number of assumptions are made to simplify the calculation presented in this Section. This system of equations can then be solved analytically. The solutions obtained are not accurate enough to be used to compare the theoretical model to the observations, but they highlight the main areas of physics involved very clearly.

Approximate solution to the evolution equations

The analytic approximation assumes that recombination is instantaneous so that the photons will go straight from the tightly-coupled epoch, where they can be described solely by fluid equations, to being completely decoupled from the rest of the plasma so that their evolution depends only on the expansion of the Universe. This approximation means that only the first two multipoles, Θ_0 and Θ_1 are needed to describe the photon distribution and that the two metric perturbations are given by $\Psi = -\Phi$, so that only one metric perturbation term is needed⁵ (Hu and Sugiyama (1995)). A second assumption is that the Universe is totally matter-dominated at the recombination epoch. This means that the metric perturbations will be constant during and after recombination as the photon

⁵This follows from another component of the Einstein equations for the metric perturbation:

$$k^2(\Psi + \Phi) \propto \Pi \quad (1.25)$$

where Π is a component of the anisotropic stress. Although this gives no new information over Equations 1.21, it clearly illustrates that we have $\Psi = -\Phi$ as we are assuming that the anisotropic stress at this epoch will be negligible.

oscillations will have no effect on the metric. The photon perturbations at recombination can then be described simply in terms of acoustic oscillations of the coupled photons and baryons inside potential wells due to the perturbations in the metric created by CDM. The monopole and dipole at decoupling can be calculated using simplified versions of equations 1.20 - 1.24 to form a simple harmonic oscillator equation in which the potentials provide the driving force for the oscillations in the plasma. In this picture there are three main parameters needed to calculate the temperature perturbation at a particular point on the sky at decoupling:

- The density of the photons at recombination (Θ_0). This will give the photons an intrinsic temperature.
- The gravitational potential (Ψ) at recombination. This will create a gravitational redshift or blueshift of the photon as it escapes from the potential well.
- The velocity of the photons at recombination, (Θ_1) due to their oscillatory motion. This will create a Doppler shift in the radiation.

This simple model can be used to predict the size of each mode in the temperature perturbation. For modes which are too big to have entered the horizon before decoupling there are no oscillations in the plasma. It can be shown (Sachs and Wolfe (1967)), that the temperature perturbation due to the under density or over density of the photons is $\Theta_0 = -\frac{2}{3}\Psi$. The gravitational redshift the photon experiences when it leaves the potential well will be Ψ . This gives the total large scale temperature perturbation as:

$$\Theta_0 + \Psi = \frac{1}{3}\Psi \quad (1.26)$$

This is known as the **Sachs-Wolfe effect**. As the photons are redshifted, the temperature perturbations on large scales correspond to cold spots in the CMB. For modes which have entered the horizon before decoupling, the metric perturbations will remain constant (as they entered the horizon in the MDE), but the photon perturbations can begin to collapse. The density of the photons will therefore increase and the gravitational redshift term no longer be dominant as we move to smaller scales. This will be the case for large-scale sub-horizon modes. For smaller modes which entered the horizon sooner, the photons will have begun to oscillate and so the amplitude of the mode will depend upon what stage the oscillation has reached by decoupling. In addition, the sub-horizon modes will also have a contribution from the dipole perturbation as the oscillations will create a fluid velocity in the photons, this will be out of phase with the monopole term. When the density perturbation is at a maximum the fluid velocity will be zero and when the density perturbation is zero, the velocity perturbation will be maximum. This adds a smaller term which is 90° out of phase with the monopole to the temperature perturbation.

Despite its simplicity, this analytic solution to the perturbed Boltzmann-Einstein equations can predict most of the key features that come out of the full solution. However, a number of other physical effects are also very important and must also be discussed in order to understand the observations of CMB temperature anisotropies. These effects will also be important when we go on to discuss the physics of CMB polarization.

Diffusion damping

The model used so far assumes that photons and baryons can be treated as a single fluid throughout recombination. However, the photons are able to move a small distance through the photon-baryon plasma given by the photon mean free path, so this fluid approximation breaks down on small scales. The photons can random walk a number of mean free paths in the time before decoupling, giving a characteristic distance that the photons can travel, the **diffusion length**. This motion will damp out fluctuations on scales smaller than the diffusion length as photons from hot and cold regions can mix and smooth out the temperature distribution. This means that before recombination, the smallest scale fluctuations will be very strongly damped. During recombination, before the photons completely decouple, the diffusion length will increase and perturbations on larger scales will become damped. This creates an exponential drop-off in the amplitude of the perturbations at small scales, with the smallest scales being damped the most as these will have been within the diffusion length for the longest time. This effect is often called Silk damping as it was first calculated by Silk (1968).

Integrated Sachs-Wolfe effect (ISW)

The Sachs-Wolfe effect is the change in energy of photon due to gravitational red-shift as it climbs out of a region where the metric perturbation is high. This occurs at last scattering when the photons decouple from matter. However, the same effect can also occur when the photons pass through metric perturbations as they travel towards us from the last scattering surface. For most of this journey the blue-shift a photon experiences as it falls into an over-dense region is cancelled by the red-shift it experiences as it climbs back out. However, if the amplitude of the metric perturbation changes during this time, there will be a change in the photon's energy. This situation can occur at two different epochs:

Early time ISW: In the matter dominated era, the metric perturbations will not vary in the time it takes a photons to travel through them. However, for a short period after recombination the Universe is not completely matter dominated and the effects of radiation in the metric will still be important. Radiation causes the amplitude of a perturbation to oscillate once the scale of the perturbation enters the horizon. The temperature distribution on scales that enter the horizon just after recombination will

therefore show an increased anisotropy at around the scale of the horizon at recombination due to this effect.

Late time ISW: At present, the Universe is thought to be changing from an epoch of matter domination to an epoch in which dark energy dominates. This causes the expansion of the Universe to accelerate and so the metric perturbations will begin to stretch and so will decay as the CMB photons travel through them. On small scales this effect will be negligible as the photons will travel through roughly the same number of under densities as over densities and so there will be no net change to the temperature anisotropy. However, this cancellation will not occur on larger scales. At this effect occurs at late times, the angle subtended by these scales will be large and so the late-time ISW causes an increase in the temperature anisotropy on very large scales.

Early reionization

Diffusion damping causes a decrease in the size of the perturbations on scales below the diffusion length at recombination. A similar effect will occur when the Universe reionizes due to the first generation of stars and quasars (Hu and White (1997b)). The diffusion length at this time will be the size of the horizon and so all modes inside the horizon when reionization occurs will be damped by the same amount. The earlier reionization occurs, the more severe the damping will be as there will have been more time for the anisotropies to become damped.

We now have a picture of the fluctuations in the CMB at the time of decoupling, and of how these fluctuations have evolved since then. However, we do not directly observe the individual modes of the fluctuation, instead we observe these modes projected onto the curved surface of the sky. This introduces a mapping between the three-dimensional photon distribution we have discussed so far and the two-dimensional surface over which the fluctuations are observed.

1.1.3 Observing the CMB

When we decompose the fluctuations of the photon distribution into k -modes we are simply taking the Fourier transform of the distribution. As the Universe can be assumed to be infinite, this gives a continuous spectrum of k values. When the photon distribution is projected onto the surface of a sphere, the Fourier transform can no longer be used. Instead, the most suitable functions for describing fluctuations on the surface of a sphere are spherical harmonics, $Y_{\ell m}(\theta, \phi)$. The subscripts ℓ and m are the integers describing the mode of radiation where, $\ell = 0, 1, \dots, \infty$, and for each ℓ value, $m = -\ell, \dots, \ell$. A sphere has well defined boundaries and so the spectrum of different modes has now become discrete. In this case, the integral used to define the Fourier transform becomes a summation over

discrete modes:

$$\frac{\Delta T(\theta, \phi)}{T_o} = \sum_{\ell} \sum_m T_{\ell m} Y_{\ell m}(\theta, \phi) \quad (1.27)$$

where ΔT is the deviation of the temperature field from its average value T_o . For the spherical harmonic expansion, the mode amplitudes, $T_{\ell m}$ are known as multipole moments.

The variance of each moment is then:

$$\langle T_{\ell m}^* T_{\ell' m'} \rangle = C_{\ell}^{TT} \delta_{\ell \ell'} \delta_{m m'} \quad (1.28)$$

C_{ℓ}^{TT} is the temperature power spectrum and contains all the information about the temperature field fluctuations. This is the spherical harmonic equivalent of the usual Fourier power spectrum described in Appendix A. To obtain the power spectrum we are effectively averaging over the different values of m for each multipole. This can be done because the Universe is isotropic and so each value of m can be thought of as a different realization of the same measurement. There is only a single Universe in which the CMB can be measured and there are only $2\ell + 1$ possible measurements of each multipole. This sets a fundamental limit on how well each multipole can be measured due to the sample variance associated with measuring a quantity from a finite sample of data. This is known as **cosmic variance**. The cosmic variance is higher for low multipoles as there are fewer values of m to average over.

It is important to note that these multipole moments are **not the same** as those used in the angular expansion of the photon perturbations in Section 1.1.2. In this case, $T_{\ell, m}$ are the multipole moments of the temperature distribution projected using spherical harmonics onto a sphere surrounding the Earth today. In the previous case, $\Theta_{\ell}(\mathbf{x}, t)$ are the multipole moments of the radiation field surrounding a particular point, \mathbf{x} , in the Universe at a time t projected out using Legendre polynomials. The CMB temperature power spectrum is related to the multipoles in the photon temperature distribution seen today by (Seljak and Zaldarriaga (1996)):

$$C_{\ell}^{(X)} = (4\pi)^2 \int k^2 dk P_{\Psi} | \Theta_{\ell}^{(X)}(k, t = t_0) |^2 \quad (1.29)$$

where X is either S (for scalar contribution) or T (for tensor contribution). The total power spectrum will be the sum of the tensor and scalar parts. P_{Ψ} is the power spectrum of the initial perturbations to the metric. This will be discussed further in Section (1.1.4).

To find the anisotropies in the CMB temperature which are seen today, the perturbations at decoupling need to be projected out onto a sphere surrounding the Earth at the distance the radiation has travelled since decoupling, D . This projects the spatial fluctuations at decoupling into the angular anisotropies we can observe today. By simple geometry, a perturbation with a wavenumber k (so a size of $1/k$) will subtend an angle

$1/\ell \approx 1/kD$ on the sky, so the dominant contribution to the power spectrum for each ℓ will be from modes with $k \approx \ell/D$. For the tight-coupling approximation in the previous section, this projection can be expressed as (Hu and Sugiyama (1995)):

$$\begin{aligned} \Theta_\ell(\eta_0, k) \approx & [\Theta_0 + \Psi](\eta_*) (2\ell + 1) j_\ell(kD) \\ & + \Theta_1(\eta_*) [\ell j_{\ell-1}(kD) - (\ell + 1) j_{\ell+1}(kD)] \end{aligned} \quad (1.30)$$

where j_ℓ are spherical Bessel functions, the conformal time, η , is defined as $d\eta = dt/a(t)$, η_0 is the conformal time at present and η_* is the conformal time at recombination. The first term represents the contribution of the monopole at recombination to the anisotropy seen today for each k -mode, and the second term is the same for the dipole. The total anisotropy on each angular scale is then found by summing the contribution from each k -mode as in Equation 1.29. Fig. 1.3 shows the spherical Bessel function for a number of different multipoles. The functions peak when $kD \approx \ell$, so that, as stated previously, the main contribution to C_ℓ for each ℓ will come mainly from a single k -mode at recombination.

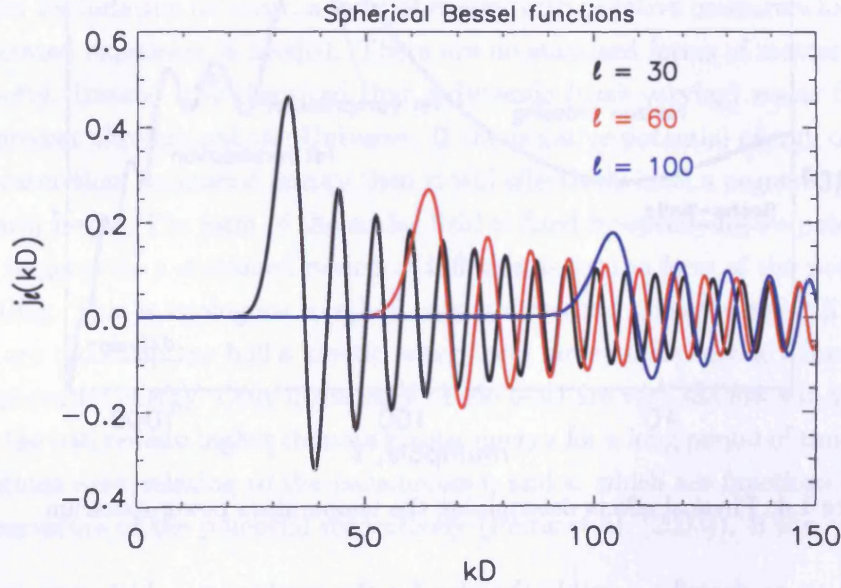


Figure 1.3: Spherical Bessel function used in the projection of spatial perturbations at recombination to angular anisotropies seen today. The functions peak at $kD \approx \ell$ so that the dominant contribution to the anisotropy on each angular scale comes from a particular k -mode.

This correspondence between k -mode at last scattering and ℓ -scale in the anisotropy spectrum means it is possible to interpret the temperature power spectrum in terms of the amplitude of the modes on different scales. On large scales, the anisotropy will be due to large scale modes which have not entered the horizon by decoupling and so the

spectrum should be flat, as predicted by the Sachs-Wolfe effect. There is a slight excess of power on the largest scales due to the late time integrated Sachs-Wolfe effect. The anisotropy will then increase as the modes enter the horizon until the first peak in the power spectrum is reached. The series of acoustic peaks will then correspond to modes that have had time to oscillate since entering the horizon. The first peak is due to the mode which has had to just reach its first maximum compression at decoupling, the second peak is due to the mode which has compressed and then rarefied etc. The 90° phase shift in the velocity perturbations means that the dipole contribution fills in the troughs in the power spectrum so that the difference in amplitude between the peaks and the troughs is smaller. At small scales the amplitude of the acoustic peaks is reduced due to photon diffusion. The different parts of the temperature power are shown in Fig. (1.4).

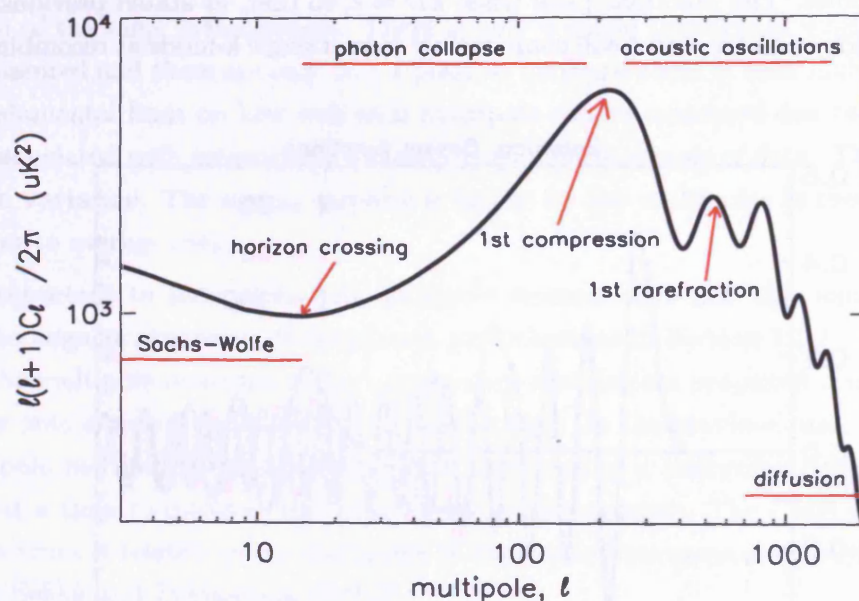


Figure 1.4: Physical effects determining the temperature power spectrum

We now go on to describe possible theories for the mechanism which generates the initial perturbations which create the CMB anisotropy.

1.1.4 Initial conditions - inflation

Inflation is a period in which the expansion of the Universe accelerates. In itself, the theory of inflation does not explain how the perturbations in the Universe at the time of decoupling came to be. Instead it is a mechanism by which fluctuations in the energy distribution in the primordial Universe, which occur naturally as a result of the quantum

nature the Universe at this time, became the large scale fluctuations needed to generate the CMB anisotropies.

Inflation was initially proposed by Guth (1981) in order to solve a number of problems in the Big Bang model. The problem most relevant to the CMB is the horizon problem. The detection of the CMB as a uniform background indicates that the Universe is isotropic even on very large scales that could never have been in causal contact, as there has not been time for information to travel over such large distances. However, inflation proposes a period of accelerated expansion during which the size of the Universe grows much faster than the horizon size. This means that scales which were initially inside the horizon will be stretched outside the horizon. Once inflation has finished, scales which were previously inside the horizon will no longer be in causal contact, but because there was thermal equilibrium over these distance before inflation the Universe will still have large scale homogeneity. This period of expansion also allows the tiny quantum fluctuations to stretch to much larger scales and so explains the existence of large-scale fluctuations after inflation.

In order for inflation to occur, a form of energy with negative pressure which can drive the accelerated expansion is needed. There are no standard forms of matter which have this property. Instead it is theorized that a dynamic (time varying) scalar field, Φ , was initially present through-out the Universe. If the negative potential energy of this scalar field is greater than its kinetic energy then it will effectively have a negative pressure and inflation will begin. The form of the scalar field is fixed by specifying its potential $V(\Phi)$. One way to generate a sustained period of inflation is for the form of the potential to be **slow rolling**. This is analogous to a ball rolling down the side of a bowl. If the sides of the bowl are too steep the ball's kinetic energy will increase and quickly become greater than its' potential energy. Only if the sides of the bowl are very shallow will the potential energy of the ball remain higher than its kinetic energy for a long period of time. Two slow roll conditions exist relating to the parameters η and ϵ , which are functions of the slope and the curvature of the potential respectively (Peiris et al. (2003)). If the conditions:

$$\eta \ll 1, \quad \epsilon \ll 1 \quad (1.31)$$

are met then inflation will occur. If the form of the potential is chosen such that these conditions are met then the potential is a valid inflationary potential. There are many different inflationary models corresponding to different forms of the potential. For a given potential, the size of the fluctuations when inflation ends can be found, as this will occur when the slow roll conditions are violated. This can then be evolved backwards in time using the equations of motion of the scalar field to the point at which a given scale exits the horizon. Once this has occurred, the perturbation cannot evolve until it re-enters

the horizon after inflation and so this will be the initial size of the perturbation which creates the metric perturbations influencing the CMB. The range of scales influencing the CMB will all exit the horizon at about the same time. It is therefore possible to define the **energy scale of inflation** as the size of the potential when these scales exited the horizon.

The initial scalar perturbations are parameterized by:

$$\Delta_{\mathcal{R}}^2(k) = \Delta_{\mathcal{R}}^2(k_0) \left(\frac{k}{k_0} \right)^{n_s-1}, \quad (1.32)$$

where $\Delta_{\mathcal{R}}^2(k)$ is the power spectrum of \mathcal{R} , the curvature perturbation in the comoving gauge (one in which the observer's coordinates stretch along with the expansion), and n_s is the slope of the scalar power spectrum. The tensor perturbations are given by:

$$\Delta_T^2(k) = \Delta_T^2(k_0) \left(\frac{k}{k_0} \right)^{n_t}, \quad (1.33)$$

where $\Delta_T^2(k)$ is the power spectrum of gravitational waves from inflation and n_t is the slope of the gravitational wave power spectrum. The amplitude terms are evaluated at the pivot wave number, $k_0 = 0.05 \text{Mpc}^{-1}$. When discussing inflation it is useful to define the scalar perturbation in terms of a curvature perturbation, \mathcal{R} , instead of directly using the Newtonian potential Ψ defined in Section 1.1.2. This is because \mathcal{R} is directly related to the inflation potential at horizon exit and remains constant until a given scale has re-entered the horizon (as opposed the actual scalar field perturbations which do not). The perturbations generated by inflation can therefore be described in the simplest case by four numbers, the amplitude of the scalar spectrum, $\Delta_{\mathcal{R}}^2(k_0)$, the tilt of the scalar spectrum, n_s , the amplitude of the tensor spectrum $\Delta_T^2(k_0)$, and the tilt of the tensor spectrum, n_t . However, instead of referring directly to the amplitudes of the two power spectra, it is often convenient to define two alternative parameters, A , the amplitude parameter, and r , the tensor to scalar ratio. A is a number of order unity. If the scalar power spectrum is calculated assuming that $\Delta_{\Psi}^2(k_0) = 1$, then A is the factor which this quantity needs to be scaled to match the observational data. This definition is used in order that a direct comparison with the WMAP results can be made. In the version of CMBFAST used in the WMAP analysis, the scalar perturbations are defined in terms of Ψ , as opposed to \mathcal{R} , and a value of $\Delta_{\Psi}^2(k_0) = 1$ is used to give the unnormalized CMBFAST output. The parameter A is related to $\Delta_{\mathcal{R}}^2(k_0)$ by (Peiris et al. (2003)):

$$\Delta_{\mathcal{R}}^2(k_0) = 800\pi^2 \frac{25}{9} \frac{1}{T_{CMB}^2} A \quad (1.34)$$

The tensor to scalar ratio⁶ is defined as:

$$r = \frac{\Delta_T^2(k_0)}{\Delta_{\mathcal{R}}^2(k_0)}. \quad (1.37)$$

A generic prediction of slow roll inflation is that r and n_t are not independent but are related by:

$$r = -2n_t. \quad (1.38)$$

This is called the **consistency relation**. The key observational parameters which can be used to distinguish between simple inflationary models are therefore r and n_s . These parameters are directly related to the inflationary potential. In particular, the amplitude of the tensor spectrum gives us the size of the potential at horizon crossing and hence the energy scale of inflation. A measurement of r is therefore one of the holy grails of observation cosmology as knowing this energy scale would allow us to determine the state of the Universe during inflation allowing us to probe back in time to the earliest moments of the Universe. However, even in the most optimistic models, r is predicted to be extremely small and so a detection of this signal is a huge experimental challenge.

A key test for the concept of inflation is the presence of super-horizon fluctuations in the CMB power spectra. These can only occur if there is some inflation-like mechanism which can stretch the primordial fluctuations out to this scale. Other mechanisms for structure formation can only create perturbations on sub-horizon scales and so are ruled out by the presence of large-scale fluctuations. The presence of acoustic oscillations in the CMB can also be seen as a signature of inflation. In inflationary models, all modes of a given scale will begin to oscillate at exactly the same time (when the mode re-enters the horizon). This means they will oscillate in phase. This phase coherence is needed for acoustic oscillations to be created at decoupling. In other models, perturbations on the same scale can be created at different times and so will not necessarily oscillate in phase and could therefore cancel out over time. If super-horizon fluctuations and acoustic oscillations are not present in the CMB spectrum this would rule out inflation. The most solid test for inflation would be an observational validation of the consistency relationship as it is highly unlikely that any other mechanism would produce exactly the

⁶A number of different definitions are used in the literature. The most common alternatives are to define r in terms of the Newtonian potential:

$$r_\Psi = \frac{\Delta_T^2(k_0)}{\Delta_\Psi^2(k_0)}, \quad (1.35)$$

so that $r_\Psi \simeq (5/3)^2 r$, or in terms of the CMB radiation quadruples:

$$r_Q = \frac{C_2^T}{C_2^S} \quad (1.36)$$

The relation between r and r_Q depends on the cosmological parameters used in the model.

same relationship. However, measuring n_t is even more difficult than measuring r .

The simplest possible model for the initial perturbations is that of a scale-invariant ($n_s = 1$) spectrum (often called a Harrison-Zel'dovich spectrum). This is motivated by the fact that conditions will not change much over the short timescale in which all of the relevant modes will exit the horizon. There is strong observational evidence that $n_s \approx 1$ (e.g. WMAP first year results). Any deviations from this gives a red ($n_s < 1$) or a blue spectrum ($n_s > 1$). A further extension to this model is to allow the spectral index to vary with scale. This is referred to a 'running of the spectral index' and is parameterized by defining the spectral index as:

$$n_s(k) = n_s(k_0) + \frac{dn_s}{d \ln k} \ln \left(\frac{k}{k_0} \right). \quad (1.39)$$

It is possible to generate a wide range of possible values of these parameters by defining different forms for the potential. It is also possible to extend the model even further to include more than one dynamic potential using hybrid inflation models.

The perturbations discussed so far are actual perturbations to the metric and hence the curvature of space-time. These are called **adiabatic** perturbations as there is no change in the entropy of the Universe due to the perturbation (a more descriptive name is isentropic perturbations). However, it is also possible for fluctuations to occur in the relative abundances of different particles (entropy fluctuations) without changes the curvature. These are called **isocurvature perturbations**. Hybrid inflation would be needed to explain the existence of this kind of perturbations as it cannot be generated with a single scalar field. This would also complicate the parameterization further by introducing any number of new initial power spectra corresponding to different types of isocurvature fluctuations.

1.1.5 Status of CMB temperature observations

The detection of the CMB by Penzias and Wilson (1965) paved the way for a generation of experiments attempting to measure the CMB anisotropies. The COBE satellite (Smoot et al. (1992)) confirmed the presence of anisotropies in the CMB and its measurement of this anisotropy on large angular scales supported the case for the existence of super horizon fluctuations at last scattering.

The large-scale COBE measurement was followed by a series of ground-based and balloon experiments aiming to measure the first peak in the temperature power spectrum. If the current paradigm is correct, the position of this peak gives the size of the horizon at recombination. The angular scale subtended by the peak depends on the curvature of the Universe, and so the position of this peak can be used to infer if the Universe

flat. Measurements from a number of experiments, in particular, BOOMERANG (Masi, S. et al (2003)) and MAXIMA (Hanany, S. et al. (2000)) confirmed the existence of the first acoustic peak at $\ell \sim 200$. This location is consistent with a flat Universe. These measurement were then extended out to smaller angular scales by interferometric experiments such as the VSA (Grainge, K. et al. (2003)), DASI (Halverson, N. W et al. (2002)) and CBI (Pearson T. J. et al. (2003)), confirming the existence of the series of acoustic peaks which can only be created if the initial perturbations are coherent, ruling out a number of competing theories to inflation.

CMB temperature measurements culminated in the recent results of the WMAP satellite which measured the temperaure anisotropy out to $\ell \sim 600$ (Hinshaw, G. (2003)). These results are cosmic variance limited up to $\ell \sim 350$ and this range will be extended with future data sets. The WMAP observation allowed the key cosmological parameters to be measured to high precision with a single data-set. The best fit parameters were consistent with measurements made from previous observations and reinforced the emerging concordance model. The WMAP best-fit parameters are given in Table 1.1. The

Parameter	A	n_s	$dn_s/d \ln k$	h	$\Omega_m h^2$	$\Omega_b h^2$	r
Value	0.84	0.96	-0.042	0.74	0.135	0.023	< 0.71
Error	0.1	0.03	0.02	0.03	0.006	0.001	-

Table 1.1: WMAP best fit cosmological parameters. Taken from Table 9 of Spergel D.N. et al. (2003). The analysis assumes a flat Universe and so a value of Ω_{de} of 0.75 can be obtained from the matter density. This model also includes the reionization optical depth, but this is derived from polarization measurements and is discussed later in Section 1.2.5.

data favours the simplest model of a flat Universe with a near scale-invariant spectrum of gaussian adiabatic perturbations composed of baryons, dark matter and dark energy. The only hint of any deviation from this simple model is the possibility of a running of the scalar spectral index, which is favoured if additional non-CMB observations (2dF galaxy redshift survey and Lyman α forest measurements) are added to provide information from different redshifts.

The future of CMB temperature measurements therefore lies in making high resolution observations in order to constrain the higher multipoles in the power spectrum. This will not greatly improve constraints on the cosmological parameters measured by WMAP, but will begin to probe secondary effects occurring at lower redshift such as the Sunyaev-Zel'dovich (SZ) effect which causes a small spectral distortion of the CMB blackbody spectrum when CMB photons scatter off hot electrons in galaxy clusters. This will allow the CMB to be used to investigate the growth of large scale structure and the properties of clusters. Measurements as higher angular scales will also allow tighter constraints to be made on the primordial spectral index n_s . However, as this measurement requires a

knowledge of the power spectrum over a range of angular scales, combining the results from a low resolution experiment of the whole sky (such as WMAP) and a high resolution measurement on a small patch of sky (as would be obtained from a ground-based measurement) would be difficult as this would require a accurate knowledge of any calibration differences between the two experiments. However, Planck, a full-sky high-resolution satellite mission is currently under construction and is set to launch in 2007. This will provide a cosmic variance limited signal up to high ℓ . The Planck satellite will therefore provide the most precise possible measurement of the CMB temperature power spectrum on all but the smallest angular scales.

1.1.6 Key points

- The CMB is a relic of the radiation created at a redshift of 1100 when the recombination of electrons and photons allowed photons to decouple from the rest of the matter in the Universe. This radiation has been redshifted to microwave wavelengths.
- To zeroth-order the Universe can be described by a perfectly homogeneous and isotropic expanding fluid. This can be parameterized by the expansion rate, given by the Hubble parameter, h , and density parameters for baryons, Ω_b , cold dark matter, Ω_{CDM} , radiation, Ω_r , and dark energy, Ω_{de} .
- There are small initial perturbations to this homogeneous background which can begin to grow once the Universe becomes matter dominated. At recombination these perturbations are still small, but they can be observed through the anisotropies they create in the CMB.
- The level of the CMB anisotropies on different scales depend on the values of each of these densities at recombination and on the expansion of the Universe as the photons propagate through it. The CMB can therefore be used to constrain the values of the cosmological parameters.
- The initial perturbations can be decomposed into two parts, scalar perturbations and tensor perturbations. These are parameterized by power-law spectra giving four perturbation parameters, the amplitude of scalar perturbations A , the power law index (or tilt) of the scalar spectrum, n_s , the ratio of tensor-to-scalar perturbations, r , and the tilt of the tensor spectrum, n_t .
- A possible mechanism for generating these fluctuations is inflation. Measurements of these perturbation parameters can be used to test and refine the inflationary model. In particular a measurement of r directly probes the energy scales of inflation.
- The CMB anisotropies measured on the sky today are decomposed into multipole moments to give the temperature power spectrum, C_l^{TT} . This encodes all of the information on cosmological and perturbation parameters contained in the anisotropies if the initial perturbations are gaussian. The limit on how well this power spectrum can be measured is set by cosmic variance.
- The temperature power spectrum on different angular scales has been measured by a number of experiments, culminating in the recent results of the WMAP satellite. This has allowed the CMB to put tight constraints on a number of parameters.

- The upcoming Planck satellite will allow a cosmic-variance-limited measurement of the CMB up to high multipoles. The focus of future CMB temperature measurements will therefore be on observing at very small scales to look at secondary effects occurring after recombination.
- The next big challenge in CMB observations is the measurement the CMB polarization.

1.2 The polarization of the CMB

1.2.1 The Stokes parameters

We begin the discussion of the polarization of the CMB by discussing the basics of polarized light. The most fundamental way to describe electromagnetic (EM) radiation is in terms of the variation of the magnitude and orientation of its electric field vector, \mathbf{E} . For a sinusoidally varying EM wave travelling in the z direction with wavevector, k , and angular frequency, ω , the electric field at each time, t , can be described in terms of the superposition of two orthogonal waves:

$$E_x(z, t) = E_{0x} \cos(kz - \omega t) \quad (1.40)$$

$$E_y(z, t) = E_{0y} \cos(kz - \omega t + \xi) \quad (1.41)$$

For unpolarized radiation, the ratio of the amplitudes of the two components, E_{0x}/E_{0y} , and their phase difference, ξ will vary randomly with time. However, if these quantities remain constant for a time which is long compared to the vibration period of the wave, the radiation is said to be polarized. If these quantities are always constant the radiation is completely polarized.

The sense of the polarization depends on the value of ξ . If ξ is an integer multiple of π the radiation is linearly polarized and the electric field vector oscillates in a fixed plane. If ξ takes any other value the radiation is elliptically polarized and the tip of the electric field vector traces out an ellipse. We expect the CMB to be linearly polarized and so can restrict the discussion to the parameters of linearly polarized radiation. Completely polarized radiation can be represented by a vector diagram such as that in Figure (1.5). If we specify the two parameters E , the maximum amplitude of the electric field vector, and χ , the angle of the vibration with the reference direction, the polarization is completely defined.

However, experimentally it is difficult to measure the size of the electric field vector and the polarization angle. The parameter of the radiation which can actually be measured

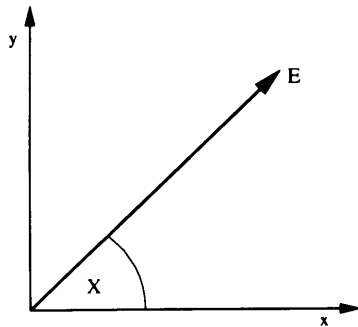


Figure 1.5: Parameters used to define completely polarized radiation

is its intensity, I , where $I = \langle E^2 \rangle$ (the angled brackets denote a time average). It is therefore useful to define the polarization state in terms of the intensities I , Q and U , the Stokes parameters. This is described fully in Tinbergen (1996). A polarimeter is a device which detects the intensity of the component of the radiation in one particular direction. If we orientate one polarimeter (co-polar, x) along the reference direction and another (cross-polar, y) at right angles to the first, the intensity detected by each polarimeter is (from Figure (1.5)):

$$I_x = \langle E^2 \cos^2 \chi \rangle \quad (1.42)$$

$$I_y = \langle E^2 \sin^2 \chi \rangle \quad (1.43)$$

The Q Stokes parameter is defined as the difference between the intensity measured by these two detectors:

$$Q = I_x - I_y = I \cos 2\chi \quad (1.44)$$

If the whole system is then rotated by 45° we detect two new intensities:

$$I_{x(45)} = \langle E^2 \cos^2(\chi - 45^\circ) \rangle \quad (1.45)$$

$$I_{y(45)} = \langle E^2 \sin^2(\chi - 45^\circ) \rangle \quad (1.46)$$

The U Stokes parameter is defined as the difference between these two intensities:

$$U = I_{x(45)} - I_{y(45)} = I \sin 2\chi \quad (1.47)$$

The third Stokes parameter, I , is just the total intensity.

These definitions only apply if the radiation is completely polarized. However, in general, radiation will only be partially polarized. It is useful to represent this case as the sum of a polarized intensity, I_p and an unpolarized intensity I_{up} :

$$I = I_{up} + I_p = I_{up} + \langle E_p^2 \rangle \quad (1.48)$$

The degree of polarization, p , is then defined as:

$$p = \frac{I_p}{I} \quad (1.49)$$

For the unpolarized component the electric field direction will vary randomly between all possible values of χ . On average the two orthogonal detectors will each detect half of the unpolarized intensity:

$$I_x = I_y = \frac{1}{2} I_{up} \quad (1.50)$$

The Q and U Stokes parameters are now defined in terms of the polarized intensity only:

$$Q = I_x - I_y = I_p \cos 2\chi \quad (1.51)$$

$$U = I_{x(45)} - I_{y(45)} = I_p \sin 2\chi \quad (1.52)$$

The Q and U Stokes parameters are related to the total polarized intensity by:

$$Q^2 + U^2 = I_p^2 \quad (1.53)$$

The Stokes parameters, Q and U, are therefore easily measurable intensities which can be used to obtain the fundamental polarization parameters, p and χ .

1.2.2 E-B decomposition

Definition of E and B fields

The Stokes parameters are a useful representation of the polarization field as they are relatively easy to measure experimentally. However, because Q and U depend on the angle between the direction of the polarization and the axes of the reference system they are coordinate-dependent quantities. This is because polarization is not a scalar quantity so cannot be defined by a single quantity at each point. Instead, the polarization can be thought of as a tensor quantity of the form:

$$P = \frac{1}{2} \begin{pmatrix} Q & U \\ U & -Q \end{pmatrix}. \quad (1.54)$$

where Q and U are defined on a flat plane perpendicular to the direction of propagation of the radiation. The polarization tensor transforms as $P' = R^T P R$ where R is the standard rotation matrix. This gives Q and U in a coordinate system rotated by an angle θ as:

$$\begin{aligned} Q' &= Q \cos(2\theta) + U \sin(2\theta) \\ U' &= -Q \sin(2\theta) + U \cos(2\theta) \end{aligned} \quad (1.55)$$

It is therefore useful to re-parameterize the polarization tensor in terms of two rotationally invariant quantities. These are denoted by E and B. The technique used to achieve this decomposition is similar to the decomposition of a vector, \mathbf{V} , into a irrotational part, \mathbf{V}_{ir} ($\nabla \times \mathbf{V}_{ir} = 0$), and a divergenceless part, \mathbf{V}_{dl} ($\nabla \cdot \mathbf{V}_{dl} = 0$). This can be done by expressing \mathbf{V}_{ir} as the gradient of a scalar potential, ϕ (as all gradients are irrotational, $\nabla \times (\nabla \phi) = 0$), and expressing \mathbf{V}_{dl} as the curl of a vector potential, \mathbf{A} (as all curls are divergenceless, $\nabla \cdot (\nabla \times \mathbf{A}) = 0$). The decomposition of a vector is therefore given as:

$$\mathbf{V} = \nabla \phi + \nabla \times \mathbf{A}. \quad (1.56)$$

For a 2×2 symmetric trace-free tensor such as the polarization tensor, an equivalent (although slightly more complicated) decomposition can be made in which P is expressed as:

$$P = f_g(\phi_E) + f_c(\phi_B) \quad (1.57)$$

where ϕ_E and ϕ_B are scalar potentials. The functions f_g and f_c are the tensor equivalents of the gradient and curl operators. These operators are functions of second derivatives, reflecting their tensor nature, as opposed to the operators used in the vector case which are all functions of first derivatives. The exact form of these operators is given in Appendix B. The E and B fields are then defined as $E = \nabla^2 \phi_E$ and $B = \nabla^2 \phi_B$. B is known as a pseudo-scalar field as it is invariant under rotation but changes sign under reflection. The B-field therefore has opposite parity to the scalar T and E fields. The E-B notation is an analogy with the vector case for electromagnetism where the electric field is irrotational and the magnetic field is divergenceless.

As E and B depend on the second derivatives of Q and U they are therefore non-local quantities and represent the global properties of the polarization field. In the small-scale limit, we can make a Fourier decomposition of the polarization field (Seljak (1997)). The relationship between the Fourier components of the two representations is relatively simple (see Appendix B):

$$\begin{aligned} E(\ell) &= Q(\ell) \cos(2\phi_\ell) + U(\ell) \sin(2\phi_\ell) \\ B(\ell) &= -Q(\ell) \sin(2\phi_\ell) + U(\ell) \cos(2\phi_\ell) \end{aligned} \quad (1.58)$$

where ϕ_ℓ is the angle between the x -axis of the coordinate system and the polarization direction. For an E-field the direction of the polarization at each point is perpendicular or parallel to the direction in which the polarization strength is changing most rapidly. For a B-field the direction of polarization is a $\pm 45^\circ$ to this direction. An example of the polarization pattern for a pure E-field and a pure B-field is shown in Fig. 1.6. The E-field shows a divergence-like patterns around areas in the which the polarization peaks where-as the B-field shows rotational patterns.

For scales on which the curvature of the sky is significant a simple Fourier decomposition is not possible and a spherical harmonic expansion, similar to that used in for the temperature field, can be made. However, because the field is now determined by two quantities, two sets of basis functions are needed. The basis functions must also have the same transformation properties as the polarization field. There are two alternative formalisms which can be used to make the expansion. The first is that of Kamionkowski et al. (1997b). This extends the idea of the polarization as a tensor field, but on the

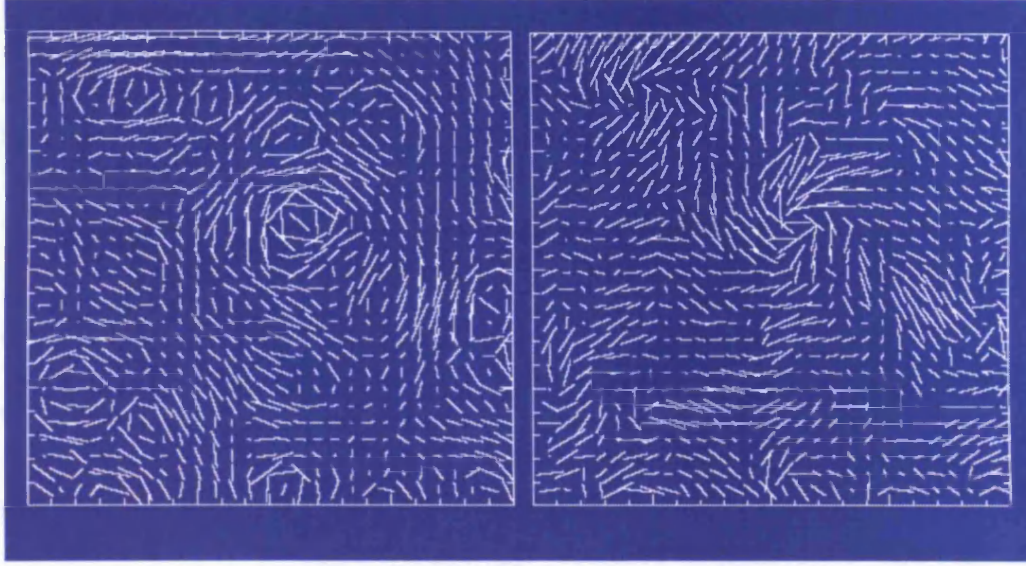


Figure 1.6: The polarization field can be represented by lines where the the length of the line gives the polarized intensity ($\sqrt{Q^2 + U^2}$) and the orientation gives the polarization angle at each point. For an E-field (left) the lines are orientated parallel or perpendicular to the direction in which the field is changing most rapidly giving circular patterns. For a B-field (right) the lines are orientated at $\pm 45^\circ$ to this direction creating spiral patterns. Figure taken from <http://kong.physics.berkeley.edu/~yuki/CMBpol/>

surface of a sphere instead of on a plane. The polarization matrix is now:

$$P = \frac{1}{2} \begin{pmatrix} Q & -U \sin(\theta) \\ -U \sin(\theta) & -Q \sin^2(\theta) \end{pmatrix}. \quad (1.59)$$

where θ and ϕ are the standard spherical coordinates. This polarization tensor can be expanded in terms of tensor spherical harmonics, $Y_{(\ell m)ij}^E$ and $Y_{(\ell m)ij}^B$ (these are quantities derived from the second derivatives of spherical harmonics) giving:

$$P_{ij}(\theta, \phi) = \sum_{\ell m} \left(E_{\ell m} Y_{(\ell m)ij}^E(\theta, \phi) + B_{\ell m} Y_{(\ell m)ij}^B(\theta, \phi) \right). \quad (1.60)$$

E and B are still the tensor equivalent of a curl-free and divergence-free fields, but the decomposition is more complicated as the second derivatives are over a curved surface instead of a flat plane.

An alternative expansion is given by Zaldarriaga and Seljak (1997). This definition is becoming common place as it is used in the CMBFAST Boltzmann code. In this case, instead of defining polarization as a tensor field, the two complex quantities $(Q \pm iU)$ are used. These are spin-2 quantities as they transform under rotation by an angle θ as:

$$(Q \pm iU)' = e^{\mp 2i\theta} (Q \pm iU) \quad (1.61)$$

which is alternative way of expressing the relations in Equation 1.55. The spin-2 property is related to the fact that a polarization ‘vector’ is head-less so it can be rotated back to its initial position after a 180° rotation as opposed to the 360° rotation needed for a spin-1 quantity such as a vector. These spin-2 quantities can be decomposed in terms of spin-2 spherical harmonics $_{-2}Y_{(\ell m)}$ and $_{2}Y_{(\ell m)}$ (these are again formed from the second differentials of spherical harmonics, but are not the same as tensor spherical harmonics) giving (Lewis et al. (2002)):

$$Q \pm iU = \sum_{\ell m} (E_{\ell m} \mp iB_{\ell m})_{\mp 2} Y_{\ell m}. \quad (1.62)$$

A detailed discussion of how this decomposition can be described in terms of spin-2 differential operators is given by Bunn et al. (2003).

The two point statistics of the CMB can therefore be completely described in terms of the covariances of the multipole moments, $T_{\ell m}$, $E_{\ell m}$ and $B_{\ell m}$:

$$\begin{aligned} \langle T_{\ell m}^* T_{\ell' m'} \rangle &= C_\ell^{TT} \delta_{\ell\ell'} \delta_{mm'} & \langle E_{\ell m}^* E_{\ell' m'} \rangle &= C_\ell^{EE} \delta_{\ell\ell'} \delta_{mm'} \\ \langle B_{\ell m}^* B_{\ell' m'} \rangle &= C_\ell^{BB} \delta_{\ell\ell'} \delta_{mm'} & \langle T_{\ell m}^* E_{\ell' m'} \rangle &= C_\ell^{TE} \delta_{\ell\ell'} \delta_{mm'} \\ \langle T_{\ell m}^* B_{\ell' m'} \rangle &= C_\ell^{TB} \delta_{\ell\ell'} \delta_{mm'} & \langle E_{\ell m}^* B_{\ell' m'} \rangle &= C_\ell^{EB} \delta_{\ell\ell'} \delta_{mm'}. \end{aligned} \quad (1.63)$$

As the B-field has opposite parity to the T and E fields the TB and EB correlations are zero if we can assume that parity is conserved. If the CMB is a Gaussian random field, as predicted if the metric fluctuations are generated from zero-point fluctuations by inflation, the statistical properties of the CMB temperature and polarization fields are completely defined by the four power spectra, C_ℓ^{TT} , C_ℓ^{EE} , C_ℓ^{BB} and C_ℓ^{TE} . The scalar and tensor contributions to these power spectra are shown in Fig. 1.7.

The two different formalisms produce power spectra which are exactly equivalent up to an all important factor of two where $C_\ell^{E,B(ZS)} = 2C_\ell^{E,B(KKS)}$ and $C_\ell^{TE(ZS)} = \sqrt{2}C_\ell^{TE(KKS)}$.

The E-B decomposition is chosen in this way not only as a convenient way of comparing different observations, but also from a deeper theoretical motivation. Due to the geometric properties of the B-mode polarization signal, B-modes cannot be produced by scalar perturbations at decoupling (as will be discussed in the next section). This means that **any B-mode signal produced at decoupling is a direct signature of tensor metric perturbations** (Seljak and Zaldarriaga (1997), Kamionkowski et al. (1997a)). This is extremely useful as the tensor contribution to the temperature and E-mode anisotropies is expected to be much smaller than the scalar contribution and so cannot be untangled from the scalars. This is because the measurement of the tensor component is limited by the cosmic variance of the much bigger scalar signal, particularly on the large scales where the tensor signal is significant (as shown in Fig. 1.7). It will therefore never be possible to reduce the variance in these large-scales measurements. The measurement (or

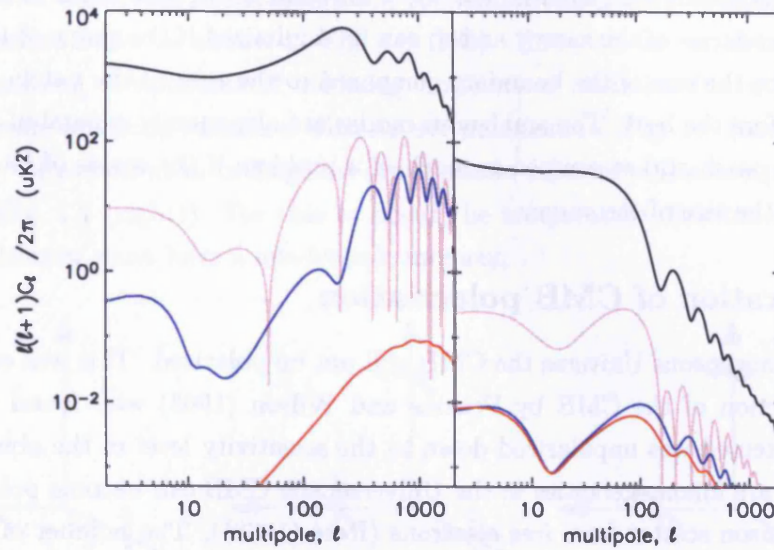


Figure 1.7: The scalar (left) and tensor (right) components to the four CMB power spectra (black - TT, grey - TE, blue - EE, red - BB). The scalar contribution to the B-mode signal is a secondary effect due to gravitational lensing and is generated after last scattering. A tensor to scalar ratio of 0.1 is used.

definite non-detection) of this B-mode signal is one of the only⁷ tools which can be used to investigate inflation.

Mode-mixing

For a full-sky map the definition of E and B modes is unique and any polarization can cleanly separated into these two components. However, if the surface on which the polarization field is defined has boundaries the E/B decomposition is no-longer unique (Bunn (2002)). A finite patch of sky can be decomposed into an E-field and a B-field, but there will be some power left over that satisfies the conditions for both E ('curl-free') and B ('divergence-free') modes. These are called ambiguous modes (Bunn et al. (2003)). Using the full sky definitions for E and B to separate the map into its two components will mix some of this ambiguous mode into the pure E and B fields. This is particularly a problem for measuring the cosmological B-field. This is expected to be very small and so mixing a component which is not part of the true B-field into the signal could potentially swamp this small signal. This process is therefore also known as E-B leakage as it will result in some of the full-sky E-mode leaking into a partial sky measurement of the B-modes. Methods of separating a finite polarization field into pure E and B modes without losing too much information to the ambiguous mode have been derived by Lewis et al. (2002)

⁷It is also possible that space-based gravitational detectors will one day be able to directly measure tensor perturbations on smaller scales

and Bunn et al. (2003). These authors also show that the ambiguous mode is generated mainly at the boundaries of the survey and so can be minimized if the shape of the patch is chosen to reduce the size of the boundary compared to the area of the patch. Circular patches are therefore the best. The ambiguous modes are also mainly generated on scales of the size of the patch and so are not as much of a problem if the scales of interest are smaller than the size of the survey.

1.2.3 Generation of CMB polarization

In a perfectly homogeneous Universe the CMB will not be polarized. This was confirmed by the first detection of the CMB by Penzias and Wilson (1965) who found that the radiation they detected was unpolarized down to the sensitivity level of the observation. However, if there are inhomogeneities in the Universe, the CMB can become polarized as the photons Thomson scatter from free electrons (Rees (1968)). The number of photons which are polarized is very small, creating a polarization anisotropy which is less than 10% of the temperature anisotropy. This is because polarization can only be created if there is a quadrupole temperature distribution surrounding the scattering electron. As discussed in Section 1.1.2, before recombination begins the tight coupling between photons and electrons washes out any angular dependence in the temperature distribution around an electron other than the monopole and the dipole. After recombination there will be very few electrons available to scatter the photons. The primary polarization can therefore only be generated in the short period of time in which tight coupling has broken down enough for there to be a significant quadrupole distribution around an electron, but the electron density is still high enough for frequent Thomson scattering to occur. A secondary polarization epoch which increases the polarization signal on large-scales can occur when the Universe is reionized.

In this Section we first look at how radiation can become polarised by Thomson scattering. We then discuss the features of the polarization anisotropy spectra, in particular the acoustic oscillations in the anisotropy spectra and the differences between the polarization generated by scalar and tensor perturbations. The discussion here is based on review articles from Hu and White (1997a), Kosowsky (1999) and Zaldarriaga (2003).

Polarization from Thomson scattering

Electrons are charged particles and so interact with the electromagnetic field of incoming radiation. If the energy of the incoming photon is low, then Thomson scattering will occur in which the radiation scatters without changing its energy. The interaction is such that the intensity of the out-going radiation peaks in a direction perpendicular to the direction of the incoming radiation. Only the electric field components perpendicular to

the direction of scattering are transmitted, so this process generates linear polarization from unpolarized light, as shown in Fig. 1.8 (left). However, for an isotropic radiation field, the outgoing components of incoming unpolarized radiation for orthogonal directions will create outgoing radiation with no net polarization (Fig. 1.8 (middle)). Only if the intensity of radiation in orthogonal directions is different will a net polarization be generated (Fig. 1.8 (right)). For this to occur the temperature distribution around the scattering electron must have a quadrupole moment.

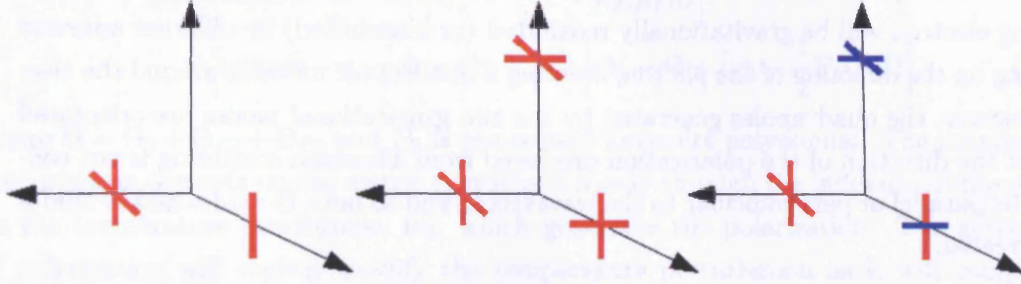


Figure 1.8: Generation of polarization from Thomson scattering. The electron is sitting at the centre of the grid in each case and the lines represent the polarization of the incoming radiation in the direction parallel to each line. Left: Electron generates polarized radiation as it will preferentially re-emit radiation whose polarization is orthogonal to the scattering direction. Middle: An isotropic distribution does not generate polarization. Right: A quadrupole distribution will generate polarization.

Polarization from scalar and tensor perturbations

As discussed in the last Section, the polarization field generated is different for tensor and scalar perturbations. Scalar perturbations can only produce E-mode polarization, whereas tensor perturbations typically produce an equal amount of E-modes and B-modes. This is related to the different type of quadrupole produced by the different types of perturbations. A quadrupole can be described in terms of the spherical harmonic distributions, Y_{20} , $Y_{2\pm1}$, $Y_{2\pm2}$, each of which leads to a different type of polarization field. For scalar perturbations, an $m=0$ quadrupole is produced due to the radiation in different directions being Doppler-shifted by different amounts. We consider a single density mode with an electron in a trough of the density perturbation. If the mode is in an expanding phase of its oscillation the photons from the two directions parallel to the direction of expansion will be moving away from the electron and so the radiation field in this direction is Doppler shifted, whereas photons from directions perpendicular to this will not be moving. This creates a quadrupole field around the electron which can generate a polarization either perpendicular or parallel to the direction of the density perturbation. This creates an E-mode pattern in the polarization field as the polarization direction is either parallel

or perpendicular to the direction in which the polarization strength is changing. This is the only mechanism for generating polarization from scalar perturbations, hence scalar perturbations can only produce E-modes.

For tensor perturbations, an $m=2$ quadrupole is produced. A gravitational wave will stretch spacetime in two different directions, corresponding to the two different gravitational wave polarization states, $+$ and \times . The $+$ mode stretches spacetime alternately in directions parallel and perpendicular to the direction of the perturbation, whereas the \times modes stretches spacetime in directions at $\pm 45^\circ$. This means that photons surrounding a scattering electron will be gravitationally redshifted (or blueshifted) by different amounts depending on the direction of the photon, creating a quadrupole moment around the electron. However, the quadrupoles generated by the two gravitational modes are orientated such that the direction of the polarization produced from Thomson scattering is not confined to be parallel or perpendicular to the wavevector and so both B-modes and E-modes can be created.

Polarization power spectra

The TE and EE power spectra will exhibit the same series of acoustic peaks as in the temperature power spectrum. However, the peaks occur at different places. This is because the perturbations in the quadrupole at last scattering are coupled not to the overall density perturbations (the monopole), which are the dominant source of the acoustic oscillations in the CMB temperature power spectrum, but to the perturbations in the velocity of the fluid (the dipole). As the photon-baryon fluid oscillates, the fluid will be at maximum velocity in the middle of the oscillation, when the density perturbation is the smallest. This means that the oscillation in E-mode power spectra will be exactly out of phase with those in the temperature spectrum (Kosowsky (1999)) so the EE spectrum has peaks at the position of the dips in the TT spectrum.

The peak of the EE power spectrum will occur on smaller scales to the peak in the temperature spectrum. This is because a quadrupole can only be created over scales on which tight coupling has broken down and so large scales have less time to generate polarization than small scales. On small scales, the temperature perturbations, and hence the quadrupole, are lower because of Silk damping. The E-mode spectrum therefore peaks on scales of $\ell \sim 1000$.

The tensor perturbations decay once they have entered the horizon and fall off dramatically for scales smaller than the horizon size at last scattering. This means that the primordial B-mode signal will also fall-off at these scales and so peaks on larger scales than the E-mode spectrum at around $\ell = 100$.

1.2.4 Calculating the polarization at recombination

The polarization power spectra can be calculated in a similar way to the temperature spectrum using the Boltzmann and Einstein equations given in Section 1.1.2. This requires an additional Boltzmann equation for the polarized contribution to the photon perturbation Θ_P and a slight modification to the Boltzmann equation for the total photon distribution so that (Seljak and Zaldarriaga (1996)):

$$\begin{aligned}\dot{\Theta}_P + ik\mu\Theta_P &= -\dot{\tau} \left[\Theta_P + \frac{1}{2}(1 - \mathcal{P}_2(\mu))\Pi \right] \\ \dot{\Theta} + ik\mu\Theta &= -\dot{\Phi} - ik\mu\Psi - \dot{\tau} \left[\Theta_0 - \Theta + \mu v_b - \frac{1}{2}\mathcal{P}_2(\mu)\Pi \right]\end{aligned}\quad (1.64)$$

where $\Pi = \Theta_2 + \Theta_{P2} + \Theta_{P0}$ and \mathcal{P}_2 is the second Legendre polynomial. The polarization perturbation depends on the metric perturbation only through the influence of the metric on the temperature quadrupole, Θ_2 , which generates the polarization. The generation of polarization will slightly modify the temperature perturbation as it will complicate the process of recombination. This is shown by the inclusion of $\Theta_{P2} + \Theta_{P0}$ into the scattering term in the Boltzmann equation. The CMBFAST code includes the generation of polarization and can be used to predict the polarization power spectra from a set of input cosmological and initial perturbation parameters.

1.2.5 Secondary polarization anisotropies

Polarization anisotropies are not only created at last scattering. When the Universe reionizes it will again be possible for Thomson scattering to occur and produce polarization. This creates a reionization signal at large scales in the polarization power spectra. Gravitational lensing by large-scale structure will also affect the CMB polarization and results in the conversion of E-mode polarization into B-mode polarization.

Reionization

On small scales the effect of reionization on the CMB polarization is the same as that for the temperature anisotropies, a damping of the signal on scales inside the horizon during reionization. The damping effect on the first peak in the E-mode power spectra is shown in Fig. 1.9. However, on large scales reionization causes a significant increase in the power in the polarized anisotropies which does not occur in the temperature case (Zaldarriaga (1997)). This polarization is generated in the same way as during recombination, through Thomson scattering of a quadrupole temperature distribution. However, at the reionization epoch, free streaming has greatly increased the size of the temperature quadrupole and the amount of polarization produced is significantly larger. This creates a ‘reionization bump’ at low values of ℓ in the polarization power spectra as shown in Fig. 1.9. The

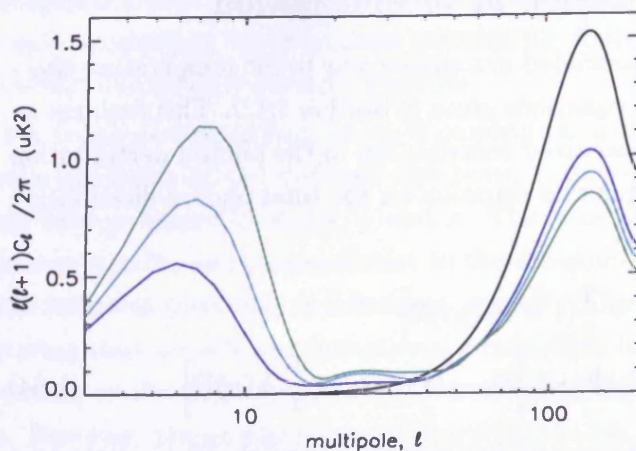


Figure 1.9: E-mode power spectra for reionization optical depths of 0.2 (dark blue), 0.25 (light blue) and 0.3 (green) compared to a model with no reionization. Increasing the optical depth increases the height of the reionization bump and also pushes the bump out to smaller angular scales. The first acoustic peak is also shown which exhibits the reionization damping also present in the temperature case.

height of this bump will depend on the reionization optical depth, τ . This parameter depends upon the distance a photon will have travelled since the Universe reionized and the number of free electrons it will encounter on its journey. For a high τ , more photons will be able to last scatter after reionization has occurred and so the bump will be higher. The position of the peak depends mainly on the time at which reionization took place. If reionization occurs further back in time, the scale over which reionization occurs will be smaller and so bump will be shifted to higher ℓ .

The height of the reionization bump tells us when reionization first began to occur given a model for the reionization history. This complements an alternative observational technique of detecting the signature of neutral hydrogen in spectra of high redshift quasars. Finding such a signature at high redshift tells us how far back in time we need to go to find significant amounts of neutral hydrogen. This means that reionization must still be occurring up until this redshift, and so gives a lower redshift limit on when reionization occurred. Quasar spectra indicate that there is a significant amount of neutral hydrogen present in the Universe at redshifts greater than 6 (Becker R. H. et al. (2001)). However current CMB polarization constraints for the WMAP measurement of the large-scale TE correlation (see Section 2.3) give a reionization optical depth of 0.17, which gives a reionization redshift of between 11 and 30, depending on the model used for the reionization history (Kogut, A. et al. (2003)). This suggests that the Universe began to reionize at higher redshift and the process gradually proceeded until reionization was completed at $z=6$. A high sensitivity measurement of the reionization bump would allow the details of this reionization history to be studied (Kaplinghat et al. (2003a)).

Gravitational lensing

At recombination, the photons feel the gravitational effects of inhomogeneities in the Universe due to their coupling to the baryons. Without this coupling the perturbations to the homogeneous background are too small to influence the photons and after decoupling the photons can free-stream through the Universe. However, as matter collapses to form large-scale structure this density contrast will increase and the photons will again be influenced gravitationally by any inhomogeneities. One way this can occur is through **weak gravitational lensing**. This causes random deflections of the CMB photons as they propagate through the Universe (Seljak (1996)). The effect of these deflections on the CMB temperature signal is to smooth out any differences in the anisotropy on different scales. This smears out any sharp features in the power spectrum. The same effect occurs for the EE power spectrum. This is shown in Fig. 1.10. The peaks in the EE spectrum

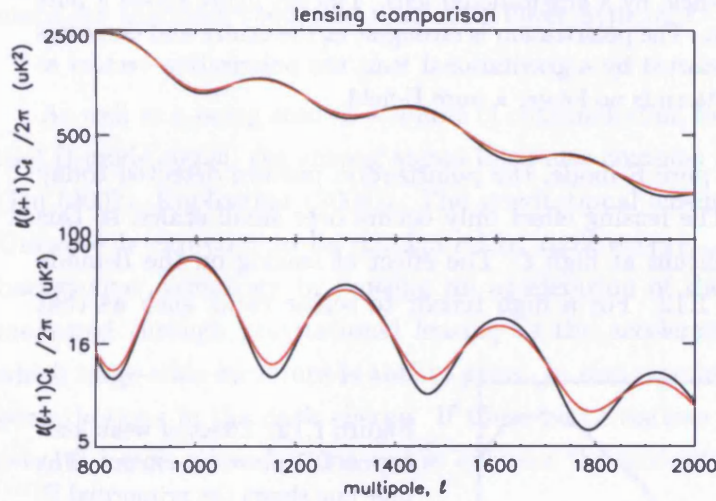


Figure 1.10: Effect of weak lensing on TT (top) and EE (bottom) power spectra. The black lines shows the power spectra without lensing and the red lines include lensing. The acoustic peaks become smeared out by gravitational lensing. The effect is more pronounced for the EE spectra as the peaks are sharper than for the temperature spectrum.

are sharper than those in the TT spectrum. This is because the TT oscillations have contributions from both the monopole and the dipole at decoupling. These oscillations are out of phase and so the smaller dipole contribution increases the power in the dips in the power spectrum and so the acoustic oscillation signature in the power spectrum is smeared out. For the EE spectrum the oscillations are due predominantly to the dipole and so this smearing does not occur. The effect of gravitational lensing is therefore more noticeable for the EE spectrum.

The effect of lensing on the B-mode spectrum is much more severe (Zaldarriaga and Seljak (1998)). Lensing not only changes the amplitude of the primordial signal, it also mixes E and B mode polarization. When a photon is deflected it will disrupt the global polarization pattern. For example, a pure E-field polarization field may have all of its polarization vectors orientated parallel to the direction in which the polarization amplitude

is changing most rapidly. If each of these vectors will be shifted by a different amount as the field is deflected around a gravitational lens, the lensed field will no longer be a pure E-field; a B-field component has been generated by the lens. This is shown in Fig. 1.11. This means that although the polarization pattern generated at last scatter-

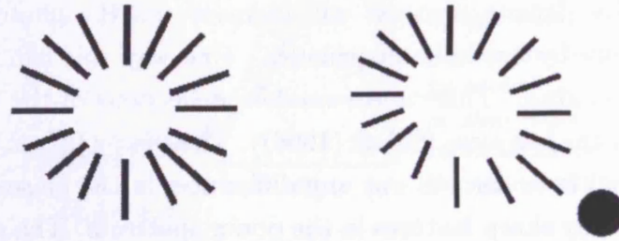


Figure 1.11: Distortion of a pure E-field by a gravitational lens. The left figure shows a pure E-field around a polarization hot spot. The polarization is strongest at the centre and decreases radially outwards. If this field is distorted by a gravitational lens, the polarization vectors at each point will be moved and the pattern is no longer a pure E-field.

ing from scalar perturbations is a pure E-mode, the polarization pattern detected today will have a B-mode component. The lensing effect only occurs over small scales, so this scalar B-mode signal is only significant at high ℓ . The effect of lensing on the B-mode power spectrum is shown in Fig. 1.12. For a high tensor to scalar ratio, such as that

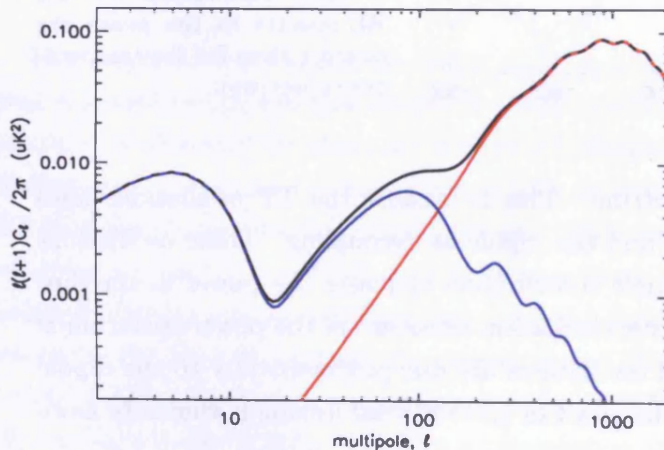


Figure 1.12: Effect of weak lensing on BB power spectrum. The blue line shows the primordial B-mode signal (which is only generated by tensor perturbations) for a tensor to scalar ratio of 0.1. The red line shows the signal generated from the weak lensing of the E-mode polarization due to scalar perturbations. The black line shows the total B-mode signal.

shown in Fig. 1.12, the peak in the primordial signal is still detectable above the lensing signal, but for smaller signals the lensing signal will act as an extra source of foreground contamination. This will increase the variance in the measurement of the tensor signal and so puts a limit on the minimum value of r for which tensors can still be detected of

around 2×10^{-4} (Knox and Song (2002), Kesden et al. (2002)). This treatment requires a knowledge of the shape and amplitude of the lensing power spectrum, but this can be calculated from a high-precision measurement of the temperature spectrum. The recent WMAP results indicate that there will be a large reionization bump and so on large scales the limit may be slightly lower. These authors also show that if the lensing signal can be accurately reconstructed it could be removed from the polarization maps, instead of being treated as an unavoidable source of noise. Methods for reconstructing the deflection field have been suggested (Hu and Okamoto (2002), Kesden et al. (2003)) which use the fact that lensing introduces correlations between the different multipoles of the map. This reduces the minimum tensor to scalar which can be detected by about a factor of 10, as the measurement is then only limited by the residual noise left over from the subtraction. This subtraction requires an actual measurement to be made of the deflected polarization field, as opposed to just an estimate of its statistical properties. High resolution polarized maps are therefore needed to reach this lower limit on r .

As well as being seen as a source of contamination for a measurement of the primordial B-mode signal, the lensing signal itself also contains useful cosmological information (Hu (2002), Kaplinghat (2003)). The gravitational lensing occurs in an epoch when the Universe is expected to be dominated by dark energy. Dark energy will influence the background cosmology by causing an acceleration of the expansion rate. This can be measured through gravitational lensing as the acceleration will determine the rate at which large-scale structure is able to grow. In some models it is also possible to generate perturbations in the dark energy. If these perturbations are present it will increase the over-all metric perturbations and so enhance the amount of lensing.

The effect of neutrinos on the lensing of the CMB has been highlighted by Kaplinghat et al. (2003b). Free-streaming of massive neutrinos will suppress the clustering of dark matter on small scales for which the gravitational force is not strong enough to overcome the pressure due to the neutrino velocity dispersion. The scales at which this suppression occurs will depend on the neutrino mass and so a measurement of the lensing potential would help to constrain the mass of the neutrino.

The B-mode lensing signal is useful as it can be used to determine the clustering of large-scale structure at intermediate redshifts ($z > 2$). This is complementary to other techniques, such as cosmic shear measurements (which measure the effect of weak lensing on the shapes of galaxies) and galaxy redshift surveys, which probe the distribution at lower redshifts ($z < 2$).

1.2.6 Degeneracy breaking

There are a number of degeneracies in the temperature power spectrum which limit the precision with which the key cosmological parameters can be measured. A number of these degeneracies can be broken using CMB polarization data.

In order to understand these degeneracies it is important to understand how different parameters influence the CMB temperature power spectrum. The key feature that allows the CMB power spectrum to determine parameters are the position of the first acoustic peak and the relative heights and positions of each of the other peaks. The position of the peaks depends on two scales: the size of the sound horizon at last scattering which determines the amplitude and phase of each mode in the photon distribution, and the distance to the last scattering surface as this will determine the angular scale onto which these modes at last scattering are projected. The sound horizon size depends on the baryon density⁸, $\Omega_b h^2$, (as this gives the sound speed and so determines how fast each mode will oscillate and hence its phase at recombination) and the cold dark matter density, $\Omega_{CDM} h^2$ (as this sets the horizon size at recombination and so determines which modes will have begun to oscillate), whereas the angular distance depends on the expansion of the Universe since recombination and so is determined by the total matter density, the curvature of the Universe, the Hubble constant and the vacuum energy density. The relative amplitude of the peaks depends on the tilt of the primordial spectrum, n_s , and also on the baryon density. If the baryon density is high this will increase the gravitational force acting on the photons and so the peaks in the power spectrum corresponding to compressions of the photon distribution will be higher than those corresponding to rarefactions.

The main CMB degeneracy is termed the **geometric degeneracy** (Efstathiou and Bond (1999), (Zaldarriaga et al. (1997))). As the acoustic peaks will be the same for models with a given set of initial perturbations (n_s, A) and the same values of $\Omega_b h^2$ and $\Omega_m h^2$, it is possible to use different combinations of the parameters h , Ω_b and Ω_m to obtain the same pattern. This will give almost the same power spectrum if the angular projection is kept the same by varying Λ and the curvature to compensate for the changes to h and Ω_m . The most important consequence of this is that the CMB cannot be used to set independent bounds on both the curvature of the Universe and the cosmological constant (Efstathiou and Bond (1999)). This degeneracy can be reduced using the ISW (see Section 1.1.2), but cannot be removed completely due to the high cosmic variance on the large scales at which the ISW occurs. This degeneracy is normally broken by using information from other astronomical observations to constrain either the Hubble

⁸Each density Ω_i , is given by ρ_i/ρ_c . The critical density, ρ_c , is proportional to h^2 and so the physical density of a quantity ρ_i is proportional to $\Omega_i h^2$.

constant, the cosmological constant or the matter density (Efstathiou and Bond (1999)). However, it is also possible to use the effect of gravitational lensing on the power spectrum to break this degeneracy (Stompor and Efstathiou (1999)). This is because lensing occurs at later epochs and so has a dependence on dark energy. This effect is unlikely to be broken by temperature data as the effect of lensing is so small, but can be broken using the polarization spectra.

A degeneracy between n_s and the cosmological parameters occurs because the shift in the amplitude of the first few peaks occurring if $n_s \neq 1$ can be mimicked by changing the baryon and matter densities (Tegmark and Zaldarriaga (2002)). Polarization data will break this degeneracy because the peaks in the polarization spectrum are out of phase with those in the temperature spectrum. This means that while a change in n_s will cause the amplitude of both the TT and EE spectra to go down on all scales, a change in Ω_m would cause the two spectra to move in opposite directions at each scale.

As well as constraining the reionization optical depth, τ , the reionization bump also breaks a degeneracy between τ and A (Zaldarriaga et al. (1997)). For the TT spectrum, changing τ will just shift the amplitude of the spectrum up and down, as discussed in 1.1.2, and so the effects of τ and A are indistinguishable. The obvious reionization bump in the polarization data therefore breaks this degeneracy allowing a more precise determination of A .

Using CMB temperature data to constrain the amplitude of tensor perturbations in addition to the parameters already mentioned greatly increases the uncertainty on a number of these parameters, in particular $\Omega_b h^2$ and $\Omega_{CDM} h^2$ (Efstathiou (2002)). This is because the inclusion of tensors changes the power spectrum in a similar way to the ISW, an increase of the amplitude on large scales. This means that the ISW can no longer be used to reduce the geometric degeneracy and so the uncertainty in the parameters affected by this degeneracy will increase (Zaldarriaga et al. (1997)). Polarization data will reduce this degeneracy by tightening constraints on the tensor-to-scalar ratio.

1.2.7 Key points

- The CMB becomes polarized during recombination due to Thomson scattering between photons and electrons. Polarization is only generated if there is a quadrupole temperature distribution surrounding the electron. The quadrupole at recombination is small and so only 10% of the photons are polarized.
- Linear polarization is measured in terms of the two Stokes parameters Q and U . However, these parameters depend on the orientation of the co-ordinate system. The polarization field is therefore decomposed into two-rotationally invariant quantities, the E and B fields. These are defined in terms of the second derivatives of Q and U at each point and so represent the global properties of the field.
- The information in the CMB for Gaussian initial perturbations is completely defined by the four power spectra C_ℓ^{TT} , C_ℓ^{EE} , C_ℓ^{BB} and C_ℓ^{TE} .
- The E-field is the tensor equivalent of a curl-free field and the B-field of a divergenceless field. For a pure E-field the polarization vectors are orientated either parallel or perpendicular to the direction in which the polarization is changing most rapidly. For a pure B-field the vectors are orientated at $\pm 45^\circ$ to this direction.
- During recombination, the acoustic oscillations are set up in the photon distribution due to the competing forces of photon pressure and gravitational infall acting on the photons. This creates velocity gradients in the photon-baryon fluid and so allows a quadrupole distribution to be generated as photons from orthogonal directions will be Doppler shifted by different amounts.
- For scalar perturbations, the quadrupole created will always cause a polarization either perpendicular or parallel to the direction in which the perturbation, and hence the size of the quadrupole, is changing. This means that scalar perturbations can only create E-mode polarization. Tensor perturbations can create generate both E and B-modes.
- The primordial B-mode signal is therefore a unique probe of the tensor perturbations at decoupling as it is not contaminated with the signal due to scalar perturbations, unlike the other CMB power spectra. The measurement of this B-mode signal is one of the few ways in which inflation can be tested.
- The presence of large-scale anisotropies in the CMB polarization spectrum is a definite signature of super-horizon perturbations at decoupling. This is not the case for temperature measurements as a large-scale signal can be generated by the ISW effect.

- Early reionization creates a bump at low ℓ in the CMB polarization spectra. This means that the CMB can be used to investigate the reionization history of the Universe.
- Gravitational lensing of the CMB photons will cause the CMB anisotropy to be sensitive to dark energy and the neutrino mass. This effect is very weak for the temperature anisotropy, but is detectable in the polarization power spectra.
- Gravitational lensing also generates a scalar B-mode signal which will contaminate the measurement of the primordial tensor signal.
- The information contained in the CMB polarization spectra can be used to break degeneracies which occur if only temperature data is used and so will tighten CMB constraints on cosmological parameters.
- The E-mode polarization has been detected by the DASI experiment and the large-scale TE correlation has been measured by WMAP (as discussed in the next chapter).

1.3 Thesis overview

In this introduction I have described the theory of the CMB and how it can be used as a tool for cosmology. The key point is that observations are now reaching the limit of what temperature-only measurements can tell us about the evolution of the Universe. The next challenge in CMB observations is therefore to make high resolution, high precision polarized measurements. In the rest of this thesis I describe work I have carried out for the QUaD project, a telescope specifically designed to measure the CMB polarization. The thesis is organised as follows:

Chapter 2 gives a brief description of the QUaD instrument and an overview of the current status of other CMB polarization instruments.

Chapter 3 reviews the current estimates of polarized astrophysical foregrounds and predicts the expected levels at the QUaD observing frequencies.

Chapter 4 presents a calculation of the expected sensitivity of QUaD.

Chapter 5 predicts the science goals that can be achieved with QUaD.

Chapter 6 discusses the QUaD observing strategy.

Chapter 7 presents the simulations of time-ordered data for QUaD.

Chapter 2

The QUaD experiment

In this Chapter we describe the design of the QUaD instrument. We also discuss previous experiments to measure the CMB polarization and describe a number of other projects currently underway. The design and manufacture of QUaD is a joint project between a number of institutions. Cardiff University is responsible for the telescope, optics and cryogenics, Stanford University for the focal plane and waveplate, University of Ireland, Maynooth for the optical design; and the University of Chicago for the telescope mount.

2.1 Measuring CMB polarization with QUaD.

QUaD (QUEST and DASI) has been built specifically to measure the CMB polarization signal discussed in the previous Chapter. QUEST (**Q** and **U** Extra-galactic **S**urvey Telescope) is a purpose-built telescope which will focus millimetre wave radiation onto an array of polarization-sensitive detectors. QUEST will be attached to the mount of DASI (**D**egree **A**ngular **S**cale Interferometer) at the South Pole, replacing the previous DASI detector system.

QUaD is optimized to detect polarized radiation. This is done using a set-up in which two detectors sensitive to orthogonal polarization states absorb the radiation from the same point on the sky. The unpolarized component of the radiation will be distributed equally between the two detectors so that differencing the two outputs will remove the unpolarized radiation. This unwanted signal is called the **common mode signal**. The removal of this common mode signal is an integral part of the QUaD design. Without this, the signal would be dominated by temperature fluctuations from the atmosphere and it would be impossible to detect the weaker polarized signal. As the emission from the atmosphere is not linearly polarized (Keating et al. (1998)) there is no need for QUaD to use the chopping or nodding procedures needed in a ground-based total power experiment.

However, even without this common mode signal, the CMB polarization signal is still very small in comparison to the random noise generated by statistical fluctuations in the

emission from the atmosphere and the telescope components. This photon noise is the limiting factor determining the minimum amplitude of the signal which can be measured. A full discussion of photon noise will be presented in Chapter 4. In order to achieve the high sensitivity required, most of the optics chain is cooled to 4K to reduce the thermal loading from the telescope, and the detectors are cooled to below 300 mK to minimize any thermal noise generated in the detection process.

The QUaD observing frequencies have been chosen to match windows in the sub-mm atmospheric emission (this will be discussed in Chapter 4). At the South Pole site, the transmission in these windows is very high, and so the loading from the atmosphere is as low as possible. The frequencies are also located at the minimum of the combined sub-mm emission from astrophysical foregrounds. Using multi-frequency observations it is also possible to reduce the foreground contamination during the data analysis. QUaD will therefore operate at two frequencies, 100 GHz and 150 GHz.

The noise from most physical processes will tend to be higher for the low frequency components of the signal. This decomposition of the signal into components with different signal frequencies is discussed in Appendix A. This is called $1/f$ noise as the low frequency end of the noise spectrum falls off as the inverse of the signal frequency. The noise spectrum can be described by two parameters, the white noise level and the $1/f$ knee. White noise is the completely random component of the noise due to statistical variations in the signal being measured (as discussed in Chapter 4). The $1/f$ knee is the signal frequency at which the contribution to the spectrum from $1/f$ noise is equal to the contribution from white noise. Fig. 2.1 shows a typical realization of white noise compared to a realization of $1/f$ noise. There are a number of places at which $1/f$ noise enters into the CMB polarization signal:

- **Instrumental polarization (IP):** as the radiation is reflected and refracted through the optical chain, some of the common mode signal can become polarized. IP will generate a signal after the differencing which contains a contribution from the atmospheric fluctuations and from any temperature drift in the instrument.
- **Detector gain differences:** if the two detectors are not perfectly matched the differenced signal will contain a contribution from the common mode signal.
- **Bolometer and electronics noise:** each signal will be subject to different detector noise and will pass through a different electronics chain. Any noise added to the signals at this stage will therefore be different in both channels and so cannot be removed by differencing.

These effects will be discussed in more detail in Chapter 7.

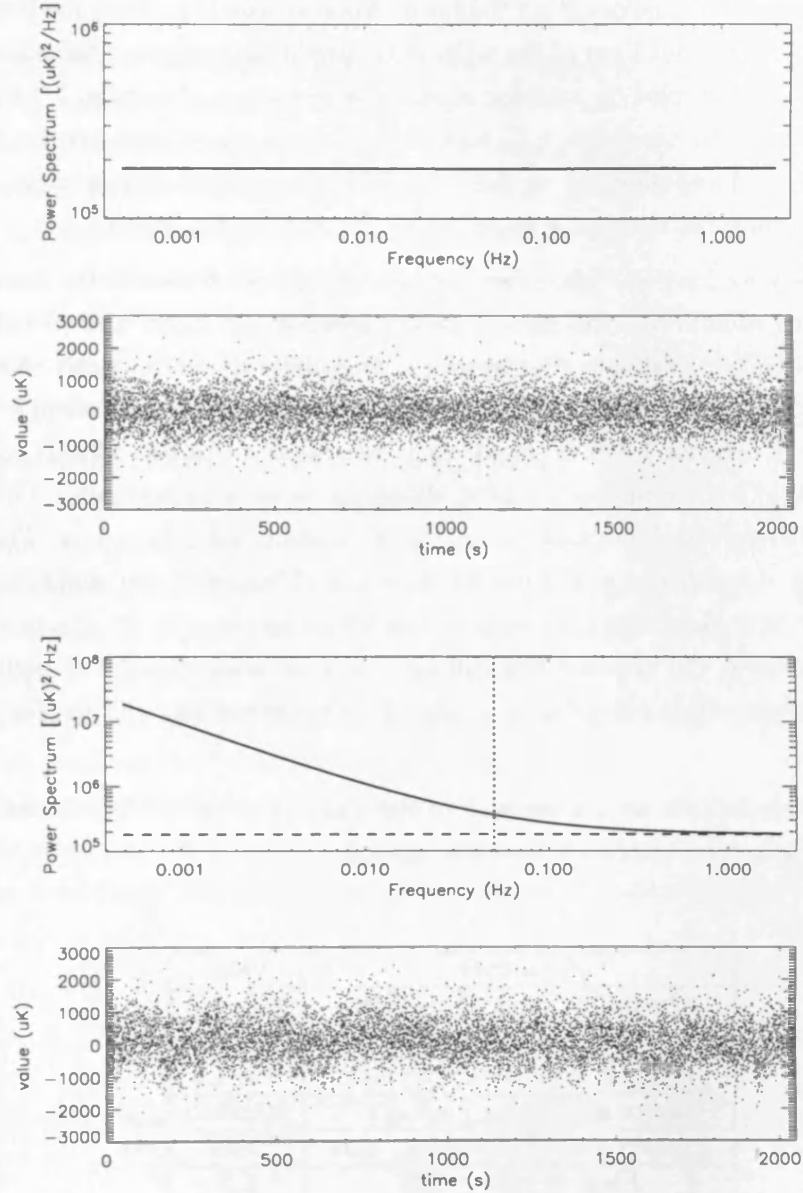


Figure 2.1: Power spectra and a realization of noise with this spectrum for white noise (top) and $1/f$ noise (bottom). The timestream including $1/f$ noise is less uniform due to the extra power at low frequencies. The dashed line on the $1/f$ spectrum shows the position of the $1/f$ knee at 0.05Hz.

It is important that the fluctuations in the signal occur at a higher frequency than the $1/f$ knee of the noise, otherwise the signal will be swamped by this noise. For the atmospheric noise, this can be achieved by scanning the telescope fast enough on the sky. This will be discussed in more detail in Chapter 6. Another way of pushing the frequencies of interest up above the $1/f$ knee of the noise is to amplitude modulate the signal. The signal of interest is multiplied by a carrier signal of a frequency above the $1/f$ knee, this shifts the true signal fluctuations up to higher frequencies where they can be detected above any noise produced after the modulation. This is explained in Appendix C. This can be used to reduce the electronics noise by AC biasing the bolometers.

A continuously rotating waveplate (an optical element which rotates the polarization angle of incoming radiation) could also be used to modulate the signal and so reduce the noise from low-frequency drifts in the detectors. Originally it was intended that QUaD would have a continuously rotating waveplate which would rotate fast enough to push the signal over the detector $1/f$ knee. However, it was found to be too difficult to include a motor that could run continuously whilst observations were being made. The QUaD waveplate will therefore only be rotated when the telescope is not taking data. The QUaD telescope also has the ability to rotate around the z -axis. This could also be used to modulate the signal, but it is unlikely that the telescope can rotate fast enough for this modulation to be useful. However, this rotation can still be used to characterize the IP signal. The use of the waveplate and z -axis rotation in the QUaD observations will be discussed in Chapter 6.

In the following Section we discuss each of the main parts of the QUaD instrument. A summary of the key parameters is given in Table 2.1.

Parameter	Value
Operating frequency / GHz	100, 150
Number of feeds	12 , 19
Angular resolution / arcmin	6.3, 4.2
Detector sensitivity / $\mu K Hz^{-1/2}$	300, 340
Primary mirror diameter / mm	2640
Field of view / deg	1.5
Focal ratio	2.33
Horn side lobe / dB	-20
Detector operating temp / mK	250

Table 2.1: QUaD experimental parameters. For parameters which are different in each channel the 100 GHz value is given first.

2.2 The QUaD instrument

2.2.1 Telescope and optics

The QUaD optics is a cassegrain design in which a large primary mirror (2.6m) focuses radiation onto a smaller secondary mirror which directs the light through a hole in the centre of the primary to the detector system. The cassegrain design is chosen because it is axially symmetric so that any instrumental polarization signal should be distributed symmetrically. It is difficult to support the secondary mirror without breaking this symmetry. QUaD will use a continuous foam cone made out of a material which is transparent to microwaves instead of using individual supports. In order to prevent emission from the cryostat bouncing off the secondary mirror and back towards the detectors, there is a small hole at the centre of the secondary through which this emission can escape.

The focus of the secondary mirror occurs in front of the primary. It would not be possible to locate the detector array at this point as this would be too difficult to support without dramatically reducing the field of view. The image created here is therefore re-imaged by a system of two lenses to a position behind the primary mirror. The position of the optical elements is shown in Fig. 2.2. The lenses also make the rays converge, so that they can all pass through the small waveplate located between the lenses and the focal plane and decrease the effective focal length so that the field of view is larger ($F=2.33$). The radiation reaching the focal plane is controlled by the Lyot stop. This is a cold piece of metal with a precisely defined inner diameter positioned at an image of the primary mirror. This stops any off-axis rays that may have scattered in to the optical path from reaching the focal plane. The path of radiation through the system is shown in Fig. 2.3.

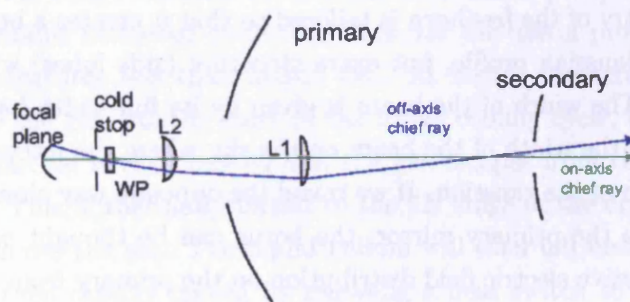


Figure 2.2: Schematic of optics chain (from Creidhe O'Sullivan)

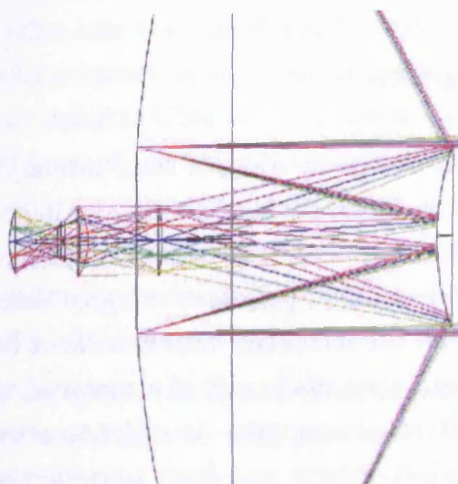


Figure 2.3: Ray tracing diagram of path through QUaD optics (from Creidhe O'Sullivan).

2.2.2 Focal plane and feed horns

The focal surface consists of a set of feedhorns which transmit the radiation onto the detectors. There are 12 feeds at 100 GHz and 19 at 150 GHz. The surface onto which the radiation is focused is curved with a radius of curvature of 175 mm.

The image of the sky produced at each point on the focal plane will not be a single point of radiation. Instead the radiation is spread out into a diffraction pattern. For a perfect circular aperture such as the telescope primary mirror, the pattern will be a central diffuse spot (the Airy disk) surrounded by increasingly fainter rings (the side lobes). The central disk contains nearly all of the energy. The size of this ring will be much bigger than the surface area of the detector. The radiation is therefore coupled to the detector using a feedhorn. The geometry of the feedhorn is tailored so that it creates a beam which is well approximated by a Gaussian profile, but extra structure (side lobes) will remain at the edges of the profile. The width of the beam is given by its full-width half-maximum size (FWHM) which gives the width of the beam on the sky where the intensity is half of the value at the maximum of the gaussian. If we travel the opposite way along the optic path, from the feedhorns to the primary mirror, the horns can be thought of as illuminating the primary. The effective electric field distribution on the primary from this illumination will be the Fourier transform of the beam produced from the feed horn. To reduce the side lobes, the horn can be made so that it under-illuminates the primary. This reduces the width of the Gaussian field pattern at the mirror, and so reduces contamination from any spillover from the ground, but at the price of increasing the width of the beam on the

sky. The edge taper is a ratio of the effective electric field strength at the centre of the primary to that at the edge. For QUaD the edge taper is fairly high (-20dB, so the field at the edge of the mirror is 0.01 times smaller than at the centre) so the FWHM beam size is much broader ($1.7 \lambda/D$) than its diffraction limited value ($1.22\lambda/D$).

A single focal plane is used for both the 100 GHz and 150 GHz horns so that the sky can be mapped at both frequencies simultaneously. The layout of the focal plane will be discussed in detail in Chapter 6.

2.2.3 Cryogenics

In order to achieve the high sensitivity needed to measure the CMB polarization, the detectors need to be cooled to temperatures a fraction of a degree above absolute zero. This reduces the thermal noise which would otherwise swamp the weak cosmological signal. A number of stages are needed to cool the detectors from room temperature (300K) to this operating temperature. The first two stages are achieved using a cryostat. For QUaD, the cryostat consists of two toroidal tanks. An outer tank is filled with liquid nitrogen which has a temperature of 77K. An inner tank is filled with liquid helium (^4He) which has a temperature of 4K, for which the 77K stage provides a shield against the outside to stop the helium boiling away too quickly. This then creates a 4K surface at the centre of the cryostat. There is a vacuum shield between each of the stages so minimize any heat transfer. The basic features of this design are shown in Fig. 2.4. The cooling from 4K to 250 mK is achieved using a three stage sorption fridge which uses cryopumps to cool liquid helium by reducing vapour pressure at the surface of the liquid. Two different isotopes are used, ^4He and ^3He . As shown in Fig. 2.5, ^4He will condense at temperatures below 4.2K at atmospheric pressure. If the vapour pressure at the surface of the liquid is then reduced, the liquid phase can be cooled to temperatures below 2K. A single stage sorption fridge contains three main elements, a pump, a condenser and a still. The pump contains activated charcoal. This has the useful property of absorbing helium gas at temperatures less than about 18K. At higher temperatures ($\sim 40\text{K}$) the charcoal will release the gas. At the start of the fridge cooling cycle, the pump is full of helium gas. The charcoal is then heated and the gas escapes from the pump and flows into the condenser. This is thermally linked to the 4K stage of the cryostat so it will be cold enough to condense the gas. The liquid helium will then fall under gravity into the still. The pump is then rapidly cooled by releasing a heat switch to the 4K stage, and so begins to absorb the helium, reducing the vapour pressure in the still and cooling the helium.

To reach lower temperatures, a two stage fridge with a ^4He pump and a ^3He pump can be used. ^3He has a slightly lower condensation temperature of 3.2K. The ^4He pump is

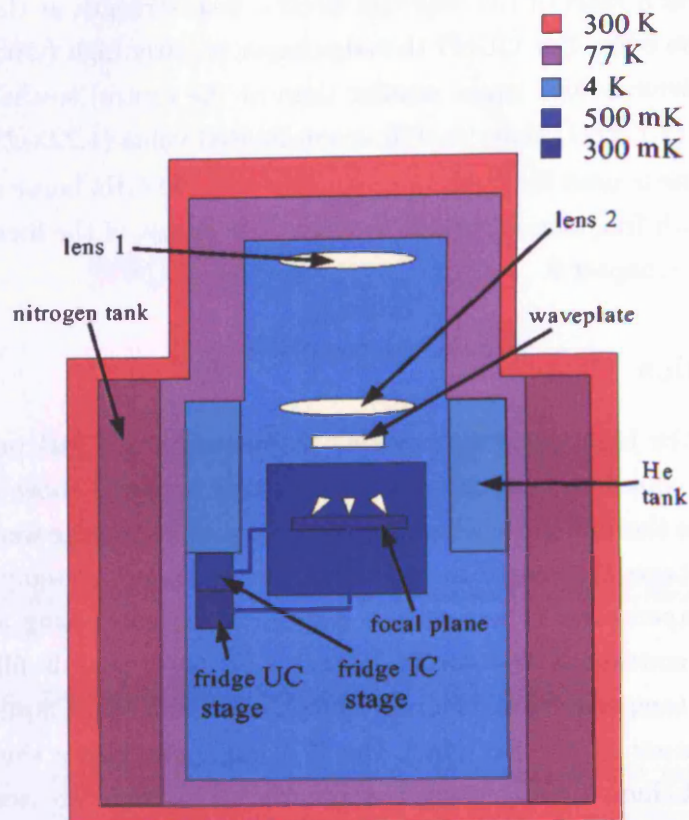
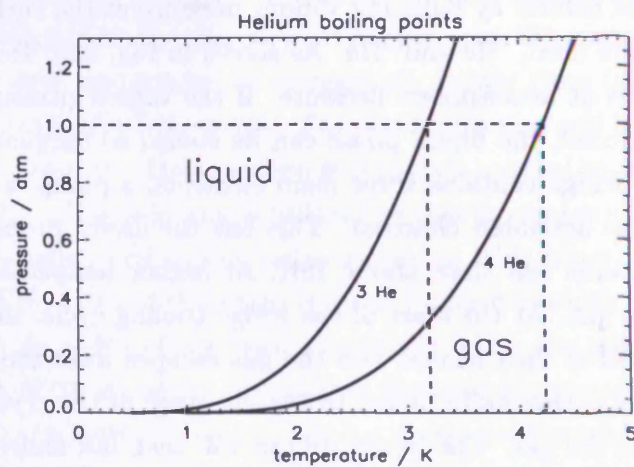


Figure 2.4: Schematic of cryostat.

Figure 2.5: Helium phase diagram. At atmospheric pressure ^4He will condense from gas to liquid at 4.2 K and ^3He at 3.2 K.

therefore used as a pre-cooling stage to cool the condenser to below 3.2K. The ^3He pump then works in exactly the same way as the ^4He pump giving temperatures in the still of around 300 mK. For QUaD an additional ultra cold (UC) stage is needed giving a three stage fridge. This is described in detail by Bhatia et al. (2002). The previous set-up is used to provide an intermediate cold (IC) stage and an additional ^3He pump is run at the same time, using the low temperatures at the IC still to condense the helium instead of the condenser attached to the 4K stage. The IC stage therefore provides a thermal barrier against the 4K loading of the cryostat and so allows the UC stage to cool down to 250 mK. A schematic of a three stage fridge is shown in Fig. 2.6. The focal plane is

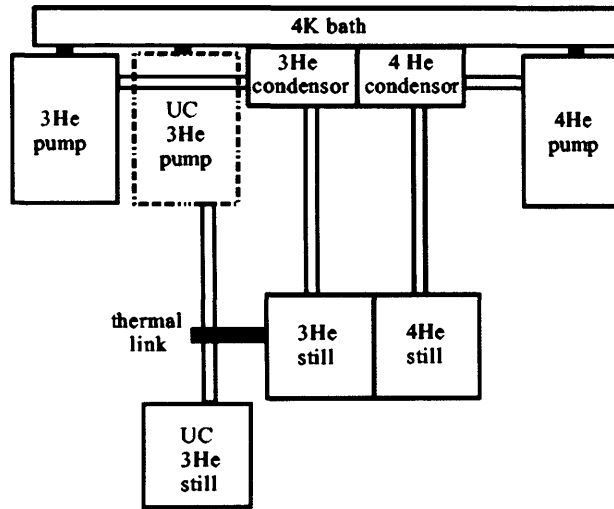


Figure 2.6: Schematic of fridge.

linked to the UC stage in order to cool the detectors to their background limited operating temperature of 300 mK. An additional box linked to the IC stage provides a 500 mK shell around the focal plane and the horns to further shield the detectors.

A large heat load from the sky enters through the cryostat window. The detectors absorb radiation at all frequencies and so at each stage there are filters which only allow a narrow frequency band of radiation to reach the focal plane. This reduces the total loading on the detectors and allows the specific QUaD observing frequencies to be targeted. Each of the feedhorns has a separate filter at the 4K to 300 mK interface. The filters give bandwidths of 25% of the central frequency at each of the two operating frequencies.

2.2.4 Detectors

At the CMB frequencies used by QUaD, bolometers are the most sensitive detectors currently available. These are devices which detect incident power by measuring changes in resistance due to heating by the incoming radiation. The main components of a bolometer are shown in Fig. 2.7. An absorber with heat capacity, C , intercepts the incoming

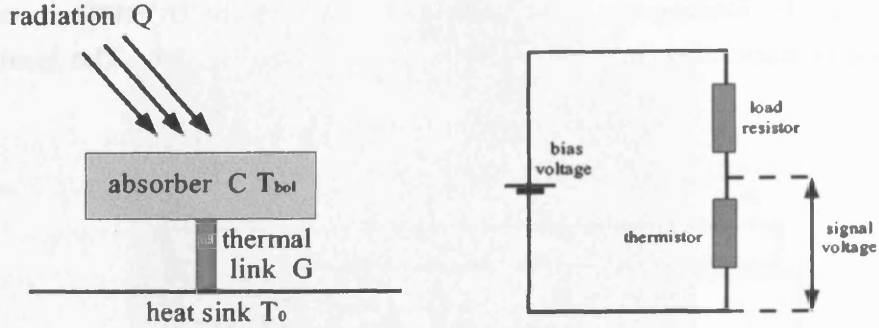


Figure 2.7: Left: Main components of a bolometer. Right: Circuit used to pass current through a bolometer.

radiation. This heats up a thermistor made of a semi-conducting material attached to the absorber. The absorber has a weak thermal link of conductivity, G , to the ultra-cold stage of the fridge at a temperature T_0 . The thermistor is attached in series to a high resistance load resistor. A bias voltage is applied across the two components and the voltage across the thermistor is measured. If the incoming radiation is constant, the temperature of the bolometer, T_{bol} , will settle to its equilibrium value so that the power into the bolometer from the incident radiation and electrical heating is equal to the power escaping through the thermal link. If the incident power increases, the thermistor will heat up and its resistance will increase. The load resistor maintains a constant current across the thermistor and so the fluctuation in incident power will be proportional to the output voltage. The responsivity of the bolometer, S , gives the output voltage per unit change in power. This parameter depends on the background power loading and is found by calibrating the detector.

The bolometer will experience a temperature change ΔT proportional to the change in power, but this response is not instantaneous. The bolometer has an exponential response to any change in power such that (Hanany et al. (1998)):

$$T_{bol} = T_{av} + \Delta T(1 - e^{-t/\tau}) \quad (2.1)$$

where T_{av} is the temperature of the bolometer if there were no fluctuations and t is the

time since the fluctuation. τ is the bolometer time constant which gives the time taken for the thermistor to change by a temperature $\Delta T(1 - 1/e)$. This is related to the other bolometer parameters by $\tau = C/G$. The response of the bolometer acts as a low pass filter on the fluctuating signal, suppressing fluctuations which occur over short time-scales. The sampling frequency should therefore be smaller than $1/\tau$. In practice the sampling frequency for QUaD will be limited by constraints on the scanning speed and not by the bolometer time constant, as discussed in Chapter 6.

Bolometers are incoherent detectors and so respond to changes in the total intensity of the radiation, but do not directly measure the electric field strength or its phase. A normal bolometer can not therefore be used to measure the polarization of the radiation. However, as described in Section 1.2.1, the Stokes parameters can be obtained by measuring the signal with two separate polarization sensitive bolometers (PSBs), each sensitive to orthogonal polarization states of the radiation. The PSB design is described in detail by Jones et al. (2003). The polarization sensitivity is achieved through the geometry of the absorber. In a bolometer, the absorber is not generally made from a continuous sheet of material, instead a mesh of dielectric material coated in metal is used. The separation of the strands of material in the mesh is smaller than the wavelength of the microwave radiation to be absorbed. This reduces the surface area of the absorber, lowering the heat capacity and hence reducing the time constant of the bolometer. A ‘spider-web’ bolometer used for total power measurements is shown in Fig 2.8 (a). In a PSB, a square Si^3N^4 mesh is used, but the metallic coating is only on either the horizontal or the vertical axis of the grid. The mesh then acts in a similar way to polarizing wire grid, allowing only the electric field component in the direction of the metal lines to be absorbed. A doped germanium thermistor is placed at the top of the grid. A single PSB device is shown in Fig. 2.8 (b). A pair of orthogonal grids separated by a fraction of a

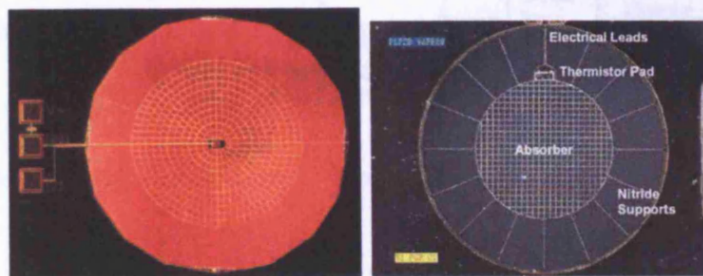


Figure 2.8: Bolometer absorber geometries (a) a spider web mesh (Masi, S. et al (2003)) (b) PSB mesh (Jones et al. (2003)).

millimetre absorb the radiation from a single feed. Both bolometers will therefore observe exactly the same point on the sky and the radiation absorbed by each detector will have

passed through the exactly the same optical path. This ensures that the common mode signal will be removed when the output of the two PSBs is differenced. The possible systematic effects associated with this design are discussed in Chapter 7.

2.2.5 Electronics

The electronics is split into two sections, the cold electronics inside the cryostat and the warm electronics outside the cryostat. There are two circuits used in the QUaD cold electronics, the bias circuit and the read-out circuit. These are shown in Fig. 2.9. The bias circuit passes a current through the bolometer thermistor and the two load resistors on either side of the thermistor. The resistance of the load resistors is much bigger than that of the thermistor so that the current through the thermistor stays constant, but the voltage across it will change in response to changes in its resistance. The read-out circuit measures the voltage across the thermistor. This voltage is passed through a JFET amplifier before being passed onto the warm electronics. The JFET stage is needed because the electronics used to directly read-out the bolometer voltage must have a very high impedance so that it draws as little current out of the bias circuit as possible. If this were not the case the read-out would influence the voltage reading. JFETs are specially designed to operate with a very small input current. The JFETs then produce an amplified signal with a much higher current. This is important as the low current signal from the bolometers is very susceptible to microphonics and so could not be carried all the way out of the cryostat.

In order to reduce the effect of electronics $1/f$ noise an AC bias signal is used. This modulates the signal bandwidth above the $1/f$ knee. The modulated output is then passed onto the warm electronics. This amplifies the signal (preamp), filters out the unwanted frequencies from modulated signal (bandpass filter), then demodulates this signal (lockin amplifier and low pass filter), removes the DC offset and then produces a digital signal (A/D convertor) which can be stored. This is shown in Fig. 2.9 (b). The modulation / demodulation process is explained in more detail in Appendix C.

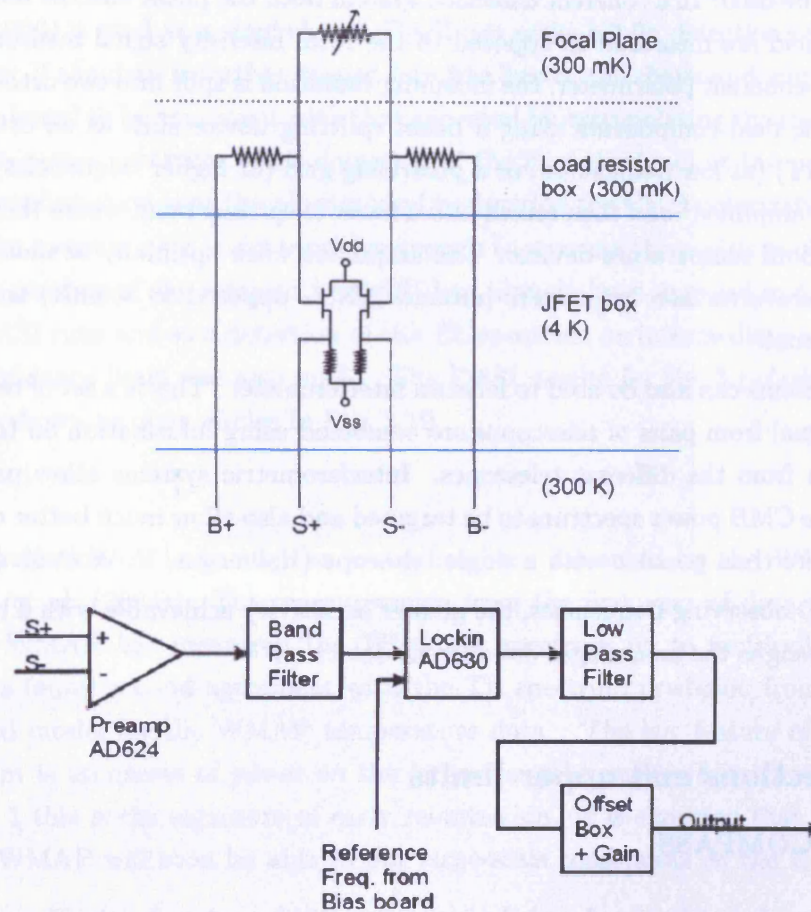


Figure 2.9: Cold electronics circuit (top). Warm electronics circuit (bottom). (from J. Hinderks).

2.3 Other CMB polarization experiments

The technology used to detect the CMB can be split into two classes depending on the type of detection system used. The choice of system is usually a compromise between raw sensitivity and minimizing systematics. At the high frequency end of the CMB window, **bolometric** systems such as that used by QUaD are the most suitable, whereas at the low frequency end, **coherent** systems, which use techniques borrowed from radio astronomy, can be used. In a coherent detection system both the phase and the magnitude of the electric field are measured as opposed to the total intensity signal measured by a bolometer. In a coherent polarimeter, the incoming radiation is split into two orthogonally polarized electric field components using a beam splitting device such as an orthomode transducer (OMT) (at low frequencies) or a polarizing grid (at higher frequencies). These components are amplified¹ and then mixed into a lower frequency band where they can be detected with room temperature devices. The amplifiers work optimally at much higher operating temperatures than bolometers (around 20K as opposed to 300mK) and so are much easier to cool.

Coherent systems can also be used to form an interferometer. This is a set of telescopes in which the signal from pairs of telescopes are combined using information on the phase of the radiation from the different telescopes. Interferometric systems allow particular multipoles in the CMB power spectrum to be targeted and also allow much better rejection of the atmosphere than possible with a single telescope (Halverson, N. W et al. (2002)).

At the QUaD observing frequencies, the greater sensitivity achievable with a bolometric system out-weighs the advantages of coherent detection.

2.3.1 Detections and upper limits

POLAR and COMPASS

The POLAR experiment has produced the best upper limit to date for the E-mode spectrum on large angular scales (Keating et al. (2001)). This was a single horn correlation receiver operating in three bands around 30 GHz in Wisconsin, USA. The POLAR experiment was upgraded to observe on smaller angular scales by adding a lens and a mirror to the focus radiation onto the receiver. This formed the COMPASS experiment. COMPASS set an upper limit on E-mode anisotropies of 33.5 μ K in the multipole range $\ell = 200 - 600$ (Farese P. C. et al. (2004)).

¹For CMB experiments, the most commonly used amplifiers are HEMTs (High Mobility Electron Transistors).

DASI

The DASI experiment was the first to actually detect the CMB polarization signal (Kovac et al. (2002)). DASI uses 13 feed horns as a interferometric array operating between 26 and 36 GHz. The instrument operated initially as a small-scale temperature experiment, but in summer 2000-2001 waveguide polarizers were inserted between the feedhorns and amplifiers to make a polarization sensitive interferometer. Two small patches of sky (3.4°) were observed for a total of 271 days. If the entire observable range of multipoles ($150 < \ell < 900$) is used as a single band, DASI can make a 4.9σ detection of the E-mode polarization. If the data is further binned into five bands, the shape and amplitude of the spectrum is found to be consistent with that expected by extrapolating the results from the temperature power spectrum. This detection of the E-mode signal at the predicted level is a strong confirmation that the physics used to describe the CMB polarization is correct. However, the measurement is not sensitive enough to measure the positions of the acoustic peaks. The patches of sky mapped by DASI had already been mapped in total power in previous DASI runs and so a detection of the TE spectrum on intermediate angular scales at a 2σ confidence limit was also made. The DASI results for the 3 polarization power spectra are shown as open circles in Fig. 2.10.

WMAP

The TE correlation on large angular scales has been measured by the *WMAP* satellite (Kogut, A. et al. (2003)). The measurements from the first year of data are shown in Fig. 2.10. WMAP has measured the TE power spectrum up to multipoles of around 450 and has found a good agreement with the TE spectrum predicted from the best fit cosmological model for the WMAP temperature data. The key feature of the WMAP measurement is an excess of power on the largest angular scales ($\ell < 10$). As discussed in Chapter 1 this is the signature of early reionization. It is expected that the two year data from WMAP will soon be able to put large-scale constraints on the E-mode power spectrum.

ARCHEOPS

The ARCHEOPS² experiment is a proto-type for the bolometer technology which will be used by the Planck satellite (discussed below). ARCHEOPS is a balloon experiment which was flown from Kiruna in Sweden. The instrument operates at four different frequencies, but only the six detectors in the 353 GHz channel are polarization sensitive. This channel uses a similar design to the PSBs used by QUaD, but the radiation is split at the exit of each of the three feedhorns by a polarizing beam splitter and the two beams

²<http://www.archcops.org/>

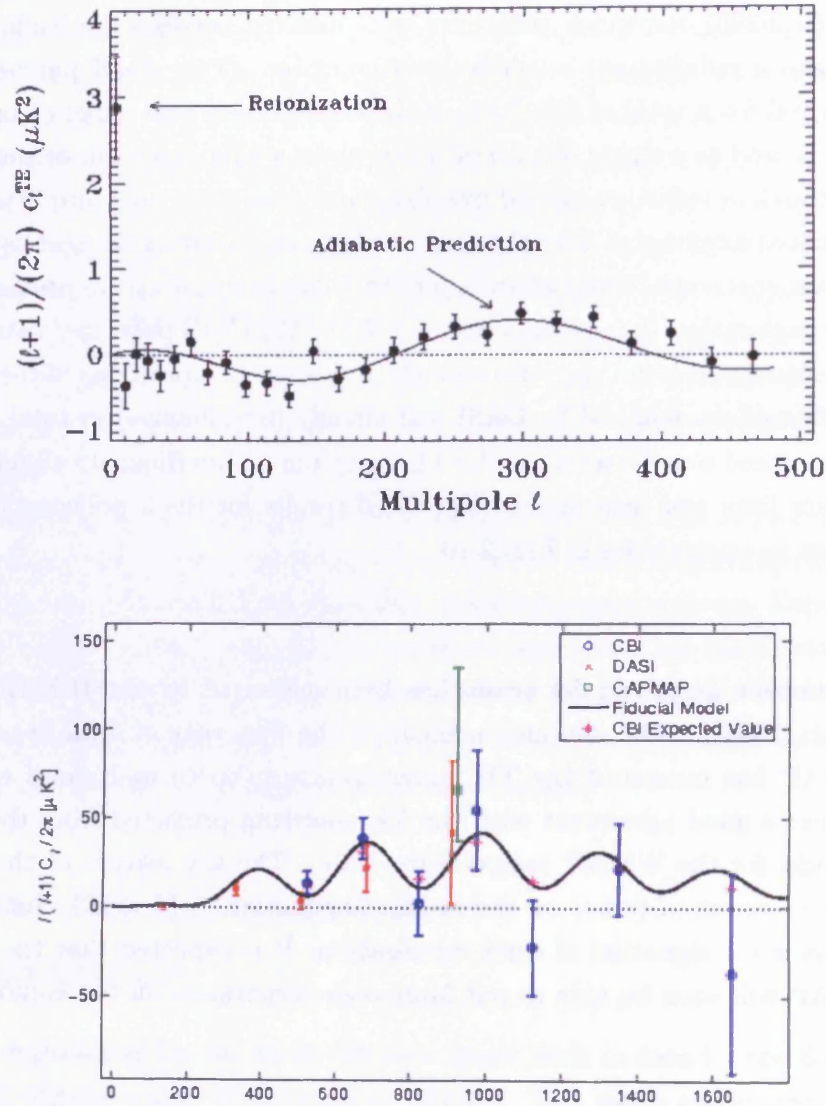


Figure 2.10: Detections of CMB polarization. Top: WMAP measurement of TE spectrum (from Kogut, A. et al. (2003)). This clearly shows the oscillatory nature of the spectrum and the excess of power on large angular scales. Bottom: Measurements of the EE spectrum from recent ground-based experiments (from Readhead et al. (2004)).

are directed onto adjacent orthogonally orientated detectors, creating 3 pairs of polarization sensitive devices. The experiment was not designed specifically to measure the CMB polarization signal, instead it focused on polarized galactic foregrounds (Benoît, A. (2004)). The ARCHEOPS measurement of polarized emission from dust is discussed in detail in Chapter 3.

CBI

CBI is an interferometric experiment which works in a similar way to DASI but using larger baselines which allow it to observe on smaller angular scales ($300 < \ell < 2000$). CBI operated as a temperature experiment for two years and was then upgraded in 2002 so that it was optimized for polarized observations (Readhead et al. (2004)). CBI has detected the E-mode signal with high confidence (7σ). This measurement is sensitive enough to resolve the acoustic peaks. The phase of these peaks is consistent with a phase shift of π relative the temperature spectrum. This provides further evidence that the standard cosmological model is correct.

2.3.2 Experiments currently in operation

There are a number of CMB polarization experiments which are currently in operation, or in process of analyzing data.

MAXIPOL

MAXIPOL is an upgrade to the MAXIMA experiment (Johnson B. R. et al. (2003)). This was a bolometric balloon-borne experiment operating at 140 GHz and 420 GHz at angular scales between 2° and $10'$. MAXIMA was made polarization sensitive by adding a rotating half waveplate and wire grid polarizer to the existing hardware. The wire grid in front of the feed makes each detector act like a single PSB by rejecting one polarization state of the radiation. The differencing between two detectors used by QUaD is not needed as MAXIPOL is able to continuously rotate the waveplate. This will modulate only the polarized part of the signal, allowing it to be distinguished from the unpolarized background. MAXIPOL flew from the New Mexico, USA in May 2003 and the analysis of the data from this flight is currently in progress.

BOOMERANG

BOOMERANG was one of the first experiments to measure the position of the first peak in the CMB power spectrum (de Bernardis, P. et al. (2000)). The balloon-borne bolometric experiment flew around the Antarctic in 1998. After this flight, the focal plane was upgraded by replacing the original 145 GHz spider web bolometers with PSB pairs,

and placing polarizing wire grids over the top of the 245 GHz and 345 GHz feeds (Montroy, T. et al. (2003)). The grids are orientated so that pairs of spider web bolometers can be differenced to find Q and U. A 15 day flight of this array was carried out in January 2003 and the results from this flight are expected soon.

CAPMAP

CAPMAP is an array of correlation receivers at 90 GHz and 40 GHz (Barkats (2003)). These are coupled to the Crawford Hull 7-m antenna in New Jersey, USA to measure angular scales between 1° and $4'$. A test run of the instrument operating with four receivers was made for 4 months at the start of 2003 and the data is currently being analyzed. The experiment has recently been upgraded to the full 16 element array.

2.3.3 Upcoming experiments

The current generation of CMB experiments are not sensitive enough to make a high resolution measurement of the E-mode spectrum or to detect the B-mode spectrum. This is mainly because they are limited by the number of detectors on the focal plane, the available integration time or the sensitivity of the detectors. However, there are a number of other experiments currently under construction which will be able to make measurements with similar sensitivity to QUaD.

BICEP

BICEP is very similar to QUaD in experimental design (Keating et al. (2003)). It will operate at the same time as QUaD from the same site and uses identical detectors. The main difference is that BICEP is optimized to detect the gravitational wave B-mode signal which peaks on intermediate angular scales, so BICEP does not need the high resolution created by the QUaD optical system. Therefore BICEP does not need to be coupled to a telescope and the cryostat window looks straight out onto the sky. This limits the maximum resolution to about 1° . Also, BICEP does not use a waveplate, instead Q and U are obtained by continuously rotating the dewar as the telescope scans across the sky. BICEP also incorporates another level of modulation in addition to the AC biasing of the bolometers. A Faraday rotator³ will be placed in front of the feedhorns which will

³A Faraday rotator is a device which uses the Faraday effect to rotate the angle of polarization of incoming radiation. If a dielectric material is subjected to a strong magnetic field, the optical properties of the material will change so that it rotates the polarization angle of the radiation by an amount which is proportional to the field strength and to the length of the dielectric. A solenoid wrapped around the dielectric can therefore be used to modulate the polarization angle by continuously alternating the direction of the current.

continuously flip the polarization angle of the radiation with respect to the detector by 90° .

Planck

The Planck satellite⁴ will have a similar sensitivity to QUaD however, it will be able to map the whole sky (apart from the galactic plane) instead of a single patch and so will be sensitive to much lower multipoles. The Planck instrument uses both of the technologies mentioned here. The LFI (low frequency instrument) uses arrays of HEMT amplifiers at 30, 44 and 70 GHz (Lawrence (2003)). Each of these channels will be polarization sensitive.

The HFI (high frequency instrument) will use the same PSBs as QUaD at 100, 143, 217 and 353 GHz, with four feeds in each channel (Lamarre, J. M. et al. (2003)). Planck will rely mainly on the arrangement of the detectors on the focal plane to measure both Q and U as there is no method of rotating the polarization angle of the radiation, although the scanning strategy allows each pixel to be observed at a number of different orientations. Planck is set to launch in 2007.

The expected performance of QUaD compared to these other experiments will be discussed in Chapter 5.

2.3.4 Planned next generation experiments

The Planck satellite is expected to make a similar measurement of the E-mode power spectrum to that made of the temperature spectrum by WMAP. The focus of the next generation of experiments will therefore be to make a measurement of the B-mode signal. This requires a huge increase in sensitivity compared to that expected for the experiments described so far. The increase in sensitivity achievable by moving to more advanced detector technologies is fairly small, as current technologies are already very close to theoretical limits. The main technological hurdle is therefore to find ways to make large arrays of hundreds of detectors. Currently this is unfeasible due the physical size of such an array and the complexity of the electronics needed to read-out a large array without generating excessive electronic noise. There are a number of teams currently working on instruments that will address these challenges.

Clover

This is a funded European project headed by Cardiff and Cambridge in the UK (Taylor et al. (2004)). Clover will use an array of TES (transition edge sensor) detectors which operate in a similar way to bolometers. However, the detectors can be read-out

⁴<http://www.rssd.csa.int/index.php?project=PLANCK>

by frequency multiplexing using SQUID (superconducting quantum interference device) technology. This allows eight detectors to be read-out by a single electronics chain. The proposal is to build three separate telescopes, one for each observing frequency (90, 150 and 220 GHz) to enable foreground removal to be carried out. Each single telescope will have an array of 8×8 feeds, but this central array will be fed by four different arrays of feed-horns. This gives an equivalent sensitivity to that of a 256 element array, but with a much smaller focal plane. Each feed will consist of a pseudo-correlation polarimeter which creates two phase-modulated signals each of which gives a different combination of Q and U. These signals are then detected using two separate TESs. This allows Q and U to be measured simultaneously with each feed. Clover intends to operate from Dome C on the Antarctic Plateau, a site which is expected to be even more stable than the South Pole. The 15 arcmin Clover beam will enable this experiment to probe the multipole range $\ell = 20 - 1000$ and so measure the peak in the GW B-mode spectrum.

QUIET

QUIET⁵ is a proposed upgrade to the CBI experiment. The CBI detection system will be replaced with an array of approximately 1000 polarimeters which will operate in a similar way to those used by PIQUE. However, the technology has been miniaturized using MMIC (monolithic microwave integrated circuit) technology so that each polarimeter is only about an inch in diameter and each detector can simultaneously measure Q and U. QUIET will have a 3 arcmin beam and so be able to measure multipoles above $\ell = 1000$ and probe the gravitational lensing B-mode signal.

PolarBear

PolarBear is a US project led by the University of California at Berkeley⁶. The project proposes to use the same TES/SQUID technology as Clover, but will have a single array of 1000 feeds. The final version of PolarBear is set to operate from the South Pole, but a 150 element test array will first be operated from White Mountain in California.

⁵<http://cfcp.uchicago.edu/peterh/polarimetry/quiet3.html>

⁶<http://bolo.berkeley.edu/polarbear/>

Chapter 3

Astrophysical foregrounds

The signal measured by QUaD will contain a contribution from any astrophysical foreground between the surface of last scattering and the Earth which emit at millimetre wavelengths. If this foreground were constant across the sky it would simply add to the total background power. This would just cause a slight decrease in the sensitivity of the experiment by creating more photon noise. In reality, the foreground also fluctuates across the sky and so will create a signal which could be mistaken for fluctuations in the CMB. Total power foreground fluctuations will not be a big factor for QUaD as any common mode signal leaking into the polarized measurements will be swamped by the much stronger atmospheric fluctuations. However, any polarized foreground which varies across the sky could be the limiting factor determining whether QUaD can measure the CMB polarization. In this Chapter we review the current information available on polarized foregrounds and provide estimates of the level of these foregrounds. These estimates will be used later in Chapter 5 to determine the extent to which foregrounds are likely to hinder QUaD's performance and in the time ordered data simulations in Chapter 7.

Although QUaD will target an area of sky away from the plane of the galaxy, the emission from the galaxy extends to fairly high galactic latitudes and so cannot be completely avoided. The dominant sources of galactic foreground are from free-free emission, dust and synchrotron radiation. On very small scales there will also be extra-galactic emission due to point sources such as AGN.

Our knowledge of unpolarized foregrounds has recently been greatly improved by the results of the *WMAP* satellite (Bennett C. L. (2003)). The foreground levels averaged over the whole sky are shown in Fig. 3.1 for the *WMAP* bands. The CMB dominates over the foregrounds between about 30 and 200 GHz. This frequency band is known as the CMB window. At higher frequencies the emission is dominated by dust and at lower frequencies by synchrotron radiation. A template of the emission from each component can be made by observing the sky at a frequency where this component is the dominant source of emission and then using a model for the frequency dependence of the emission

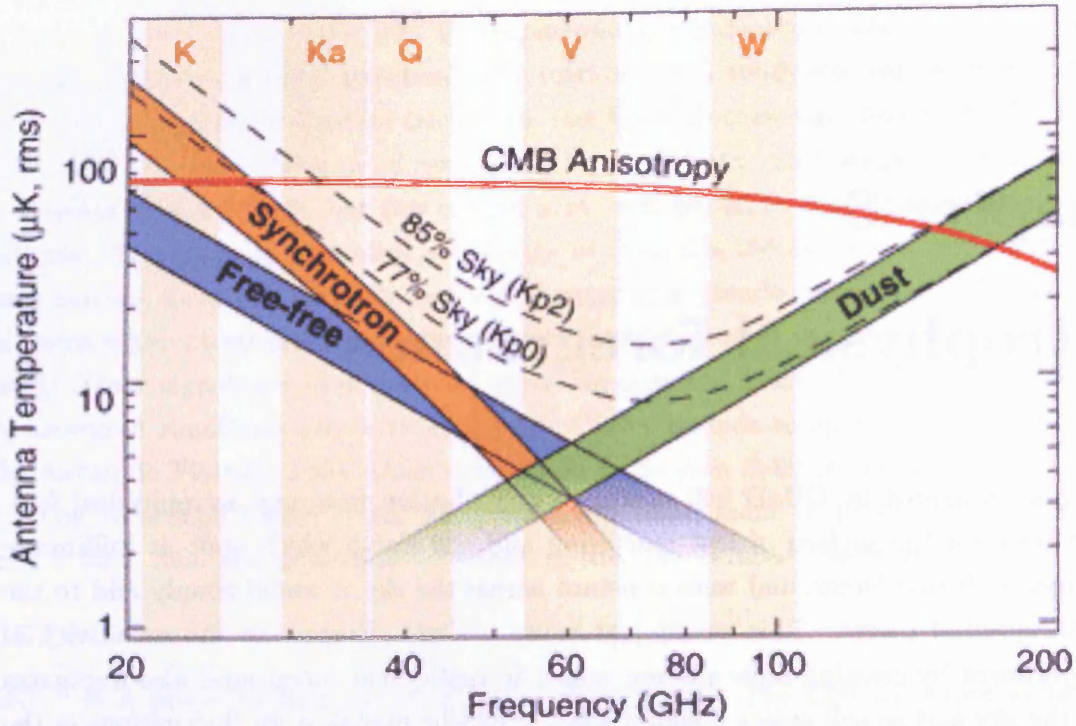


Figure 3.1: Foregrounds amplitudes measured by WMAP (Bennett C. L. (2003)).

to extrapolate the map to CMB frequencies. The frequency dependence is found by using two maps at similar frequencies to fit a theoretical model. As well as estimates of the frequency dependence and rms amplitude in the WMAP bands, the WMAP team also provided derived maps of the different foregrounds levels and spectral indices (Bennett C. L. (2003)) using a MEM (maximum entropy method) in which radio (synchrotron) and infra-red (dust) maps (discussed below) are used as priors in the analysis. These maps are the best indication of the unpolarized foreground levels and spectral indices at CMB wavelengths to date.

If it is possible to assume that the polarized emission follows the total intensity, polarized maps can be made by simply scaling these total power maps by a polarization fraction. However, the processes by which the emission becomes polarized can be complicated so this simple assumption is not always valid. Full sky polarized maps are therefore needed at CMB frequencies to determine the polarized foreground. Unfortunately, at present there are no large area polarized surveys which can be used to make templates of the polarized emission. The best that can be done is to use small-scale polarization measurements at other frequencies to provide some insight into the polarized foreground distribution and to determine if extrapolations from total power maps are valid.

In the following sections we will discuss the current estimates of polarized free-free,

dust, synchrotron and point source emission. The models we use are based on the formalism introduced by Tegmark et al. (2000), but we have updated the foreground models based on the findings of more recent analyses and observations. In each case, following Tegmark et al. (2000), we separate the foreground model into two parts, the frequency dependence of the foreground fluctuations, $\Theta(\nu)$, and its spatial distribution, specified by its spatial power spectrum, C_ℓ^{fg} . The foregrounds are specified in terms of their CMB thermodynamic temperature, T_{th} to aid comparison with the CMB signal. However, the foreground amplitudes are normally quoted in terms of antenna temperatures, T_A . The conversion between the two quantities is given by (Tegmark et al. (2000)):

$$c(\nu) = \frac{T_{th}}{T_A} = \left(\frac{2 \sinh(x/2)}{x} \right)^2 \quad (3.1)$$

where $x \equiv h\nu/kT_{cmb}$. The frequency dependence is normalized to a reference frequency:

$$\Theta(\nu) = T_A(\nu_*)(\nu/\nu_*)^{-\alpha}. \quad (3.2)$$

so that $\Theta(\nu)$ gives the fraction by which the antenna temperature fluctuation at frequency ν is different to that at the reference frequency. The units of the fluctuation are then absorbed in to the spatial power spectrum normalization, A , where:

$$C_\ell(\nu_*) = (pA)^2 \ell^{-\beta}. \quad (3.3)$$

and A is defined at the reference frequency and has units of antenna temperature. The factor p gives the fractional polarization and β is the power spectrum index. The variance of the foreground at a given frequency is then given by:

$$C_\ell(\nu) = \left(\frac{c(\nu)}{c(\nu_*)} \Theta(\nu) pA \right)^2 \ell^{-\beta} \quad (3.4)$$

A and p are found from the rms fluctuation in the foreground at the reference frequency per beam, σ :

$$\sigma^2 = \sum_{\ell=2}^{\infty} \frac{(2\ell+1)}{4\pi} e^{-\sigma_b^2 \ell(\ell+1)} C_\ell. \quad (3.5)$$

where σ_b is the rms beam size¹. Note that p is not always the same as the polarization fraction of the rms signal, f_p , which is usually the figure quoted, giving the rms polarized fluctuation per beam ($\sigma_p = f_p \sigma$). The two factors will only be equal if the slope, β of the unpolarized and polarized power are the same. The numbers used are based on the ‘middle of the road’ model in Tegmark et al. (2000). In Table 3.1 we show how the parameters we have used compare with the original models.

¹Note this is not the same as the FWHM beam size as will be discussed in Chapter 5.

Foreground	ν_*/GHz	$A/\mu K$	α	β_{up}	β_p	p (pess)	p (opt)
Synchrotron	60 (19)	3.7 (101)	2.8 (2.8)	2.4 (2.4)	1.4 (1.4)	0.19 (0.13)	0.05
Dust	100 (90)	29.3 (24.0)	2.2 (1.7)	3.0 (3.0)	1.4 (1.3)	0.007 (0.002)	0.0016

Table 3.1: Foreground parameters. Values used in Tegmark et al. (2000) ‘middle of the road’ model given in brackets for comparison.

3.1 Dust

Dust grains in the interstellar medium are expected to give the dominant contribution to the astrophysical foreground at frequencies above about 90 GHz. Dust grains absorb starlight which excites vibrational modes in the dust grain causing it to re-emit at lower frequencies. The emission peaks in the infrared at around $100\ \mu\text{m}$ (3000 GHz). Detailed full sky maps of the total power emission have been made by combining data from the IRAS satellite and the DIRBE experiment on the COBE satellite (Schlegel et al. (1998)) and a detailed model for the extrapolation of these maps to microwave frequencies has been developed by Finkbeiner et al. (1999). The recent results from WMAP have shown the predictions of this model to be in good agreement with the derived dust maps for the WMAP bands (Bennett C. L. (2003)).

This vibrational emission occurs for relatively large grains; however, it is possible that there is also a population of ultrasmall grains (PAH - polycyclic aromatic hydrocarbons) which are not large enough to emit through vibrational modes, but could be excited into emission from rotational modes (Lazarian and Prunet (2002)). No definite measurement of this emission has been made, but it could be possible that rotating dust is the cause of an observed excess foreground emission at lower frequencies (10-60 GHz) (Draine and Lazarian (1999b)). Another explanation for this anomalous emission is magnetic dipole emission from magnetic components of the dust such as iron and nickel (Draine and Lazarian (1999a)). Each of these three sources of dust emission can become polarized and so dust may present a serious problem for the detection of the CMB polarization signal.

Rotating dust and magnetic dipole emission are both predicted to occur at frequencies below the QUaD bands and so will not cause a problem for QUaD, but could be a problem for experiments at lower frequencies. There is no direct observational evidence that proves that these emission mechanisms produce a significant signal; in fact the recent WMAP results are consistent with this emission accounting for less the 5% of the total emission in the lowest frequency (23 GHz) band where this signal would give the highest level of contamination (Bennett C. L. (2003)). However, this result is contested by Finkbeiner (2003) who claims that a significant contribution from spinning dust is consistent with the WMAP data. We do not consider this component in our analysis. However, we note that it may be important if magnetic dipole emission is the main contributor to this excess

low frequency emission, as theoretical predictions estimate a significant foreground signal up to around 90 GHz (Draine and Lazarian (1999a)).

The most important emission for QUaD will be vibrating dust. A significant polarization for vibrating dust will occur if the dust grains become aligned. The grains are usually aspherical and they preferentially emit the component of the electric field aligned with the longest axis of the dust grain. If the grains are randomly oriented there is no net polarization, but if there is a mechanism by which the longer axes become aligned the overall emission will be polarized. The interaction of the galactic magnetic field with the dust grains is thought to cause such an alignment in our galaxy. The absorption of starlight by the emitting grains will also cause a polarization of optical emission. This has been analysed by Fosalba et al. (2002) who find a strong correlation between synchrotron emission and polarized starlight indicating that polarized starlight, and hence dust emission, follows the galactic magnetic field. This supports the idea that the dust grains will be aligned. The best measurement to date of polarized emission from vibrating dust comes from the ARCHEOPS experiment (Benoît, A. (2004)). A degree of polarization of 4 – 5% is found at 353 GHz for diffuse emission close to the galactic plane. This figure is in agreement with the polarized sub-mm emission estimated from starlight polarization (Fosalba et al. (2002)). This gives a possible lower limit on the polarization at higher latitudes as it is expected that the degree of polarization will decrease due to depolarization effects if there is a long line of sight between the polarized emission and the observer. This increases the polarization degree at higher latitudes compared to that in the plane of the galaxy. Depolarization will occur even if the dust grains are perfectly aligned with the magnetic field as there will be variations in the magnetic field direction along the line of sight (Lazarian and Prunet (2002)).

The ARCHEOPS measurement is the only direct measurement of polarized dust emission at CMB frequencies. To estimate the power spectrum and frequency dependence of dust emission, extrapolations need to be made from other measurements. Prunet et al. (1998) make a detailed model using theoretical predictions for the polarization of dust grains. They assume that dust emission will follow HI emission and so use observations of this emission to predict the 3D distribution of the dust. The dust emission can then be integrated along the line of sight to account for depolarization effects and a 2D map of the polarized dust emission can be made. The power spectra of these maps have a spectral index of between 1.3 and 1.4. Baccigalupi (2003) use a simpler model, in which the polarized emission is assumed to be perfectly correlated with the unpolarized dust emission, and find that this model is in good agreement with the Prunet et al. (1998) prediction. We therefore use a total power template extrapolated from that of Schlegel et al. (1998) into the QUaD 100 GHz band scaled by a 4% polarization factor as a template

to determine regions of sky likely to have high levels of polarized dust emission. This template is shown in Fig. 3.5.

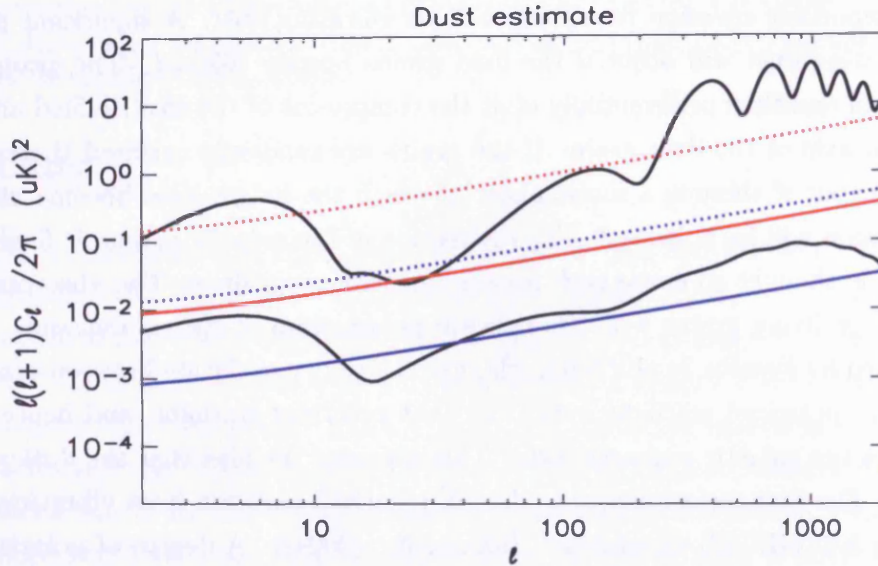


Figure 3.2: Estimated levels of polarized dust fluctuations compared to CMB. The blue lines are for 100 GHz and the red for 150 GHz. The dotted lines are for a 4% rms polarization and the solid lines a 1% rms polarization. On this plot and in the Fig. 3.3 and Fig. 3.4 the black lines show the E-mode (top) and B-mode (bottom) CMB power spectra.

To estimate the spatial power spectrum the amplitude of unpolarized dust from the WMAP results is used. This gives an amplitude of $10\mu K$ at 100 GHz. We assume an rms polarization of 4% and a power spectrum index of 1.4. We also include an optimistic model with an rms polarization of 1%. The dust can be modelled as a grey body with a certain emissivity and temperature. The emissivity scales with frequency giving a dependence of (Finkbeiner et al. (1999)):

$$I(\nu) = \frac{\nu^\alpha B(\nu, T_{dust})}{\nu_0^\alpha B_0(\nu, T_{dust})} \quad (3.6)$$

This then gives an antenna temperature of (Tegmark et al. (2000)):

$$T(\nu) = \frac{c_*(\nu)c(\nu)\nu^\alpha B(\nu, T_{dust})}{c_*(\nu_*)c(\nu_*)\nu_*^\alpha B_*(\nu, T_{dust})} \quad (3.7)$$

where the factor $c_*(\nu)$ converts from intensity to antenna temperature and is given by $c_*(\nu) \approx 10^4/x^2$ and x and $c(\nu)$ were defined at the beginning of this chapter. Finkbeiner et al. (1999) find that this model in which the dust is assumed to have a single temperature and emissivity is not a good fit to infrared data. Instead a model in which there are two species of dust with different temperatures and emissivities is a much better fit. However, over a small frequency interval a single component will dominate and so a single

dust temperature and emissivity can be used to extrapolate between different CMB frequencies. We therefore use a spectral index of 2.2 and a dust temperature of 18K (Bennett C. L. (2003)). This model then has the amplitudes $A = 29.3$ and $p = 0.0066$ (or $p = 0.0016$ for optimistic case). These estimates for the QUaD bands are shown in Fig. 3.2.

3.2 Synchrotron

Synchrotron radiation is produced when relativistic electrons interact with a magnetic field. Cosmic ray electrons produced from high energy processes such as supernova explosions will create synchrotron radiation due to the strong magnetic field present throughout the galaxy. This emission is present not only in the disc of the galaxy, but also in loops of emission at higher latitudes. At radio wavelengths, synchrotron radiation is the dominant source of galactic emission and so templates of synchrotron radiation can be made from radio maps of the sky. These templates can then be extrapolated to CMB frequencies using a power law model for the frequency dependence:

$$T(\nu) = T(\nu_*)(\nu/\nu_*)^{-\alpha}, \quad (3.8)$$

where ν_* is the reference radio frequency and α is the frequency spectral index. The radiation is expected to be polarized, with a polarization fraction, f , which depends on the structure of the magnetic field. The maximum polarization fraction occurs for a uniform field, where (Cortiglioni and Spoelstra (1995)):

$$f = \frac{3\alpha - 3}{3\alpha - 1}. \quad (3.9)$$

The frequency spectral index is in the range $2.7 - 3.0$ and so the maximum polarization is high ($\approx 75\%$). However, the complicated magnetic field structure within the galaxy means that the polarization will normally be much less than this maximum value. Although synchrotron radiation is not a problem for temperature measurements at the QUaD frequencies, where the emission from vibrating dust dominates the foreground (see Fig. 3.1), it could be significant for polarization measurements in some regions of the sky due to this potentially high degree of polarization.

There are no measurements of the amplitude or power spectrum of polarized synchrotron radiation in the CMB window. However, the upper limits from the POLAR experiment (Keating et al. (2002)) and detection by DASI (Kovac et al. (2002)) at relatively low CMB frequencies (where the contamination would be stronger than in the QUaD bands) show no significant synchrotron emission. The WMAP measurement of the TE cross correlation signal (Kogut, A. et al. (2003)) indicates that foregrounds do not

contaminate the TE signal in the WMAP bands. However, by fitting a two component model of the CMB and a foreground to the data they obtain a marginal detection of a foreground consistent with synchrotron radiation with a steep spectral index of 3.7. These results indicate that polarized synchrotron radiation may not be a problem for the measurement of the E-mode power spectrum. However, an understanding of this foreground is still important if QUaD hopes to put upper limits on the fainter B-mode signal.

A number of polarized surveys have been made at radio wavelengths. However, the extrapolation of this information into the CMB window is not simple due to the effects of Faraday rotation and depolarization. Polarized radiation can be decomposed into two circularly polarized components with opposite handedness. An ionized medium in a magnetic field will have a different refractive index for each of these two components. This causes the polarization angle of the radiation to change as it propagates through the medium. This rotation will create small scale fluctuations in the polarization field, which will increase the amplitude of the polarization power spectra at high multipoles. Faraday rotation is frequency-dependent, and is expected to be a strong effect at radio frequencies, but negligible at CMB frequencies. Therefore the small-scale structure in the polarized radio maps can not be extrapolated to higher frequencies and it is not correct to simply scale the amplitude of the power spectrum in order to predict the microwave power spectrum from that at radio frequencies. Faraday rotation causes a change to the polarization angle, but it has only a small effect on the polarized intensity, however; other effects may cause a significant depolarization (de Oliveira-Costa et al. (2003)) which is again expected to be stronger for the lower radio-frequency emission than at microwave frequencies.

The observed radio fields are at fairly low galactic latitudes, whereas for QUaD regions at higher latitudes with lower foreground contamination will be targeted. A key question is whether the results for the polarization degree at low latitude is the same as that at high latitudes. At radio frequencies, the polarized intensity does not depend strongly on galactic latitude. The effects of depolarization mean that polarized emission is due only to limited region around the observer as more distant sources from high latitudes are washed out. However, it is expected that the polarization of the radiation actually generated at high latitude will be higher. This is because the recent WMAP results have shown that the frequency spectral index steepens at higher latitudes, causing a reduction in the total power, but a increase in the polarization fraction (according to Equation 3.9). This is thought to be due to the cosmic ray electrons losing energy as they travel out of the galaxy. The magnetic field is also expected to be more uniform at high latitudes and so the upper limit set by Equation 3.9 is more likely to be met. As depolarization is not a problem at CMB frequencies it is expected that this higher polarization at high latitude

will make the degree of polarization latitude dependent in the microwave band.

The complications in extrapolating to higher frequency and higher latitude mean that current estimates of the polarized amplitudes and spatial power spectra are only educated guesses. One way to make these estimates is to use a total power template of the frequency spectral index to calculate the polarization fraction assuming the maximum polarization fraction of Equation 3.9. This can be combined with an extrapolation of the temperature map from radio frequencies to find the polarized power. For total power measurements, the most commonly used template is the Haslam 408 MHz (0.4 GHz) survey (Haslam (1981)) which maps the whole of the Southern sky. The polarization angle can be estimated from the spatial power spectrum found in polarized radio observations of small patches of sky. This approach is valid if we can assume that the spatial power spectrum does not change with observing frequency. This may not be true on small scales where Faraday rotation will create extra power in the radio band, as observed by Tucci M. et al. (2002). This approach has been used in Giardino et al. (2002) to generate maps and power spectra of polarized synchrotron radiation at 100 GHz and 30 GHz. Another approach is to find the scalar power spectra of the small patches corresponding to just the polarized intensity (i.e. including no information on the polarization angle) as this will not be greatly affected by Faraday rotation. The amplitude of these spectra can therefore be more confidently extrapolated to CMB frequencies. This has been done by Baccigalupi, C. (2001) and Bruscoli M. et al. (2002). Each of these three authors find that synchrotron radiation will not greatly affect the E-mode measurement at QUaD frequencies. For the work done in the following chapters we use the publicly available map of Giardino et al. (2002) at 100 GHz as a template for the polarized synchrotron emission as shown in Fig. 3.5. For the spatial power spectra, we take the rms antenna temperature at 60 GHz of $2\mu K$ per 1° beam (Bennett C. L. (2003)), which gives a value for A of $3.65\mu K$. We take $\alpha = 2.8$ and values for β of 2.4 (unpolarized) and 1.4 (polarized) as used in Giardino et al. (2002). The rms polarization fraction is still very uncertain and so we take two cases, the upper limit of 73% given by Equation 3.9 and the more realistic value of 20% found by de Oliveira-Costa et al. (2003). These give values for p of 0.05 and 0.19 respectively. The level of these estimates in the two QUaD bands compared to the CMB power spectra are shown in Fig. 3.3.

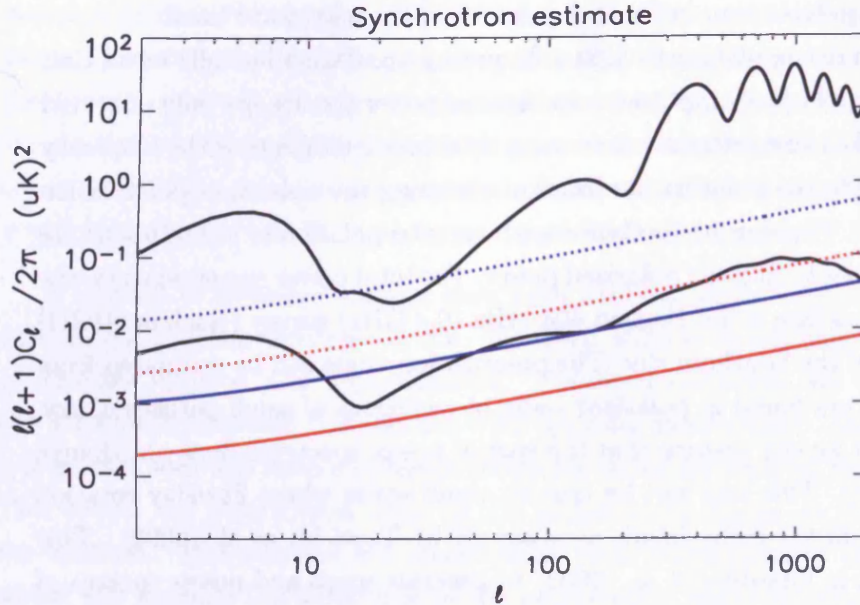


Figure 3.3: Estimated levels of polarized synchrotron fluctuations compared to CMB. The blue lines are for 100 GHz and the red for 150 GHz. The solid lines give the best guess at the synchrotron level (20% rms) and the dotted lines give the maximum levels possible (73% rms) given the amplitude of unpolarized synchrotron and the frequency spectral index used here.

3.3 Free-free emission

Free-free emission, often known as Bremsstrahlung radiation, is due to the deceleration experienced by a free electron when it moves through the electric field of a heavier ionized particle. This causes the electron to radiate. In the galaxy, regions of ionized hydrogen generate free-free emission at radio wavelengths. The photons produced by this process will not be polarized initially (Rybicki and Lightman (1979)) but they are likely to Thomson scatter from free electrons in these ionized regions and so the radiation can become polarized. However, the maximum level of this polarization is relatively low, about 10%, (Keating et al. (1998)). As free-free emission is important over the same frequency range as the highly polarized synchrotron radiation it will give a negligible contribution to the total polarized foreground. Free-free emission will therefore not give a significant contribution to the QUaD data and so is not considered further.

3.4 Point sources

Extragalactic point sources are expected to be the dominant polarized foreground on very small angular scales. There are two populations of objects, radio point sources, due mainly to synchrotron emission from the centre of galaxies, and infrared point sources, due to

dust emission in star-forming galaxies. The theoretical modelling of point source emission is more complicated than for galactic foregrounds as the effects of redshift and galaxy evolution more become important as observations become more sensitive. A number of models have been proposed that predict the number counts of galaxies at different observing frequencies. The most commonly used is that of Toffolatti et al. (1998). This has been shown to give a good fit to data at both radio frequencies (where the emission is strongest) and at CMB frequencies, up to an unknown scaling factor. As with galactic foregrounds, estimates of the temperature distribution of the foreground have been greatly improved by the WMAP observations. These results have shown that the Toffolatti et al. (1998) model gives a consistent fit to the WMAP data, although it slightly over-estimates the number of radio point sources and so an offset factor of about 0.75 is needed to scale the model predictions (Tucci et al. (2004)). The brightest point sources can be masked from the data and so will not add to the foreground. However, there will still be a remaining random distribution of faint sources. This can be modelled as Poisson distribution, which gives a spatial power spectrum of (Tegmark and Efstathiou (1996)):

$$C_\ell(\nu) = [A(\nu)c(\nu)c_*(\nu)]^2 \int_0^{S_c} n(S, \nu) S^2 dS, \quad (3.10)$$

where $n(S)$ is the differential source count per steradian at a flux density S (predicted from a theoretical model), S_c is the cut-off flux above which point sources can be confidently removed and $A(\nu)$ is the scaling factor derived from observations.

Attempts have been made to extend this model to include polarized sources by a number of authors (Tucci et al. (2004), Mesa et al. (2002), Tegmark et al. (2000)). The simplest approach to take is to simply multiply the power spectra by a constant polarization percentage (Tegmark et al. (2000)). However, as with synchrotron radiation, the most complete polarized observations are at radio frequencies and so an extrapolation has to be made into the CMB window. This is complicated by depolarization effects which are expected to be high at radio frequencies, but very small at CMB frequencies. Mesa et al. (2002) find strong evidence for this depolarization using the observations of Klein et al. (2003) at 1.4, 2.695, 4.85 and 10.6 GHz, and determine that this effect can be corrected for by increasing the polarization percentage for CMB frequencies by a factor of 3 over that at 1.4 GHz. This work has been extended by Tucci et al. (2004) who calculate an analytic formula for the frequency dependence of the degree of polarization based on observations from a range of surveys at different frequencies. They find that at frequencies above 15 GHz the effects of depolarization are not significant and so there polarization degree becomes independent of frequency, but below this frequency the polarization degree is

definitely reduced. They calculate the polarization power spectra as:

$$C_\ell^{EE} = \frac{1}{2} C_\ell^{TT} \langle p^2 \rangle \quad (3.11)$$

where $\langle p^2 \rangle$ is the mean squared value of the polarization degree, giving a value of $\langle p^2 \rangle = 0.046$ at 100 GHz. C_ℓ^{TT} is calculated using the Toffolatti et al. (1998) model for the source counts scaled by 0.75. We use this model in our analysis. A comparison of the model with the expected CMB signal is shown in Fig. 3.4. In order to use this model, a cut-off flux density is needed above which we can assume any point sources will have been masked. We follow Tegmark et al. (2000) and calculate this figure based on the instrument noise expected from QUaD, assuming that any sources with a flux at least five times the noise level can be removed.

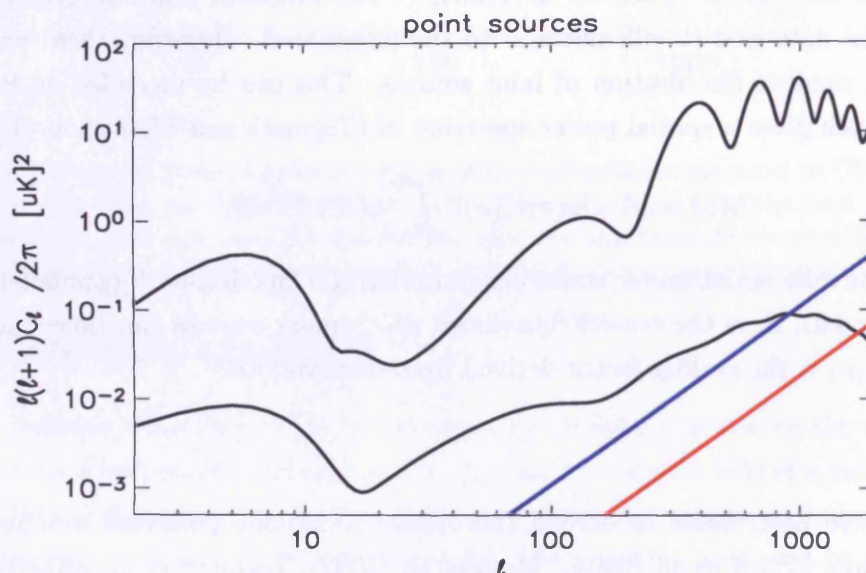


Figure 3.4: Estimated levels of polarized point source fluctuations compared to CMB. The blue lines are for 100 GHz and the red for 150 GHz.

An interesting point raised by Tucci et al. (2004) is that if the point source removal is done using polarized maps the subtraction is much less efficient due to the higher noise and reduced point source flux compared to a temperature map. They estimate that the point source power spectrum could be up to a factor 10 higher in this case.

3.5 Conclusions and Outlook

The success of the WMAP satellite and other total power experiments have shown that astrophysical foregrounds do not create a serious problem for the detection of the CMB

temperature anisotropy. The only measurements strongly affected are those on large angular scales as the sample variance on these scales is increased when regions of sky which are heavily contaminated by the galaxy are cut. The estimates we will use for the foreground power spectra are shown in Fig. 3.2, 3.3 and 3.4. For E-modes, the situation seems to be almost as promising as for the temperature signal. The levels of synchrotron, dust and point sources are below the E-mode in at least one of the QUaD bands for the higher angular scales which QUaD will target. However, as the foreground power spectra estimates are based on extrapolations from other frequencies this cannot be proven until more CMB frequency polarized data become available. For the B-mode signal foreground contamination is much more serious and foreground removal techniques will need to be developed to have any hope of measuring the B-mode tensor spectrum. It also appears that foregrounds will pose a problem for measurements of the peak in the gravitational lensing B-mode signal.

Figure 3.5 shows estimates of the distribution of the polarized emission across the sky. These estimates are very uncertain as they are made from extrapolations from different frequencies and applying theoretical models to the temperature data. The full sky maps show that these estimates predict that the polarized synchrotron emission will extend to higher latitude than dust. However, the dust template does not take into account the possible increase in polarization with galactic latitude. The maps of the region available to QUaD show that there are regions of sky which are clean from both dust and synchrotron. If QUaD can target these clean regions it will be possible to reduce the foreground levels for the QUaD patch.

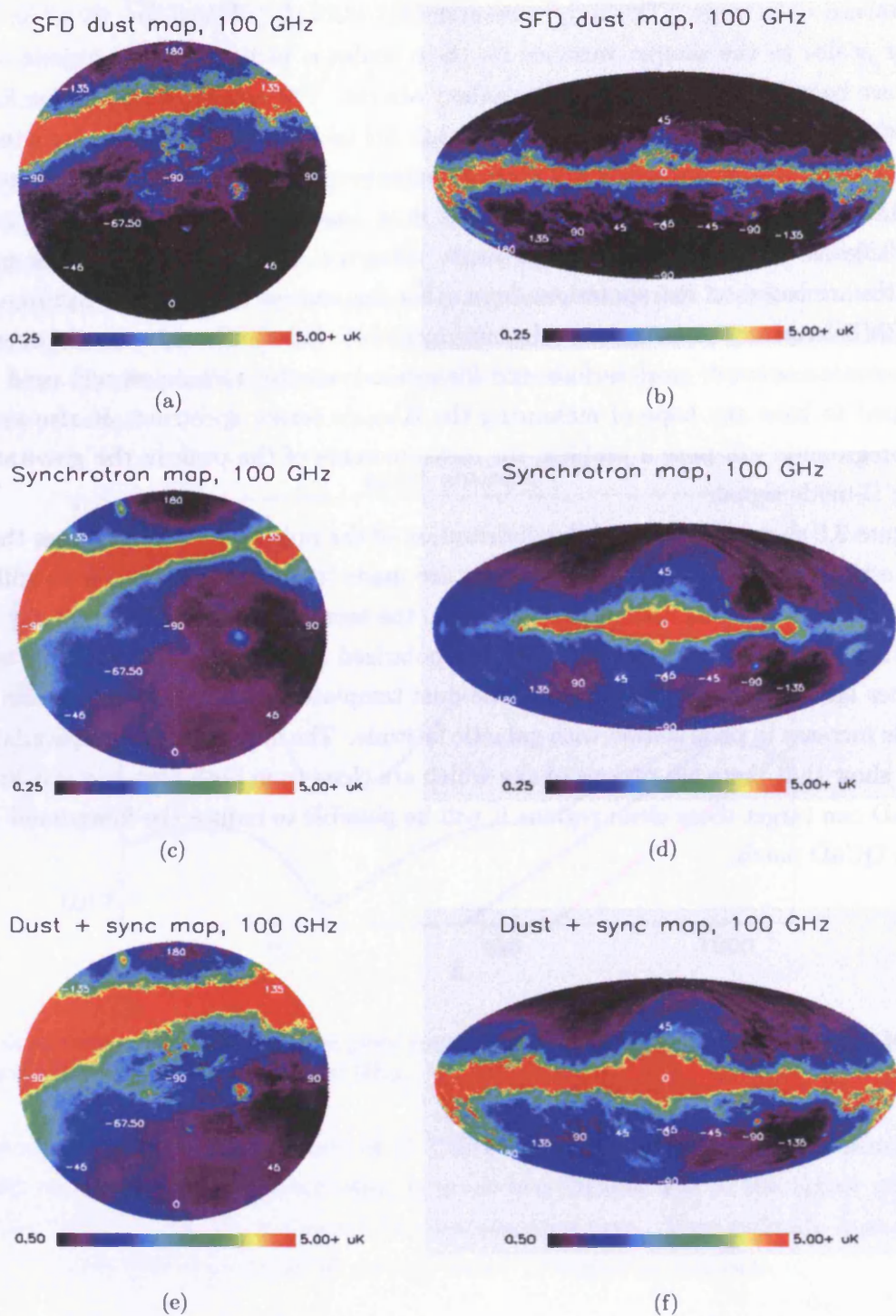


Figure 3.5: Foreground templates used to predict regions with low foreground contamination. The 3 maps on left show the contribution from dust (top), synchrotron (middle) and dust and synchrotron combined (bottom) in equatorial coordinates centred on the South Pole. The highest declination shown is -45° . The 3 maps on the right show the same foreground in galactic coordinates for the whole sky.

Chapter 4

Sensitivity calculation

In this chapter the expected sensitivity of the QUaD telescope is calculated. This gives the fundamental white noise limit which determines how well QUaD will be able to measure the CMB if all the systematics can be controlled. This is important for work in later chapters when the expected QUaD performance (Chapter 5) and observing strategy (Chapter 6) is evaluated, and for making estimates of the noise in data simulations (Chapter 7). This work was also used in the initial planning stages of the QUaD experiment to aid in choosing the observing site. We therefore evaluate the difference in the sensitivity which can be achieved at three different possible locations and for two different optical layouts.

4.1 Formalism for describing random noise

The time-stream of data from QUaD will be made up of many other signals in addition to the CMB signal we are trying to measure. However, any unwanted signals which do not vary with time will just create a background level to the signal which can in principle be removed. The noise in the signal is the fluctuation in this background which is not due to variations in the CMB polarization as we scan across different points on the sky. There will be many different contributions to the noise in QUaD: the atmosphere, emission from the telescope, signals generated in the read-out electronics etc. If the noise is due to some predictable physical process, for example, the motion of the Sun heating up part of the telescope, then it is possible to predict what this signal will be and, in theory, it can be removed from the data-stream. However, many sources of noise are due to completely random processes. The signal generated will follow a certain probability distribution, so it is possible to predict the statistics of the signal, such as its mean level and its variance. However, it is impossible to predict exactly what the level of the signal will be at any particular point in time. This random noise cannot be removed from the data-stream and so sets the fundamental limit to how well we can measure the signal from the CMB. However, the fact that this noise is completely random means that if we make a number

of different measurements of the noise signal it will on average be a particular positive value the same number of times as it is the same negative value. The mean value of the noise will therefore approach zero as we take more and more measurements as the noise from different measurements will cancel out. It is therefore possible to reduce the amount of random noise if we increase the integration time.

This can be expressed formally using the central limit theorem. This can be stated as follows (Riley, K. F., Hobson, M. P., and Bence, S.J. (1997)):

If we take a number, N , of independent random signals, $f_i(t)$, with different means μ_i and variances, σ_i^2 , and sum them to create a combined signal, $c_i(t) = \sum f_i(t)$, and a mean signal, $m_i(t) = \frac{1}{N} \sum f_i(t)$, then:

1. *the mean value of the combined signal will be $\sum \mu_i$ and the mean value of the mean signal will be $\frac{1}{N} \sum \mu_i$*
2. *the variance of the combined signal will be $\sum \sigma_i^2$ and the variance of the mean signal will be $\sum \sigma_i^2 / N^2$.*
3. *As $N \rightarrow \infty$ the probability distribution of both the combined signal and the mean signal will tend towards a Gaussian.*

For each measurement we make of the CMB, the random noise value will come from the same probability distribution, as the noise will always be due to the same physical random processes, and so can be modelled using the same mean and variance. If we measure the same point on the sky N times, the variance will be $N\sigma^2/N^2 = \sigma^2/N$, so the noise in measurement of the CMB will reduce as we take more measurements. The noise will be due to many different random processes, and so we can model the noise in each measurement as coming from a Gaussian probability distribution with zero mean and a certain variance. This variance can be found using a statistical model for each of the individual processes which contribute to the random noise and summing these to find the total variance.

The problem of estimating the random noise in a signal can therefore be reduced to that of finding this variance, the variance for each separate measurement we make in the TOD. However, this would then give us a figure that depends on how fast we sample the data, as the noise per sample will reduce if allow more time between samples, so is not very useful for comparing different experiments. Instead, the figure of merit used is the noise we expect if we integrate for a fixed time. This is called the noise equivalent power, NEP . The NEP_s^2 gives the noise variance we would expect if we take the average of one second of data:

$$NEP_s^2 = \frac{1}{N_s^2} \sum_{n=0}^{N_s-1} s_n^2 \quad (4.1)$$

(from the central limit theorem, assuming the data has zero mean) where N_s is the number of samples per second, which is equal to the sampling frequency, f_s . It is also useful to

define the NEP in the frequency-domain as the variance in a one Hertz band of data:

$$NEP_{Hz}^2 = \Delta f \sum_{m=0}^{N_{Hz}-1} P_m \quad (4.2)$$

where $N_{Hz} = 1/\Delta f$ is the number of frequency components per Hertz. This is a useful if we are defining the performance of a detector, as opposed to thinking about how well the experiment can measure a point on the sky. The noise in the detector output will depend on the bandwidth of signal frequencies being used (by signal frequency we mean the Fourier components of the time-ordered data, not the wavelength of the input radiation). If there are more frequencies the total noise will increase as we are combining more signals. The variances of each component will add in quadrature and so the noise is proportional to the square-root of the bandwidth. The NEP_{Hz} gives a bandwidth independent figure of merit.

For uncorrelated random noise, the amplitude of the power spectrum will be the same in each band as each frequency will contribute equally to the total power. It is therefore called **white noise** in analogy to white light which contains an equal amount of each possible wavelength of visible radiation. For white noise, the NEP^2 is just the amplitude of the power spectrum so that $NEP_{Hz}^2 = P_m^{white}$.

It is important to note that these two definitions of the noise equivalent power are not the same. This can be shown using Equation (A.5). The average value of the variance per sample for a set of N points will be:

$$\langle s_n s_n^* \rangle = \frac{1}{N} \sum_{n=0}^{N-1} s_n^2. \quad (4.3)$$

If we consider a timestream of data for which the total time is $T = 1s$, we will have $N = N_s$ and the average value of the variance for this set of data will be (from Equation 4.1):

$$\langle s_n s_n^* \rangle = \frac{1}{N_s} \sum_{n=0}^{N_s-1} s_n^2 = N_s NEP_s^2 = f_s NEP_s^2. \quad (4.4)$$

The value of P_m at every point is NEP_{Hz}^2 so Equation (A.5) gives:

$$\begin{aligned} \langle s_n s_n^* \rangle &= \sum_{m=0}^{N/2} P_m \Delta f \\ f_s NEP_s^2 &= \Delta f \sum_{m=0}^{N/2} NEP_{Hz}^2 \\ &= \Delta f \frac{N}{2} NEP_{Hz}^2 \end{aligned} \quad (4.5)$$

so:

$$NEP_s^2 = \frac{NEP_{Hz}^2}{2}. \quad (4.6)$$

This factor of 2 is due to the fact that NEP_{Hz} is the amplitude of the one-sided power spectrum and so the power per Hertz is twice the power per second. Another way to think of this is that NEP_{Hz} is the noise in a half second integration time.

4.2 Contribution to the NEP for a bolometric experiment

The aim of this chapter is to calculate the white noise level for QUaD. In order to do this we need to identify the dominant sources of white noise. White noise is generated only by completely random uncorrelated processes. Other sources of noise, such as fluctuations in the background from turbulence in the atmosphere, will be present, but these can in principle be removed from the signal in the data analysis pipeline. The white noise gives the fundamental limit on how well we can measure the CMB. The white noise fluctuations are due to the fact that energy is quantized. For the bolometric detector system used in QUaD this quantization occurs in the electromagnetic energy hitting the bolometer (photon noise), in the thermal energy transferred from the bolometer to the heat sink (phonon noise) and in the electrical energy flowing through the bolometers (Johnson noise due to the electrons). The quanta of energy will not flow at a constant rate, but instead the number detected in a fixed time will vary randomly. We can therefore only predict the **probability** that a certain number of quanta will be detected from the theoretical probability distribution for each process. From this probability distribution we can calculate the variance of the quantum noise signal which will give the NEP for each process. The total NEP can then be found by adding the different contributions in quadrature.

The noise from each process can be calculated if we know the parameters of the bolometer. There are standard results for a total power (not polarization sensitive) bolometer (Mather (1982), Holland et al. (2002)):

- Johnson noise:

$$NEP_j^2 = 4k_B T_b R / S^2 \quad (4.7)$$

where T_b is the temperature of the bolometer, R is its resistance and S is its responsivity.

- Phonon noise:

$$NEP_p^2 = 4k_B T_b^2 G \quad (4.8)$$

where G is the thermal conductance of the link between the absorber and the heat sink.

- Photon noise:

$$NEP_{ph}^2 = 4 \frac{A\Omega(k_B T)^5}{c^2 h^3} \int \frac{\eta \epsilon x^4}{e^x - 1} \left[1 + \frac{\eta T \epsilon}{e^x - 1} \right] dx. \quad (4.9)$$

where $x = h\nu/k_B T$. The photon noise is defined for separate components (the atmosphere and the different parts of the telescope) and then the different parts are added in quadrature to give the total photon noise. For each component we define a physical temperature, T , an emissivity, ϵ , and a transmission, η . The optical throughput is given by $A\Omega$.

For a polarization sensitive bolometer, the first two of these noise sources will be the same as for a total power bolometer as they depend on only the properties of the bolometer and not the incident radiation. However, the photon noise will change slightly, due to fact that only a single polarization state of radiation will be absorbed by each bolometer. For clarity we will therefore go through the derivation of the photon noise to show how the polarization of the incident radiation is included (this mainly involves putting factors of 2 in the correct places).

4.3 Derivation of photon noise for a PSB

To find an expression for the photon noise we need to look at the statistical distribution of the photons. This is given by the Bose-Einstein distribution function, $f(\nu)$, which gives the number of photons per mode of phase space at a given frequency, ν , (the same as in Chapter 1 when the photon distribution at decoupling was derived):

$$f(\nu) = \frac{1}{e^{h\nu/kT} - 1} \quad (4.10)$$

The total number of photons, $n(\nu)$, is the product of $f(\nu)$ and the number of modes, $g(\nu)$, where:

$$g(\nu)d\nu = 4\pi p \frac{\nu^2}{c^3} V d\nu \quad (4.11)$$

where V is the volume of space being considered and p is the number of polarization states being detected so that $p = 1$ for a PSB and $p = 2$ for a total power bolometer. For the NEP we need the number of photons hitting the detector per second, so the volume will be $V = A\Omega c/4\pi$ where A is the area of the detector, Ω is the solid angle over which the detector will absorb photons and c gives the distance a photon can travel in one second. For a Bose-Einstein distribution the variance in the number of photons hitting

the detector, δn^2 , is:

$$\delta n(\nu)^2 = n(\nu) + \frac{n(\nu)^2}{g(\nu)}. \quad (4.12)$$

To find the total energy per second, $P(\nu)$, we multiply the number of photons per second by the energy per photon, $h\nu$. The power at the detector will also depend on the transmission between the source and the detector, η , and the emissivity of the source ϵ :

$$P(\nu)d\nu = p \frac{h}{c^2} A \Omega \eta \epsilon \frac{\nu^3}{e^{h\nu/kT} - 1} d\nu. \quad (4.13)$$

The variance in this power is then found by multiplying the variance in the number of photons by $(h\nu)^2$. The NEP is usually quoted in units of $\text{WHz}^{-1/2}$ so this variance for the power in one second is multiplied by two to get the final expression:

$$\text{NEP}^2 = 2 \int h\nu P(\nu) d\nu + 2 \int \frac{c^2 P(\nu)^2}{p A \Omega \nu^2} d\nu \quad (4.14)$$

If we set the number of polarization states to 2, as will be the case for unpolarized radiation, this expression is exactly equivalent to Equation 4.9 for the total power case. There are a number of different approaches to converting this expression to the NEP for a PSB which can lead to confusion, especially with where to put factors of 2. In this thesis we define the NEP of a PSB as the noise in a measurement of an unpolarized source if we use a **single** PSB to make the measurement. A PSB will only absorb a single polarization state of radiation and so we have $p = 1$ in both of the last two equations.

Equivalently, we can think of a PSB as being a normal bolometer, but with half the efficiency. This can be modelled by including an extra factor of $1/2$ in η in equation 4.13 and setting $p = 2$. However, we will still have $p = 1$ in Equation 4.14.

The two terms in the NEP equation are called the shot noise (first term) and the wave noise (second term). If the arrival of a photon at the detector was a completely random process, the variance of the photons would follow the central limit theorem and would be proportional to the incident power. This is the case if we include only shot noise. However, for bosons, there is a slightly stronger probability of detecting another photon straight after one photon has been detected. This is known as photon bunching. The wave noise is therefore not completely random and is proportional to the total power, not the square root of the power. If we think of the radiation in terms of waves instead of photons then photon bunching can be thought of in terms of the interference of coherent waves. This means that if the wave noise is significant we cannot just add the NEP from different components (e.g. the atmosphere and the telescope) in quadrature as the processes are not completely independent as the radiation from different sources can interfere. Although this interference can be modelled (Lamarre (1986)), the analysis is complicated. Instead we assume here that as a first approximation it is possible to add

the wave noise in quadrature, although this will over estimate the wave noise contribution in general (Runyan, M. C. et al. (2003)).

In order to reduce the background noise, the feed-horns which direct the radiation onto the detectors are single-moded. The diffraction pattern produced on the focal plane can be thought of as being made up of many different Gaussian beams or modes. The fundamental mode will be a single Gaussian at the centre of the diffraction pattern and will contain most of the power from the image on the sky. If we only detect this mode then we cut out a large fraction of the noise without reducing the power from the signal. For a single-moded feed horn it can be shown that the throughput, $A\Omega$, is given by:

$$A\Omega = \frac{c^2}{\nu^2} \quad (4.15)$$

This is known as the **antenna theorem** (Kraus (1997)). This simplifies the expressions for the power and NEP.

In a CMB experiment it is often more useful to think of the signals in terms of their temperature instead of their total power. To convert to a noise equivalent temperature, NET, we divide the derivative of the power from the source (the CMB):

$$NET_s = \frac{NEP}{\eta \partial B / \partial T} \quad (4.16)$$

with:

$$\left. \frac{\partial B}{\partial T} \right|_{T_{cmb}} = p\eta \frac{k_b T_{cmb}}{h} \int \frac{x^2 e^x}{(e^x - 1)^2} dx \quad (4.17)$$

where, $x = h\nu/k_B T_{cmb}$ and B is the power from a black body. The factor η converts from the signal measured at the detector to the signal at the source. This is needed as the NET is defined as the signal needed from the source to give a signal to noise ratio of one. Again, the fact that the PSB detects only a single polarization state must either be taken into account by setting $p = 1$ in the $\partial B / \partial T$ term, or by adding an extra factor of $1/2$ into the efficiency factor.

This expression gives the sensitivity for a measurement of the **temperature** of the CMB with a **single** PSB, NET_s .

However, the final signal is obtained by differencing or summing a pair of orthogonal bolometers. It is therefore also useful to quote the sensitivity of a pair of PSBs. If we measure the temperature with a pair of PSBs we have two different measurements of the same signal so the noise, NET_{pair} , will be reduced:

$$NET_{pair} = NET_s / \sqrt{2} \quad (4.18)$$

This gives the same value we would expect if the measurement had been made with a

single total-power bolometer.

For a measurement of polarization we define a quantity called the NEQ. This is the signal needed to give a signal-to-noise ratio of unity for a 1Hz bandwidth for a **completely polarized source** with its polarization angle aligned with the reference direction of the measurement. This means that the polarization is completely defined by the Q Stokes parameter and the U Stokes parameter for this measurement will be zero. As the source is now assumed to be completely polarized, the extra factor of two needed previously in Equation 4.17 to account for the PSB only detecting half of the incident radiation is no longer required as the detector will absorb all of the radiation from the polarized source. The NEQ for a pair of orthogonal PSBs is then:

$$NEQ = \frac{\sqrt{2}}{2} NET_s = \frac{NET_s}{\sqrt{2}} \quad (4.19)$$

In the central part of this equation the $\sqrt{2}$ in the numerator is due the fact that we are differencing the output of the two PSBs and the 2 in the denominator is to account for the extra 2 used when calculating the NET_s , which is not needed in this case. In this thesis whenever I give the NET of a detector I am referring to NET_s in units of $\mu K Hz^{-1/2}$ unless it is specifically stated otherwise.

4.4 Calculating QUaD sensitivity

To calculate the NET for QUaD we find the photon NET from the atmosphere and from each of the optical components and then add these values in quadrature to the phonon and Johnson noise. This calculation was made in the design stages of the experiment to assess the limiting noise level at different possible observing sites and to compare two possible optical designs. As the frequency bands over which we are observing are fairly narrow, it is possible to approximate the integrals in equations 4.13 and 4.14 by performing the calculation at the central frequency of each band, ν_c and multiplying the result by the bandwidth, $\Delta\nu$ so that:

$$P = h\nu_c \eta \epsilon \frac{\Delta\nu}{e^{h\nu/k_b T} - 1}$$

$$NEP^2 = 2h\nu_c P + \frac{2P^2}{\Delta\nu} \quad (4.20)$$

where the power is half that expected for a total power bolometer i.e. we have set $p = 1$. The QUaD bands are centred around 92, 146 and 220¹ GHz and have widths of 22.4, 33.9 and 44.0 GHz respectively. The transmission for each component is the product of the

¹This work was carried out when it was planned for QUaD to have an additional observing band at 220 GHz.

transmission of each of the elements in front of this component, η_i , and the feedhorn-to-bolometer efficiency, χ :

$$\eta = \chi \prod_i \eta_i \quad (4.21)$$

and the emissivity of each component is given by $\epsilon_i = 1 - \eta_i$. The parameters for each of the telescope components are given in Table 4.1 for the two possible designs. The difference between the two models is the temperature of the lenses and the waveplate. The initial design was to keep these elements at 77K, but it was later suggested that they be moved to the 4K stage. This would complicate the cryogenic design of the experiment and the wave plate rotation mechanism would be much more difficult to run. However, it will also decrease the photon noise if these optical elements are cooler. The aim of this calculation is to decide if the increase in sensitivity would be significant.

Element	Transmission	Temperature / K
cone	0.990	300
primary	0.990	300
secondary	0.995	300
window	0.990	300
blocking filter	0.950	77
lens 1	0.940	4 (77)
lens 2	0.940	4 (77)
waveplate	0.850	4 (77)
4K filters	0.900	4

Table 4.1: Telescope parameters, the temperature values in brackets are the values used in a previous possible optics design (warm optics) which we compare to the current design (cold optics). We assume a feedhorn-to-bolometer efficiency of 0.485, giving a total end-to-end efficiency of 0.3.

We model the atmosphere using the AT (Atmospheric Transmission) code (Grossman, E. (1989)). This computes the atmospheric transmission taking into account the altitude, pressure, temperature and humidity of the site. The humidity is expressed as the amount of precipitable water vapour per mm (pwv mm). This has been estimated for different quartiles (Chamberlin et al. (1997)) such that we expect the amount of water vapour to be below the 50% value for at least 50% of the year and below the 75% value for at least 75% of the time. In the frequency range of interest for QUaD the main lines in the transmission spectrum are due to water vapour and oxygen. The strength of the oxygen lines depends mainly on the altitude of the site and the water lines depend mainly on the humidity. The results for the three possible sites, the Amundsen-Scott station at the South Pole, Chajnantor in Chile, and Teide in Tenerife, are shown in Figure 4.1. The parameters used in these models are given in Table 4.2. For the altitude we use the effective altitude each site would have if it were at the equator. This is because the atmosphere is thinner further

from the equator due to the rotation of the Earth, this is particularly important for the South Pole which has actual altitude of 2.8 km, but an effective altitude of 3.2 km. The South Pole has better transmission as it is very dry, although in the 100 GHz band there is very little difference between Chile and the South Pole. This is because the oxygen line dominates the transmission in this band and so the altitude of the site becomes more important. We assume an average elevation, θ , of 50° to calculate the actual atmospheric transmission, η , from the zenith transmissions, η_z , given in Table 4.3, where:

$$\eta = \eta_z^{1/\cos(90-\theta)} \quad (4.22)$$

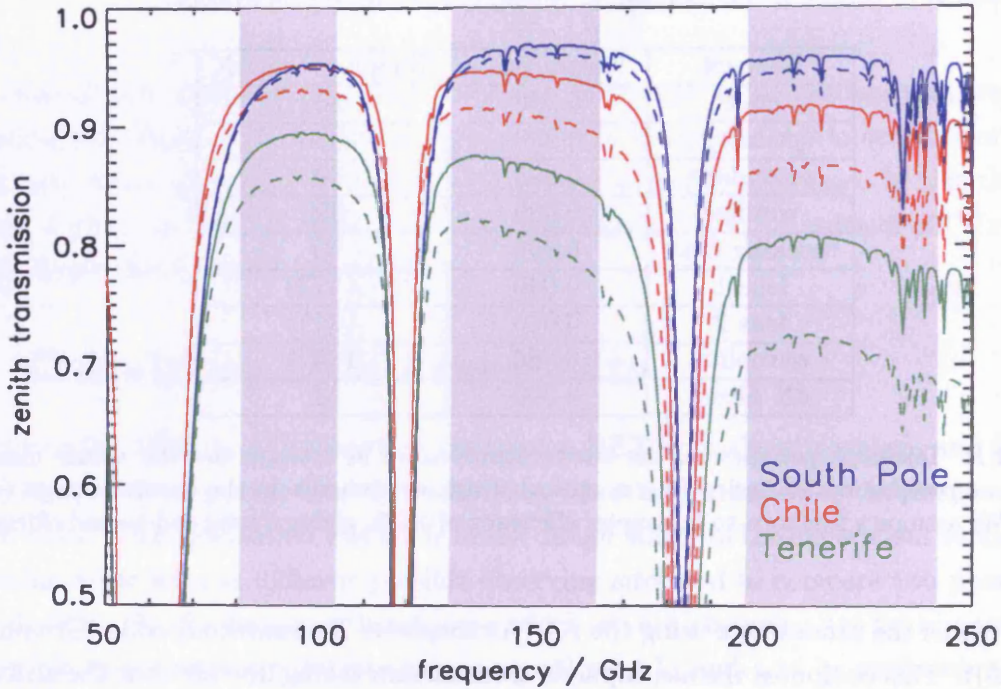


Figure 4.1: Atmospheric transmission at different sites. Solid lines are for 50% quartile pwv and dotted lines for 75% quartile. The absorption lines are due to water vapour (183, 325 and 380 GHz) and oxygen molecules (56, 119 and 368 GHz). The grey bars show the QUaD frequency bands.

The NET can then be calculated for each of the different sites using the two different optical set-ups. The 50% quartile values for the humidity are used as QUaD will be taking data during the driest parts of the year. The properties of the detectors will be optimized so that the combined detector noise from the different sources will be at the same level as the background photon noise. This means that the detectors will be background limited. The total NEP is therefore given by $NEP_{tot}^2 = 2NEP_{ph}^2$.

Site	South Pole	Chile	Tenerife
Latitude /°N	-89.99	-22.96	28.25
Effective altitude /km	3.2	5.2	2.4
Sky temperature /K	203	273	270
Pressure /mbar	657	540	729
pwv 50% quartile /mm	0.25	1.00	2.00
pwv 75% quartile /mm	0.32	1.60	3.00

Table 4.2: Atmospheric model parameters

Band	100 GHz	150 GHz	220 GHz
South Pole	0.955 (0.948)	0.970 (0.965)	0.955 (0.945)
Chile	0.955 (0.930)	0.940 (0.910)	0.910 (0.865)
Tenerife	0.895 (0.860)	0.870 (0.810)	0.806 (0.720)

Table 4.3: Zenith transmission at the centre of the QUaD bands. Values are for 50% quartile with 75% quartile values in brackets.

4.5 Results

The results are shown in Table 4.4 and in Fig. 4.2.

Site	NET / $\mu K Hz^{-1/2}$					
	Cold optics			Warm Optics		
	100 GHz	150 GHz	220 GHz	100 GHz	150 GHz	220 GHz
South Pole	425	482	1026	631	751	1482
Chile	483	721	1683	672	938	2032
Tenerife	884	1287	3269	1019	1448	3530

Table 4.4: Predicted sensitivity at each site in the 3 QUaD frequency bands.

The key point to take from these results are:

- The difference between the cold and warm models depends on the site. For Tenerife the atmospheric loading dominates the total power, as can be seen from Fig. 4.2, so there is little difference in the sensitivity for the two models. However, there is a significant difference of $\sim 40\%$ for Chile and $\sim 50\%$ for the South Pole.
- The difference between the sites is greater for the cold optics model, but both models follow the same trends.
- For cold optics the Tenerife sensitivity is over a factor of two worse than the South Pole and just under a factor of two worse than Chile in all of the bands.
- In the two higher frequency bands, the South Pole has a factor of 1.5 better sensitivity than Chile, but at 100 GHz there is only a small difference.

In conclusion, the South Pole is the better site, but there is very little difference between the South Pole and Chile unless the 220 GHz band is included. At the South Pole and Chile there is a significant increase in sensitivity if the cold optics model is used, but at Tenerife there is no significant increase.

The site for QUaD has now been chosen to be the South Pole. The main factor in deciding between Chile and the South Pole was related to the logistics of the site and not sensitivity. As the DASI experiment ran previously from the South Pole and it was possible to re-use the DASI mount for QUaD, running the experiment from the South Pole will substantially decrease the amount of work needed to set up the telescope. The infrastructure at the South Pole is also much more evolved, as a number of previous experiments have been run from the South Pole site, whereas the site in Chile is only just beginning to be exploited.

The cold optics model has been chosen, partly because of the increase in sensitivity shown here, but mainly due to a systematic effect by which the waveplate will generate an instrumental polarization signal from incident unpolarized radiation. This effect will be much stronger if the waveplate is warm.

It was found that including a 220 GHz channel greatly complicates the optical design of the telescope, so the first version of QUaD will only include the two lower frequency channels. However, it is possible that the extra band could be included in a later upgrade.

In the rest of this thesis we therefore use the sensitivity values for the 100 GHz and 150 GHz channel for the cold optics model at the South Pole, so that the sensitivities are $300 \mu K s^{1/2}$ and $340 \mu K s^{1/2}$ respectively. We use the higher values of $340 \mu K s^{1/2}$ and $500 \mu K s^{1/2}$ when investigating the possible sky coverage in Chile as this work was completed before a definite decision about the site had been made. These sensitivity values are the best we can possibly achieve, assuming that we can remove all of the $1/f$ noise and that all of components work as specified.

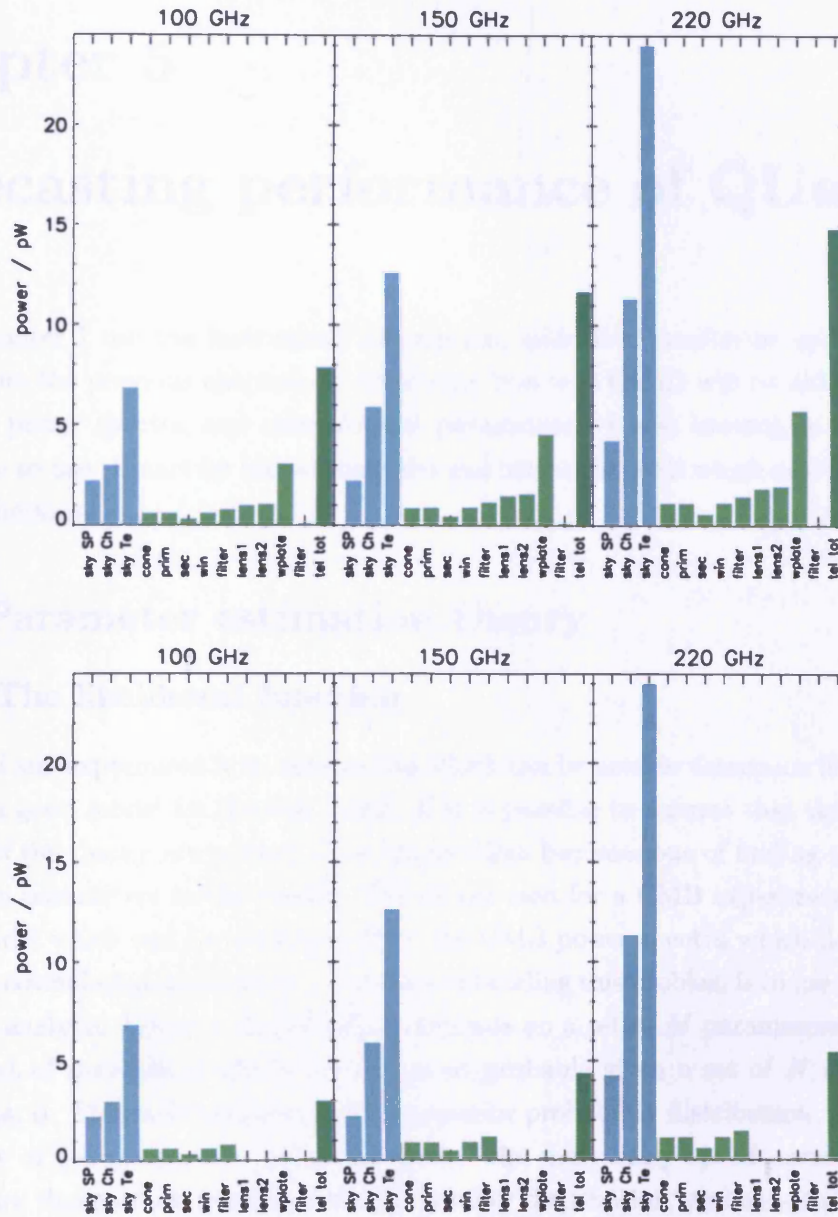


Figure 4.2: Power from each of the telescope components (light green) compared to that from the atmosphere at the different site (light blue) and the total power from the telescope (dark green) for warm optics (top) and cold optics (bottom).

Chapter 5

Forecasting performance of QUaD

In this chapter I use the instrument description, estimated sensitivity and foreground models from the previous chapters to determine how well QUaD will be able to measure the CMB power spectra and cosmological parameters. I also investigate the optimal survey size to use. I start by introducing the mathematical tools which are used to make these predictions.

5.1 Parameter estimation theory

5.1.1 The likelihood function

The aim of any experiment is to obtain data which can be used to determine if a particular theory is a good model for the real world. If it is possible to assume that the underlying concepts of the theory are correct, then the problem becomes one of finding the values of the various parameters in the theory. This is the case for a CMB experiment, where we have a model which can be used to predict the CMB power spectra which depends on a number of cosmological parameters. One way of tackling this problem is to use a maximum likelihood analysis. Given a theory which depends on a set of M parameters, α , we can find the set of parameters which are the most probable given a set of N experimental data points, \mathbf{d} . This is determined by the posterior probability distribution, $P(\alpha; \mathbf{d})$, the probability of the parameters given the data. The most likely set of parameters given the data are those which maximise the probability distribution, and so satisfy the set of equations:

$$\frac{\partial P}{\partial \alpha_i} = 0 \quad i = 1 \dots M \quad (5.1)$$

The probability of the data given a certain model, the likelihood function, $L(\mathbf{d}; \alpha)$, can be found easily from the data. Luckily, this quantity is related in a very simple way to the quantity we are trying to find, the probability of the model given a set of data. If the data points come from a Gaussian distribution, which is a good approximation is most

cases, the probability of the data set given that a certain theory is correct is given by a multivariate gaussian:

$$L(\mathbf{d}; \boldsymbol{\alpha}) = \frac{1}{(2\pi)^{N/2} |C_d|^{1/2}} \exp \left(-\frac{1}{2} (\mathbf{d} - \boldsymbol{\mu})^T C_d^{-1} (\mathbf{d} - \boldsymbol{\mu}) \right) \quad (5.2)$$

where \mathbf{d} is the data vector, the set of data from the experiment. The mean vector, $\boldsymbol{\mu}$, is the expected value of each point and C_d is the $N \times N$ data covariance matrix, both of which can be predicted theoretically. This can be used to obtain $P(\boldsymbol{\alpha}; \mathbf{d})$ using **Bayes theorem** which states that the probability the theory is specified by the parameter set $\boldsymbol{\alpha}_k$ given that the set of data \mathbf{d} has occurred is:

$$P(\boldsymbol{\alpha}_k; \mathbf{d}) = \frac{L(\mathbf{d}; \boldsymbol{\alpha}_k) P(\boldsymbol{\alpha}_k)}{\sum_{\ell} P(\boldsymbol{\alpha}_{\ell}) P(\mathbf{d}; \boldsymbol{\alpha}_{\ell})} \quad (5.3)$$

where $P(\boldsymbol{\alpha})$ are the *a priori* probabilities of the parameters. This gives the probability of the parameter set, $\boldsymbol{\alpha}_k$, obtained using all the information available before the experiment has taken place and the data from the experiment. The factor in the denominator normalises the probabilities and is the sum of the probability of all of the possible data sets, $\boldsymbol{\alpha}_{\ell}$. **Bayes postulate** is to assume that, if nothing is known to the contrary, all the *a priori* probabilities should be taken as equal. This gives:

$$P(\boldsymbol{\alpha}; \mathbf{d}) = CL(\mathbf{d}; \boldsymbol{\alpha}) \quad (5.4)$$

where C is some unknown constant which can be ignored as it affects only the magnitude of the likelihood function and not the position at which it peaks.

If the errors in the data are Gaussian distributed we can minimize the exponent of the Gaussian distribution, instead of dealing with the full likelihood function. This is often called a **chi-squared** fit, where the χ^2 statistic is:

$$\chi^2 = (\mathbf{d} - \boldsymbol{\mu})^T C_d^{-1} (\mathbf{d} - \boldsymbol{\mu}). \quad (5.5)$$

The values of best fit χ^2 parameters are equivalent to the maximum likelihood values as long as the Gaussian approximation is valid and the errors are independent of the parameters. The value of the Gaussian likelihood function can be calculated for different values for the minimum χ^2 . The probability distribution depends on the number of degrees of freedom, ν (the number of data points, N , minus the number of parameters to be fitted, M) and is given by the incomplete gamma function, Γ , so that $P(\alpha_1 \dots \alpha_M; \mathbf{d}) = \Gamma(\nu/2, \chi^2/2)$.

5.1.2 Confidence limits and the Fisher matrix

The maximum likelihood approach gives a method of finding the most likely set of parameters given a set of data. The variance of these maximum likelihood values can be obtained from the **Fisher information matrix** (Tegmark et al. (1997)). This is defined as:

$$F_{ij} = \left\langle \frac{\partial^2 \mathcal{L}}{\partial \alpha_i \partial \alpha_j} \right\rangle \quad (5.6)$$

where the derivative is evaluated at the maximum likelihood values of the parameters and $\mathcal{L} = -\ln L$. The angled brackets denote that this is the mean value we would expect from a number of different realizations of the data. The inverse of the Fisher matrix gives the parameter co-variance matrix, C_{ij} , for the theoretical parameters:

$$C_{ij} = F_{ij}^{-1} \quad (5.7)$$

The diagonal elements of the covariance matrix give the variance of each of the parameters, and the off diagonal elements give the covariances between different parameters. If the parameters are uncorrelated, the matrix will be diagonal and the variance with which a parameter can be estimated from the data is given by:

$$(\Delta \alpha_i)^2 = 1/F_{ii}. \quad (5.8)$$

These error estimates are only valid if the maximum likelihood method has been used to find the best-fit parameters. However, it can be shown that the maximum likelihood method will always give us the smallest possible parameter errors, and so we can use the Fisher matrix to predict the best possible performance of the experiment. This is expressed in the **Cramer-Rao inequality**:

$$\Delta \alpha_i \geq 1/\sqrt{F_{ii}} \quad (5.9)$$

where the inequality will become an equality if the maximum likelihood parameters are found and there are no correlations between any of the parameters.

The form of Equation (5.6) can be justified if we take the simple case of a model which depends on a single parameter, α . The likelihood function will be approximately Gaussian around its peak value and so close to the maximum likelihood value, α_m , can be approximated by the form:

$$L(\alpha) = A e^{-(\alpha - \alpha_m)^2 / 2\sigma^2}$$

where A is the amplitude of the gaussian and σ^2 is the variance, so that:

$$\mathcal{L} = -\ln L = -\ln A + \frac{1}{2\sigma^2}(\alpha - \alpha_m)^2.$$

If we compare this to a Taylor expansion of \mathcal{L} around the maximum likelihood value (which is valid as we are only considering values close to this point), we have:

$$\mathcal{L}(\alpha_m + \delta\alpha) = \mathcal{L}(\alpha_m) + \frac{1}{2} \left(\frac{\partial^2 \mathcal{L}}{\partial \alpha^2} \right)_{\alpha_m} (\delta\alpha)^2.$$

If we equate the terms in $\delta\alpha^2$ in the last two equations we have:

$$\left(\frac{\partial^2 \mathcal{L}}{\partial \alpha^2} \right)_{\alpha_m} = \frac{1}{\sigma^2} \quad (5.10)$$

The left hand side of this expression is the single parameter Fisher matrix and so we can see that this is related to the error in the parameter.

In the case of multiple parameters, $L(\alpha)$ can be expressed as a multi-variate gaussian:

$$L(\alpha) = \frac{1}{(2\pi)^{M/2} |C|^{1/2}} e^{-\frac{1}{2}\chi^2} \quad (5.11)$$

where:

$$\chi^2 = (\alpha - \alpha_m)^T C^{-1} (\alpha - \alpha_m) \quad (5.12)$$

where C is the $M \times M$ parameter covariance matrix and α_m are the best fit set of parameters.

An error ellipsoid defines a region around the best fit value which contains a certain percentage of the total probability distribution of the parameters. For the chi-squared fit, the value of chi-squared will increase as the values of the parameters move further away from the best fit values. If we extend the Taylor expansion in Equation (5.10) to the full set of parameters, we have:

$$\Delta\chi^2 = \chi^2(\alpha_m + \delta\alpha) - \chi^2(\alpha_m) = \frac{1}{2} \sum_{i,j} \frac{\partial^2 \chi^2}{\partial \alpha_i \partial \alpha_j} \delta\alpha_i \delta\alpha_j = \frac{1}{2} \delta\alpha^T C^{-1} \delta\alpha \quad (5.13)$$

It can be shown that $\Delta\chi^2$ is distributed as a χ^2 variable with M degrees of freedom (Press (1992)) and so the probability distribution around the maximum likelihood parameters can be easily calculated.

Instead of trying to draw a multi-dimensional ellipsoid to represent the parameter covariances and variances, it is more useful to plot two-parameter error ellipses between each of the parameters which are found by marginalizing over the rest of the parameters, i.e. the errors we would obtain if we were to only constrain two parameters from the data. The covariance matrix provides a simple way to do this, the 2×2 square of the full matrix

corresponding to the two parameters gives us their marginalized covariance matrix. The most common error ellipses are surfaces with $\Delta\chi^2 = 2.3$ or with $\Delta\chi^2 = 1$. The first ellipse encloses 68% of the probability distribution, i.e. there is a 0.68 probability that the true values of the parameters will lie within the ellipse. The second ellipse encloses less than 68% of the distribution, but the projections of this ellipse onto the two axes give the marginalized standard errors in each parameter, this is the error obtained in one of the two parameters if the other parameter is also to be found from the data. The intersection of the ellipse with each axis gives the error on each parameter, assuming that the other parameter is known and is not to be found from the data. The relation of these projections to the Fisher matrix constraints is shown in Fig. 5.1. This ellipse can be scaled up to a 68% confidence region by scaling the axes of the ellipse by $\sqrt{2.3}$.

The equation of an ellipse in polar coordinates (r, θ) for parameters α_1 and α_2 , with major and minor axes a and b , where the major axis is at an angle ϕ to the α_1 -axis is:

$$\alpha_1^2 \left(\frac{\cos^2(\theta)}{a^2} + \frac{\sin^2(\theta)}{b^2} \right) + 2\alpha_1\alpha_2 \cos(\theta) \sin(\theta) \left(\frac{1}{a^2} - \frac{1}{b^2} \right) + \alpha_2^2 \left(\frac{\sin^2(\theta)}{a^2} + \frac{\cos^2(\theta)}{b^2} \right) = 1 \quad (5.14)$$

The ellipse corresponding to a particular 2×2 covariance matrix can be found by equating terms in α_1 and α_2 in this equation to the two parameter $\Delta\chi^2$ equation:

$$\Delta\chi^2 = \alpha_1^2 C_{11}^{-1} + 2\alpha_1\alpha_2 C_{12}^{-1} + \alpha_2^2 C_{22}^{-1} \quad (5.15)$$

The ellipse can then be drawn using the parametric equation:

$$\begin{aligned} \alpha_1 &= a \cos \theta \cos \phi - b \sin \theta \sin \phi \\ \alpha_2 &= b \sin \theta \cos \phi - a \cos \theta \sin \phi. \end{aligned} \quad (5.16)$$

where θ is the angle from the α_1 axis.

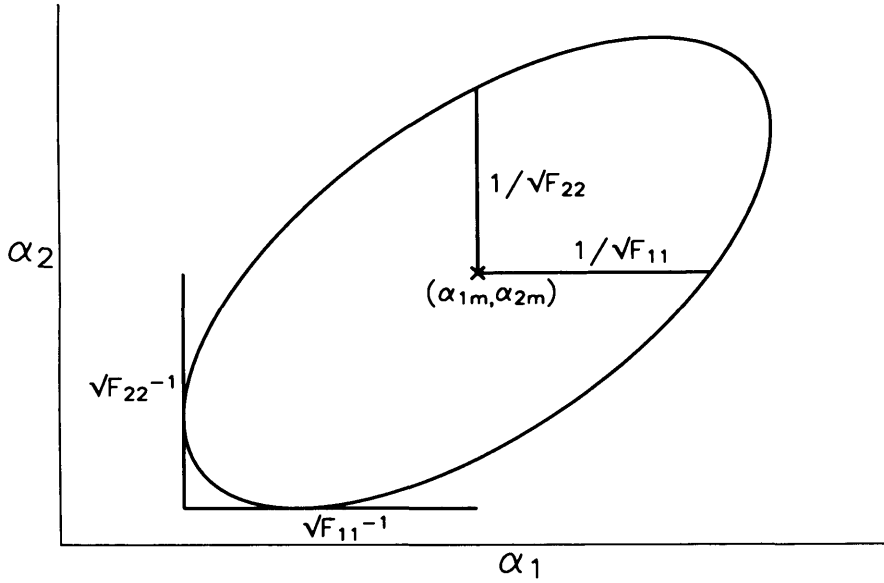


Figure 5.1: $\Delta\chi^2 = 1$ two parameter error ellipse. If there are other parameters in the model to be fit to the data, these parameters have been marginalized over and so can take any value (subject to the constraints imposed by any priors used in the analysis). The variances and covariances used to draw the ellipse are found by taking the 2×2 matrix corresponding to the two parameters from the covariance matrix (inverse of full Fisher matrix, F_f) for the full set of parameters. The two parameter Fisher matrix (F_2) is given by the inverse of this 2×2 covariance matrix. The projection of the ellipse onto each axis gives the standard 1-sigma error on each parameter assuming that the other parameter has been marginalized over. This is equal to the variance on this parameter given by the corresponding element of the inverse of the full Fisher matrix ($\sqrt{F_{fii}^{-1}}$). The intercept with the axis gives the 1-sigma error on the parameter given that the other parameter is known. This is given by the reciprocal of the corresponding 2×2 Fisher matrix element ($1/\sqrt{F_{2ii}}$). The error in a single parameter if all of the remaining parameters are known is given by the reciprocal of the corresponding element of the full Fisher matrix ($1/\sqrt{F_{fii}}$). If the parameters are uncorrelated then there will be no distinction between these different errors.

5.2 Application to CMB polarization

In this subsection I will apply the Fisher matrix analysis to two different cases:

- predicting the variance in the measurement of bands in the CMB power spectra from the CMB maps,
- predicting the variance in the measurement of the cosmological parameters from the four CMB power spectra.

In the first case the data are co-efficients of the spherical harmonic transform of the maps, $a_{\ell m}$ and the parameters are the bands of the power spectra at different multipoles. In the second case, these band powers are the data and the parameters are the cosmological parameters used in the model from which the theoretical power spectra are calculated.

The maps made of the CMB will be the signal from the CMB convolved with the instrument beam, b , combined with the white noise in each pixel, n_{pix} :

$$T^{map} = T \otimes b + n_{pix} \quad (5.17)$$

The spherical harmonic components of the map, $a_{\ell m}^{map}$, will then become:

$$a_{\ell m}^{map} = a_{\ell m} \mathcal{B}_{\ell m} + n_{\ell m} \quad (5.18)$$

where $\mathcal{B}_{\ell m}$ is the spherical harmonic transform of the beam and $n_{\ell m}$ is the contribution from the pixel noise. If we assume a Gaussian beam, $\mathcal{B}_{\ell m} = e^{-\ell(\ell+1)\sigma_b^2/2}$, with $\sigma_b = \theta_b/\sqrt{8 \ln 2}$ where θ_b is the FWHM beam size. The variance in these components will then be:

$$\langle a_{\ell m}^{map} a_{\ell' m'}^{map} \rangle = \left(C_\ell e^{-\ell(\ell+1)\sigma_b^2} + 4\pi \frac{\sigma_{pix}^2}{N_{pix}} \right) \delta_{mm'} \delta_{\ell\ell'} \quad (5.19)$$

This provides us with an expression for the data covariance matrix for the components of the map which can be used to determine the Fisher matrix, and hence the covariance matrix, for the measurement of the CMB power spectrum. This was first derived for a temperature-only experiment by Knox (1995). For a single power spectrum, the covariance matrix gives the variance with which each multipole can be measured:

$$(\Delta C_\ell)^2 = \frac{2}{(2\ell+1)} (C_\ell + N_\ell)^2. \quad (5.20)$$

where N_ℓ give the power on each scale due to instrument noise. This expression can be split up into two components. The noise variance, $\frac{2}{(2\ell+1)} N_\ell^2$, is due to random noise in the experimental data which can be reduced by increasing the integration time or increasing the sensitivity of the instrument. The sample variance, $\frac{2}{(2\ell+1)} C_\ell^2$, is due to the fact that for each value of ℓ there are only $2\ell+1$ independent measurements with which to calculate

the power spectrum on a particular angular scale. In the limit of full sky coverage, this sample variance is called **cosmic variance** and this sets a fundamental limit on how well the CMB power spectra can be measured.

However, Equation 5.20 only applies to a full sky survey. If only a fraction of the sky, f_{sky} , has been covered this variance will change. The measured CMB map is now a product of the CMB signal and the survey window function, $W(\theta, \phi)$, where in the simplest case $W = 1$ inside the survey and $W = 0$ outside the survey. This produces an observed power spectra which is the convolution of the true spectrum with the spectrum of the window function and so introduces a correlation between different modes. These correlations have two major effects on the power spectrum (Hobson and Magueijo (1996)). Firstly, the power spectrum variance at each multipole increases by a factor $1/f_{sky}$ as the sample variance must increase to account for the fact that there are now fewer independent measurements for each multipole. Secondly, the spectral resolution is reduced such that independent measurements of the power spectrum are no longer possible at each multipole. Instead, only the power in bands of width $\Delta\ell = \pi/\Theta$ where Θ is the smallest dimension in the survey, can be measured. The covariance matrix will now only give the variance for measurements of **band powers**:

$$(\Delta C_\ell)^2 = \frac{2}{(2\ell + 1)f_{sky}\Delta\ell}(C_\ell + N_\ell)^2. \quad (5.21)$$

When we include polarization maps as well, the covariance matrix becomes more complicated as there will be correlations between the measurement of the different power spectra. The full symmetric matrix for each multipole, $\Xi_\ell \equiv \text{Cov}(C_\ell^{xx'} C_\ell^{yy'})$ is given by:

$$\Xi_\ell = \begin{pmatrix} \Xi_\ell^{TT,TT} & \Xi_\ell^{TT,EE} & \Xi_\ell^{TT,TE} & 0 \\ \Xi_\ell^{TT,EE} & \Xi_\ell^{EE,EE} & \Xi_\ell^{EE,TE} & 0 \\ \Xi_\ell^{TT,TE} & \Xi_\ell^{EE,TE} & \Xi_\ell^{TE,TE} & 0 \\ 0 & 0 & 0 & \Xi_\ell^{BB,BB} \end{pmatrix}. \quad (5.22)$$

where $(x, y) = (T, E, B)$. The terms in the power spectra covariance matrix are given by:

$$\begin{aligned} \Xi_\ell^{xy,x'y'} &= \frac{1}{(2\ell + 1)f_{sky}\Delta\ell} \\ &\times [(C_\ell^{xy'} + N_\ell^{xy'})(C_\ell^{yx'} + N_\ell^{yx'}) \\ &\quad + (C_\ell^{xx'} + N_\ell^{xx'})(C_\ell^{yy'} + N_\ell^{yy'})]. \end{aligned} \quad (5.23)$$

where it is assumed that the noise power spectra are Gaussian. This expression was derived by both Kamionkowski et al. (1997b) and Zaldarriaga and Seljak (1997). The noise term, N_ℓ^{xy} includes the effects of the beam, the pixel noise and the pixel solid angle

Ω_{pix} :

$$N_\ell^{xy} = \Omega_{pix}^x (\sigma_{pix}^x)^2 |\mathcal{B}_\ell^x|^{-2} \delta_{xy}. \quad (5.24)$$

The pixel noise depends on survey design and instrument parameters. For an experiment covering an area Θ^2 for an integration time t_{obs} , with N_{PSB} detectors, a solid angle per pixel Ω_{pix} and a sensitivity NET, the pixel noise is:

$$\sigma_{pix}^2 = \frac{NET^2 \Theta^2}{t_{obs} N_{PSB} \Omega_{pix}}. \quad (5.25)$$

We assume that the pixel size used in the map will be the same as the beam size of the telescope. For an experiment using PSBs such as QUaD, the observation time for a polarized map will be half that available for a temperature map as it is not possible to measure Q and U with a single feed at the same time. The pixel variance for the EE and BB spectra is therefore double that for the TT spectra. As described in Chapter 4, the definition of the NET can often be confusing. We use the NET for a single PSB, so that N_{PSB} is the total number of bolometers. If the NET or NEQ of a single feed (a pair of PSBs) is used, N_{PSB} is then the number of feeds.

In QUaD there will be measurements made in two different frequency bands. The noise variance in the two bands will be different due to the different number of detectors, beam size and sensitivity in the two bands. A separate variance is therefore calculated for each band, $N_{\ell,c}$, and the combined variance is calculated from an inverse variance weighting of the noise in each channel:

$$N_\ell = \left(\sum_c \frac{1}{N_{\ell,c}} \right)^{-1}. \quad (5.26)$$

By choosing this weighting scheme at each multipole we combine the signals by giving the most weight to the channels with the smallest detector noise.

The power spectrum covariance matrix (Equation 5.22) can then be used as the data covariance matrix to estimate how well an experiment can measure the cosmological parameters. The Fisher matrix in this case is given by (Kamionkowski et al. (1997b), Zaldarriaga and Seljak (1997)):

$$F_{ij} = \sum_\ell \sum_{XY} \frac{\partial C_\ell^X}{\partial \alpha_i} [\Xi_\ell]_{XY}^{-1} \frac{\partial C_\ell^Y}{\partial \alpha_j}, \quad (5.27)$$

where X and Y are either TT, TE, EE or BB.

In this chapter I will compare the constraints possible with WMAP alone to those which would be obtained by combining the WMAP results with the those expected from QUaD. We therefore need a method of combining the covariances from different experiments. In the simplest case, in which N_{exp} experiments observe different patches of sky,

the combined Fisher matrix, F^C , is the sum of the individual Fisher matrices, F^e (Hu (2002)):

$$F_{ij}^C = \sum_{e=1}^{N_{exp}} F_{ij}^e. \quad (5.28)$$

If any of the patches of sky overlap, each overlapping region is considered as a separate patch. In these patches, each experiment can be thought of as contributing a set of different frequency channels to the patch. The channels in the overlapping patch can then be thought of as belonging to a single experiment and the noise variance for the patch calculated as for a signal multi-channel experiment using the inverse variance weighting in Equation 5.26. For QUaD we assume that a measurement of the temperature power spectrum will not be made and so there is no contribution from QUaD to N_ℓ^{TT} .

5.3 Multipole coverage

The maximum multipole which can be measured from the QUaD data will be determined by the beam size as it is not possible to resolve any structure on scales smaller than the beam unless the beam profiles can be very accurately measured. This gives $\ell_{max} = \pi/\theta_b$ and so the maximum multipoles are 1714 and 2771 in the 100 GHz and 150 GHz bands respectively. For multipoles higher than 1714 we therefore only use the 150 GHz band in the noise variance.

If the atmosphere were perfectly stable, the minimum multipole would be given by the survey area, as it is not possible to measure differences between points greater than the largest dimension of the survey, giving:

$$\ell_{min} = \pi/\Theta. \quad (5.29)$$

However, even though the instrument will reject most of the total power signal, there will still be a fraction of this unpolarized component in the timestream. These residual atmospheric fluctuations could still be large at low frequencies and so some high-pass filtering of the timestream may be needed to remove them. This limits the maximum time over which two timestream data points can be compared, as any changes to the CMB signal on long timescales will be filtered out. In turn, this will limit the maximum angular scale on the sky across which different pixels can be compared and so set a minimum value to the range of multipoles across which the polarization power spectra can be measured. This limit will depend on the stability of the atmosphere and on how fast the instrument can scan across the sky. We estimate the sky will be stable on time scales of between one and two minutes which gives a minimum multipole of between 25 and 50 depending on the scan speed. This is explained in more detail in Chapter 6.

5.4 Including foreground models

In Chapter 3, I predicted the level of the foreground contamination in measurements of the CMB. These estimates were then used to estimate foreground power spectra giving the variance of the foregrounds in each frequency band. These foregrounds can be added as an extra source of variance in the power spectrum covariance matrix to predict the extent to which foregrounds will reduce our sensitivity to the CMB signal.

I include this effect by treating the foregrounds as an extra source of noise with power spectra $N_{\ell(fg)}$ for each different power spectra in each frequency channel. This gives us the maximum possible foreground contamination, i.e. the contamination assuming that no foreground removal will be attempted. However, unlike the detector noise, the foregrounds will be correlated between power spectra and between frequency channels. To include these correlations we follow the technique developed in Tegmark et al. (2000) (thereafter T00). We define a $3F \times 3F$ noise matrix, \mathcal{N}_ℓ , for each multipole, where F is the number of frequency channels in the experiment:

$$\mathcal{N}_\ell = \begin{pmatrix} \mathbf{N}_\ell^{TT} & \mathbf{N}_\ell^{TE} & 0 \\ \mathbf{N}_\ell^{TE} & \mathbf{N}_\ell^{EE} & 0 \\ 0 & 0 & \mathbf{N}_\ell^{BB} \end{pmatrix}, \quad (5.30)$$

where each component of this matrix, $\mathbf{N}_\ell^{XX'}$, is an $F \times F$ matrix giving the variances and covariances of the noise in the F channels. Each element in \mathcal{N}_ℓ is the sum of the contribution from each of the possible foregrounds, $\mathbf{N}_{\ell(k)}^{XX'}$ and the detector noise, $\mathbf{N}_{\ell(det)}^{XX'}$:

$$\mathbf{N}_\ell^{XX'} = \mathbf{N}_{\ell(det)}^{XX'} + \sum_k \mathbf{N}_{\ell(k)}^{XX'}, \quad (5.31)$$

where the sum over k is a sum over each of possible foregrounds which could contribute to the signal.

We define the $3F \times 3$ scan matrix, \mathbf{A} , where:

$$\mathbf{A} = \begin{pmatrix} \mathbf{e} & 0 & 0 \\ 0 & \mathbf{e} & 0 \\ 0 & 0 & \mathbf{e} \end{pmatrix}, \quad (5.32)$$

and \mathbf{e} is a column vector of height F consisting entirely of ones. If $F = 2$ as would be the case for QUaD then:

$$\mathbf{A} = \begin{pmatrix} 1 & 0 & 0 \\ 1 & 0 & 0 \\ 0 & 1 & 0 \\ 0 & 1 & 0 \\ 0 & 0 & 1 \\ 0 & 0 & 1 \end{pmatrix}. \quad (5.33)$$

The weighted noise for each polarization is then obtained by calculating the 3×3 covariance matrix, Σ_ℓ , where:

$$\Sigma_\ell = (\mathbf{A}^T \mathcal{N}_\ell \mathbf{A})^{-1} = \begin{pmatrix} N_\ell^{TT} & N_\ell^{TE} & 0 \\ N_\ell^{TE} & N_\ell^{EE} & 0 \\ 0 & 0 & N_\ell^{BB} \end{pmatrix}. \quad (5.34)$$

The terms, N_ℓ^{XX} are now the noise terms used in equation (5.23) to calculate the power spectra covariance matrix. If the noise is not correlated between T and E and not correlated between channels (as is the case if we include only detector noise) then \mathcal{N}_ℓ becomes diagonal and the procedure is identical to the minimum variance weighting of equation (5.26).

The assumption has been made in this analysis that the foregrounds are Gaussian. This is an approximation and the foregrounds are likely to be non-Gaussian at some level. This would correlate different modes, reducing the number of independent measurements of the foreground noise for each band power and so is likely to increase the variance on the measured band powers.

5.5 Determining area of sky to observe

In this section I show how the optimal survey area to use for QUaD is determined. This section of work was carried out before a final decision was made on the observing site so I have looked at the optimal area to use in Chile as well as at the chosen site at the South Pole.

5.5.1 Formalism for finding optimal survey area

In all CMB experiments the area chosen will be a compromise between two conflicting factors.

- For a fixed total observing time, the integration time per unit area (or pixel) is inversely proportional to the total area; a smaller map will therefore result in a lower pixel noise.

- For a smaller map there are fewer independent modes from which to measure each multipole (i.e. the averaging in Equation 1.27 will be made over fewer values of m) and so the sample variance will increase. For a smaller map the total number of multipoles which can be measured will also decrease.

To find the optimal survey area we need to find the area with the smallest possible errors for a measurement of the polarization power spectra. The error for each multipole is given by Equation 5.21. This is complicated by the fact that different scales in the power spectrum are affected by the choice of area in different ways. On large scales cosmic variance will be the most important factor for low multipoles there are a smaller number of m modes over which to average. On small scales the pixel noise is the most important factor as this increases as the time per pixel decreases. To simplify the calculation we therefore choose to minimize the error in a single parameter for each power spectrum, the amplitude of the spectrum, A^X . The variance in this parameter $(\Delta A^X)^2$, can be found from the Fisher matrix, F . As only one parameter is being constrained, the variance is simply $1/F_{A^X A^X}$. From Equation 5.27 for the Fisher matrix, the error in A^X is:

$$(\Delta A^X)^2 = \left(\sum_{\ell} \frac{1}{(\Delta C_{\ell}^X)^2} \frac{(C_{\ell}^X)^2}{(A^X)^2} \right)^{-1}, \quad (5.35)$$

where $(\Delta C_{\ell}^X)^2$ for each power spectrum are given by the diagonal elements of the power spectrum covariance matrix. I then define a figure of merit parameter as the signal to noise ratio in the measurement of each power spectrum, SNR, which is given by:

$$\text{SNR} = \left(\frac{A^X}{\Delta A^X} \right) = \sqrt{\sum_{\ell} \left(\frac{C_{\ell}^X}{\Delta C_{\ell}^X} \right)^2}. \quad (5.36)$$

This SNR is more useful than the actual error in the measurement. For the measurement to be statistically significant it must have a signal-to-noise ratio of at least 3 so for areas with a SNR lower than 3 it is not even possible to make a detection of the CMB signal. To find the optimal area for a measurement of each power spectrum with a specific experiment we therefore find the area which gives the highest SNR given a set of survey and instrument parameters. The sum over ℓ in Equation 5.36 is made assuming $\Delta\ell = 1$. Although this is not strictly allowed as these individual variances cannot be measured for a finite patch of sky, the SNR is independent of the size of the bands taken as we are effectively averaging over the entire power spectrum.

In order to measure the TE spectrum we assume that the QUaD polarization measurements can be combined with a temperature map from the 4 yr WMAP data.

I use three different scenarios for the foreground contamination:

- no foreground contamination,

- a best case foreground estimate and
- a worst case estimate.

The models use foreground parameters discussed in Chapter 3.

5.5.2 Chile calculation

Determining the survey timescales

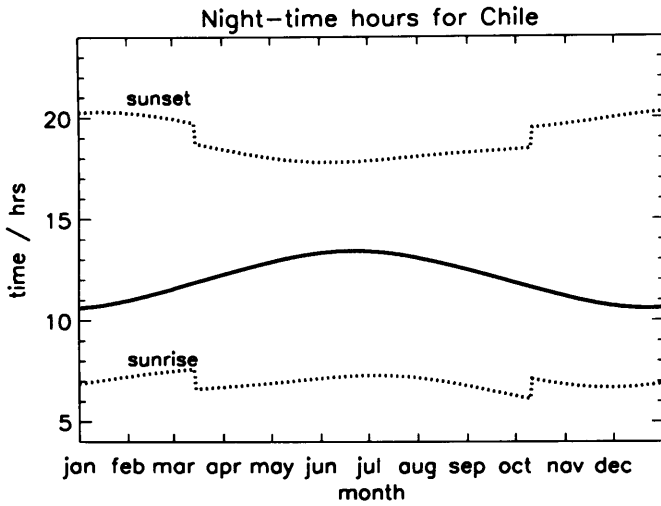


Figure 5.2: Variation in the number of hours of night-time each day for the Chile site (solid line). The dotted lines show the times of sunset and sunrise. The y-axis gives the local time in Chile.

The site at Chile is at a latitude of -23.0 and so will be affected by the apparent motion of the celestial sky due to the motion of the Earth. This means that no single region of the sky will be visible at night from Chile for the whole year. The number of night-time hours will also vary throughout the year as shown in Fig. 5.2. This ranges from 10.6 in the middle of December to 13.4 in the middle of June. The sudden dips in the time of sunset and sunrise are due to change to (midnight on the 2nd Saturday of October) and from (midnight on the 2nd Saturday in March) daylight savings time in Chile. Fig. 5.3 shows the number of hours in a year for which each position in the celestial sphere is visible during the night, which is defined as the time during which the Sun is below the horizon. We have also accounted for the position of the moon by including a 40° moon avoidance zone. To find this zone we find the position of the moon and the source on the celestial sphere at intervals throughout the night and then calculate the angular separation of these two points, θ , using the spherical trigonometry relation:

$$\cos(\theta) = \sin(\delta_m) \sin(\delta_s) + \cos(\delta_m) \cos(\delta_s) \cos(\Theta_m - \Theta_s) \quad (5.37)$$

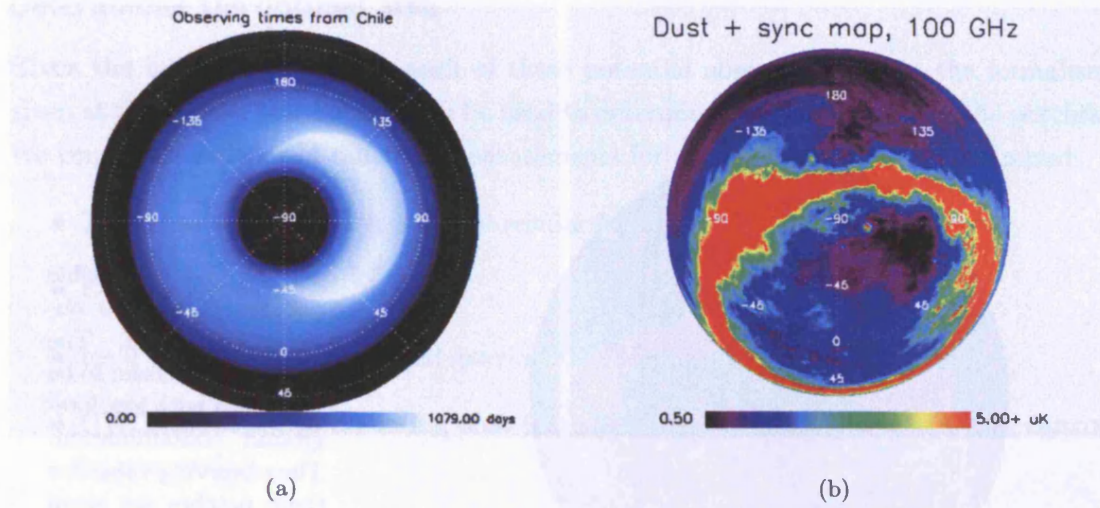


Figure 5.3: Left: Region of sky observable from Chile site assuming a minimum elevation of 50° . The colour gives the number of days of observing time for each point on the celestial sphere. Right: Foreground estimates as in Chapter 3.

where the right ascension and declination of the moon and the source are (Θ_m, δ_m) and (Θ_s, δ_s) respectively. The times shown in Fig. 5.3 are the number of hours the source is above an elevation of 50° and more than 40° away from the moon when the sun is below the horizon. This 50° minimum for the elevation is chosen as it is preferable to observe at high elevation so that the line of sight through the atmosphere is smaller. The combined foreground estimate from Chapter 3 for the region of sky accessible to Chile is shown next to this figure for comparison.

As it is not possible in Chile to observe a single region of sky for the whole year, a number of patches will be chosen which are visible at different times. The patches of sky observed should be as well separated as possible in order to get the maximum integration time on the CMB. Five possible patches are shown on Fig. 5.4 and the number of hours for which each of these patches can be observed according to the conditions stated are given in Table 5.1. The patches are chosen to be in regions where the foreground amplitude is low and so are away from the plane of the galaxy. From a possible 4400 night time hours these patches are only observable for a total of 3934 hours. There is also some overlap in the times when each of the patches can be observed, this reduces the total time to 3415 hours. One possibility is to use these night time hours when the CMB cannot be observed to make study of polarized galactic foregrounds. Some of this time could also be used for calibration and beam mapping.

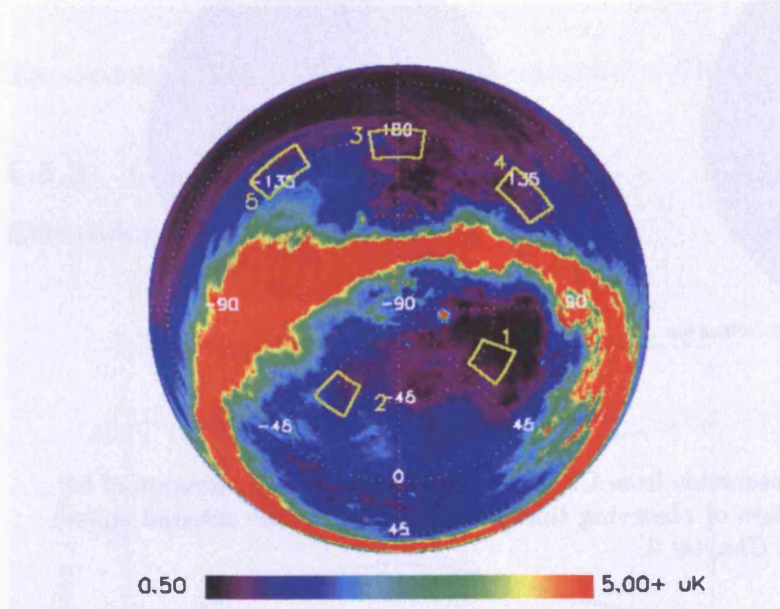


Figure 5.4: Possible patches of sky to observe from Chile. The patches are chosen to be in regions with low foreground contamination. The observing times for these patches are given in Table 5.1.

Total available hours					8766
Total night time hours					4400
Field	RA	Dec	Hours visible at night	Moonless hours visible at night	Overlap
1	60	-39	1047	1047	75.5 (4)
2	-35	-40	1064.5	872	0
3	180	-5	904.5	706	233 (5) 210 (4)
4	132	-4	882.5	729	210 (3)
5	-140	5	711	580	233 (3)
Total observing hours					3934
Total observing hours minus overlap					3415

Table 5.1: Observing times per year for 5 possible patches observable from Chile. We assume a 60% observing efficiency, giving a total of **2049 hrs** per year to observe the CMB.

Determining the optimal area

Given the integration time for each of these potential observing regions, the formalism given at the start of this Section can be used to determine the optimal size for the patches. We consider a number of different measurements for which QUaD could be optimized:

- TE signal using the 4 yr WMAP results for the temperature signal.
- E-mode signal
- total B-mode signal included gravitational lensing (GL)
- GW B-mode signal assuming that the lensing signal is a foreground which cannot be removed
- GW B-mode signal assuming that the lensing signal can be completely removed.

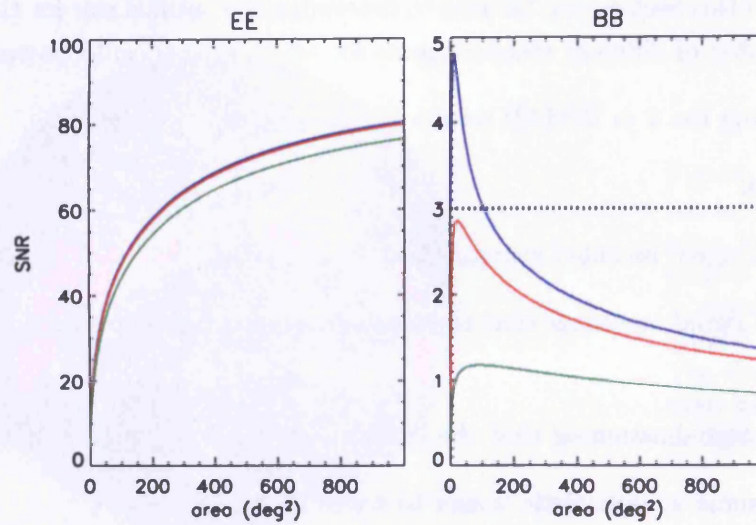
In each case we assume an optimistic tensor to scalar ratio of 0.1.

As shown in Chapter 4, the expected sensitivities for QUaD in Chile are $340 \mu K s^{1/2}$ and $500 \mu K s^{1/2}$ at 100 GHz and 150 GHz respectively. We assume an observing efficiency of 60% to account for calibration and bad weather. As a starting point we assume that the total integration time will be divided equally between the 5 patches. This gives a total observing time per year of 2049 hours. Splitting the survey into 5 separate patches will not change the total area used to calculate SNR, however it will limit the minimum multipole which can be measured, given by Equation 5.29, where the area used should now be the area of a single patch, not the full survey. We assume a cut-off for the minimum ℓ of $\ell_{min} = 25$ due to atmospheric instability as discussed in Section 5.3. The results for this survey are given in Table 5.2 and Fig. 5.5.

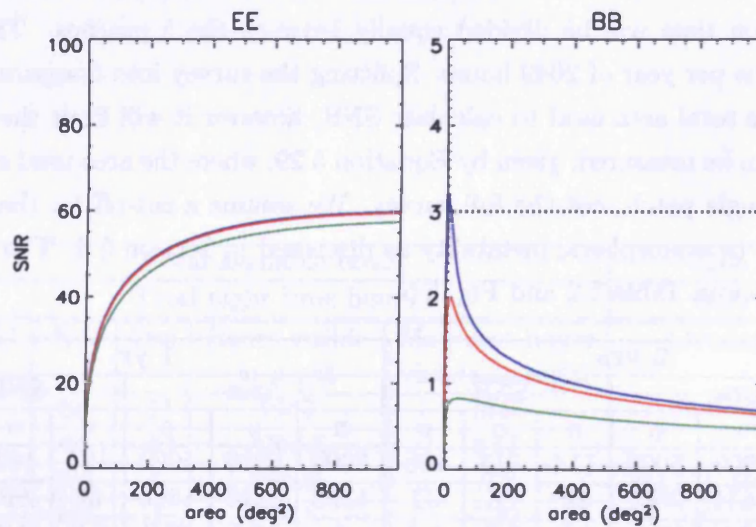
	2 yrs						1 yr					
	Area			SNR			Area			SNR		
Model	n	o	p	n	o	p	n	o	p	n	o	p
TE	5000	5000	5000	114	113	108	5000	5000	5000	104	103	100
EE	2394	2424	2611	85	85	82	1198	1213	1306	60	60	58
BB ^a	11.0	23.5	86.0	4.8	2.8	1.2	6	13.5	46.0	3.2	2.0	0.8
BB ^b	231	386	1661	1.0	0.6	0.2	193	293	1039	0.5	0.4	0.1
BB ^c	271	426	1691	1.0	0.6	0.2	231	293	1039	0.5	0.4	0.1

a: total B-mode signal, b: GW signal with lensing signal as noise, c: GW signal, no lensing

Table 5.2: Results for a one/two year survey for 5 equal size patches for the case of no foregrounds (n), optimistic foregrounds (o) and pessimistic foregrounds (p).



(a)



(b)

Figure 5.5: Variation of SNR with area in Chile for 5 equal size patches for a two year survey (top) and a one year survey (bottom). The different colour lines give the results for the different foreground models: blue - no foregrounds, red - optimistic model, green - pessimistic model.

The results show that from Chile QUaD can make a good measurement of the E-mode signal and could make a detection of the B-mode lensing signal. However, it is not possible to detect the GW signal from Chile, even if the foreground and lensing contamination can be completely removed. A large area is favourable for an E-mode measurement, but a small area is needed for a detection of the B-mode signal. This is because the stronger E-mode signal is limited by sample variance up a survey size of around 2000 deg^2 . In contrast B-mode signal is pixel-noise-limited after around 10 deg^2 . This means it is not possible to optimize the survey size for both signals at the same time. The foreground contamination does not significantly affect the E-mode measurement, even for the pessimistic model, but it does significantly reduce the SNR for the B-mode signal, in fact the total B-mode signal is only detectable ($\text{SNR} > 3$) for the no foreground case. One possibility is to choose the largest possible total area which can be used without pushing the B-mode detection below the $\text{SNR} > 3$ limit needed to make a feasible detection. With no foregrounds, this occurs at around 60 deg^2 , which gives a BB SNR of 3.5. This reduces the EE SNR to 40, about half of the maximum possible value. If we include foregrounds, the BB detection is very marginal and so reducing the E-mode SNR in order to detect the B-mode signal would not be advisable unless the foreground contamination can definitely be reduced.

If the B-mode SNR were slightly higher, an alternative would be to divide the time equally between the two surveys, spending the first year covering the optimal area for a one year E-mode survey and the second year covering the area optimal for a one year B-mode detection. From Fig. 5.5 (b) we can see that this will give an EE SNR of around 60, better than for the previous suggestion, but the BB detection is reduced to just above the $\text{SNR} > 3$ limit. Again, if foreground contamination cannot be removed this would be counter productive and it would be more useful to spend the full two years on a large area of sky.

Another possible solution is vary the size of each of the patches so that we have more integration time on a number of smaller patches, but we observe a large enough area in total for the E-mode measurement not to be degraded significantly. As a first attempt to model this, I split the survey into 2 sub-surveys, a large area survey and a small area survey. Each survey contains a certain number of patches and the total time for each sub-survey is the sum of the total time available for each of the patches in the sub-survey. In this approximate model we assume that the total time is split evenly between the patches in a sub-survey. The total SNR is then found by adding the SNR for the two sub-surveys in quadrature.

I take four different cases in which we allocate the observing time to the large area and small area surveys in different proportions. This is achieved by distributing the overlap time between the patches differently in each case. The observing times per year for the

different time allocations are:

1. 3 small area patches (1,2,3) - **2106 hrs**, 2 large area patches (4,5) - **1309 hrs** (total overlap time taken from small area patches),
2. 3 small area patches (1,2,4) - **2362 hrs**, 2 large area patches (3,5) - **1053 hrs** (286 hrs overlap time taken from small area patches, 233 hrs from large area patches),
3. 3 small area patches (1,2,3) - **2625 hrs**, 2 large area patches (4,5) - **790 hrs** (total overlap time taken from large area patches).

These times are multiplied by a factor of 1.2 (2×0.6) to account for observing for 2 yrs with a 60 % observing efficiency.

Survey	Foreg model	sub-survey area / deg ²		SNR	
		small	large	EE	BB
1 year single size 50:50	n	6	1198	60	3.2
	o	13.5	1213	60	2.0
	p	46	1306	58	0.8
1 60:40	n	6	918	55	4.1
	o	16	928	57	2.4
	p	61	1001	61	1.0
2 70:30	n	6	738	50	4.3
	o	16	748	52	2.5
	p	66	806	58	1.0
3 77:23	n	8.5	553	45	4.5
	o	18	561	48	2.6
	p	71	603	54	1.1

Table 5.3: Results for a 2-scale two year survey in Chile. The ratios give the split of the integration time between the two sub-surveys.

The results for the two-scale survey are given in Table 5.3. We also include the previous results for a one year survey in this table as this is effectively a 50:50 split of the integration time between the large and small area surveys if we observe a patch of the optimal size for the E-modes for the first year and a patch of the optimal size for the B-modes for the second year. Comparing these results to Fig. 5.5 it is clear that using a two scale survey allows us to make a detection of the B-mode signal without degrading the E-mode detection by as much as if a single area is chosen. In each case, both the E-mode and B-mode SNRs are higher for the two scale survey than if we use a single patch size of 60/5 deg² (EE SNR=40, BB SNR=3.5) as suggested previously. As the time allocated to the small area sub-survey increases, the BB SNR becomes slightly better, but E-mode SNR decreases. Although the increase in the B-mode SNR is very

small, any slight increase is important as the SNR is still very close the detection limit. Unfortunately, if foregrounds are included, the B-mode signal is still not detectable.

Conclusions for Chile optimal area

- QUaD operating from Chile can make a good measurement of the E-mode signal. This conclusion is not affected by the foreground level as even for the most pessimistic foreground estimate the foreground level is below the level of the CMB signal.
- To make this measurement five patches of sky must be observed in order to get the maximum possible integration time on the CMB.
- A detection of the B-mode signal can also be made, but this requires a much smaller survey area to be used which would seriously degrade the E-mode measurement.
- One way to overcome this problem would be to use a two scale survey, observing three of the patches at the optimal area for B-modes and two at a larger area optimal for E-modes.
- There are a number of possible ways of allocating the integration time between these large and small sub-surveys. To get the maximum B-mode SNR, a total small area of around 10 deg^2 and large area of 550 deg^2 should be used and the maximum possible integration time given to the small area sub-survey (survey 3). This will give two large patches of 275 deg^2 and three small patches of 3 deg^2 .
- This is only the best solution if the foreground contamination can be completely removed. If the foreground contamination is at the level of the optimistic model, the B-modes cannot be detected at a significant level. Unless it can be shown that the foreground contamination can be substantially reduced or that the levels estimated here are too high, the best strategy would be to concentrate only on the E-modes and use five patches of $2000/5 \text{ deg}^2$.

5.5.3 South Pole calculation

Determining survey timescale

The observing time at the South Pole is much simpler to calculate as the Sun does not rise and set each day. Instead, the sun is above the horizon between October and March (the austral summer) and is below the horizon for the rest of the year. This gives six complete months that can be used for observations of the CMB, during which the same region of

sky is always visible. Also, because the sky rotates about the zenith a patch on the sky will only move in azimuth and so will always be at the same elevation. The moon is also not a problem at the South Pole as it only contaminates a small part of the observable region of sky. This is shown in Fig. 5.6 which shows the number of hours for each point on the celestial sphere is observable from the South Pole for a minimum elevation of 50° . It is fortunate that the area of sky contaminated by the moon does not overlap with the regions with the lowest foreground contamination. It is therefore possible to choose a patch of sky to observe with a low foreground level that can be observed for the full six month observing time.

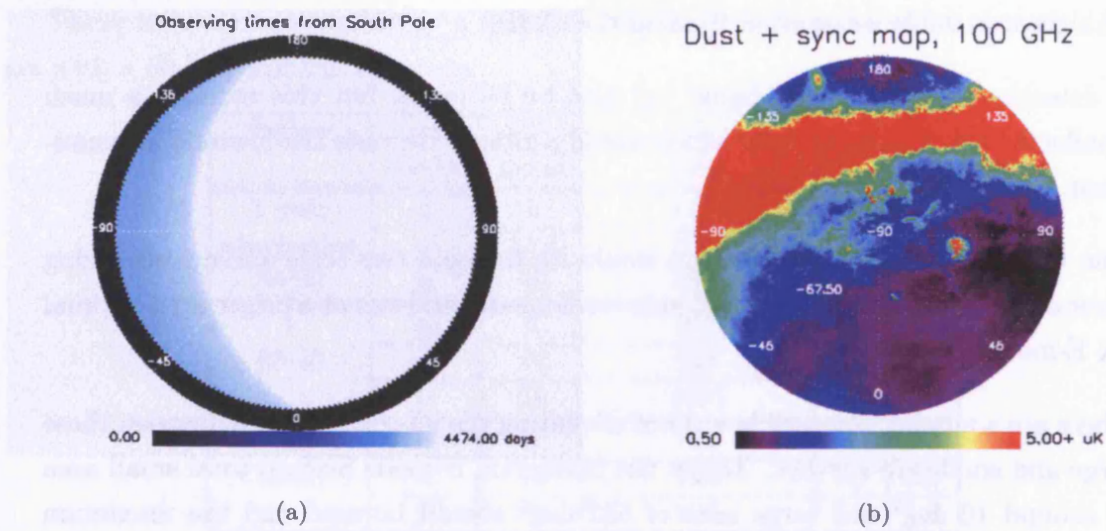


Figure 5.6: Left: Number of hours of observing time for each point on the celestial sphere from South Pole site. Right: Foreground estimates as in Chapter 3 for region of sky accessible from South Pole.

We estimate the total observing time by assuming that QUaD will observe at the South Pole for two years during the austral winter for 22 hours each day and assuming that 20 per cent of this total time will be lost due to bad weather, instrument maintenance and calibration time. These estimates are based on the experiences of the DASI team at the South Pole site Kovac et al. (2002). This gives a total time spent observing on the CMB of 3210 hours per year. The maximum size patch of sky that can be used without overlapping into regions with heavy foreground contamination or looking at elevations below 50° is about 1000 deg^2 . Two possible regions are shown in Fig. 5.7.

Determining optimal area

We investigate the SNR for the same five measurements used in the Chile case, but in this time we assume that only a single patch of sky will be covered for the full two year

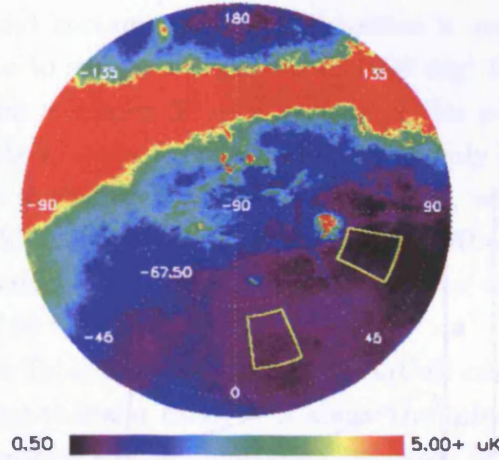


Figure 5.7: Possible patches of sky to observe from South Pole. Both of these patches can be observed for the full observing time of 3210 hrs per year.

integration time. We use sensitivities of $300 \mu K s^{1/2}$ and $340 \mu K s^{1/2}$ at 100 GHz and 150 GHz respectively as calculated in Section 4. The result are shown in Table 5.4 and Fig. 5.8.

Comparing these results to those obtained for the Chile site, we see the same situation in

	2 yrs						1 yr					
	Area			SNR			Area			SNR		
Model	n	o	p	n	o	p	n	o	p	n	o	p
TE	1000	1000	1000	58	58	56	1000	1000	1000	57	57	84
EE	1000	1000	1000	111	110	104	1000	1000	1000	90	89	84
BB ^a	21	66	264	8.4	4.7	1.8	11	35	132	5.9	3.3	1.3
BB ^b	178	568	1000	2.4	1.1	0.3	112	284	1000	1.6	0.8	0.2
BB ^c	207	636	1000	2.2	1.0	0.3	144	318	1000	1.5	0.7	0.2

Table 5.4: Results for a one/two year survey at the South Pole for a single patch of sky.

which the B-modes are pixel-noise limited and the E-modes are sample-variance limited up to the maximum 1000 deg^2 patch size and so again it is not possible optimize the survey area for E and B modes simultaneously. However, due to the longer integration and the higher sensitivity achievable at the South Pole the maximum SNR which can be achieved is higher than for Chile. The difference for the E-mode measurement is fairly small as the noise is dominated by sample variance and so reducing the pixel noise does not cause a significant reduction in the SNR. However, for the total B-mode signal the SNR almost doubles. The B-mode signal is still detectable at the South Pole if the optimistic foreground is used, but the SNR falls below the detection limit for the pessimistic model.

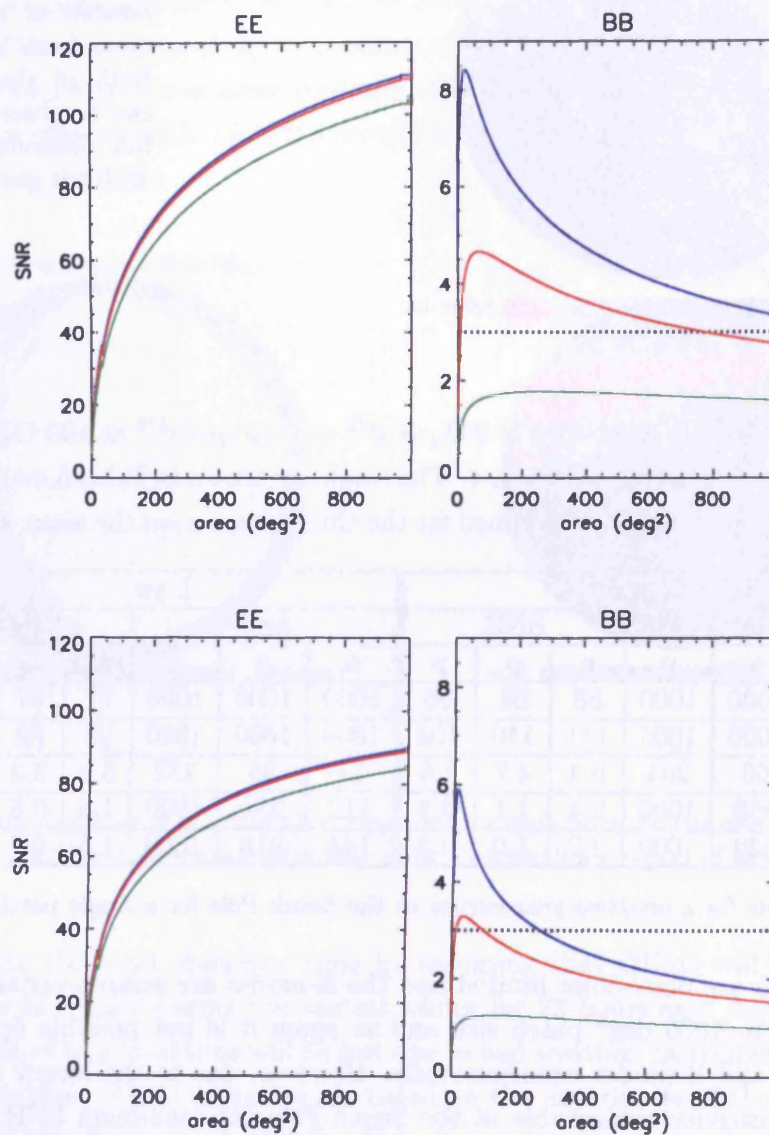


Figure 5.8: Variation of SNR with area for a single patch of sky at the South Pole for 2 yrs (top) and 1yr (bottom). The different colour lines give the results for the different foreground models: blue - no foregrounds, red - optimistic model, green - pessimistic model.

For a one-year integration time, the B-mode signal can still be detected, although with foreground contamination this detection is very marginal ($\text{SNR}=3.3$). One possibility would be to survey a large area of 1000 deg^2 for the first year, and then integrate more deeply on a smaller 30 deg^2 portion of this patch for the second year. For a two-year survey the E-mode SNR begins to drop sharply below around 300 deg^2 , so another possible solution would be to use a 300 deg^2 patch, which still gives a detection of the B-mode signal ($\text{SNR}=5.2$ if no foregrounds and $\text{SNR}=3.9$ for optimistic foreground model) and only decreases the E-mode SNR by a factor of 0.7 from its maximum value of 110 to a value of 80.

From Table 5.4 it is evident that QUaD cannot detect the GW B-mode signal unless the tensor-to-scalar ratio, r , is above the value of 0.1 used here, even if the foreground contamination can be completely removed. We have therefore extended the calculation to higher values of r up to the current upper limit of 0.36 (Leach and Liddle (2003)). Fig. 5.9 shows how the optimal area for a measurement of the GW signal with QUaD varies with r .

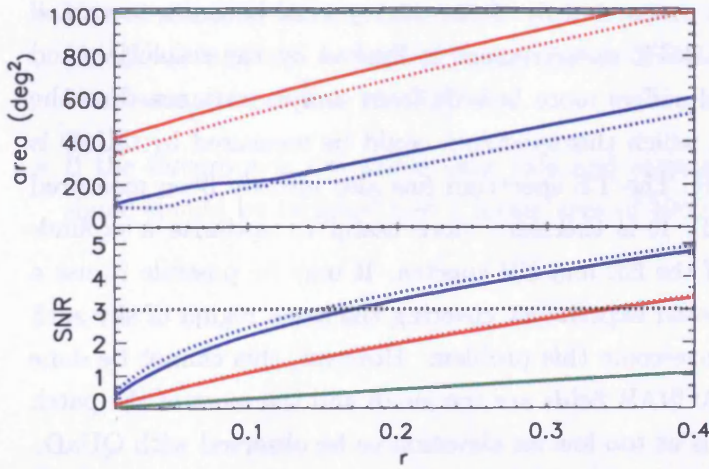


Figure 5.9: Variation of optimal area (upper panel) and achievable SNR (lower panel) as a function of tensor-to-scalar ratio for the GW signal. The different colour lines give the results for the different foreground models, blue: no foregrounds, red: optimistic model, green: pessimistic model. The dotted lines give the results if the lensing signal could be completely removed. The dotted black line shows the $\text{SNR} = 3$ detection limit.

The optimal area changes significantly as r increases. For the optimistic foreground model it is only possible to detect the GW signal for r greater than 0.35, and for the pessimistic model a detection is not possible. However, for the large areas which are best for detecting this high GW signal, the SNR for the total B-mode signal would drop significantly. It is therefore not possible to pursue both science goals simultaneously. However, if the foreground contamination can be completely removed, the lowest detectable value of r drops to 0.17. The optimal area also decreases as the detector noise becomes the dominant factor. In the no foreground case it would be possible to detect the GW signal using the 300 deg^2 survey discussed above. The calculation made here assumes that the GL signal has not been removed and acts as an extra foreground. If the GL signal can be

removed, the GW signal becomes slightly easier to detect (as shown by the dotted lines in Fig. 5.9) , but only if the foregrounds can be subtracted as the combined foreground contamination is larger than the GL signal over most of the multipole range which can be covered from the ground.

The effects of the mixing of E and B modes due to partial sky coverage will not significantly influence the results found here. Bunn (2002) finds that the mixing will only have a large effect for the B-mode signal on the scale of the survey size. If we use a 300deg^2 patch the GL B-mode signal will therefore not be affected. For a detection of the GW signal this effect will become more important. However, Lewis et al. (2002) discuss this problem and calculate the minimum detectable r as a function of survey size. They find that for the large surveys (greater than 50°) the minimum value is not changed if the mixing effects are included. For the areas discussed here the GW results will therefore not be influenced by E-B mixing if an optimal method is used to separate the E and B modes.

The results for the TE measurement are also shown in Table 5.4. As with the EE spectrum, the measurement is sample-variance-limited and the largest possible area of 1000 deg^2 is best. The SNR also drops sharply if the survey area becomes too small ($\leq 100\text{ deg}^2$). However, the QUaD TE measurement is limited by the resolution and sensitivity of the WMAP map and suffers more heavily from sample variance than the smaller EE signal. The SNR with which this spectrum could be measured by QUaD is therefore smaller than the EE SNR. The TE spectrum has also already been measured in this multipole range by WMAP. It is therefore more useful to optimize a ground-based survey for a measurement of the EE and BB spectra. It may be possible to use a temperature map from a ground-based experiment covering the same region of sky such as ACBAR or BOOMERANG to overcome this problem. However, this cannot be done for the whole patch of sky as the ACBAR fields are too small and the most of the patch of sky covered by BOOMERANG is at too low an elevation to be observed with QUaD.

We have also investigated the effect of increasing the minimum ℓ value used in the calculation. For the TE, EE and total BB spectra, an increase in the minimum ℓ from 25 to 100 has a negligible effect, as most of the power in these spectra is from the higher multipoles. However, as would be expected, increasing the minimum ℓ does affect the GW B-mode detection. If the minimum ℓ is increased to 100 the GW is no longer detectable below the current upper limit of $r = 0.36$.

Conclusions for the South Pole

- At the South Pole, a good measurement of the E-mode signal and a significant detection of the B-mode signal can be made.

- The optimal area to use for both science goals is different, with the E-modes requiring a much larger area than the B-modes.
- Due to the increase in sensitivity and integration time compared to Chile, a compromise of a 300 deg^2 area will still give a detection of the B-mode signal without significantly degrading the E-mode measurement. This is true even if the foregrounds cannot be removed if the foreground level is not higher than in the optimistic model. However for the pessimistic model the B-mode signal cannot be detected.
- If the tensor to scalar ratio is just below current upper limits then it is possible to detect the gravitational wave signal, however, the optimal area for this is much larger than that for the total B-mode signal and so it would not be possible to optimize for both B-mode signals. Given that the B-mode lensing signal needs to be measured accurately before the gravitational wave can be detected (unless the tensor to scalar ratio is very high), optimizing for the gravitational wave signal would not be sensible for QUaD.
- If the optimistic foreground model can be assumed to be correct, the best solution for QUaD is to use a single 300 deg^2 patch of sky. **This is the strategy which has been chosen for the QUaD.**
- If the foregrounds are worse than this and cannot be removed, only the E-mode signal should be targeted and a larger area of 1000 deg^2 used.

5.6 Power spectrum predictions

In this Section I investigate how well QUaD will be able to measure the two polarization power spectra, C_ℓ^{EE} and C_ℓ^{BB} from the South Pole. For each spectrum, the variance for each of the measureable band powers is given by Equation 5.21:

$$(\Delta C_\ell)^2 = \frac{2}{(2\ell + 1)f_{sky}\Delta\ell}(C_\ell + N_\ell)^2,$$

where the noise term N_ℓ includes the combined error due to detector noise and foreground variance. The factor $\Delta\ell$ gives the bandwidth of the measurement. For a finite size patch of sky of size Θ , this must be greater than the minimum multipole which can be measured from this patch, $\ell_{min} = \pi/\Theta$. In practice, it is often useful to make the bandwidth larger than this to increase the signal-to-noise ratio per band. However, this will decrease the resolution of the measurement. The SNR measured in the last section was effectively just measuring the variance for a single band which contains the entire measureable multipole range.

To investigate measurements achievable with QUaD, I assume a 300 deg^2 square patch of sky will be observed for two austral winters. This gives an observing time of 3210 hours per year as explained in Section 5.5. I use the sensitivities calculated in Chapter 4 of $300 \mu\text{K s}^{1/2}$ and $340 \mu\text{K s}^{1/2}$ for QUaD at the South Pole. Fig. 5.10 shows the

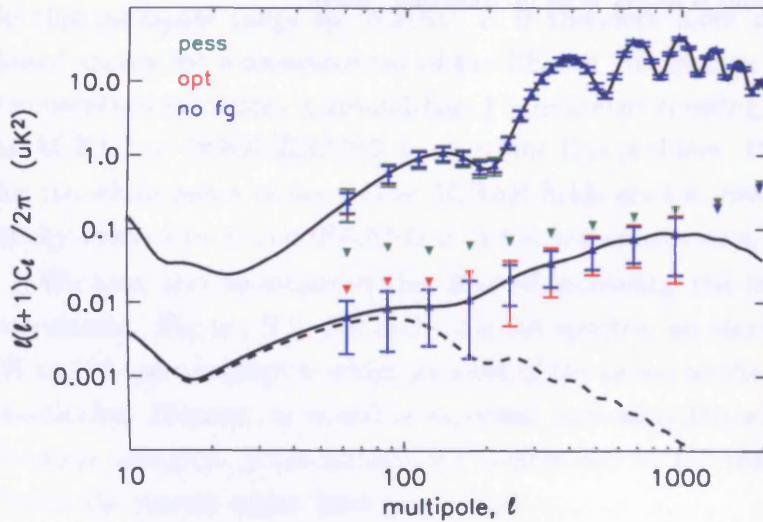


Figure 5.10: Comparison of QUaD measurements for different foreground models, blue: no foregrounds, red: optimistic and green: pessimistic. In this plot and the following plots in this section, error bars indicate one-sigma detections and the free symbols shown are upper limits. The solid black lines show the EE (top) and total BB (bottom) spectra and the dashed line shows the GW BB spectrum.

expected measurements for the different foreground models (optimistic and pessimistic) compared to the best possible case of no foregrounds. As expected from the results for the total SNR in the last section, QUaD can make a high resolution measurement of the

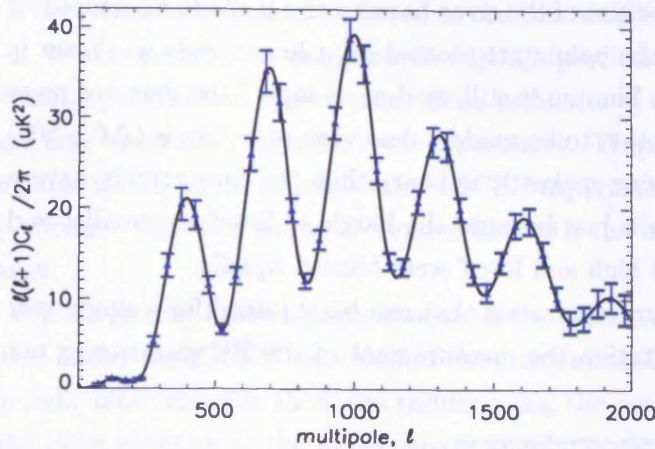


Figure 5.11: As in Fig. 5.10 but using a linear axes. Also a linear binning with $\Delta\ell = 50$ is used as opposed to the logarithmic binning used in Fig. 5.10.

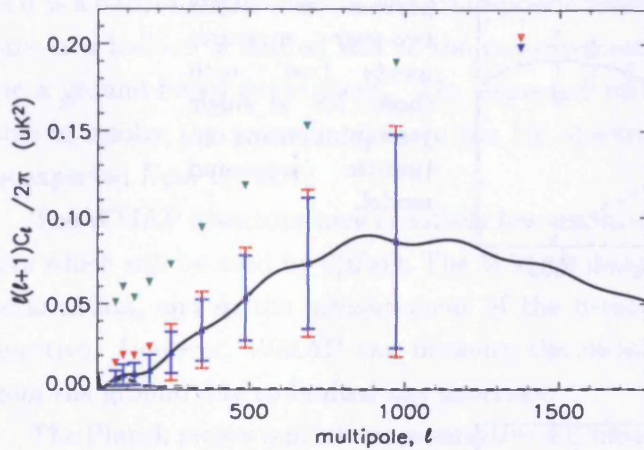


Figure 5.12: BB power spectrum error bars of QUaD using a linear scale but still using logarithmic binning.

E-mode spectrum, but will only make a detection or place upper limits on the B-mode signal. As shown in Section 5.5, the foreground level has very little effect on the E-mode measurement, but for the B-mode measurement it gives the difference between a detection and an upper limit. In Fig. 5.10 I have chosen to use logarithmic binning, so the bands at small scales are much bigger than those at large scales. This hides the increase in the variance due to detector noise at high ℓ . This can be seen more clearly for the EE spectrum in Fig. 5.11 and for the BB spectrum in Fig. 5.12 which use linear axes.

In the EE spectrum the error bars at lower multipoles ($\ell < 300$) are actually smaller than at high ℓ , which is not immediately obvious from Fig. 5.10, but is shown clearly in Fig. 5.11. The logarithmic scale also makes it appear that the effect of foregrounds is greater at low ℓ , but this is just because the the small difference between the error bar for

each foreground model is emphasised for the low ℓ points as the position of these points on the y-axis is lower. The increase in the size of the error bars for the B-mode measurement at high ℓ is also more easily seen if the points are plotted on a linear scale as shown in Fig. 5.12. In this figure a logarithmic binning is still used as at high ℓ the detector noise level is too high for a one-sigma detection to be made unless very wide bands ($\Delta\ell > 500$) are used. Also the logarithmic binning makes it appear that the foregrounds have a larger effect on larger scales, but this is just because the bands at low ℓ are smaller and would not be the case if the bands at high and low ℓ were binned equally.

Fig. 5.13 shows the power spectrum constraints that can be obtained for a single year of integration. For a one-year integration the measurement of the EE spectrum is not

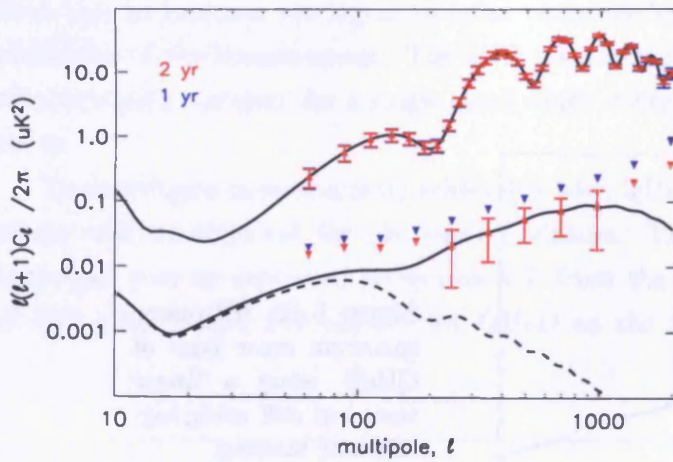


Figure 5.13: Comparison of QUaD two-year measurements (red) with those for a single year (blue) using optimistic foreground model.

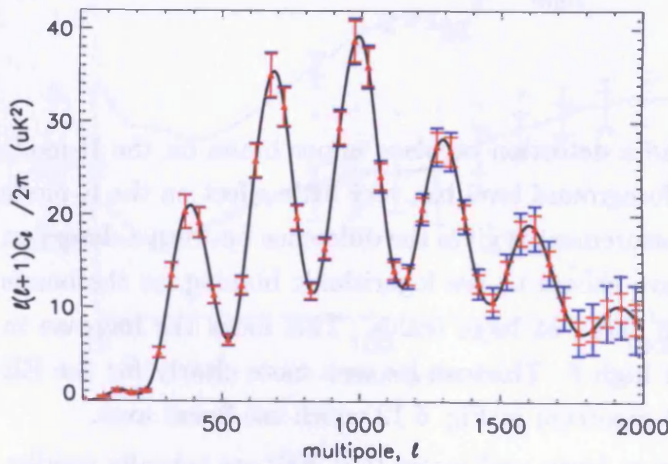


Figure 5.14: EE measurements as in Fig. 5.13 but using linear binning $\Delta\ell = 50$ and linear axes.

significantly worse than that for a two-year integration for $\ell < 1500$. This can be seen more clearly in the case of linear binning as shown in Fig. 5.14, where the only noticeable

difference is at very high ℓ . However for the B-mode signal the full two years are needed for a detection to be made, as noted in the last section.

It is also possible to compare the QUaD predictions to those expected from other upcoming polarization experiments given estimates of the sensitivity, resolution, sky coverage and integration time for each experiment. These are given in Table 5.5. Fig. 5.15 compares QUaD to the ground-based BICEP experiment and the BOOMERANG balloon experiment. Fig. 5.16 shows a comparison with the two satellite missions, WMAP and Planck.

For the ground-based missions we show the expected errors if there are no foregrounds as this allows the BICEP detection of the gravitational wave bump at $\ell \sim 100$ to be seen. The light blue triangles show the results using the optimistic foreground model. BICEP is the more sensitive at the intermediate angular scales needed to lower the limits on the level of the gravitational signal, but the superior angular resolution of QUaD allows it to make measurements on smaller scales. BOOMERANG has a higher instrument sensitivity as it is a balloon experiment so the atmospheric loading is much lower. However, the flight time of a balloon is limited and so the measurements will have more detector noise than for a ground-based experiment. The expected results from BOOMERANG should be able to resolve the acoustic peaks in the EE spectrum, but not with the same precision as expected from QUaD.

The WMAP detectors have relatively low sensitivity compared to the bolometric detectors which will be used by QUaD. The WMAP design was also not optimized to measure polarization, and so the measurement of the E-mode spectrum for WMAP is not very sensitive. However, WMAP can measure the reionization bump which cannot be done from the ground due to limited sky coverage.

The Planck makes a much more sensitive EE measurement, except on very small scales where the Planck measurement is dominated by pixel noise due to its lower integration time per pixel, as shown in Fig. 5.17. The high sensitivity Planck measurement of the first few acoustic peaks will allow it to reach a higher resolution than QUaD and so make the Planck data more useful for probing effects such as weak lensing. However, the QUaD measurement is not too far behind and so a ground-based experiment with the same resolution as QUaD, but with slightly higher sensitivity, would be able to measure the acoustic peaks as well as Planck.

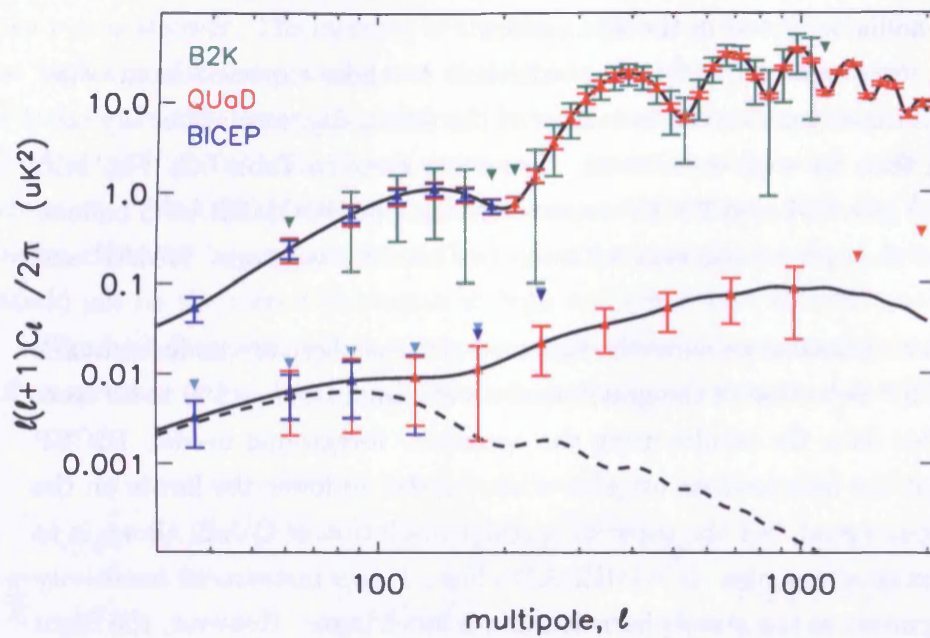


Figure 5.15: Comparison of QUaD measurements (red) with other ground-based experiments, BOOMERANG (green) and BICEP (dark blue). These errors assume that there are no foregrounds. For comparison, the BICEP upper limits which can be achieved if the optimistic model is used are shown as light blue triangles.

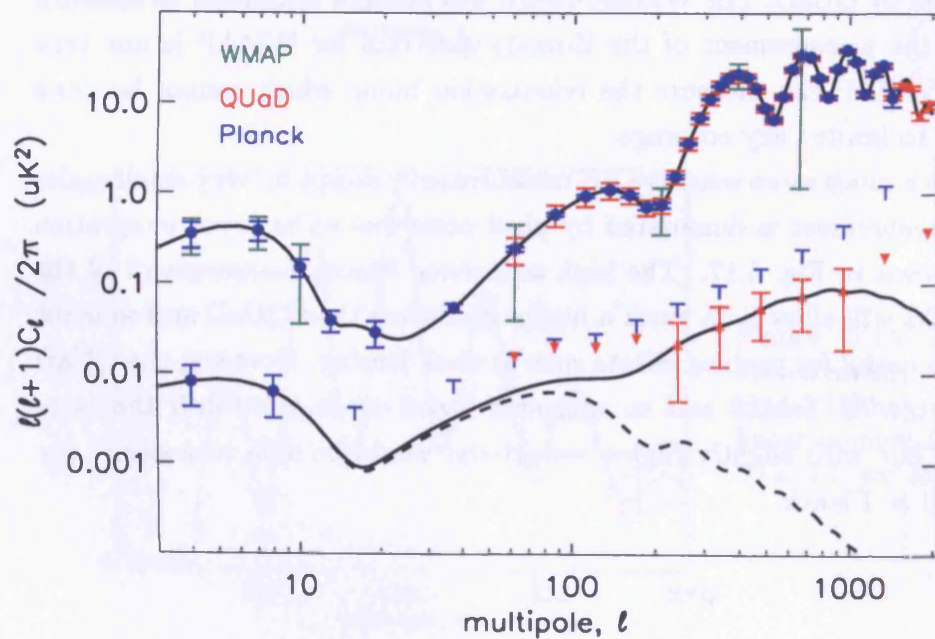


Figure 5.16: Comparison of QUaD 2yr measurements (red) with upcoming satellite constraints with the four year WMAP data (green) and two-year Planck data (blue).

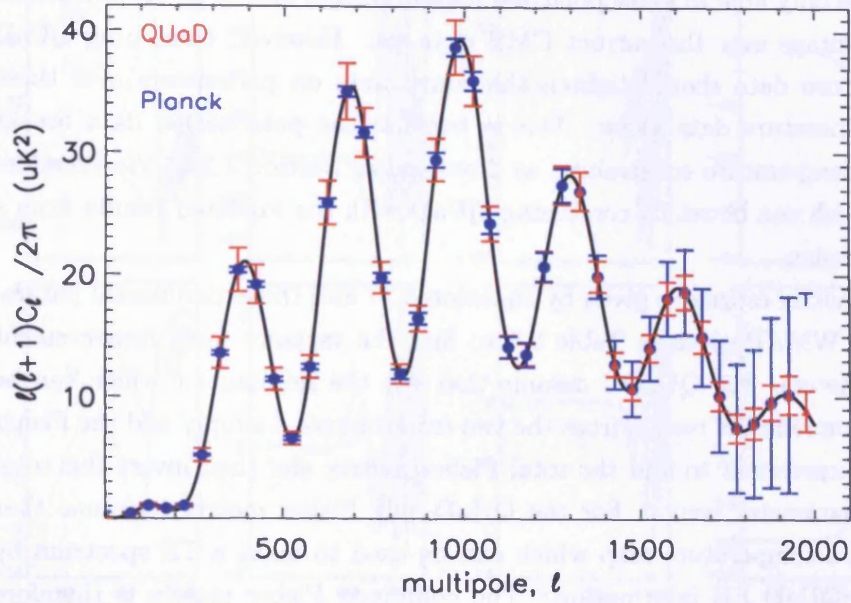


Figure 5.17: As Fig. 5.16, but for linear binning.

Experiment	Freq / GHz	NET / $\mu K s^{1/2}$	Integration time / hrs	Observing area / deg ²	Beam size / arcmin	PSB no.
QUaD	100, 150	300, 340	6420	300	4.2, 6.3	38, 24
BICEP	100, 150	270, 300	6420	500	60, 40	48, 48
B2K	150	200	90+215	1280+90	9.0	8
WMAP	70, 90	1521, 2071	26915	31666	19.8, 12.6	8, 16
HFI	100, 150, 220	96, 80, 120	13458	31666	10.0, 7.0, 5.0	8, 8, 8

Table 5.5: Experimental parameters used to calculate error bars. For B2K (BOOMERANG polarized flight) a large field was covered for 90 hrs and then a smaller patch inside this field was covered for a further 215 hrs. For Planck I only use the HFI (high frequency instrument) as the LFI (low frequency instrument) will be used mainly as a foreground monitor. For the same reasoning only the highest two WMAP frequencies are used. I assume a four year WMAP mission and a one-year (two cycle) Planck mission.

5.7 Parameter forecasts

In this section we investigate how well QUaD will be able to measure the key cosmological parameters. QUaD is only able to make polarized measurements and so on its own would not have much advantage over the current CMB data-set. However, combining QUaD with CMB temperature data should tighten the constraints on parameters over those achievable from temperature data alone. This is because the polarization data breaks degeneracies in the temperature constraints, as discussed in Section 1.2.6. We therefore look at the limits which can be set by combining QUaD with the expected results from a four year WMAP mission.

I use the Fisher matrix estimates given by equation 5.27 and the experimental parameters for QUaD and WMAP given in Table 5.5 to find the variance for a measurement of each of the parameters. For QUaD I assume that the minimum ℓ which can be measured is 25. To combine the results from the two experiments, I simply add the Fisher matrices from each experiment to find the total Fisher matrix and then invert this total matrix to find the parameter errors. For the QUaD-only Fisher matrix I assume that WMAP will provide a temperature map which can be used to make a TE spectrum by combining with the QUaD EE information. The combined Fisher matrix is therefore given by:

$$F_{ij}^T = \sum_{\ell} \sum_{XY} \frac{\partial C_{\ell}^X}{\partial \alpha_i} [\Xi_{\ell}^{MAP}]_{XY}^{-1} \frac{\partial C_{\ell}^Y}{\partial \alpha_j} + \sum_{\ell} \sum_{X'Y'} \frac{\partial C_{\ell}^{X'}}{\partial \alpha_i} [\Xi_{\ell}^{QU}]_{X'Y'}^{-1} \frac{\partial C_{\ell}^{Y'}}{\partial \alpha_j} \quad (5.38)$$

where X and Y can be TT, TE, EE or BB, but X' and Y' can only be TE, EE or BB as QUaD will not make a temperature map. For the combined Fisher matrix I also only use the TE constraints for QUaD at those multipoles which cannot be measured by WMAP (greater than $\ell = 850$).

The first step in the calculation is to calculate the parameter derivatives $\partial C_{\ell}^X / \partial \alpha$. CMBFAST is used to calculate the power spectra for the WMAP best fit parameters given in Table 1.1, but with the running of the spectral index set to zero and a tensor to scalar ratio of 0.01. A number of models are then run with a single parameter increased by 1% and then decreased by the same amount. The derivative can then be estimated numerically using:

$$\frac{\partial C_{\ell}}{\partial \alpha} = \frac{C_{\ell}(\alpha + d\alpha) - C_{\ell}(\alpha - d\alpha)}{2d\alpha}. \quad (5.39)$$

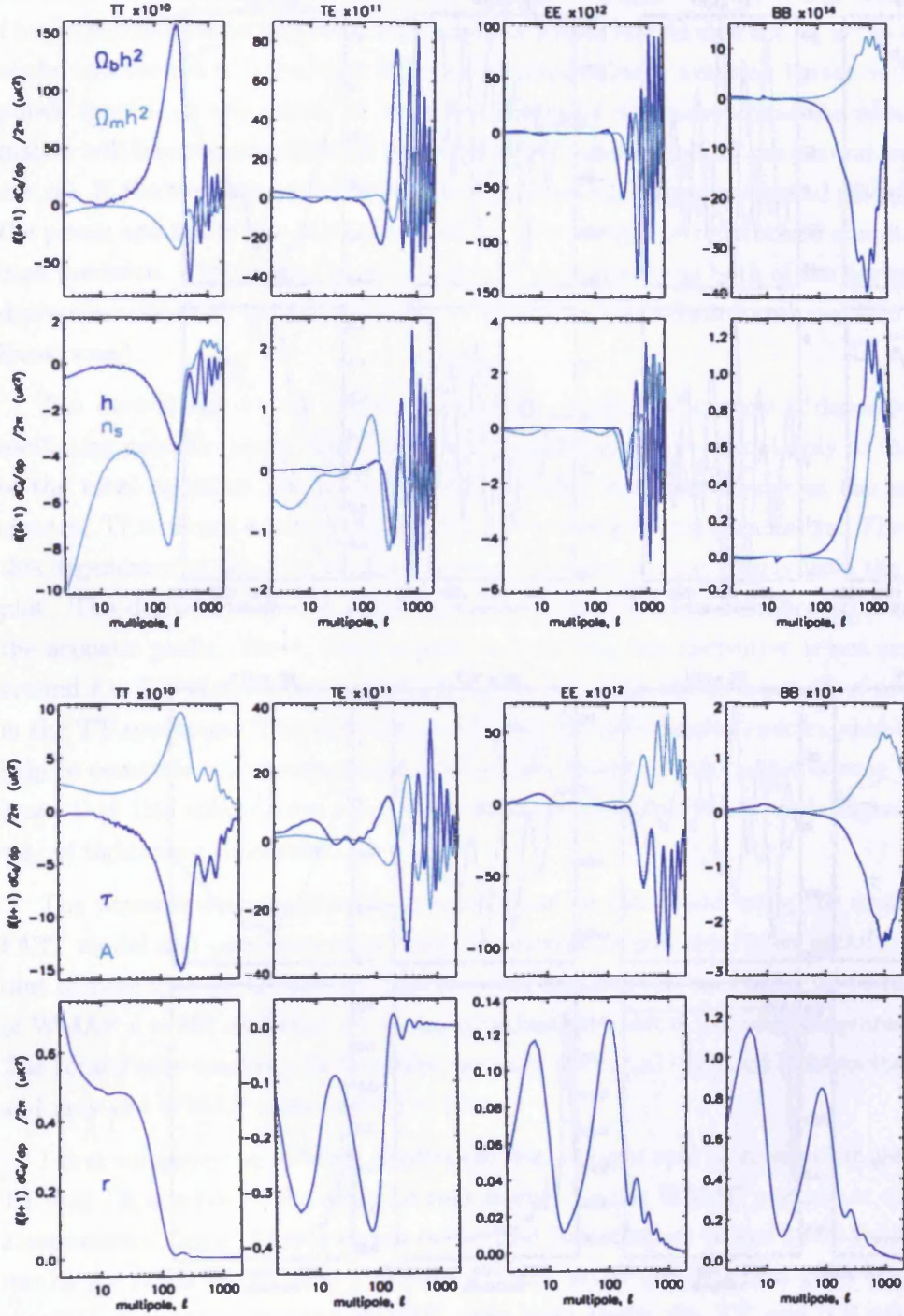


Figure 5.18: Parameter derivatives (log axes).

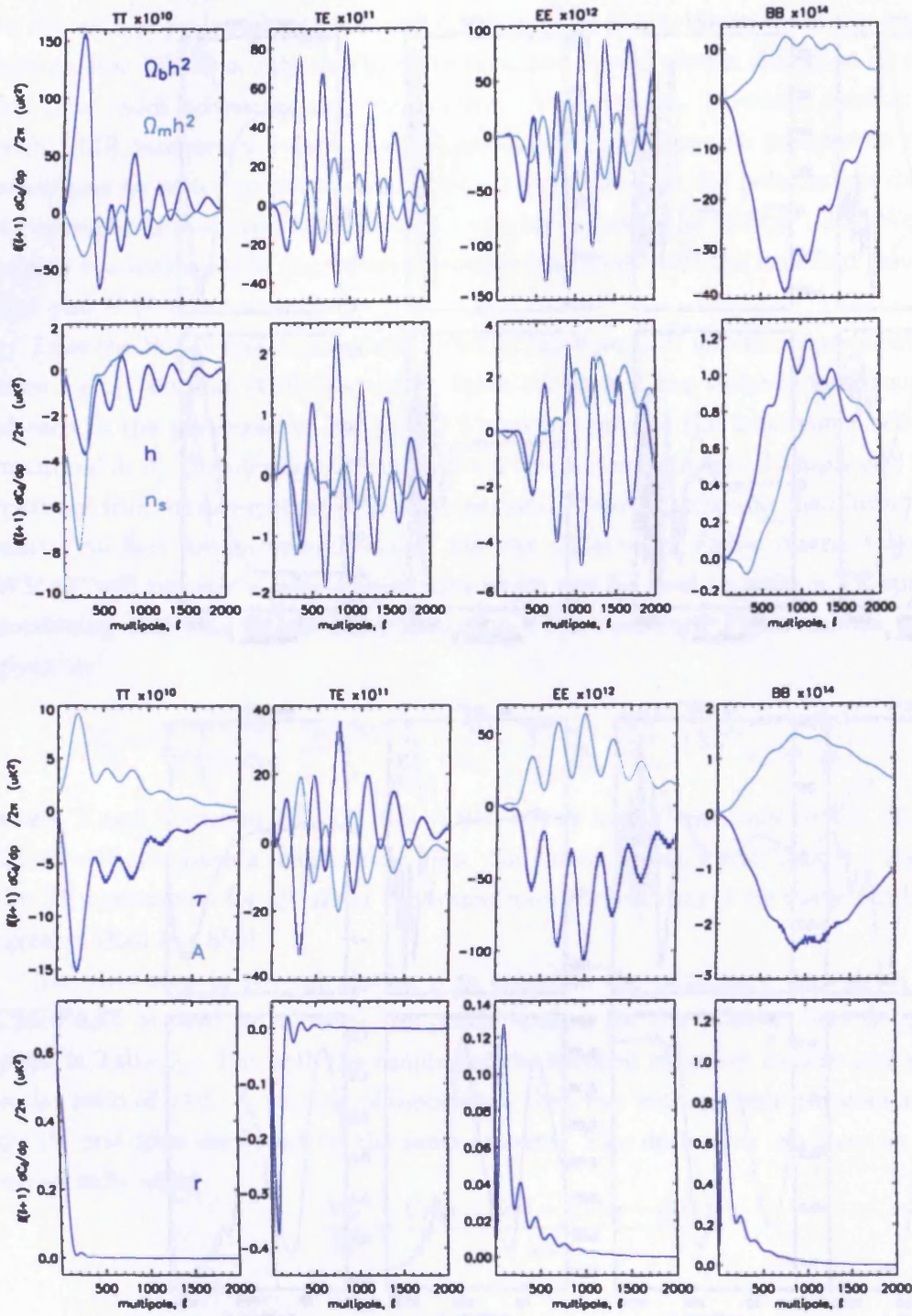


Figure 5.19: Parameter derivative (linear axes).

A useful interpretation of the Fisher matrix is given by Tegmark et al. (1997). The derivatives can be thought of as vectors of dimension $\ell_{max} - 1$ (where ℓ_{max} is the maximum ℓ in the summation in Equation 5.27) and the Fisher matrix element F_{ij} is the dot product of the two vectors $\partial C_\ell / \partial \alpha_i$ and $\partial C_\ell / \partial \alpha_j$. Each ℓ value is weighted by the variance in the power spectra at this point. If any two parameter derivatives have the same shape the matrix will become singular and so it is not possible to find the parameter covariance matrix. If the two derivatives have similar shapes the two cosmological parameters affect the power spectra in the same way and so they cannot be determined simultaneously to high precision. This results in an increase in the variance in both of the parameters. The derivatives obtained are shown in Fig. 5.18 (using logarithmic axes) and Fig. 5.19 (using linear axes).

The derivatives for all of the parameters except for r show a dependence on the oscillating acoustic peaks. For A and n_s this dependence is related only to the amplitude of the total signal as the derivatives have nearly the same shape as the actual power spectra. This causes a strong degeneracy between these two parameters. The breaking of this degeneracy at low ℓ by the polarization data can be seen clearly from the logarithmic plot. The derivatives of the other parameters have a more complicated dependence on the acoustic peaks. For r , there is information (i.e., the derivative is not zero) up until around $\ell = 500$ in the three polarization spectra compared to a cut-off of around $\ell = 30$ in the TT spectrum. This shows that TE and EE polarization spectra should be able to help to constrain r at intermediate multipoles. However, in practice cosmic variance will mean that this information cannot be obtained and that the B-mode signal is the only way of tightening constraints on r .

The power spectrum covariance matrix can be calculated using the unaltered CMB-FAST model and combined with these derivatives to give the Fisher matrix. It is important to note that for QUaD the TE spectrum can only be calculated up to the resolution of WMAP $\ell = 857$ and that all of the polarization spectra are only measured for $\ell > 25$. The total Fisher matrix will therefore use only the QUaD EE and BB spectra for $\ell > 857$ and only the WMAP spectra for $\ell < 25$.

I first compare the WMAP predictions for a single year of integration using only the TT and TE spectra to the actual errors quoted for the WMAP parameter constraints as a consistency check. This is shown in the first two columns (a and b) of Table 5.6. These results are taken from Table 1 of Spergel D.N. et al. (2003) which gives the parameters obtained from the one year WMAP data only (both the TT and TE spectrum, but not adding any external data) for a six parameter fit. The results agree for all of the parameters except for the total matter density, which is lower than the WMAP result. However this is not a problem as the Fisher matrix gives the smallest possible achievable

errors and a large number of factors could push the actual experimental value higher than this lower limit. If the EE and BB spectra are added to the Fisher matrix analysis (column (c)) the error on all the parameters is reduced slightly, with the biggest decrease occurring for τ and n_s . This shows that even though the one year WMAP data cannot make a high precision measurement of the E-mode spectrum, even a low signal to noise detection of the EE reionization bump can reduce the parameter errors. The estimate for the four year WMAP data (column (d)) reduces these errors by at least a further factor of two in each case. Column (e) shows the predicted results if the QUaD data is added to the four year WMAP data. For this six parameter fit the QUaD data only gives about a 25% decrease in the errors compared to the four year WMAP data.

Parameter	Value	Error				
		a	b	c	d	e
$\Omega_b h^2$	0.0224	0.001	0.001	0.0009	0.0006	0.0004
$\Omega_m h^2$	0.135	0.02	0.013	0.011	0.005	0.004
h	0.71	0.05	0.05	0.040	0.025	0.019
τ	0.17	0.08	0.078	0.043	0.021	0.018
n_s	0.93	0.04	0.035	0.03	0.016	0.012
A	0.83	0.1	0.12	0.076	0.034	0.027

a: actual 1yr WMAP errors (TT and TE) d: 4yr WMAP
b: 1yr WMAP (TT and TE only) e: 4yr WMAP +QUaD
c: 1yr WMAP (including EE and BB)

Table 5.6: Fisher matrix estimates if r is not included in analysis (six parameter fit) in the case of no foregrounds.

Parameter	Value	Error					
		f	g	h	i	j	k
$\Omega_b h^2$	0.0224	0.0008	0.0008	0.0009	0.0004	0.0004	0.0005
$\Omega_m h^2$	0.135	0.0064	0.0065	0.0070	0.0039	0.0043	0.0053
h	0.71	0.0367	0.0371	0.0410	0.019	0.021	0.027
τ	0.17	0.0212	0.0213	0.0238	0.0177	0.0184	0.0216
n_s	0.93	0.0262	0.0265	0.0294	0.012	0.013	0.018
A	0.83	0.034	0.034	0.0372	0.027	0.029	0.034
r	0.01	0.180	0.183	0.210	0.026	0.071	0.154
r	0.1	0.184	0.187	0.212	0.040	0.078	0.157

f: WMAP, no foreg. i: WMAP +QUaD, no foreg.
g: WMAP, optimistic foreg j: WMAP +QUaD, optimistic foreg.
h: WMAP, pessimistic foreg. k: WMAP +QUaD, pessimistic foreg.

Table 5.7: Fisher matrix estimates for different foreground models for a seven parameter fit.

Table 5.7 shows the four year WMAP (4yr WMAP) predictions and four year WMAP combined with QUaD (WMAP+QUaD) predictions for a seven parameter fit in which

the tensor to scalar ratio, r , is now added to the parameter set. The results are shown for the three different foreground models. The first point to note is that the foreground level has almost no effect on the WMAP data (columns (f-h)). This is because the WMAP data includes only a relatively low signal to noise ratio measurement of the EE spectrum (see Fig. 5.16) and so the detector noise will dominate over the foreground noise even for the pessimistic foreground model. For QUaD there is almost no increase in the errors for the optimistic model compared to the no foreground case in all the parameters except for r , which increases by a factor of 2.7. For the pessimistic model there is a slight increase in the errors for most of the parameters, but only by about 20%, but again there is a significant increase in the error on r of a factor of 6 over the no foreground case. The foregrounds level will therefore have a large impact on the ability of polarization data to constrain r . This is shown in Fig. 5.20 which shows how the two parameter error ellipse for the inflationary parameters r and n_s changes if the foregrounds levels are increased from no foregrounds to the pessimistic model.

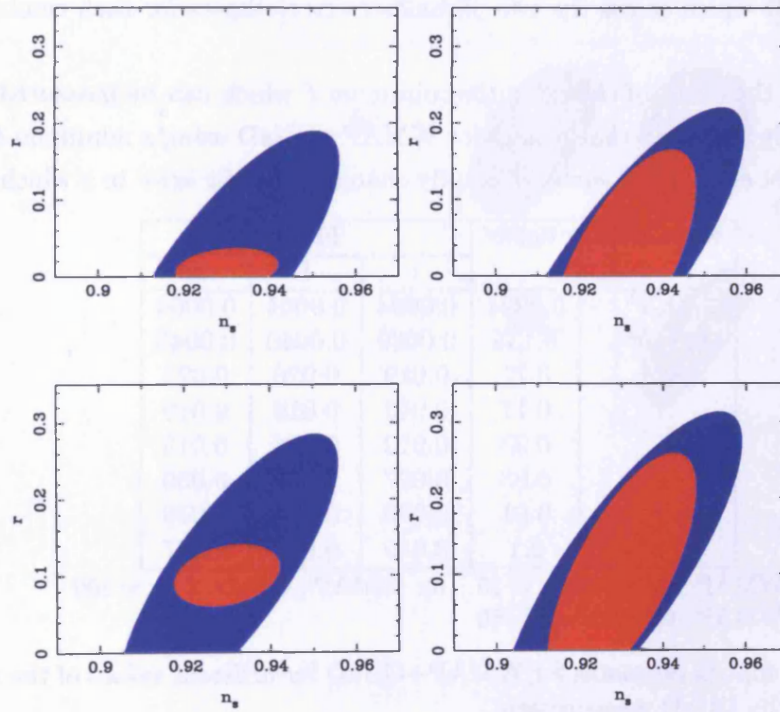


Figure 5.20: Marginalized $\Delta\chi^2 = 1$ error ellipses for r and n_s for a cosmological model with $r = 0.01$ (top) and $r = 0.1$ (bottom). The outer blue ellipses are predictions for four years of WMAP data and the inner red ellipses show the improvement which can be made by adding the QUaD data. The left-hand figures are for the no foreground case and the right-hand figures are for the pessimistic foreground model.

It is also interesting to compare the no-foreground estimate for a seven parameter

fit in Table 5.7 (columns (f) and (i)) to that for a six parameter fit excluding r in Table 5.6 (columns (d) and (e)). For WMAP, comparing models (d) and (f) shows that adding r to the fit increases the errors on the other parameters. However for QUaD (comparing models (e) and (i)) there is no noticeable change (the actual increase is around 1%). This is because there is not enough information in the WMAP data to constrain r , whereas the QUaD upper limit on the B-mode signal provides enough information to mean that adding this additional parameter does not increase the errors in the other parameters. Most importantly, comparing the WMAP only to QUaD+WMAP results in Table 5.7 shows that if r is included, QUaD can provide a significant decrease in the error for $\Omega_b h^2$, $\Omega_m h^2$, h , n_s and r , reducing the error by at least a factor of two in each case. The decrease in the error on r becomes even more significant if there are no foregrounds, increasing to a factor of 6. However for τ and A there is only a small decrease in the error (about 20%). This is because QUaD still provides no large scale polarization data which can be used to break the degeneracy between A and τ . The improvement in each of the parameter errors between the 4yr WMAP predictions and the QUaD+MAP prediction is shown in Fig. 5.21 which shows the two parameter error ellipses for each combination of parameters.

I also look at the effect of changing the minimum ℓ which can be measured from the QUaD data. Table 5.8 shows that results for WMAP+QUaD using a minimum ℓ of 25, 50 and 100 are almost exactly the same. The only change is for the error in r which increases

Parameter	Value	Error		
		i	l	m
$\Omega_b h^2$	0.0224	0.0004	0.0004	0.0004
$\Omega_m h^2$	0.135	0.0039	0.0040	0.0043
h	0.71	0.019	0.020	0.021
τ	0.17	0.018	0.019	0.019
n_s	0.93	0.012	0.012	0.013
A	0.83	0.027	0.030	0.030
r	0.01	0.026	0.033	0.076
r	0.1	0.040	0.047	0.087

i: WMAP+QUaD, $\ell_{min} = 25$ m: WMAP+QUaD, $\ell_{min} = 100$

l: WMAP+QUaD, $\ell_{min} = 50$

Table 5.8: Fisher matrix estimates for WMAP+QUaD for different values of the minimum observable ℓ for the QUaD measurement.

slightly for $\ell_{min} = 50$ and by over a factor of two for $\ell_{min} = 100$. This shows that the measurement of the B-mode spectrum below $\ell = 100$ where the gravitational wave signal can be measured contains most of the information on r . However, because for the QUaD data r is not degenerate with any of the other parameters increasing the minimum ℓ up to 100 (the worst case scenario for QUaD) does not affect any of the other parameters.

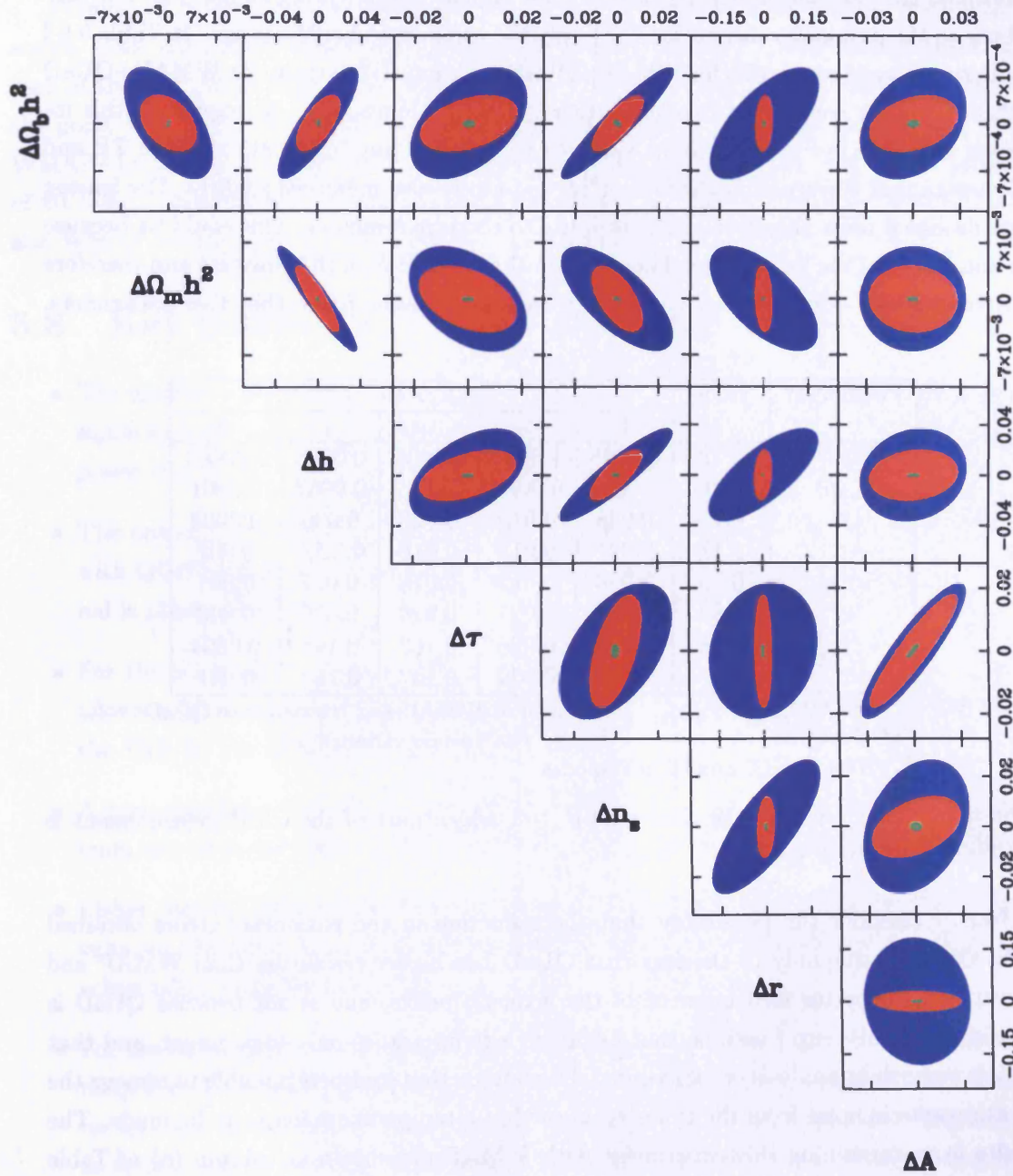


Figure 5.21: Marginalized $\Delta\chi^2 = 1$ error ellipses. The projection of the ellipses onto each axis gives the one sigma error of each for each parameter. The outer blue ellipses are predictions for four years of WMAP data and the inner red ellipses show the improvement which can be made by adding the Quid data. The green point at the centre of each ellipse is the cosmic-variance-limited error ellipse.

To determine if the lensing signal plays any part in reducing parameter errors I also performed the calculation without the B-mode signal. If the lensing signal does not contribute to the parameter estimation then only the error on r should change. In Table 5.9 I compare the previous results for WMAP+QUaD (column (i)) to those for WMAP+QUaD with no B-mode contribution to the Fisher matrix (column (n)). As expected, this increases the error in r as the cosmic variance will swamp any information in the TE and EE spectra, but the errors in $\Omega_b h^2$, $\Omega_m h^2$, h and n_s are also increased slightly. The lensing B-mode signal must therefore also contribute to these parameters. This could be because the amplitude of the lensing signal depends on the expansion of the Universe and therefore constraining this amplitude breaks any degeneracies between h and the other parameters.

Parameter	Value	Error				
		f	i	n	o	p
$\Omega_b h^2$	0.0224	0.0008	0.0004	0.0005	0.0005	0.00004
$\Omega_m h^2$	0.135	0.0064	0.0039	0.0052	0.0057	0.0001
h	0.71	0.038	0.019	0.026	0.030	0.0003
τ	0.17	0.021	0.018	0.018	0.0200	0.002
n_s	0.93	0.026	0.012	0.018	0.017	0.001
A	0.83	0.034	0.027	0.029	0.030	0.003
r	0.01	0.180	0.026	0.163	0.148	0.0004
r	0.1	0.184	0.040	0.167	0.152	0.001

f: 4yr WMAP only

o: WMAP and temperature QUaD

i: WMAP+QUaD

p: cosmic variance limit

n: WMAP+QUaD, excluding B-modes

Table 5.9: Fisher matrix estimates used to test which part of the CMB measurement is providing information.

Next I consider the possibility that the reduction in the parameter errors obtained using QUaD is due only to the fact that QUaD has higher resolution than WMAP and so can make a better measurement of the acoustic peaks, and is not because QUaD is polarized. In this case I assume that QUaD is a temperature-only experiment, and that there is some data analysis or experimental technique that makes it possible to remove the $1/f$ atmospheric noise from the timestream so that a temperature map can be made. The results from combining this experiment with WMAP are shown in column (o) of Table 5.9. Comparing these results to those in column (f) for the WMAP only results, this extra data reduces the errors in $\Omega_b h^2$ and n_s , which is to be expected as these parameters are very sensitive to the position and relative amplitudes of the acoustic peaks. However, the other parameter errors are not reduced significantly. Comparing these results to column (i) for polarization-sensitive QUaD measurements shows that in all cases more information is added if QUaD measures the polarization spectra than if QUaD were to make only total

power observations.

Finally, in column (p) of Table 5.9 I shown the cosmic-variance-limited parameter errors. This calculation assumes that a cosmic variance limited (CVL) measurement of each of the four power spectra in the range $\ell = 3 - 2000$ has been made. This emphasizes the point that QUaD is still far from this fundamental limit. For most parameters, the WMAP+QUaD constraints are a factor of 10 away from the CVL error, and for r a factor of 60 away. These level of these constraints compared to those achievable with QUaD and WMAP is shown by the small green ellipses in Fig. 5.21.

5.8 Key points

- The optimal survey area to use for QUaD has been investigated by maximizing the signal to noise ratio (SNR) for a measurement of the amplitude of each polarization power spectrum.
- The optimal area for E-modes and B-modes is different. For the scales observable with QUaD, the E-mode signal is cosmic-variance-limited where-as the B-mode signal is pixel-noise-limited.
- For the South Pole a compromise is to use a single 300 deg^2 patch of sky. This allows a detection of the B-mode signal to be made without significantly reducing the SNR for the E-mode measurement.
- A high-significance measurement of the acoustic peaks in the E-mode power spectrum can be made with QUaD, as well as a detection of the B-mode lensing signal.
- Fisher matrix parameter constraints have been used to compare the expected results for the four year WMAP data combined with QUaD observations to those achievable using WMAP alone.
- For the seven parameter fit considered here, QUaD can make a factor of 2 improvement over WMAP alone for most of the parameters. For r , this improvement could be up to a factor of 6 if there is very low foreground contamination. However, as QUaD cannot measure the reionization bump, only a 20% improvement can be made for A and τ .

Chapter 6

Observing strategy

In this Chapter I investigate the best observing strategy to use for QUaD. I discuss the strategy for both the South Pole and Chile sites as most of this work was carried out before a final decision on the site had been made. I look at two different problems: the position of the feeds on the focal plane and the scanning strategy. In the final section I summarize the observing strategy which will be used by QUaD at the South Pole.

6.1 Focal plane layout

In this section we discuss the design for the layout of the detectors on the focal plane. As discussed in Chapter 2, QUaD will observe simultaneously at two frequencies with 12 feeds at 100 GHz and 19 feeds at 150 GHz. This is done by arranging all of the 31 detector on the same focal plane. The best position and orientation of the detectors depends on a number of different factors. We will discuss each of these factors and then go on to show how the QUaD focal plane gives the best compromise between each of these effects.

6.1.1 Factors to consider for focal plane layout

Measuring Q and U

A single PSB will measure an output signal, S , which is a combination of the three Stokes parameters, T , Q and U given by:

$$S = \frac{1}{2}(T \pm (Q \cos(2\alpha) + U \sin(2\alpha))), \quad (6.1)$$

where α is the angle between the axis of the detector and the reference direction for the signal being measured. For each feed the T component can be removed by simply differencing the two PSBs in each feed orientated at 90° to each other as the unpolarized intensity gives an equal contribution to each PSB (assuming the gains of the two detectors can be matched as will be discussed in 7). However, the differenced signal will still be a

combination of Q and U. This means that at least two measurements of the same pixel on the sky are needed to measure Q and U individually. The measurements should ideally be made in quick succession so that the atmospheric and instrument contamination does not change between each measurement. For QUaD the most useful strategy would be to continuously rotate the waveplate fast enough that each pixel is sampled with the waveplate in a number of different orientations as the telescope scans across the sky. This will continuously vary the polarization of the radiation incident on the detector in an easily measureable way. However, as discussed in Section 6.2, it is very difficult to produce continuous rotation without excessive extra noise and it was decided that this would not be used for QUaD. The alternative is to rotate the waveplate at the end of every scan. If the same strip of sky is scanned again straight away with a different waveplate orientation, Q and U can be found if the atmosphere does not change between the scans.

However, it is not certain that the atmosphere will be stable enough for this to be done. Another alternative is to position at least two PSBs with different orientations along the same line of pixels. If the telescope is scanned with the focal plane in the correct orientation then Q and U can be obtained as long as the relative calibration between the different feeds is known accurately. This method has been used by BK2 and will be used by Planck. Couchot et al. (1999) have shown that the smallest possible errors on Q and U for a combination of n separate PSBs are obtained if the PSBs are orientated at an angle π/n to each other i.e. if they are evenly spaced in orientation. For measuring Q and U with a pair of feeds this corresponds to the PSBs being orientated at 45° to each other.

The main consequence of this for the focal plane layout is that **at least two feeds of each colour with different orientations must scan across the same positions on the sky for each scan.**

Systematics

The optical aberrations will be more severe for positions away from the centre of the focal plane. The image for the outer detectors will therefore still suffer from aberrations. The instrumental polarization signal will also be worst at the edges of the focal plane as the path of the radiation to these positions will not be completely symmetric. This means that the focal plane should be as tightly packed as possible to avoid the edges of the focal plane.

The instrumental polarization will either be tangential or parallel to the radial line from the centre of the focal plane to the centre of the feed. This provides a way to remove the instrumental polarization, for if the PSB pair is orientated at 45° to this direction an equal instrumental polarization signal will be measured by each PSB and so it will

not contaminate the differenced signal. However, this will not work if the waveplate is used since when the waveplate is rotated the instrumental polarization angle will also be rotated and so the orientation of the PSB will no longer be correct. Orientating the PSBs at 45° to the radial lines would also make it difficult to have detectors separated by equal differences in orientations positioned along a line of PSBs.

Even sky coverage and fast mapping speed

It is useful to have a map with the same sensitivity across the sky. If the integration time per pixel across the map is patchy then it will not be possible to compare the polarization level on different angular scales without having to down-grade the sensitivity in the over-sampled regions and which would waste integration time. To achieve this it is preferable to arrange the feeds so that there is as little space as possible between scans made by separate rows of feeds. This makes it easier to map complete areas of sky. For Chile there is also the problem of sky rotation which will mean that if it takes too long to cover a complete strip then the sky will rotate enough so that scans at constant elevation will no longer be parallel to each other and so will not give even sky coverage. As QUaD measures two frequencies simultaneously, it is also useful to be able to make maps of the sky with even coverage in both frequencies at the same time.

As discussed in Chapter 2, the QUaD beams will have roughly Gaussian profiles. The ideal situation would be if the telescope could scan across the sky and observe a full strip of sky with no gaps between the scans made by individual horns. For this to be the case the centre of the scan made by adjacent beams must be separated by less than half the FWHM beam size. This is shown in Fig. 6.1. For a horn-filled array this is not always

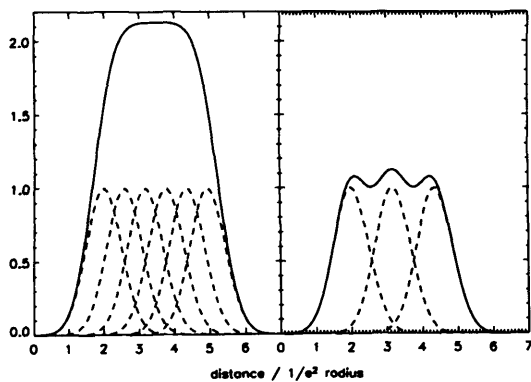


Figure 6.1: Coverage for a line of overlapping Gaussian beams. In left figure the beam centres are separated by $1/2$ a FWHM beam width required for an even scan. In the right figure the centres are separated by a full FWHM beam width which gives uneven coverage.

possible as the actual size of the beam on the sky compared to the minimum distance between adjacent horns, imposed by the physical size of the horns, may be too small. For an unpolarized, single frequency array, the usual strategy is to pack the horns as close together as possible (Griffin et al. (2002)). For example in SCUBA, the hornsize is

$h_{SC} = 2F\lambda$, where F is the focal ratio of the telescope ($F = f/D$, the ratio of the focal length and the telescope aperture), and the FWHM beam size, θ_{SC} , is $\theta_{SC} = \lambda/D$ giving an effective beam size at the mouth of each horn of $F\lambda$, half the hornsize. If the array is scanned at an angle of 14° to the lines of horns, it is possible to fully sample the sky with this layout. This is shown in Fig 6.2.

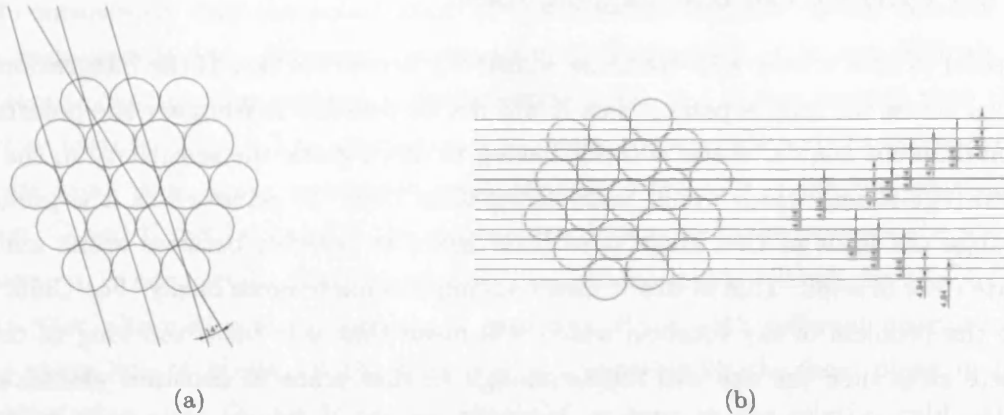


Figure 6.2: (a) Hexagonal close packed array layout used in SCUBA. The 14° scanning angle shown here allows a fully sampled strip of sky to be made in a single scan. (b) Scan lines made by SCUBA horns, the distance between scan lines made by adjacent horns is always less than half the FWHM beam size. In this diagram the horns have an arbitrary size of 20 units, so half the FWHM beam size is 5 units. Note that only two pairs of horns have overlapping scans, shown by the slightly darker lines.

For QUaD the horns are a bigger fraction of $F\lambda$, $h_{QU} = 3.25F\lambda$. However, the beam size on the sky is also broader due to the high level of edge taper so that $\theta_{QU} = 1.7\lambda/D$. This gives a beam size which is slightly over half the hornsize. A close packed hexagonal array of either the 150 GHz horns or the 100 GHz horns would give a fully sampled strip for a scan angle of 14° , as shown in Fig. 6.3 (dashed red line). However, due to the filter caps on the QUaD horns the size is increased by a further 1.5 mm. The minimum separation between adjacent scans is then slightly over half a FWHM beam width, as shown by the solid red line in Fig. 6.3. There are also two other problems with scanning in this way. Firstly, if we scan at this angle it is not possible to scan over the same line in the sky with more than one horn across the whole strip. Secondly, QUaD will have both detector colours on the same focal plane, so it would only be possible to scan in this way for one of QUaD frequencies, but not for both at the same time. In SCUBA this problem is overcome by using two separate focal plane arrays and focusing half the radiation onto each array using a dichroic beam splitter. However, this is not an option for QUaD as it would break the symmetry of the design and so could potentially create large polarization

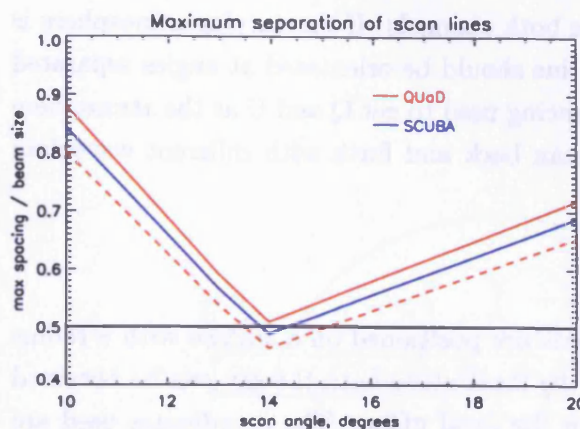


Figure 6.3: Maximum distance between adjacent scan lines if the close packed hexagonal array is scanned across the sky at different scan angles for QUA (red, solid line with filter caps, dashed line without) and SCUBA (blue). For a fully sampled strip of sky, the maximum separation must be below $1/2$ a beam width, i.e. below the black line on the diagram.

systematics.

6.1.2 Possible designs for the focal plane layout

An initial design for the focal plane is shown in Fig. 6.5. In this design, the horns are packed as close together as possible to reduce the optical aberrations at the edges of the array. In order to scan lines of horns across the sky so that different detectors on the same line can be at different orientations, the array would be scanned in the horizontal direction. For this layout it takes 5 scans, moving down $1/2$ a beam size between each scan, to fully cover a strip of sky at 150 GHz. However, this does not cover a strip at 100 GHz as there are big gaps in the 100 GHz as shown in Fig. 6.5. Also the coverage at this frequency is uneven as the lines traced out by the horns are not separated by a constant amount. A modification to this design is shown in Fig. 6.6. The 100 GHz horns are shifted outwards slightly so that the scan lines from each row of horns are evenly spaced. However more scans are needed to cover a strip at 100 GHz than at 150 GHz.

Fig. 6.7 shows a design in which the 100 GHz and 150 GHz horns are arranged so that the separation between scan lines in both channels are equal. This is done by placing all of the horns at the centres of the circles which would be produced in an array of close packed 100 GHz horns. A strip in both channels can then be covered after 6 scans. In Chile this is undesirable as the sky rotation may not be negligible in the time it takes to cover 6 scans. However for the South Pole this effect will not be important as there is negligible sky rotation.

The choice of design depends on which factor is the most important. If instrumental polarization is the biggest problem, then first design with close packed horns is the best in order to move the outer horns away from the edges of the focal plane. High instrumental polarization would also mean that it would be preferable to orientate the PSBs radially to try to reduce this effect. However, if the IP is not the most important factor, the final

design is the best as it is easier to fully sample both channels. If the varying atmosphere is the biggest concern, the PSBs along a scan line should be orientated at angles separated by 45° as this will be the main level of differencing used to get Q and U as the atmosphere is likely to change in the time it takes to scan back and forth with different waveplate positions.

6.1.3 Projection onto the sky

The focal plane surface is curved, so the horns are positioned on a surface with a radius of curvature of 175 mm. The projection of the focal plane onto the sky can be obtained using the coordinates of the PSB centres on the focal plane. The coordinates used are the radial distance from the centre of the focal plane along the curved surface, r , and the radial angle, θ . We assume that the projection leaves θ unchanged and that r scales as approximately $\phi = (FD)^{-1}r$, where ϕ is the angular size on the sky, F is the focal ratio of the telescope and D is the diameter of the primary mirror. For QUaD, $F = 2.33$ and $D = 2640$ mm giving $(FD)^{-1} \sim 0.559''\text{mm}^{-1}$. It is also possible to use an optics software package (ZEMAX) to calculate the exact projection taking into account all of the optical components of the telescope. This has been done by other members of the QUaD team (Cahill G. (2003)). The projection obtained using the ZEMAX model is shown in Fig. 6.4. The focal plane can only be scanned in the four directions shown as this keeps the detectors in the correct orientations to measure Q and U along a line of horns.

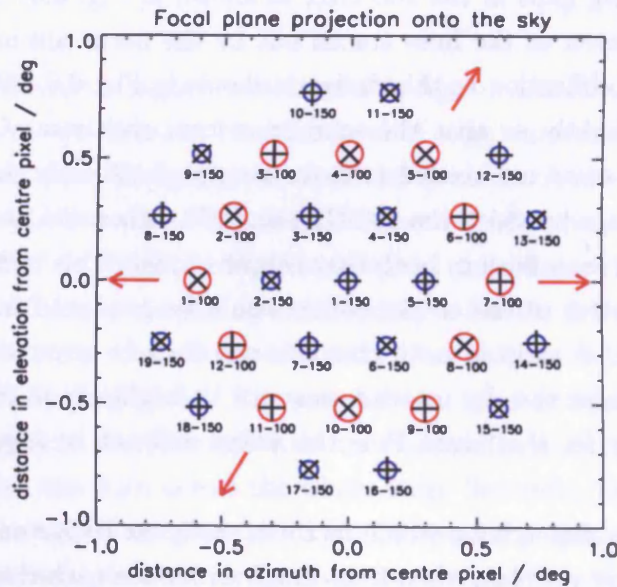


Figure 6.4: Focal plane projection onto the sky and pixel orientations.

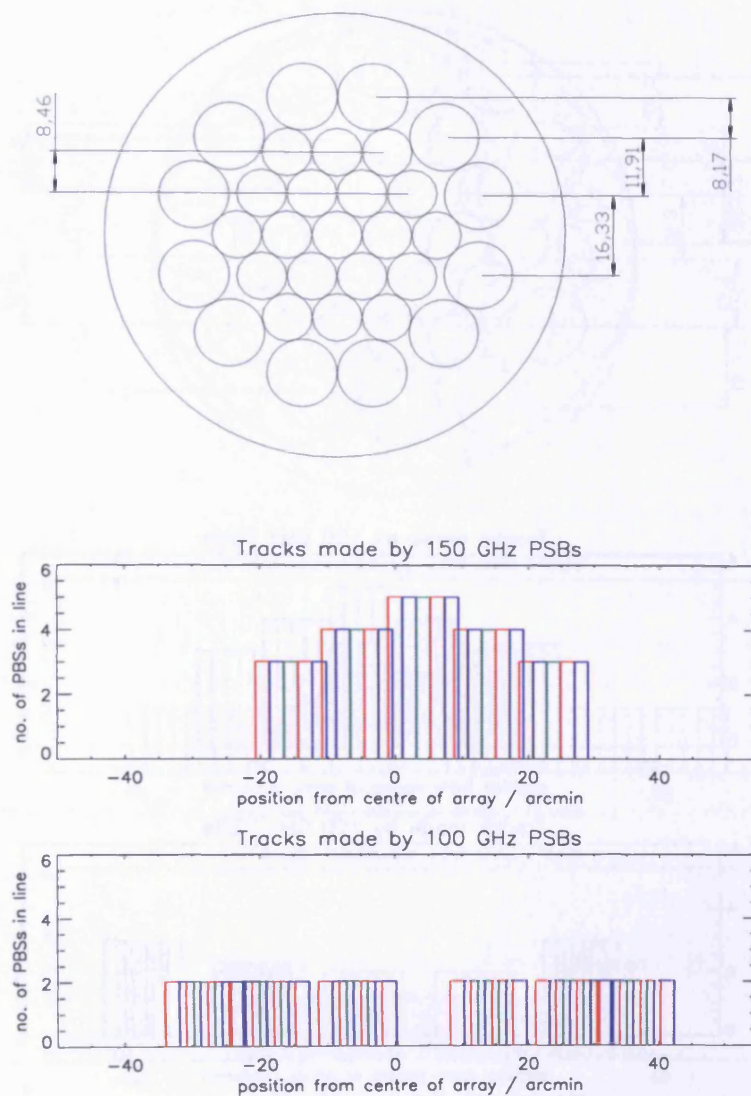


Figure 6.5: Close packed hexagonal focal plane layout. The lower figure shows the 1/2 FWHM width tracks which would be made by each line of horns for the two channels.

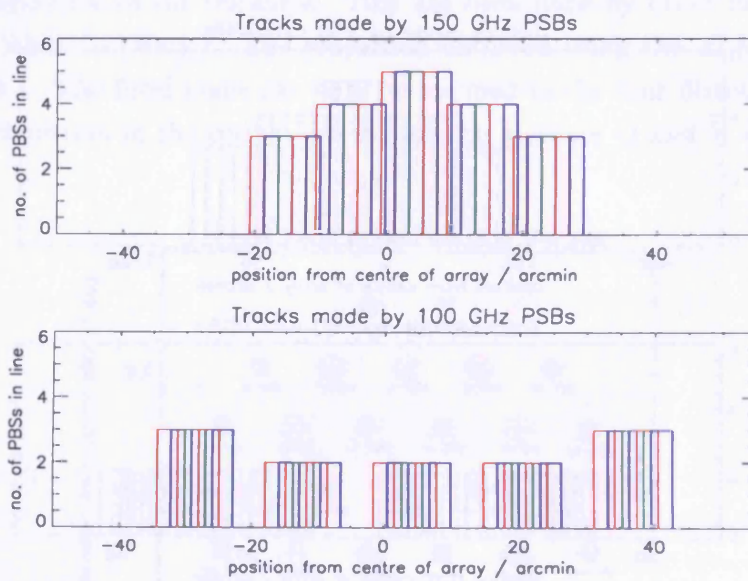
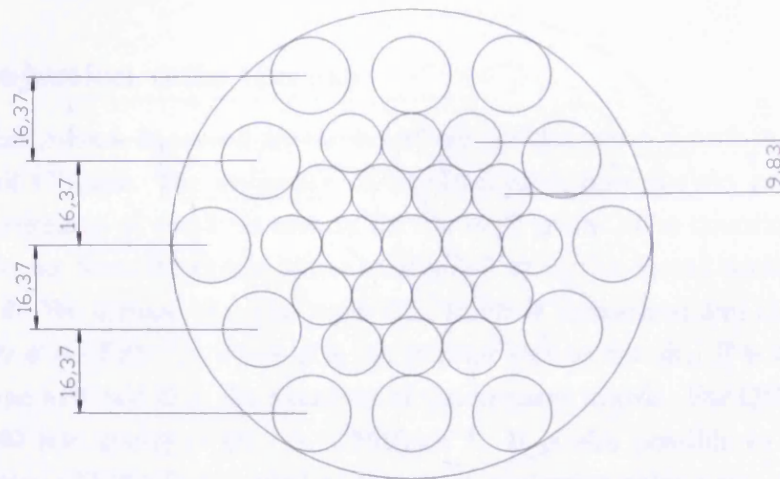


Figure 6.6: As Fig. 6.5 for close packed hexagonal with 100 GHz horns moved so evenly spaced.

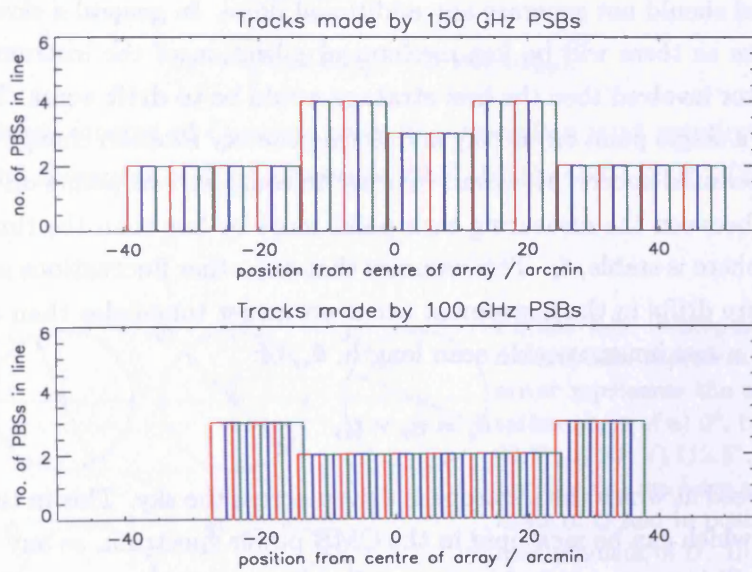
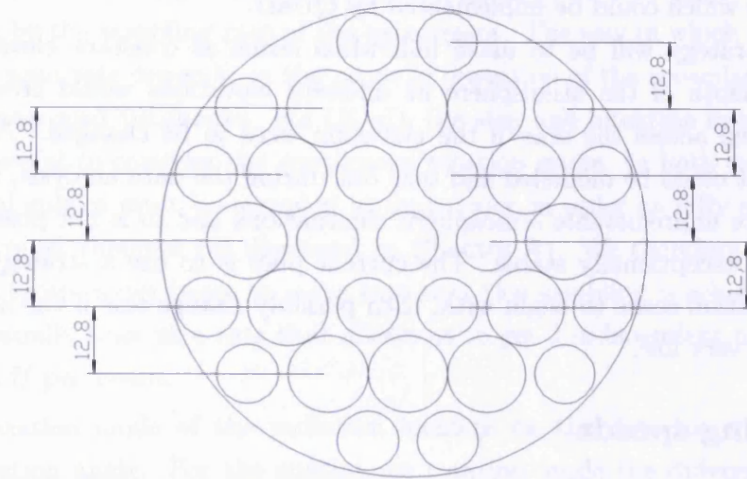


Figure 6.7: As Fig. 6.5 for array with both colours following the same scan lines

6.2 Scanning strategies

In this Section we investigate different scanning strategies which could be used at the Chile site and at the South Pole. We first discuss the specifications which must be met in order that useful maps of the sky can be made and then go on to discuss a number of possible strategies which could be implemented by QUaD.

The default strategy will be to make individual scans at constant elevation. The variation in the depth of the atmosphere at different elevations would create varying atmospheric loading across the scan if the elevation were to be changed. Although in principle this effect could be modelled and take out during the data analysis, this will be difficult if there are unpredictable atmospheric fluctuations and so is not possible unless the atmosphere is exceptionally stable. The current plan is to use a strategy involving only constant elevation scans to begin with, then possibly change this if the atmospheric noise proves to be very low.

6.2.1 Scanning speeds

The key feature of the scan strategy is that it should provide even coverage of the required patches of sky and should not generate any additional noise. In general a slower scan will generate less noise as there will be less mechanical vibration of the instrument. If this were the only factor involved then the best strategy would be to **drift scan**. This involves simply staring at a single point on the sky and letting the sky rotation change the position observed on the celestial sphere. However, in order to compare two points on the celestial sphere, the time between the measuring each point must be less than the time-scale over which the atmosphere is stable, t_s . This assumes that any other fluctuations such as those due to temperature drifts in the instrument occur on longer timescales than atmospheric drifts. This gives a maximum useable scan length, θ_s , of:

$$\theta_s = u_s \times t_s, \quad (6.2)$$

where u_s is the speed at which the telescope is driven across the sky. This in turn gives the lowest multipole which can be measured in the CMB power spectrum, as any information on larger scales will be contaminated by atmospheric noise:

$$\ell_{min} = \frac{180^\circ}{\theta_s}. \quad (6.3)$$

The atmosphere at the two observing sites is stable for around 1-2 minutes (Lay and Halverson (2000)). The rotation of the Earth gives a scanning speed of 0.25 deg/min and so the maximum scan length will be 0.5° . This corresponds to a minimum multipole as high as 720 which would mean that the first peaks in the E-mode spectrum could not be

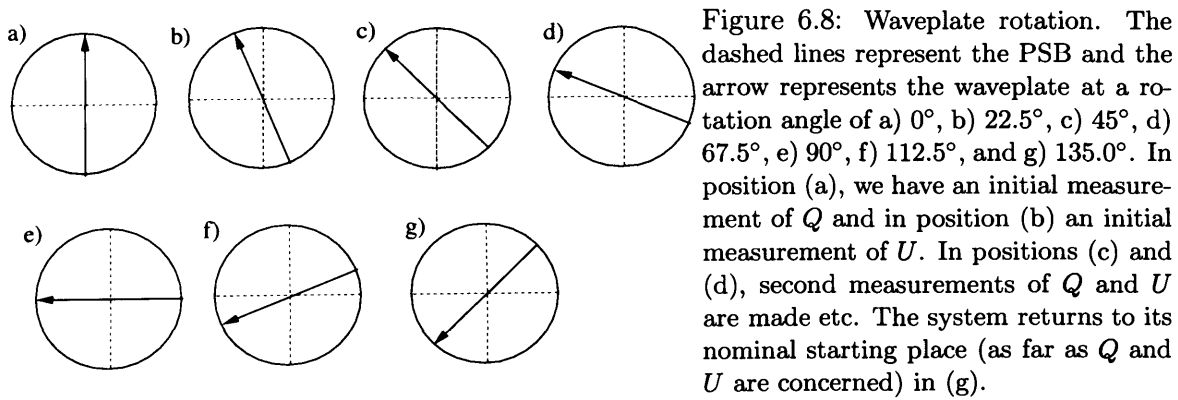
measured and would rule out the possibility of detecting the B-mode gravitational wave signal. Clearly, the telescope must be driven across the sky in order to measure the lower multipoles. This is called **raster scanning**.

The higher the scan speed, the larger the maximum measureable angular scale. However the telescope is limited mechanically to a scan speed below 1.25 deg/s. The scan speed is also limited by the sampling rate of the experiment. The way in which this determines the maximum scan rate depends on the mode of operation of the waveplate, **continuous rotation** or **step and integrate**. For QUaD, the step and integrate mode will be used, but it is still useful to consider the continuous rotation mode. In both cases, each beam on the celestial sphere must be sampled at least twice in order to fully sample the map due to the Nyquist theorem (as discussed in Chapter A). We therefore choose to set a minimum of 3 samples per beam to make sure that this sampling is achieved. For QUaD we need to spatially scan at a rate that allows us to get 3 independent measurements of each of Q and U per beam.

The polarization angle of the radiation incident on the detector will be twice the waveplate rotation angle. For the continuous rotation mode the differenced signal will vary with the waveplate rotation angle as:

$$S_d = Q \cos(4\alpha_{wp}) + U \sin(4\alpha_{wp}). \quad (6.4)$$

Independent measurements of Q occur when the waveplate is at rotation phases of 0° , 45° , and 90° and measures of U at phases of 22.5° , 67.5° , and 112.5° . This is shown in Fig. 6.8.



The waveplate must therefore rotate by $3/8$ of a full revolution in the time it takes to move a distance of one beam across the celestial sphere so that we sample each Stokes parameter three times per beam. If T_{wp} is the rotation period of the waveplate the scan

rate will be given:

$$u_s = \frac{8}{3}\theta_b f_{wp}, \quad (6.5)$$

where $f_{wp} = 1/T_{wp}$ is the waveplate rotation frequency. The required waveplate rotation frequency is determined by the sample rate. To make sure the signal is not under sampled at least 3 samples should be made in the time taken for the waveplate to rotate from a measurement of Q to a measurement of U. This gives 3 samples per 1/16 of a revolution so that $f_s = 48f_{wp}$ giving:

$$u_s = \frac{1}{18}\theta_b f_s. \quad (6.6)$$

The expected sample rate for QUaD is around 20 Hz, so the maximum scan speed which will fully sample the sky will be 4.8 deg/min. As long as we scan **slower** than this the required sampling on the sky will be made.

For the step and integrate mode Q and U will be measured independently on separate scans, so waveplate is set to a constant rotation angle for each scan. The time to travel a distance of one beam will therefore simply be the time needed to take 3 samples giving:

$$u_s = \frac{1}{3}\theta_b f_s. \quad (6.7)$$

This gives a maximum scan speed of 35 deg/min. A factor of 2 in the increase in this scan speed compared to the continuous rotation mode is due to the fact that for this mode we need to make twice as many scans to measure both Q and U. The remaining factor of 3 difference comes from sampling the signal 3 times more often in the continuous rotation mode as we would like to be able to reconstruct the signal due to the modulation of the waveplate to use to test for systematics. In the step-and-integrate mode the waveplate modulation occurs over a much longer timescale and so there is no need to increase the number of samples per measurement of Q and U over that needed to make 3 samples per beam.

The speeds quoted so far give the angle moved in azimuth per unit time. It is useful to keep this speed constant along a scan as this determines how fast the motor physically needs to rotate to drive the telescope. If this speed is varied it will change the amount of vibration. It will also change the speed of the scan with respect to the motion of the atmosphere which will vary the atmospheric noise¹. However, this needs to be translated into the angle actually moved on the celestial sphere. This is illustrated in Fig. 6.9. The relation between the two angles (marked *az* and *angle* on the diagram) can be found by equating two expressions for the actual distance moved on the celestial sphere, *s*:

$$s = az \times R \cos(el)$$

¹At the South Pole the wind is always from the same direction.

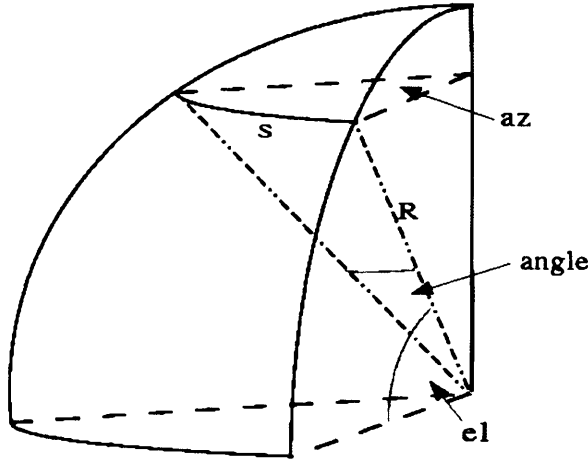


Figure 6.9: Conversion from angle moved in azimuth (az) to angle moved on celestial sphere ($angle$).

$$s = R\theta$$

giving:

$$\theta = az \times \cos(el) \quad (6.8)$$

where R is the distance to the celestial sphere, az is the angle moved in azimuth, el is the elevation of the scan and θ is the angular distance moved across the celestial sphere. Equations 6.6 and 6.7 now become:

$$u_s = \frac{\theta_b f_s}{n \cos(el)} \quad (6.9)$$

where $n = 18$ for continuous rotation and $n = 3$ for the step and integrate mode. The fastest allowed scan rate will therefore vary with elevation, being greater at higher elevations. There are two possibilities, either we change the scan rate for each different elevation used, or we always scan at the maximum allowed rate for the scan at the lowest elevation, over-sampling the scans at higher elevation.

Minimum multipole coverage for QUaD

Given these constraints on the maximum scan speed, the largest angular scale measurable from the South Pole with QUaD can now be calculated. The effective sample rate is determined by the cut-off for the low-pass filter in the electronics chain (see Section 2.2.5). For the QUaD filter response begins to drop off at 10 Hz (Hinderks (2003)) and so the effective sampling rate will be 20 Hz. The actual sampling rate will be around 50 Hz. For the step-and-integrate mode:

- Equation 6.9 gives a scan rate for the minimum elevation of 50° of 0.72 deg/s (using $\theta_b = 4.2 \text{ arcmin}$ and $f_s = 20 \text{ Hz}$).
- It would be useful to also make scans at half this scan rate as a systematic test, this gives a scan rate of 0.35 deg/s .
- The maximum time we can scan for is one minute. In this time we have to scan forwards and backwards in order that both Q and U can be measured. This gives a maximum scan length of 10.5 deg .
- The minimum multipole that can be measured is therefore $\ell_{min} = 180/10.5 = 17$.

For the continuous rotation mode there is an extra factor of 6 in Equation 6.9, but only a single scan is needed to measure Q and U so this doubles the scan length. The minimum multipole is therefore three times as big as for the step and integrate mode, giving $\ell_{min} = 50$. In the calculations in Chapter 5 I assume the step and integrate mode will be used by QUaD and so take a minimum ℓ of 25 to be sure that I definitely do not include any multipoles that QUaD cannot measure.

6.2.2 Z-axis rotation

The Z-axis will be used to help to characterize the instrumental polarization. The telescope is designed to be axially symmetric so the IP signal detected will not change if the telescope is rotated (assuming that the polarization response of each of the detectors is the same). If we rotate the telescope we change the polarization angle of the source with respect to the detector, but the polarization angle of the IP with respect to the detector remains the same. This allows the IP to be distinguished from the true signal. This procedure works well for the central detector since if we stare at a point on the sky and rotate around the z-axis the same detector will be able to observe the source at a number of different angles. However, for the other detectors this is not ideal, as a different detector will be looking at the source after the telescope has been rotated. The new detector may have a different polarization response and may be orientated at a different angle to the IP signal.

Ideally we would like to rotate the source polarization angle without changing the detector being used. This can be done using the waveplate. If the waveplate is positioned so that it intercepts the optical path of all of the detectors, rotating the waveplate will change the polarization angle of the source for each detector without changing the point on the sky being observed. To characterize the IP, the waveplate should be placed as near to the start of the optics chain as possible, as any IP generated before the waveplate will be rotated along with the sky signal. Unfortunately the size of the waveplate is restricted

as it is difficult to manufacture a large piece of material with the required homogeneity and to support and rotate a large optical element. This means it must be placed at a point in the optics chain where the column of rays heading towards the focal plane is quite narrow, and where it can be supported without blocking the incoming radiation or breaking the symmetry of the telescope design. The QUaD waveplate is therefore positioned after most of the imaging optics. This means any unwanted polarized signals produced before this point will also be rotated.

It is not possible to rotate the instrument around the z-axis after each scan as too much time would be wasted waiting for the liquid cryogenics to settle down after each rotation. The number of scans to make before the telescope is rotated will be one of the parameters in the QUaD scan strategy.

6.2.3 Possible scan strategies

The method used to investigate potential strategies is to define a strategy in terms of the azimuth and elevation (horizontal coordinates) at each time during the night, and to convert this to the path taken on the celestial sphere in right ascension and declination (equatorial coordinates). Declination is defined as the angle North (positive) or South (negative) from the celestial equator. Elevation is defined in the same way with respect to the Earth's equator. The azimuth is defined as the angle of a point from North moving in a clockwise direction towards East. To find the right ascension of a point, a local measure of its change in position during the night on the equatorial grid is needed. This is given by the hour angle, the angle from the observer's meridian (the great circle passing through the observer's zenith and the North and South poles) to the hour circle of the point (the great circle passing through the point and the North and South poles). This is related to the right ascension through the sidereal time, Θ , at the site, which is the hour angle of a specifically chosen point on the celestial equator, the vernal equinox (this is defined as the point where the path of the Sun crosses the equator). The relationship is given by:

$$\text{ra} = \Theta - \text{h}. \quad (6.10)$$

The two coordinate systems can be related by the standard relation for spherical triangles for the triangle shown in Fig. 6.10 and Fig. 6.11. The angles in the spherical triangle shown in Fig. 6.10 are related by the formulae:

$$\sin(a) \cos(B) = \cos(b) \sin(c) - \sin(b) \cos(c) \cos(A) \quad (6.11)$$

$$\cos(a) = \cos(b) \cos(c) + \sin(b) \sin(c) \cos(A) \quad (6.12)$$

$$\sin(C) \sin(b) = \sin(c) \sin(B). \quad (6.13)$$

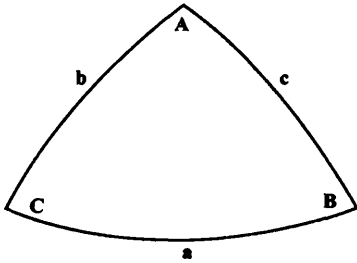


Figure 6.10: A spherical triangle. The interior angles (A, B, C) are the angles on the surface of the triangle. The exterior angles (a, b, c) are the angles subtended at the centre of the sphere by the arcs making the sides of the triangle .

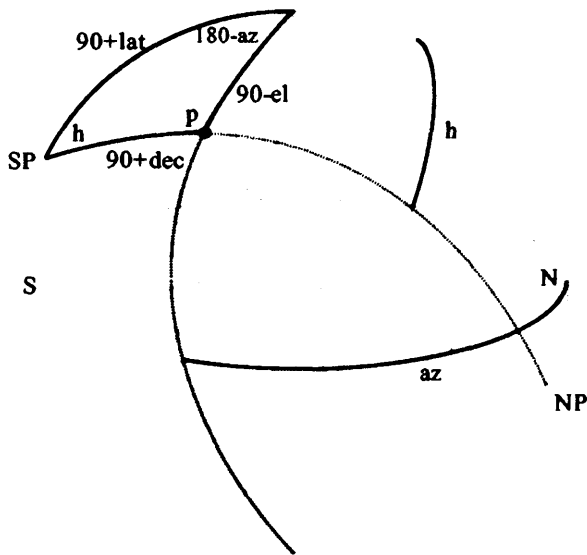


Figure 6.11: Spherical triangle for conversion between (az,el) coordinates and (ra,dec) for a point on the celestial sphere. The other two corners of the triangle are the South celestial pole (SP) and the zenith. The diagram is for a site in the southern hemisphere. The spherical triangle relates the hour angle (h), parallactic angle (p), azimuth (az), elevation (el) and declination (dec) of the point for a site at a given latitude (lat).

Fig. 6.11 shows how the azimuth and elevation of a point on the sky are related to its position in hour angle and declination at site with a given elevation. Relating the spherical triangle shown here to that in Fig. 6.10, the coordinate systems are linked by the relations:

$$\begin{aligned}\cos(\text{dec}) \cos(h) &= \sin(\text{el}) \cos(\text{lat}) - \cos(\text{el}) \sin(\text{lat}) \cos(\text{az}) \\ \sin(\text{dec}) &= \sin(\text{el}) \sin(\text{lat}) + \cos(\text{el}) \cos(\text{lat}) \cos(\text{az}) \\ \sin(p) \sin(\text{el}) &= \cos(\text{lat}) \sin(h).\end{aligned}\tag{6.14}$$

The parallactic angle gives the rotation between the angle on the sky to the angle on the celestial sphere. As the Earth rotates, the parallactic angle will change and so the Stokes parameters measured by the telescope will also change. This is discussed in more detail in Chapter 7. This rotation is useful as it provides an extra level of modulation, and could also be used as a way to provide the different angle needed to get both Q and U from the detector output. The rotation will also change the angle of constant elevation scans on the celestial sphere, and so allows the map to be cross-linked. However, the rotation also makes it more difficult to make a fully sampled map without scanning in elevation. The difference in latitude of the two sites means that very different scan strategies are needed. In Chile the sky rotation is very important, whereas at the South Pole, the sky rotates in the direction parallel to the horizon so the sky rotation only changes the polarization angle and the scan angle on the celestial sphere by a small amount.

In each case we assume that the waveplate will be stepped, the scans are made at constant elevation, all of the horns are being used and the maximum sample rate is 25 Hz.

Chile

Spiral strategy: The telescope remains at a constant elevation throughout the night. At the start of the night the telescope is driven in azimuth, starting at 90° , and continues to scan forwards in azimuth, repeatedly tracing out the same circle. The results for an elevation of 60° are shown in Fig. 6.12 (a). If this pattern is repeated every night for a whole year, a full ring around the South Pole will be made which includes each of the patches chosen in Fig. 5.4. The spiral pattern provides good cross-linking and no time is lost slowing down the telescope to change direction as the scan is continuous and at a constant speed. A possible modification would be to continuously scan backwards and forwards along a semi-circle in azimuth. This reduces the width of the ring so that a more specific range of declination can be targeted. To target the upper three patches the semi-circle is from an azimuth of 90° to an azimuth of 270° passing through 180° during the months that these patches are visible at night. This is shown for a night in April in Fig. 6.12 (b). To target the lower two patches the scan starts at 270° , then moves clockwise to 90° , passing through 0° . This is shown for a night in October in Fig. 6.12 (c).

Ring strategy: This is similar to spiral strategy, but instead of scanning a circle or semi-circle in azimuth, a smaller scan is made so that the width in declination of the ring made can be chosen to match that needed to just cover the required patches of sky. The sky then rotates through this line giving a ring of sky coverage. The pattern for a night

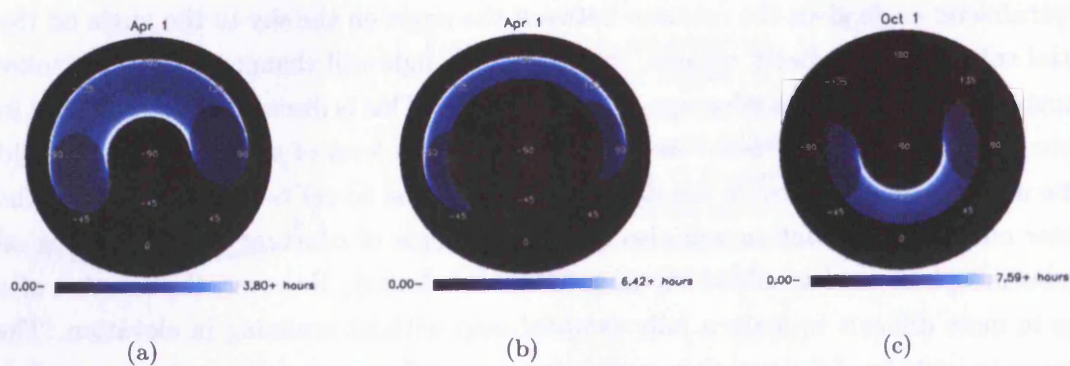


Figure 6.12: Sky coverage for spiral scan pattern, for (a) a full circle in azimuth for 1 April, (b) a semi-circle for 1 April and (c) a semi-circle for 1 October. The scan rate is 25 Hz and the elevation of the scan is 60° .

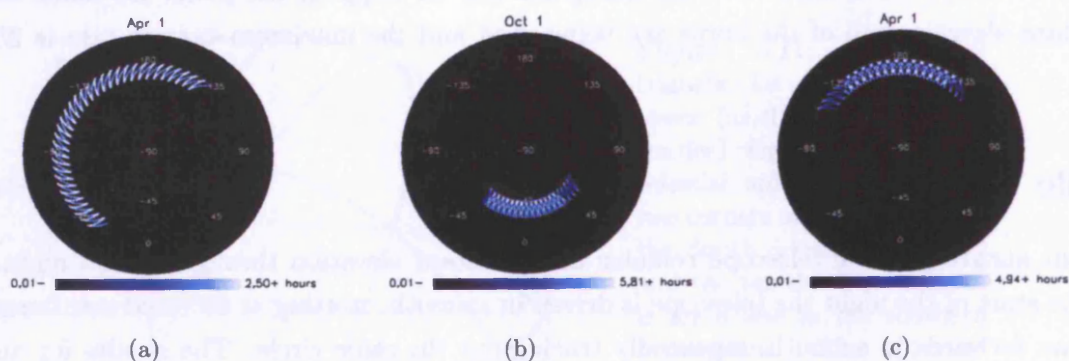


Figure 6.13: Sky coverage for the ring scan pattern. A 2Hz sample rate has been used so that the individual scans can be seen, for the full 25 Hz scan rate there are no gaps between the scan lines. (a) shows the results for a single azimuth range in April, (b) and (c) both use two azimuth ranges in April and October respectively.

in April is shown in Fig. 6.13 (a). However, this does not give any cross-linking. Another possibility is to scan backwards and forwards between the maximum and minimum azimuth of the scan until the first point on the celestial sphere to pass across the scan line has risen through the zenith and back down to the starting elevation, but now on the other side of the sky. The same scans are then made with the centre of the azimuth range shifted by 180° . This is shown for a night in April in Fig. 6.13 (b), where the initial point has a right ascension of 138° and a declination of 0° and the scans are made at an elevation of 46° . It is not possible to make the arc obtained completely cross-linked as the restriction of a minimum elevation of 50° means that the point chosen will reach the opposite side of the sky slightly before the middle of the night and so a longer arc of sky is observed for the second set of scans. Fig. 6.13 (c) shows the same pattern for a night

in October where the initial point has a right ascension of -40° and a declination of -35° and the scans are made at an elevation of 53° .

Bow tie strategy: In order to avoid covering unwanted regions of sky it may be preferable to follow a single point on the sky at it rises and sets during the night. The initial azimuth and elevation of the centre of the scan (the source) are found and a constant elevation scan is made with this point at the centre of the scan. Once a scan has been made, the new coordinates of the source are found and a scan in the opposite direction is made. The telescope continues to scan forwards and backwards across the source until the source is below the minimum elevation of 50° . The motion of the telescope in azimuth and elevation for a single night is shown in Fig. 6.14. The pattern made on the sky is

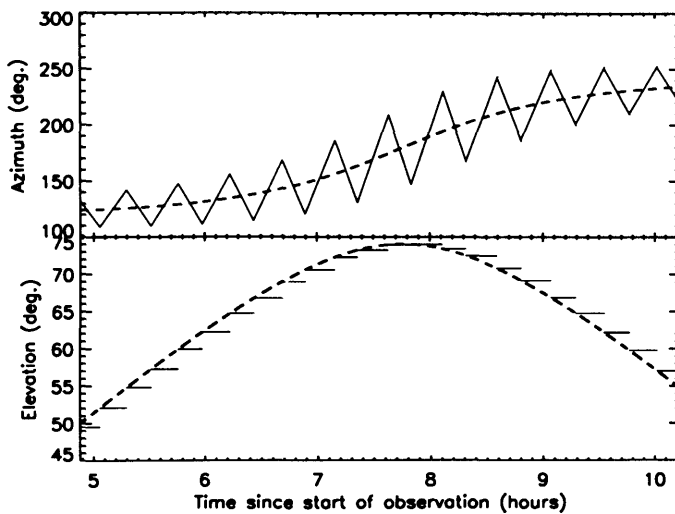


Figure 6.14: Motion in azimuth and elevation for bow tie scan strategy. For clarity, a sample rate of 1 Hz has been used so that motion in azimuth is fairly slow. For the full 25 Hz sample rate there would be many more per night.

shown in Fig. 6.15. For the night shown in October the source is visible for over half the night and so almost a full circle of scans can be made. Earlier in the year, the source will be above the maximum elevation for less time and so a bow tie shape will be made. The integration time is strongly concentrated towards the centre of the pattern and so the edges are not very well sampled. Also the central regions are the only part of the pattern which is cross-linked.

Multiple bow tie strategy: This is a possible improvement to the bow tie strategy which gives better cross-linking and a more even distribution of integration time. Instead of making a single scan at each elevation, a set number of scans are made before moving back to the centre of the patch. The number of scans which should be made depends on the scan rate and hence the sample rate. More scans can be used for a high sample rate (faster scan) as the sky will rotate less during each scan. Fig. 6.15 (c) and (d) show the pattern made on the sky for two different scan rates.

None of the strategies discussed here is completely satisfactory. However before this work was completed a definite decision was made to operate from the South Pole and so this section of work was not completed.

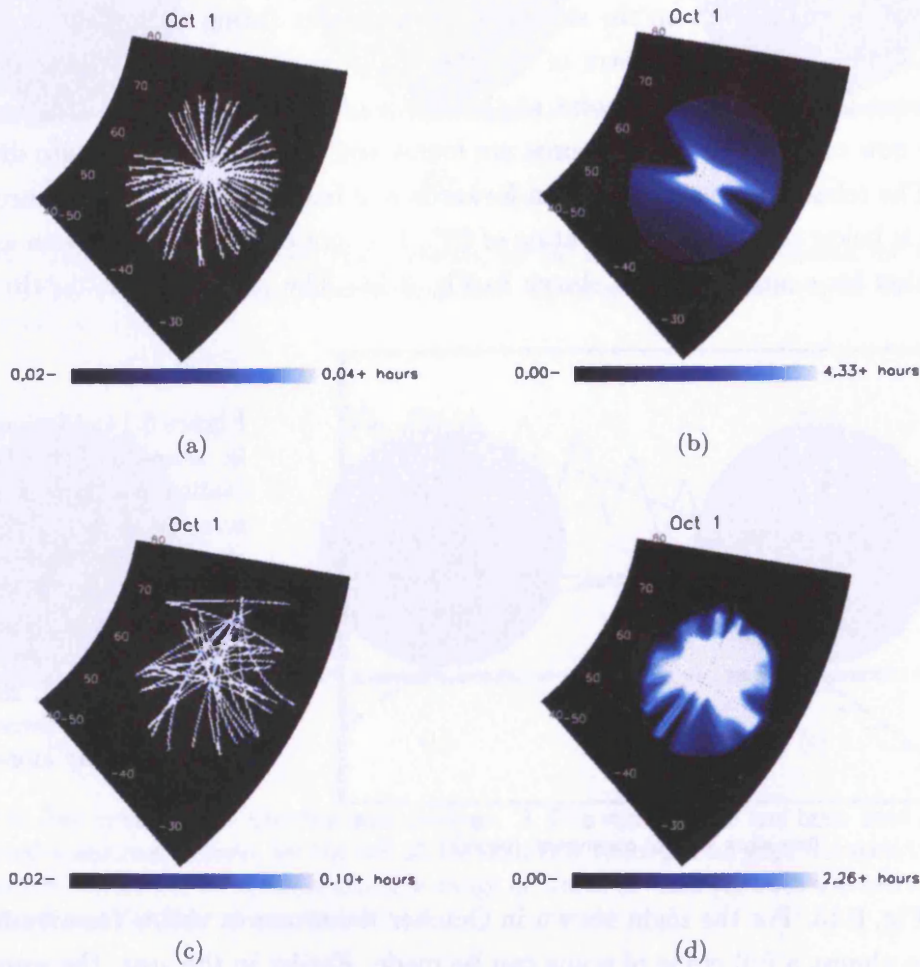


Figure 6.15: Patterns made for bow tie strategy (top) and multi-bow tie strategy (bottom) for a single night's observation of a single patch in October.

a) central horn only, maximum value shown for the integration is 100 times less than the actual maximum. All integration times above this have been reduced to this value. A sample rate of 1 Hz is used so that the individual scans are visible.

b) 25 Hz sample rate, with the maximum value five times less than the actual maximum so that the edges of the pattern are still visible.

c) same as (a), but the maximum value shown is 10 times less than the actual maximum and four scans are made at each elevation.

d) same as (b) but for the multi-bow strategy with 60 scans at each elevation.

South Pole

For the site at the South Pole there are fewer options as the sky rotates almost parallel to the horizon. This means it is not possible to vary the parallactic angle or to cross-link the maps unless we scan in elevation. However, it is easier to make fully sampled maps and to target a specific patch of sky since during the summer the patches chosen in Fig. 5.7 are visible all of the time. The basic strategy is as follows: a square of sky is defined in right ascension and declination. The horizontal coordinates of the top left side of the square are found and a scan is made in azimuth until the right side of the square is reached. The scan direction is then reversed until the left side of the square is reached. The telescope is then moved up by a third of a beam in elevation and the process repeated until the bottom of the square is reached. The elevation is then decreased after each scan. The process is then repeated, scanning up and down across the same square for the whole integration time.

There are two ways of carrying out this strategy, either the scan rate is kept constant at the speed needed to fully sample the lowest elevation used, or we vary the scan rate with elevation as given by equation 6.9. The coverage for one of the patches chosen is shown in Fig. 6.16 for these two possibilities. Varying the scan rate with elevation gives

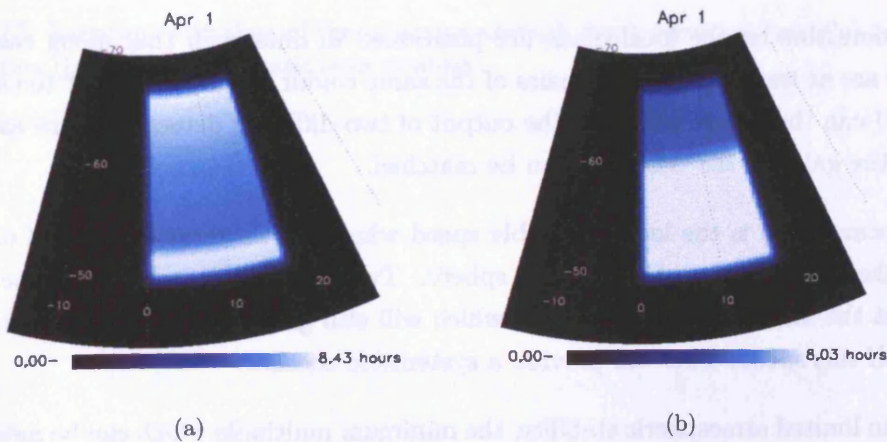


Figure 6.16: Sky coverage for South Pole strategies. (a) shows the result for a 11 hr integration with a constant scan rate, (b) shows the same for a varying scan rate.

a more even coverage of the patch, but the noise in the time stream may depend on the scan rate and so there will be different noise properties across the map.

6.3 QUaD observing strategy

- QUaD will observe a single 300 deg^2 patch of sky from the South Pole for two austral winters. The position of the patch is chosen to be in a region with low foreground contamination.
- A simple scanning strategy will be used in which we scan up and down the patch with constant elevation scans. After two scans, the starting azimuth of the scan is adjusted to follow the patch as it moves across the sky.
- There are two independent methods which can be used to obtain the Q and U Stokes parameters. These use either the waveplate rotation or the relative orientation of different pairs of detectors. Neither of these methods is ideal so both will probably be used in the analysis pipeline to provide a cross-check.
- We make a scan backwards and forwards at each elevation, rotating the waveplate by 22.5° once the telescope returns to its starting position. This means that after two scans there is enough information to measure Q and U at each position using the same horn. This assumes that the atmospheric loading does not change in the time it takes to scan forwards and backwards.
- The detectors on the focal plane are positioned in lines such that along each line there are at least two detector pairs of the same colour orientated at 45° to each. Q and U can then be found using the output of two different detectors. This assumes that the gains of the two feeds can be matched.
- The scan speed is the lowest possible speed which allows three samples of data to be taken per beam on the celestial sphere. Two different scan rates will be used, one at the maximum possible speed which will still give fully sampled sky, and one at half this speed. This will provide a systematic check.
- Due to limited atmospheric stability, the minimum multipole which can be measured is $\ell = 17$. Although it will not be possible for QUaD, for an upgraded instrument with a continuously rotating waveplate this increases to $\ell = 50$.
- The z-axis rotation can be used to give an indication of the amount of instrumental polarization. A z-axis rotation will be made each time a complete patch is covered.

This strategy is shown in Fig. 6.17. This is only an initial strategy and may be modified once the performance of the instrument has been tested at the South Pole. If the atmosphere proves to be more stable than expected it may be possible to make scans

in which the elevation varies. It may also be possible to rotate the waveplate and make a z-axis rotation more often than is proposed here.

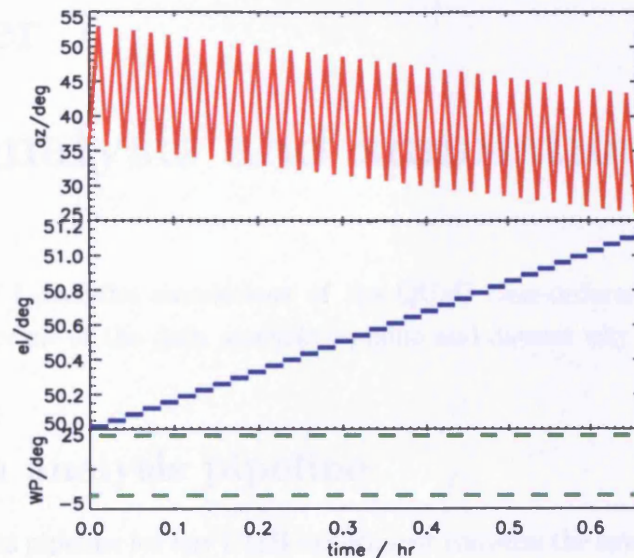


Figure 6.17: Variation with time of the telescope azimuth (top), elevation (middle) and wave-plate position (bottom) for the basic scan strategy.

Chapter 7

Data analysis and simulations

In this Chapter I describe simulations of the QUaD time-ordered data (TOD). I first give a brief overview of the data analysis pipeline and discuss why these simulations are needed.

7.1 Data analysis pipeline

The data analysis pipeline for any CMB experiment converts the raw data output from the telescope into constraints on the cosmological model. For QUaD this pipeline is broken up into three levels.

- **Level A: Telescope processing.** The output of the detectors will be a series of voltages. This electrical output is converted into files of time ordered data (TOD). This is stored into a database which also contains the position of the telescope and the housekeeping data. This includes the position of the waveplate and the telescope z-axis rotation angle.
- **Level B: Time stream reduction and map making.** The raw TOD is then cleaned. This involves locating spikes due to cosmic rays hitting the detectors and identifying sections of the data which cannot be used because of bad weather or problems with the telescope. This cleaned TOD can then be converted into maps of the Q and U Stokes parameters at the two QUaD observing frequencies.
- **Level C: Science analysis.** These maps will be used to find the polarization power spectra. The power spectra can then be used to make estimates of the cosmological parameters.

The computational methods for making maps and for reconstructing the CMB power spectrum have been developed over the past decade for the analysis of previous CMB experiments. The main complication is implementing these methods on the large data-sets produced by these experiments. These methods also need to be modified to include

polarization. The development of the pipeline is being carried out by three groups. The level A software is taken from the previous DASI system and is currently being modified at Chicago, in collaboration with Stanford. The level B software is being developed at Cardiff / IPAC and the level C software is currently in progress at Edinburgh. I have worked mainly on simulations for level B, but have also been involved in discussions about other parts of the pipeline.

7.1.1 Map making

Map making can be thought of in terms of the parameter estimation methods discussed in Chapter 5. In this case the data, \mathbf{d} , is the TOD from each detector and the parameters to be found are the values of Q and U in each pixel in the map, \mathbf{m} . The data can be modelled as:

$$\mathbf{d} = \mathbf{A}\mathbf{m} + \mathbf{n} \quad (7.1)$$

where \mathbf{n} is a vector of the noise for each measurement and \mathbf{A} is the pointing matrix. If there are N data points and M pixels in the map, \mathbf{A} is a $N \times M$ matrix which gives the pixel being observed on the sky for each sample of TOD. In the case of polarization this is complicated slightly as \mathbf{m} is a $2 \times M$ matrix because at each point we measure both Q and U . If we take a single point of data, d , then the pointing matrix would be given by:

$$d = \mathbf{A}m + n = (\cos(2\alpha) \ \sin(2\alpha)) \begin{pmatrix} Q \\ U \end{pmatrix} + n \quad (7.2)$$

Equation 7.1 can therefore still be applied to polarization if \mathbf{A} is redefined to be a $2 \times N \times M$ matrix. The values of Q and U can be found by simply minimizing the value of χ^2 for this problem:

$$\chi^2 = (\mathbf{d} - \mathbf{A}\mathbf{m})^T \Sigma_d^{-1} (\mathbf{d} - \mathbf{A}\mathbf{m}) \quad (7.3)$$

where Σ_d is the data noise covariance matrix, $\Sigma_d = \langle \mathbf{nn}^T \rangle$. For the minimum value of χ^2 , the solution is:

$$\mathbf{m} = (\mathbf{A}^T \Sigma_d^{-1} \mathbf{A})^{-1} \mathbf{A}^T \Sigma_d^{-1} \mathbf{d}. \quad (7.4)$$

The noise covariance matrix of the map will be $\Sigma_m = (\mathbf{A}^T \Sigma_d^{-1} \mathbf{A})^{-1}$. The key problem in solving this equation is that it involves the inverse of the $N \times N$ matrix, Σ_d and the $M \times M$ matrix, Σ_m . Even a single day of QUaD of data N will be $\sim 10^6$. This makes the problem computationally infeasible. It is therefore necessary to use some sort of iterative method to solve Equation 7.4. The development of this method for QUaD is currently in progress (Zemcov (2004)) and is based on a method suggested by Prunet, S. et al. (2001).

7.1.2 Power spectrum estimation

For power spectrum estimation, the data are now Q and U in each pixel in the map and the parameters are the values of the power spectrum in each band. A direct maximum likelihood approach would be to maximize the probability distribution:

$$L(\mathbf{m}; C_\ell) = \frac{1}{(2\pi)^{M/2} |\Sigma_m|^{1/2}} \exp \left(-\frac{1}{2} (\mathbf{m} - C_\ell)^T \Sigma_m^{-1} (\mathbf{m} - C_\ell) \right) \quad (7.5)$$

Again this involves the inversion of an $M \times M$ matrix so is not computationally feasible unless the map is very small or has very low resolution. An iterative method of finding the maximum likelihood solution is therefore currently being tested for QUaD (Brown (2004)).

An approach currently under development for QUaD is a Pseudo- C_ℓ analysis. If a noiseless full sky map were available then the power spectra could be found by just taking the spherical harmonic transform of the map. However, if this process is performed on a noisy cut-sky map this process will not reconstruct the actual C_ℓ 's in the map, but will give a set of pseudo- C_ℓ 's (Wandelt et al. (2001)). These will be related to the true C_ℓ 's by some coupling matrix which can be calculated analytically. The application of this procedure to polarization data is described by Brown, Castro and Taylor (2004).

7.2 Simulations

Simulations of TOD will be used for two purposes in the analysis pipeline. Firstly, TOD data is needed to test the map-making pipeline. Secondly, in the pseudo- C_ℓ power spectrum estimation an estimate of the instrument noise is needed so that the effects of this noise can be taken into account. This will be found from Monte-Carlo simulations of different realizations of noise in the TOD. A fast method of producing realizations of TOD is therefore needed for this estimate to be made. I undertook this exercise for the QUaD project.

7.2.1 Simulations of CMB signal

The first stage in the simulations is to make a time-stream of data which includes only the signal from the CMB.

I first find the sky coordinates (azimuth and elevation) for the central pixel in the focal plane for each sample. This is then used to find the coordinates of each feed using the relative position of each of the feeds to the central pixel. This is obtained from the projection of the focal plane onto the sky shown in Fig. 6.4. The position of each sample for each feed on the celestial sphere (right ascension and declination) is then found using

Equations 6.14.

Maps of the CMB are generated using the SYNFAST routine in the HEALPix data analysis package¹. This is a package of routines designed to be used with the HEALPix (Hierarchical Equal Area iso-Latitude Pixelization) scheme. This is a way of dividing the sky up into pixels which has now become the standard for CMB analysis, particularly for large areas of sky for which a flat sky approximation cannot be used. The surface of the spherical projection of the sky is split up into 12 equal area quadrilaterals, these are the base resolution elements. To obtain higher resolutions, these quadrilaterals are split into smaller sections. The HEALPix resolution parameter (N_{side}) is the number of divisions along the side of the base element needed to create the required resolution. This is shown in Fig. 7.1. The number of pixels is therefore given by $12 \times N_{side}^2$. For the QUaD maps,

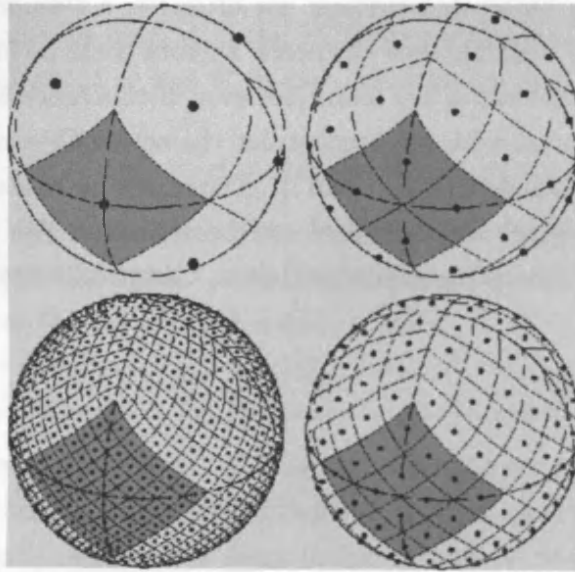


Figure 7.1: HEALPix pixelization. The top left sphere shows the 12 base pixels. The top right has a resolution of $N_{side} = 2$, the bottom right has $N_{side} = 4$ and the bottom left has $N_{side} = 8$. Taken from <http://www.eso.org/science/healpix/>.

we need to make sure that the pixelization is small enough that there are at least two pixels in the width of a FWHM beam. A resolution of $N_{side} = 2048$ has been chosen as:

- for $N_{side} = 2048$, the width of each pixel will be 1.72 arcmin, which allows just over two pixels per 4.2 arcmin beam,
- the next lowest resolution of $N_{side} = 1024$ gives a pixel width of 3.4 arcmin so would be too big.

¹<http://www.eso.org/science/healpix/>

At this resolution there will be of order 3×10^5 pixels in a 300 deg^2 map.

The HEALPix maps are smoothed with a gaussian beam with the QUaD beamwidth. Two maps are made, one at 150 GHz and one at 100 GHz. The SYNFAST routine creates a realization of a CMBFAST power spectrum. I use the standard WMAP model used throughout this thesis as the input spectrum. It is only possible to generate full sky maps with the present software, so a full sky map is generated which I then cut to only keep pixels with a declination lower than -20° to save memory when reading the map into the simulation. Three maps are generated to give the temperature, T, and Q and U Stokes parameters for each pixel.

The coordinates of the feeds are then converted into HEALPix pixel numbers to give the pixel observed on the sky for each sample, $p(t)$. The signal at time, t , for each feed is given by:

$$\begin{aligned} S_1(t) &= \frac{1}{2}(T[p(t)] + Q[p(t)] \cos(2\alpha(t)) + U[p(t)] \sin(2\alpha(t))) \\ S_2(t) &= \frac{1}{2}(T[p(t)] - Q[p(t)] \cos(2\alpha(t)) - U[p(t)] \sin(2\alpha(t))) \end{aligned} \quad (7.6)$$

where S_1 and S_2 are the signals from the co-polar and cross-polar device for each feed. The angle $\alpha(t)$ is the angle of the co-polar device with respect to the reference direction and depends on the orientation of the PSBs (α_d), the rotation angle of the waveplate (α_w), the z-axis rotation angle (α_z) and the parallactic angle between the celestial sphere coordinate system (RA and declination) and the sky coordinates (azimuth and elevation), (α_p). The definition of the reference direction is completely arbitrary. I have defined it so that $\alpha = 0$ for the central feed on the focal plane if:

- waveplate is at an angle such that the incoming radiation is not rotated,
- the z-axis rotation is such that the co-polar device of this feed is parallel to the East-West line of the local coordinate system when the telescope is pointing at zenith, and
- the parallactic angle is zero (as will be the case at the Pole).

The angle of the other PSBs will either be the same as that for the central feed or rotated by 45° . The value of α for each sample will therefore be given by:

$$\alpha = \alpha_p + \alpha_d + \alpha_z - 2\alpha_w. \quad (7.7)$$

The waveplate rotation causes the polarization angle to change in the opposite direction to the other rotations as it causes a rotation of the actual polarization vector as opposed to a rotation of the coordinate axes.

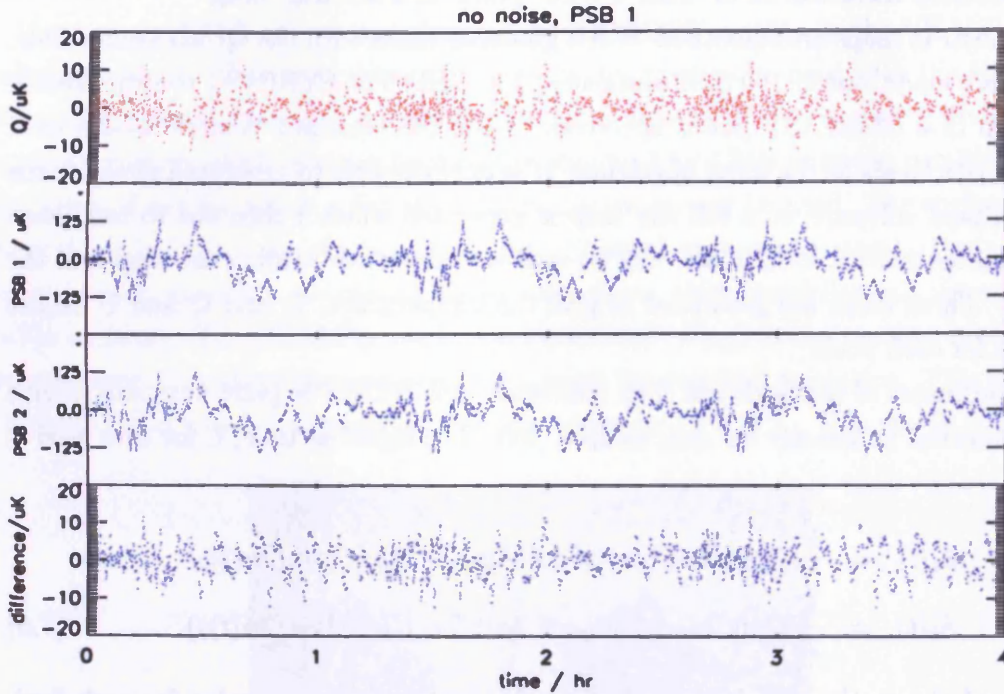


Figure 7.2: Simulated timestream with CMB signal only. The top panel shows the input signal from the CMB for the Q Stokes parameter. The middle two panels show the output from the two PSBs in the central feed. The bottom panel shows the differenced signal from these two detectors. In this case, the signal from each detector is dominated by the CMB temperature signal. This signal is then removed by the differencing as it makes an equal contribution to each detector.

Fig. 7.2 shows a sample timestream of data if we include only the CMB signal and do not change the rotation angle. The top panel shows the input Q Stokes parameter and the bottom panel shows the difference between the signals from the two PSBs in the central feed. If there is no noise and there are no systematic effects the differenced signal in this case will give the Q Stokes parameter.

7.2.2 Including noise

The next stage is to add noise into the simulation. The power spectrum of the noise is given by:

$$P(\nu) = NET^2 + NET^2 \frac{\nu_{knee}}{\nu} \quad (7.8)$$

where the first term gives the contribution from white noise and the second term gives the contribution from 1/f noise. To make a simulated noise timestream I simply generate a set of N Gaussian random numbers, g_k , with zero mean and unit variance and use these to make a realization of the real and imaginary parts of the Fourier transform of the

timestream, (r_k, i_k) . The positive frequency components are given by:

$$r_0 = g_0 \sqrt{P_0} \quad (7.9)$$

$$i_0 = 0 \quad (7.10)$$

$$r_k = g_k \sqrt{\frac{P_k}{2}} \quad k = 1 \dots N/2 \quad (7.11)$$

$$i_k = g_{N-k} \sqrt{\frac{P_k}{2}} \quad k = 1 \dots N/2 - 1. \quad (7.12)$$

As the timestream being generated must be real, the negative components can be obtained from the symmetry conditions (see Appendix A, Equation A.4):

$$r_{-k} = r_k \quad (7.13)$$

$$i_{-k} = -i_k \quad (7.14)$$

The Fourier transform of this set of Fourier components then gives a realization of the noise with the correct properties. Different realizations can be generated from the same noise power spectrum by starting with a different set of gaussian random numbers.

I model the noise as the contribution from three components.

- Atmospheric 1/f noise. This will be strongly correlated between the different detectors.
- 1/f noise from the bolometers and the electronics chain (post-detection noise). The correlations between the timestreams from different bolometers will be low as each bolometer will have its own bias current and thermal properties, and the electronics chain for each PSB is different.
- White noise from atmosphere, telescope, detectors and electronics (as discussed in Chapter 4).

In each case the white noise component will be completely uncorrelated between the different detectors. However, the correlations between the 1/f noise components is more complicated. As a first approximation I assume that the 1/f noise from the atmosphere will be completely correlated between detectors and so use the same simulated 1/f noise timestream for each detector. I then assume that the 1/f noise due to the post-detection noise will be completely uncorrelated and so use a different realization of the noise for each detector. Each of these three noise timestreams is generated separately and then added the CMB signal.

The white noise component is calculated using the NETs from in Chapter 4. The NET for the atmospheric noise is found by performing the same calculation as for the

total NET, but using only the atmospheric power loading. For the electronics noise I use estimates from Church (2003). The values used are shown in Table 7.1. The 1/f knee is

Band	100 GHz	150 GHz
Total NET / $\mu K s^{1/2}$	300	340
Atmospheric NET / $\mu K s^{1/2}$	137	137
Post detection NET / $\mu K s^{1/2}$	218	237

Table 7.1: NETs used in noise simulations.

assumed to be 1.0 Hz for the atmosphere and 0.01 Hz for the post-detection noise.

The simulated timelines with different types of noise added are shown in Figures 7.3 - 7.5. If the actual noise levels given above were used then the plots would be dominated by the noise and would not show anything useful. Instead I reduce the noise per measurement so that the average noise per pixel is the same as that which would be achieved for a 600 day integration of the full 300 deg² of patch of sky. This done by averaging the results from 600 different realizations of the noise generated for a single day of observations and adding this averaged noise timestream to the CMB signal. This reduces the noise to a low enough level for the CMB signal to still be seen. Fig. 7.3 shows the timestreams if only white noise is used. The differenced signal is now noisy, but the shape of the original input signal can still be seen. Fig. 7.4 shows the timestreams if atmospheric 1/f noise is also included. In this ideal case with no systematic effect, all of the atmospheric 1/f noise is removed when the PSBs are differenced and so the output is the same as in the white noise only case. In Fig. 7.5 the 3 different sources of noise are included. In this case, because the 1/f post-detection noise is different for each PSB in the feed, the differencing does not remove this noise and so the differenced signal contains 1/f noise.

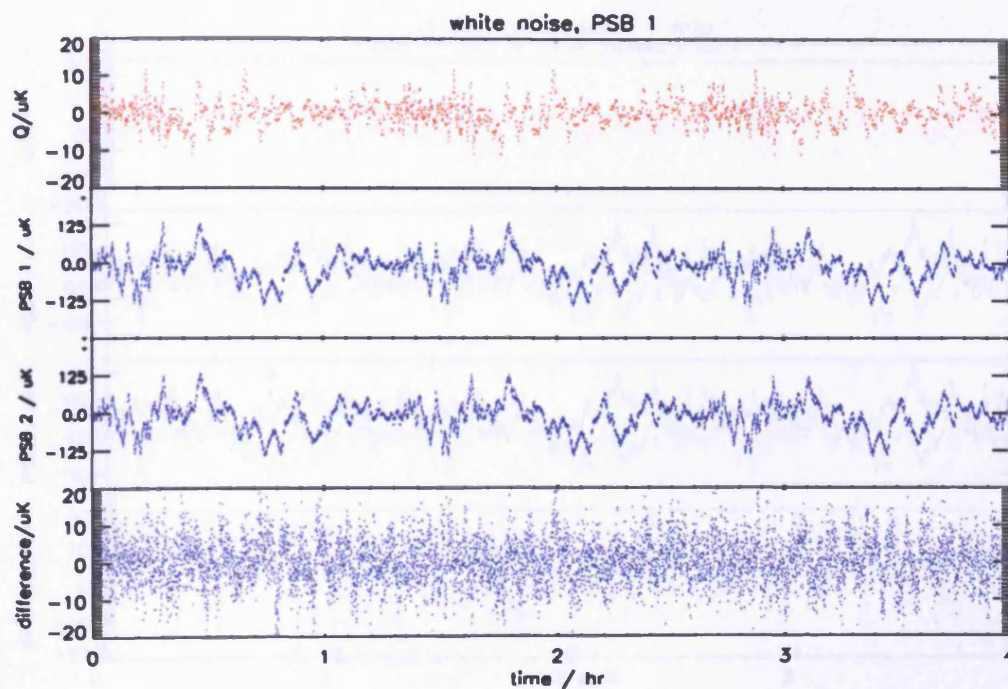


Figure 7.3: Simulated timestream with white noise. The level of the noise is very low and so it is not noticeable in the PSB output as the dominant temperature signal is much bigger than the noise. However, when the two signals are differenced the small input Q signal is now only just recognisable within the white noise.

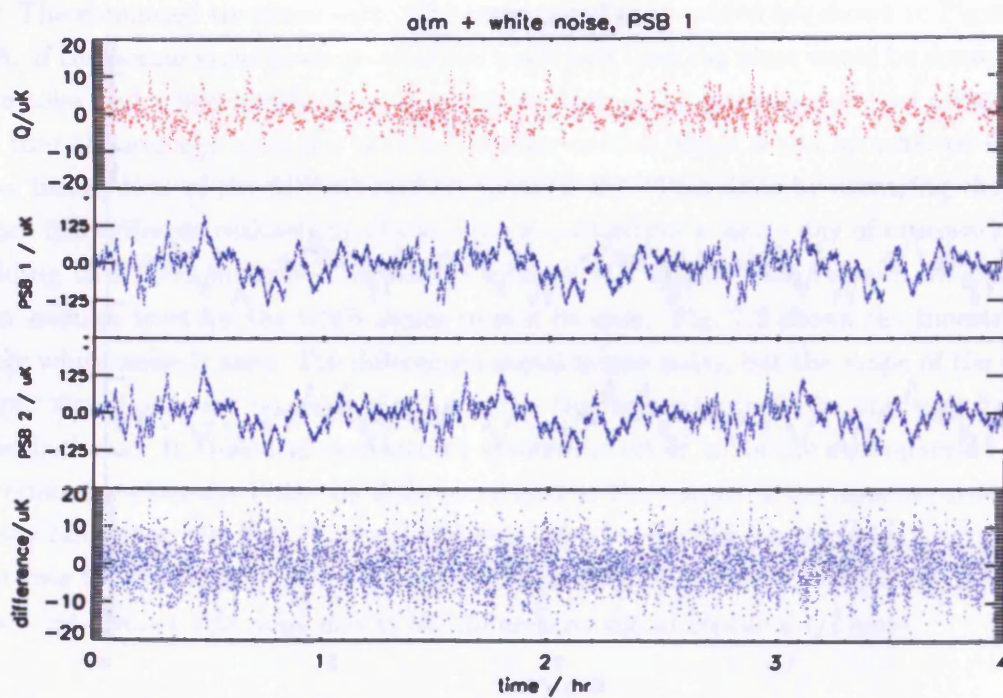


Figure 7.4: Simulated timestream with white noise and atmospheric $1/f$ noise. The level of the noise is too small to be noticeable in the output from each PSB. The atmospheric noise is completely removed by the differencing and so there is only white noise in the differenced signal.

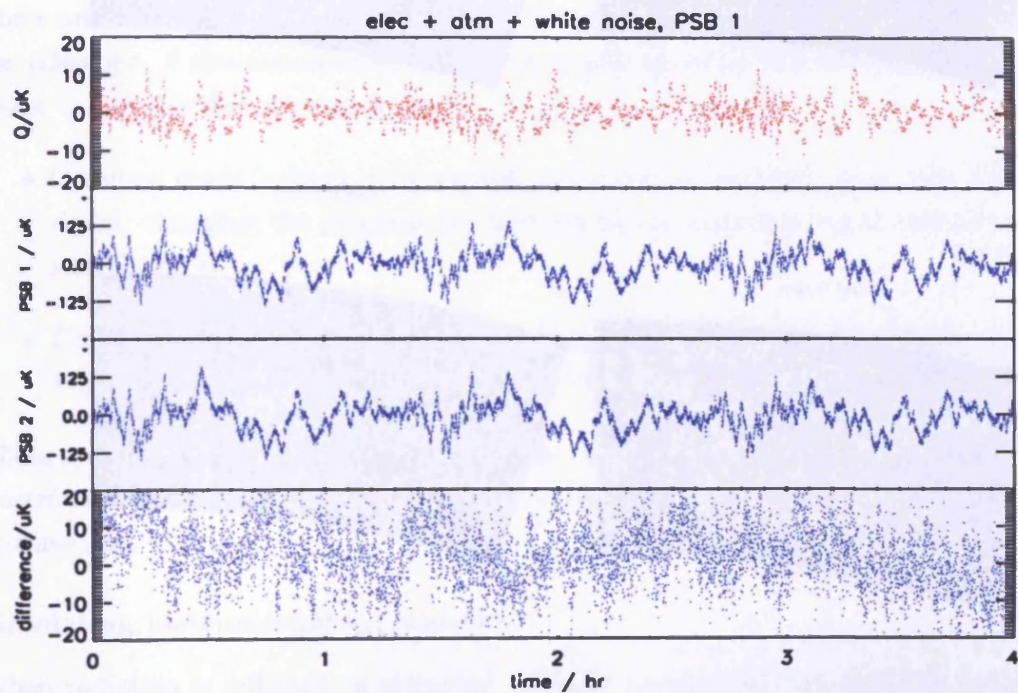


Figure 7.5: Simulated timestream with all 3 noise components. The noise is again too small to be significant in the PSB signals, but the differenced signal is dominated by 1/f noise from the bolometers and electronics.

A naive map making code (Zemcov (2004)) has been written that simply finds the observations made of each pixel and averages these observations to get the signal. The results of using the simulated data as the input to this code are shown in Fig. 7.6. If no

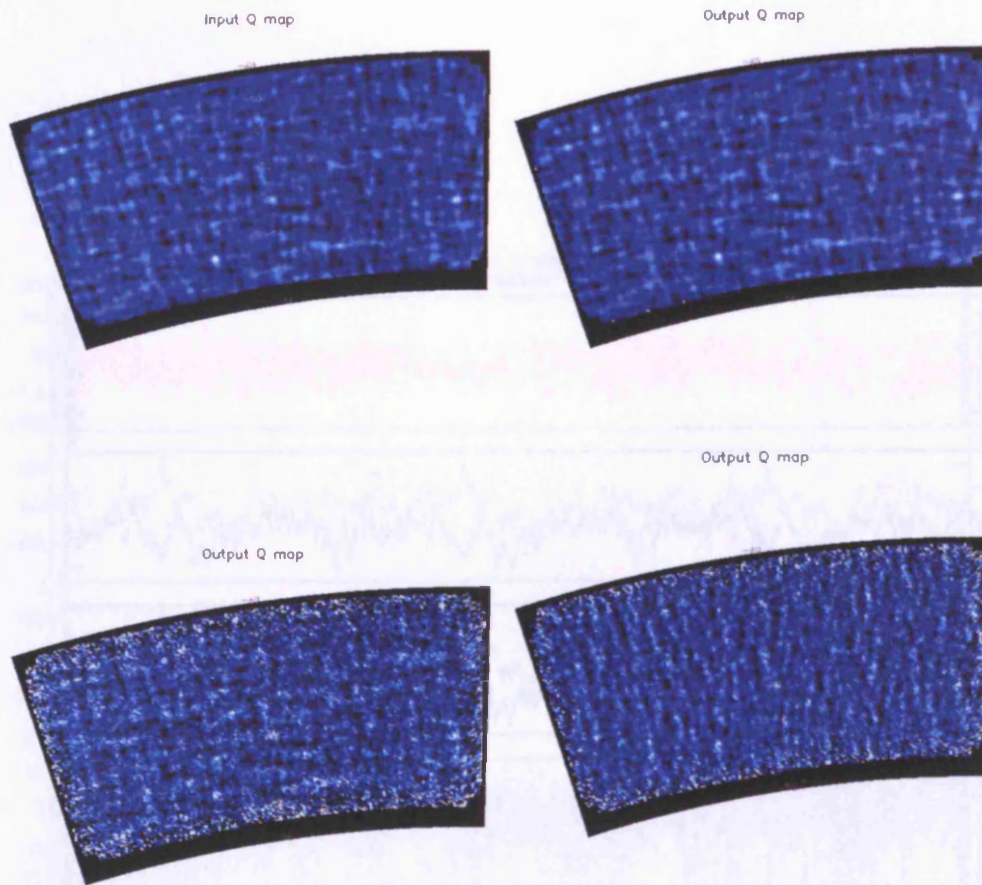


Figure 7.6: Maps made by averaging the measurements in each pixel from simulated timestreams using noise scaled to that expected from a 600 day integration time (from Zemcov (2004)). Top left: map input into simulation. Top right: map output if no noise added. Bottom left: map output if white noise added. Bottom right: map output if white and $1/f$ noise added.

noise is included then the input and output maps are exactly the same. This shows that the simulations and map making code do not introduce any errors into the map. When white noise is added then the areas of the map which have not been sampled as well (such as the edges) are clearly more noisy, but the overall structure of the map is still the same. However, adding $1/f$ noise introduces extra structure which does not come from the CMB signal and so the naive map making method needs to be improved. The naive method is equivalent to assuming that the data noise covariance matrix in Equation 7.4 is diagonal

and has the same value for each diagonal component. In this case, the noise matrix cancels out and the resulting form of Equation 7.4 simply averages each of the observations of a pixel. This will work for white noise as on average the signal will be the same for each measurement. However, when $1/f$ noise is included the noise matrix is no longer diagonal as there will now be correlations between the noise for each sample of TOD. The full inversion of the noise matrix must now be included to get the best estimate of the map. A method for iteratively solving Equation 7.4 is currently in progress (Zemcov (2004)).

7.2.3 Systematic effects

There are numerous systematic effects which could change the signal as it passes through the telescope. I concentrate here on the main effects which will affect the polarization. These can be divided into two kinds.

- Common mode leakage: this converts a fraction of the total power into a polarized signal, changing the polarization fraction of the incoming signal and converting I into Q and U.
- Cross polarization: this rotates the polarization angle of the incoming signal which will change Q and U, but will not affect the polarization fraction.

These systematics can be generated either as the radiation passes through the telescope (instrumental systematics) or when the two signals from each feed are differenced (detector systematics).

Simulating instrumental systematics

When radiation is reflected or refracted, initially unpolarized radiation can become polarized. This is known as instrumental polarization (IP) and is a form of common mode leakage. This is particularly problematic for QUaD as it will convert a fraction of the large fluctuating atmospheric total power signal into polarized radiation which could swamp the cosmological signal. For QUaD the telescope is designed to be symmetric about the z-axis so the instrumental polarization signal produced at the focal plane will also be symmetric and will increase as we move further from the centre of the focal plane. As a first approximation I assume that the IP varies linearly with radius, increasing from zero at the centre of the focal plane to 1% of the total power signal at the edge. I also assume that the polarization angle of the IP signal, α_{IP} , will always be perpendicular to radial lines from the centre of the focal plane. This is shown in Fig. 7.7.

To make a simple model of the IP I assume that a fraction η_{IP} of the unpolarized power becomes polarized before the radiation passes through the waveplate. This is reasonable

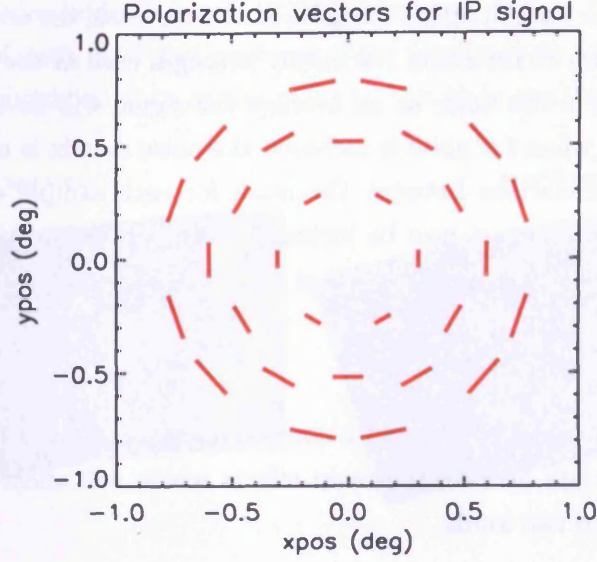


Figure 7.7: Magnitude and direction of the instrumental polarization across the focal plane. The IP varies from zero at the centre to a maximum of 1% of the total power at the edges and the polarization angles are perpendicular to this radial direction.

because most of the IP will be generated when the radiation reflects off the primary mirror. This generates a polarized signal with intensity I_{IP} where:

$$I_{IP} = \eta_{IP} \sqrt{T^2 - Q^2 - U^2} \quad (7.15)$$

where η_{IP} will depend on the position of the detector on the focal plane. It is then possible to define the Stokes parameters of the IP signal as:

$$Q_{IP} = I_{IP} \cos(\alpha_{IP}) \quad (7.16)$$

$$U_{IP} = I_{IP} \sin(\alpha_{IP}) \quad (7.17)$$

where α_{IP} also depends on the position of the detector.

The signal at the detector due to IP can then be found in the same way as we found the CMB signal (Equation 7.6) giving:

$$\begin{aligned} S_{1IP} &= \frac{1}{2}(Q_{IP} \cos(2\alpha_r) + U_{IP} \sin(2\alpha_r)) \\ S_{2IP} &= -\frac{1}{2}(Q_{IP} \sin(2\alpha_r) - U_{IP} \cos(2\alpha_r)) \end{aligned} \quad (7.18)$$

as there is no additional total power IP signal. The angle, α_r , is the angle by which the IP is rotated with respect to the reference direction. This depends only on the waveplate angle and the detector orientation as the signal is generated **after** any z-axis rotation has

occurred giving:

$$\alpha_r = \alpha_d - 2\alpha_w. \quad (7.19)$$

This IP signal is then added to the signal from the CMB and the noise. This signal will vary with time because the total power varies with time. It will have contributions from the CMB temperature signal and the atmospheric signal. Fig. 7.8 shows a simulated timestream for a detector at the edge of the focal plane (8-150 in 6.4). In this case if the IP is not accounted for then the atmospheric fluctuations will dominate the differenced signal.

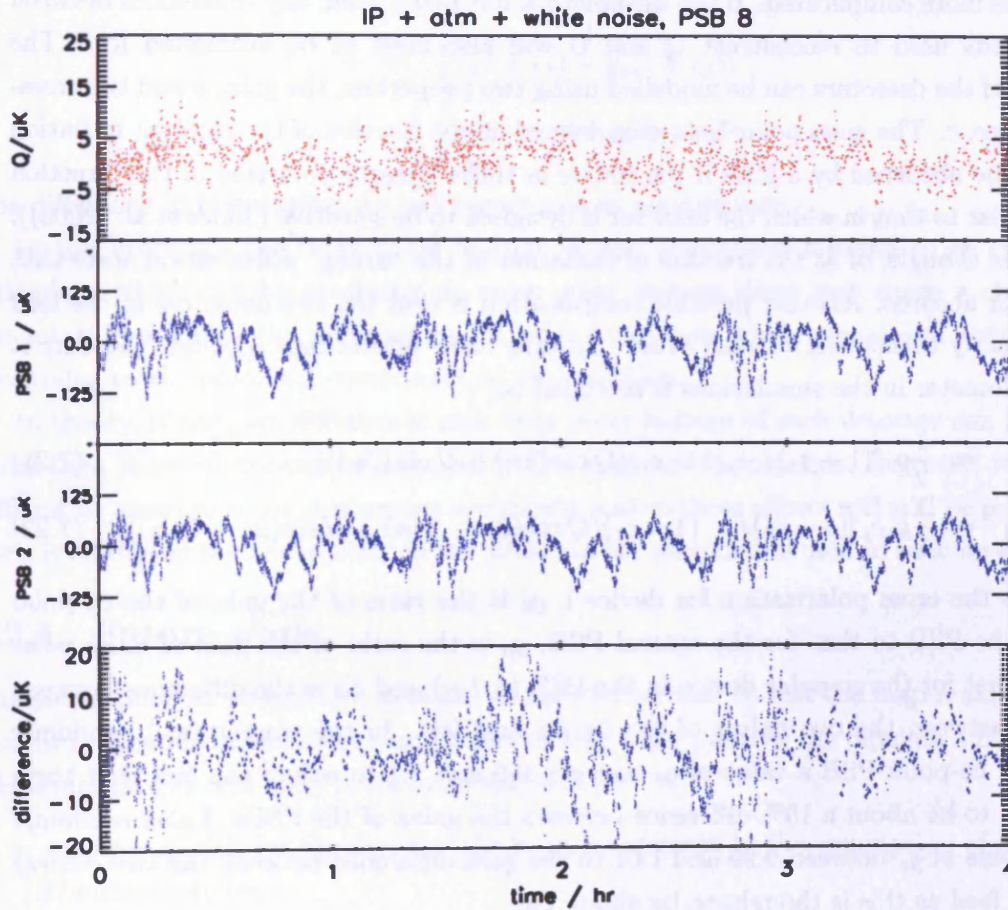


Figure 7.8: Simulated timestream with white noise, atmospheric noise and instrumental polarization for detector 8-150 (co-polar PSB).

The instrumental cross-polarization has not yet been modelled in the simulation.

Detector systematics

If the two detectors in each feed are identical then differencing the two outputs will give a linear combination of Q and U . This differenced signal is given by:

$$D = Q \cos(2\alpha) + U \sin(2\alpha). \quad (7.20)$$

If the same pixel is measured again, but with a different value of α , Q and U can be reconstructed. As discussed in Chapter 6 at the South Pole this can be achieved either by using the output from an adjacent feed which is orientated at a different angle, or using the same detector with a different waveplate rotation angle.

However if the different detectors within a feed are not identical then this procedure will become more complicated. If the waveplate is not being used, any differences between the two feeds used to reconstruct Q and U will also need to be accounted for. The properties of the detectors can be modelled using two properties, the gain, g and the cross-polar leakage, ε . The cross polar leakage is defined as the fraction of the incident radiation which will be absorbed by a PSB if the source is 100% linearly polarized in the direction perpendicular to that in which the detector is designed to be sensitive (Jones et al. (2003)). This can be thought of as the fraction of radiation in the ‘wrong’ polarization state that the detector absorbs. Another possible complication is that the two detectors in the feed are not exactly orthogonal to each other. To take these effects into account, the output of each bolometer in the simulations is modified to:

$$S_1 = \frac{1}{2}g_0 [(1 + \varepsilon_1)I + (1 - \varepsilon_1)(Q \cos(2\alpha) + U \sin(2\alpha))] \quad (7.21)$$

$$S_2 = \frac{1}{2}g_0g_p [(1 + \varepsilon_2)I - (1 - \varepsilon_2)(Q \cos(2\alpha - 2\delta\alpha) + U \sin(2\alpha - 2\delta\alpha))] \quad (7.22)$$

where ε_i is the cross polarization for device i , g_0 is the ratio of the gain of the co-polar device in the PSB to that for the central PSB, g_p is the ratio of the gain of cross-polar device to that for the co-polar device in the PSB (g_2/g_1) and $\delta\alpha$ is the difference between the angle between the two halves of the device and 90° . In the simulation I randomly assign each co-polar PSB a value of g_0 between 0.9 and 1.1 to reflect the fact that there is expected to be about a 10% difference between the gains of the PSBs. I also randomly assign a value of g_p between 0.99 and 1.01 to the gain difference between the two devices in a single feed as this is thought to be about 1%.

If these factors are not taken into account in the data analysis and we blindly assume that the gains of each detector are the same and that there is no cross polarization a number of systematic effects will occur.

- Gain differences ($g_p \neq 1$) will cause a common mode leakage into the differenced signal, contaminating the signal with a fraction $(1 - g_p)/2$ of the total power signal.

- If the cross polar leakage is the same for each PSB in the feed this effect will just cause a reduction in the sensitivity of $(1 - \epsilon)$.
- If the cross polar leakage is the different for each PSB in the feed this will cause an additional common mode leakage, increasing the contamination to a fraction of $((1 + \epsilon_1) - g_p(1 + \epsilon_2))/2$ of the total power signal.

In general, the combination of the gain difference and cross polar leakage will give a differenced output of (Jones et al. (2003)):

$$D = \gamma I + \delta(Q \cos(2\alpha) + U \sin(2\alpha)) \quad (7.23)$$

where,

$$\gamma = \frac{1}{2} ((1 + \epsilon_1) - g_p(1 + \epsilon_2)) \quad (7.24)$$

$$\delta = \frac{1}{2} ((1 - \epsilon_1) - g_p(1 - \epsilon_2)) \quad (7.25)$$

The difference in orientation, $\delta\alpha$ will cause a cross polarization.

In the literature the cross polar leakage is also sometimes referred to as cross polarization, which can be confusing as cross polar leakage **does not** cause a change in the rotation angle of the polarization, it adds a common mode signal and reduces the sensitivity to the polarized component of the radiation.

In theory, if the gain differences and cross polar leakage of each detector can be measured then these effects can be removed in the map-making pipeline. However, it will be difficult to measure these parameters accurately and so these effects will still be present at some level due to the uncertainty in the values of the parameters used in such an analysis.

7.2.4 Future work

The simulations at present are detailed enough to be used to test the map making code. However, in order to use these simulations to test other parts of the pipeline a number of additional factors will need to be included such as:

- realistic models for the shape of the beam as opposed to the assumption of a perfect Gaussian profile,
- cosmic ray hits and glitches in the data due to bad weather or instrumental failure.

It may also be useful to include the estimates of the foreground emission from Chapter 3 into the signal.

Many of the first order approximations used here will also need to be modelled in more detail.

- The correlations between different detectors for the atmospheric, bolometer and electronics $1/f$ noise should be modelled so that partial correlations between detectors can be included, instead of simply assuming the noise is either completely correlated or completely uncorrelated.
- A more realistic model for the instrumental polarization needs to be developed.
- A method of simulating the instrumental cross polarization is also needed.

When the data analysis pipeline is completed, these simulations can be used to evaluate the effect of these systematics on the QUaD science goals. This will give more realistic estimates of the polarization power spectrum measurements and the parameter estimates than those presented in Chapter 5 which assume that all the systematics can be completely removed.

Chapter 8

Conclusions and future work

In this section I summarise the main results presented in this thesis and highlight the areas for which more work could be done. I conclude with the outlook for future CMB polarization measurements.

8.1 Summary of results and future work.

I have investigated potential science goals achievable with the QUaD ground-based CMB polarization experiment. I have set out a Fisher information matrix formalism that takes into account the combination of different temperature and polarization surveys, and includes foreground contamination. The key results of this analysis are:

- QUaD can make a high-significance measurement of the EE-power spectrum over a range of multipoles from $\ell = 25$ to $\ell = 2500$, with good sampling of the acoustic oscillations. The gravitational lensed component of the BB-power spectrum can also be detected with good signal-to-noise.
- Combining a two-year QUaD experiment with a four-year *WMAP* all-sky survey allows a significantly better measurement of cosmological parameters to be made compared to that possible from *WMAP* data alone. Most parameter uncertainties can be improved by a factor two.
- If the foreground contamination can be reduced the tensor-to-scalar ratio will be dramatically improved by up to a factor of six. With such improvements, strong constraints can be placed on the potential of the inflaton field.

Only the degeneracy between the amplitude of fluctuations, A , and the optical depth to re-ionization, τ , are not significantly improved, as this requires large scales only accessible to a satellite. This analysis could be extended to investigate a larger set of parameters, in particular it would be interesting to look at the possible constraints on the neutrino density

and the dark energy density equation of state. These parameters are all sensitive primarily to the weak lensing effects in the E and B power spectrum. The lensing calculation made in the CMBFAST code used to predict the CMB spectrum would need to be modified for this calculation as the approximations currently used are not accurate enough produce the derivatives needed for the Fisher matrix analysis.

In order to make this analysis I investigated the expected levels of foreground contamination. For the foreground levels predicted the measurement of the E-mode signal is not significantly affected by this contamination, but **the B-mode detection will be severely degraded**. In this thesis I simply treat the foregrounds as an extra source of unavoidable noise. However, more sophisticated techniques could be used to actually remove the B-mode foreground signal. This would greatly improve the ability of QUaD to detect the B-mode lensing signal and to put constraints on the tensor-to-scalar ratio. This also highlights the fact that an understanding of how to reduce the contamination from polarized maps will play a crucial part in the success of any future CMB polarization experiment designed to measure the B-mode signal. The development of such techniques for QUaD will be an important part of the data analysis pipeline which has not yet been addressed.

The next stage of this calculation was to find the optimal the survey area. I have shown that a 300 deg^2 survey is a good compromise between a sample-limited E-mode survey and a detector-noise limited B-mode survey. For an area below 300 deg^2 the SNR for the E-mode survey drops rapidly, while above this a detection of the BB power spectrum becomes infeasible. This calculation makes the assumption that the mixing of E and B modes due to the finite survey area will be negligible. This assumption is based on previous work which shows that this mixing will only be important for the largest scales in the survey. In the analysis I assume that the largest scales in the map will be to contaminated by atmospheric noise and will not be used and so the mixing effect can be ignored. However, it would be useful to make calculations to confirm this assumption. If there is significant mixing on the scales of interest it will be necessary to perform an analysis such as that outlined in Bunn et al. (2003) in which the map is separated into E, B and ambiguous modes. These ambiguous modes will then not be used leading to a reduction in the amount of available data. This could reduce the precision with which QUaD can measure the power spectra and constrain cosmological parameters.

The science predictions and optimal area are predicted assuming that the instrumental noise will be completely white and that all of the systematic effects can be accounted for and perfectly removed from the data. The next stage in the analysis would be to look at the effect of realistic noise and residual systematic effects on the survey area and science results. This work has been started by making simulations of the time ordered

data as discussed in the last Chapter. The map making, power spectrum estimation and parameter estimation pipeline are currently being developed by other members of the QUaD consortium. Once this pipeline is complete it will be possible to run the simulations through the pipeline to investigate how these effects will degrade the QUaD results. The QUaD instrument is currently being installed at the South Pole and within the next few months the testing of the instrument will begin. This will provide experimental results for expected common mode leakage and cross polarization which can be used to make more realistic models of the systematics to use in the simulations. The testing will also provide data which can be used to characterise the instrumental and atmospheric noise and improve on the approximations made in the current simulations. The data analysis methods needed to account for these systematic effects also need to be developed before the first cosmological observations can be made.

The observing strategy chosen for the South Pole is to make constant elevation scans up and down a single patch of sky. This is the simplest possible strategy and is chosen because it is thought the atmosphere will not be stable enough for changing elevation scans to be made. However, if the atmosphere proves to be very stable, a strategy in which varying elevation scans are made should be used as this will provide cross-linking. The best strategy to use for this can be investigated once the map making and power spectrum estimation code have been completed and measurements of the atmospheric noise at the South Pole have been made. When this thesis was started the most likely observing site for QUaD was Chile and not the South Pole. A definite decision to go to the South Pole was made before this work was completed and so it would be useful to define a useable scan strategy that could be used by any future experiments operating from Chile.

8.2 Outlook for CMB polarization measurements

CMB polarization measurements are in a similar stage to that of CMB temperature measurements a decade ago. The COBE large scale observations confirmed the existence of CMB fluctuations and then a series of ground-based experiments went on to measure the acoustic peaks and use the CMB to test the standard cosmological model. The polarization of the CMB has now been confirmed by DASI and the large-scale TE signal has been observed by WMAP. It is likely that with the release of the two year WMAP data measurements of the large scale E-mode polarization will have been made. The recent measurements from CBI will be the first in a series of observations from small-scale ground-based experiments (such as QUaD) which will map out the E-mode acoustic peaks. The upcoming Planck satellite will provide a high precision measurement of the large scale E-mode spectrum.

The next big experimental challenge after the proper characterization of the E-mode spectrum will be a measurement of the B-mode signal which will be sensitive enough to measure the amplitude of the gravitational wave component. An important step will also be the making of high-resolution high-sensitivity polarized maps which can be used to remove the gravitational lensing contamination and to make accurate models of foreground contamination. This has already begun with the funding of experiments such as CLOVER (Taylor et al. (2004)) and new proposals such as POLARBEAR¹. The ultimate measurement of the B-mode signal would come from a next generation all sky satellite experiment. This is already under discussion as the planned NASA inflation probe². As well as producing its own science results, QUaD is therefore an important stepping stone in the development of technology needed to make more sensitive CMB polarization measurements.

CMB polarization is set to become a powerful tool in observational cosmology, working as a complementary technique to other new observations such as weak lensing and SZ measurements. These observations will either allow us to determine the nature of dark matter, dark energy and inflation or open the door to other even more exotic explanations of the cosmological concordance model.

¹<http://bolo.berkeley.edu/polarbear/>

²<http://universe.gsfc.nasa.gov/program/inflation.html>

Appendix A

Fourier transforms of sampled data

It is often useful to describe a signal in terms of the Fourier transform of the time-ordered data. This is equivalent to thinking of the signal, $s(t)$, being made up the sum of a number of sinusoidal wave components of different frequencies, f^1 . Each component will have a certain amplitude $S(f)$ and phase $\phi(f)$. The data will be taken with a sampling frequency f_s so the time between each sample will be $\Delta t = 1/f_s$. The total length of the time-stream is denoted by T . There are N data points in the time-domain, labelled by n , so that the time at which the each point was measured is $t = n\Delta t$. In the frequency domain, the N points are labelled by m , so the frequency of each Fourier component is $f = m\Delta f$, where Δf is the interval between points in the frequency domain. This is related to the length of the time-stream by $\Delta f = 1/T$. The Discrete Fourier Transform² is then given by:

$$S_m = (\Delta f)^{-1/2} \frac{1}{N} \sum_{n=0}^{N-1} s_n e^{-2\pi i m n / N} \quad (\text{A.1})$$

and the inverse transform by:

$$s_n = (\Delta f)^{1/2} \sum_{m=0}^{N-1} S_m e^{2\pi i m n / N} \quad (\text{A.2})$$

I choose the normalization factors, $(\Delta f)^{-1/2}$, and $(\Delta f)^{1/2}$ so that if s_n has units X (normally X will be either Kelvins or Watts), S_m then has units $X s^{1/2}$.

For the random noise processes I will consider, the different Fourier modes of the noise signal will not be correlated. This means the phase of each component will be completely random. The statistical properties of the noise are then completely defined by the power

¹Note that f is the signal frequency, not the frequency of the radiation being detected which we denote using ν such that the energy of a single photon of radiation is $h\nu$

²Note that there is no standard definition of the discrete Fourier transform and the $1/N$ factor is sometimes used in the inverse transform instead. The definition used here is that used by the IDL programming routines.

spectrum of the noise, \mathcal{P}_m :

$$\langle S_m S_{m'}^* \rangle = \mathcal{P}_m \delta_{m,m'}. \quad (\text{A.3})$$

This also known as the power spectral density and has units X^2s . The angled brackets denote an average over different realizations of the noise, so the power spectrum gives us the variance of the statistical distribution describing each Fourier component.

The Fourier transform has both real and imaginary components, but the time-ordered-data will be real, i.e. all its imaginary components will be zero and so contain no information. However, the amount of information in the N real points in the time-domain is the same as that in the N complex points in the frequency domain due to the symmetry condition:

$$S_{-m} = S_m^* \quad (\text{A.4})$$

For discretely sampled data it is not possible to extract information from the signal at any frequencies higher than half the sampling frequency. This is evident if we think about measuring the individual sine wave components of the signal. There must be at least two samples taken in the time it takes for a component to complete a single sine wave oscillation in order that this signal can be measured. Components with frequencies above this frequency are indistinguishable from lower frequency components as there are not enough measurements to resolve these higher frequencies. This is shown in Fig. A.1. This is called the **Nyquist sampling theorem** and the maximum measurable frequency is called the **Nyquist frequency**, $f_{max} = f_s/2$. For real discretely sampled data, defining the power spectral density in the range $0 \leq f \leq f_s/2$ gives all the possible statistical information that can be obtained about the signal.

In the Fourier transform of real data the negative frequency components can be thought of as sine waves which are 180° out of phase with the positive frequency components. As the data is real, the magnitude of these positive and negative components will be the same, as stated in equation A.4. If we define the power spectrum as the power per unit frequency interval, where we are interested only in the magnitude of the frequency and not its phase (i.e. not whether it is positive or negative), we should include both the negative and positive contribution to each frequency component. It therefore useful to redefine the power spectrum of real data as $P_m = 2\mathcal{P}_m$, where \mathcal{P}_m is the power in both positive frequencies and negative frequencies, so is double the value in the previous definition. P_m is often called the one-sided power spectrum and has units of $WHz^{-1/2}$. The power spectra is often quoted without stating whether this factor of two has been included and this often makes comparing different noise models confusing. In this thesis the term power spectrum will always refer to P_m defined only over positive frequencies and so includes this factor of two.

A useful point to note is that the average variance per sample $\langle s_n s_n^* \rangle$ is always equal

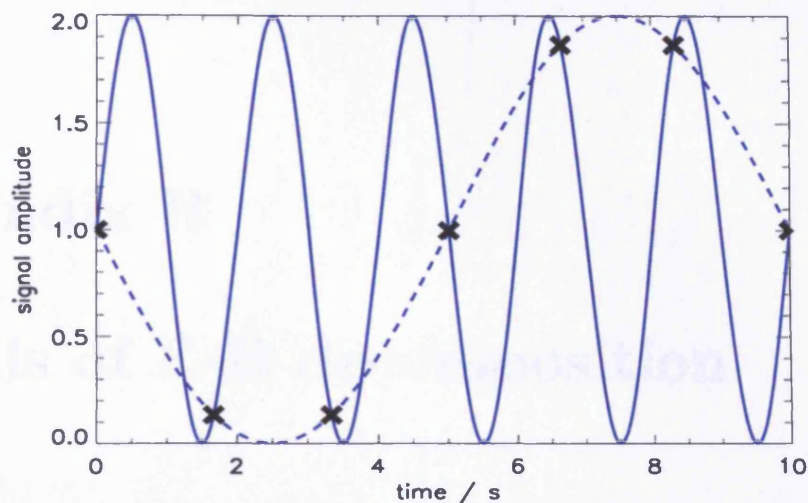


Figure A.1: This plot illustrates why the maximum frequency component we can measure in a signal must be less than half the sampling rate. The true signal (solid blue line), has a frequency of 0.5 Hz and so a sample rate of at least 1 Hz would be needed to measure this component. If the signal is sampled at less than this frequency then it would appear that this signal has a lower frequency. In this case the signal has been sampled at 0.6 Hz and we measure a signal at 0.1 Hz (dotted blue line) which is not actually present in the data.

to the total power in the power spectrum, $\sum_{m=0}^{N/2} P_m \Delta f$. This can be shown as follows:

$$\begin{aligned}
 \langle s_n s_n^* \rangle &= \left\langle \Delta f \sum_{m=0}^{N-1} S_m e^{2\pi i m n / N} \sum_{m'=0}^{N-1} S_{m'}^* e^{-2\pi i m' n / N} \right\rangle \\
 &= \Delta f \sum_{m, m'=0}^{N-1} e^{2\pi i m n / N} e^{-2\pi i m' n / N} \langle S_m S_{m'}^* \rangle \\
 &= \Delta f \sum_{m=0}^{N-1} P_m \\
 \langle s_n s_n^* \rangle &= \sum_{m=0}^{N/2} P_m \Delta f
 \end{aligned} \tag{A.5}$$

Appendix B

Details of E-B decomposition

The decomposition of the polarization field into E and B fields is made using the tensor equivalent of the gradient, f_g and curl operators, f_c . The polarization tensor can be expressed as:

$$P = f_g(\phi_E) + f_c(\phi_B) \quad (\text{B.1})$$

where $E = \nabla^2 \phi_E$ and $B = \nabla^2 \phi_B$. On a general surface with metric g_{ij} , these operators are (Kamionkowski et al. (1997b)):

$$f_g(\phi) = 2(\phi_{;ij} - (1/2)g_{ij}\phi_{;k}^k) \quad (\text{B.2})$$

$$f_c(\phi) = \phi_{;ik}\epsilon_j^k + \phi_{;jk}\epsilon_i^k \quad (\text{B.3})$$

in which ; is the covariant derivative and the convention of summation over repeated indices is used. The antisymmetric tensor used in the curl definition is given by:

$$\epsilon = \sqrt{g} \begin{pmatrix} 0 & 1 \\ -1 & 0 \end{pmatrix}. \quad (\text{B.4})$$

On a plane, the metric is simply:

$$g = \begin{pmatrix} 1 & 0 \\ 0 & 1 \end{pmatrix} \quad (\text{B.5})$$

and the polarization tensor is:

$$P = \begin{pmatrix} Q & U \\ U & -Q \end{pmatrix}. \quad (\text{B.6})$$

The expressions for Q and U are therefore fairly simple:

$$\begin{aligned} Q &= f_g(\phi_E)_{11} + f_c(\phi_B)_{11} = 2(\phi_{E;11} - \frac{1}{2}\phi_{E;k}^k) - 2\phi_{B;12} \\ U &= f_g(\phi_E)_{12} + f_c(\phi_B)_{12} = 2\phi_{E;12} + \phi_{B;11} - \phi_{B;22} \end{aligned} \quad (\text{B.7})$$

These expressions can be converted to into Fourier space, in terms of the wave-vector, \mathbf{k} , using the identities $\phi_{,a} = ik_a\phi$ (where $i = \sqrt{-1}$), $\phi_{,a}{}^a = \nabla^2\phi = k^2\phi$ and $\nabla^{-2}\phi = (-1/k^2)\phi$ where k_a is the Fourier component along a given axis and k is the magnitude of \mathbf{k} . For a flat plane, this gives:

$$Q = \frac{1}{k^2} \left((k_1^2 - k_2^2)E - 2k_1k_2B \right) \quad (\text{B.8})$$

$$U = \frac{1}{k^2} \left(2k_1k_2E + (k_1^2 - k_2^2)B \right) \quad (\text{B.9})$$

If we define the angle, θ_k , as the angle between the x-axis and the direction of the fourier component, k , then this expression simplifies to (Zaldarriaga (2001)):

$$Q(k) = [E(k) \cos(2\theta_k) - B(k) \sin(2\theta_k)] \quad (\text{B.10})$$

$$U(k) = [E(k) \sin(2\theta_k) + B(k) \cos(2\theta_k)]. \quad (\text{B.11})$$

On a curved sky, the relationship between (Q,U) and (E,B) is not as simple as the form of the metric changes to:

$$g = \begin{pmatrix} 1 & 0 \\ 0 & \sin^2(\theta), \end{pmatrix} \quad (\text{B.12})$$

making the covariant derivative in the E and B expressions more complicated. Also, instead of an expanding in Fourier space, the polarization tensor is expanded in terms of tensor spherical harmonics.

Appendix C

Amplitude modulation

Amplitude modulation (AM) is a technique used to push a signal up to higher frequencies. This is useful if low frequency noise will be added to the signal after the modulation as the signal can be moved into a part of the spectrum where the noise is lower. It also means that the noise can be filtered out without removing the low frequency components of the signal. The first stage is to modulate the signal with a carrier frequency. This is ideally a sinusoidal signal at a frequency much higher than that of the expected low frequency noise. In some cases, particularly where the signal is modulated mechanically (such as using a Faraday switch to swap between polarization states), a square wave modulation is used as it is much easier to produce. The components of the original signal will be present in the modulated signal as higher frequency components.

The modulation and demodulation process are illustrated for a signal with a single frequency component, $S(t) = \sin(\omega_s t)$, in Fig C.1. If this signal is multiplied by a carrier signal $C(t) = \sin(\omega_c t)$, the resulting signal has the form:

$$M(t) = \sin(\omega_c t) \times \sin(\omega_s t) \quad (\text{C.1})$$

$$= \frac{1}{2}(-\cos(\omega_c t + \omega_s t) + \cos(\omega_c t - \omega_s t)) \quad (\text{C.2})$$

so will have components at frequencies of $(\omega_c t + \omega_s t)$ and $(\omega_c t - \omega_s t)$. In Fig. C.1, the signal has a frequency of 2 and the carrier a frequency of 10, so components are seen in the modulated signal at frequencies of 8 and 12. For a general signal containing a range of frequency components, the two frequency spikes will be two symmetric bands of power around the carrier frequency. Any low frequency noise added to the modulated signal can then be filtered out without removing any of the signal.

To demodulate the signal, the modulated signal is multiplied again by a signal at the carrier frequency. For the single sine wave signal, this gives:

$$D(t) = M(t) \times C(t) \quad (\text{C.3})$$

$$= \frac{1}{2} [-\cos(\omega_c t + \omega_s t) + \cos(\omega_c t - \omega_s t)] \times \sin(\omega_c t) \quad (C.4)$$

$$= \frac{1}{4} [-\sin(2\omega_c + \omega_s) - \sin(\omega_s) + \sin(2\omega_c - \omega_s) + \sin(-\omega_s)] \quad (C.5)$$

so the demodulated signal will have components at $(2\omega_c \pm \omega_s)$ and at $(\pm\omega_s)$. The original signal can then be obtained by low-pass filtering the signal to get rid of the unwanted high frequency components at $(2\omega_c \pm \omega_s)$.

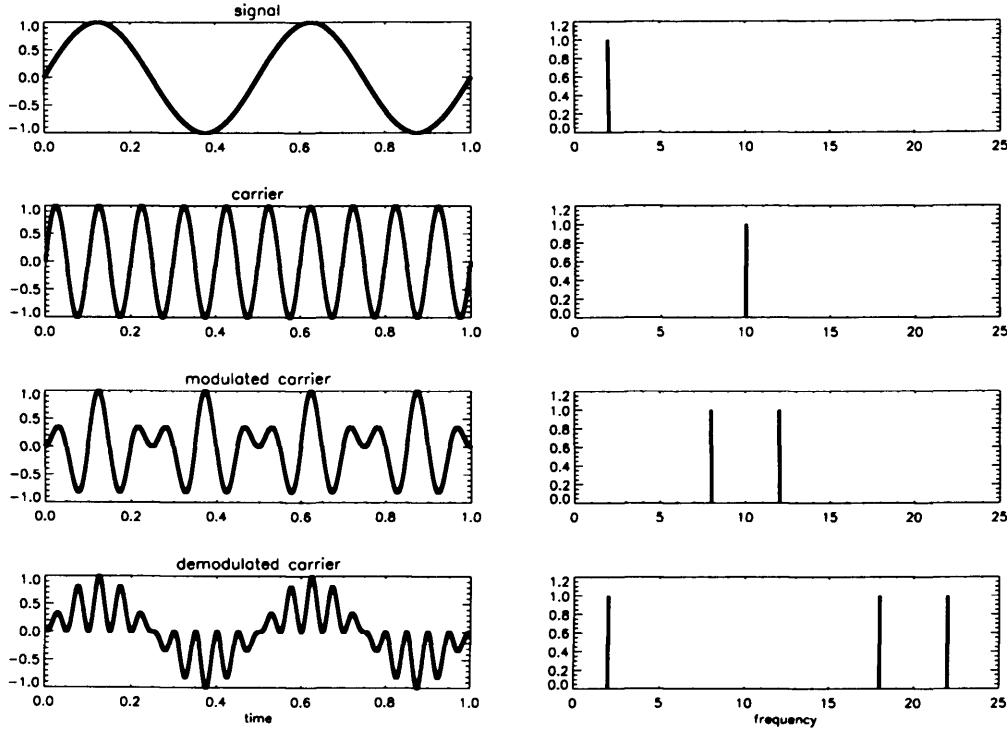


Figure C.1: Stages of modulation and demodulation in the time (left) and frequency (right) domains.

For the QUaD, amplitude modulation is used to reduce the electronics noise. The modulation is performed by using an AC voltage to bias the bolometer so that signal output from the bolometer is modulated at the bias frequency. Once the signal passes out of the cryostat and has been amplified, a band-pass filter is applied. This means that most of the low frequency amplifier noise from the JFETs and the pre-amp is removed. A lock-in amplifier then uses the original bias signal to demodulate the signal. Finally a low-pass filter cuts off the unwanted high frequency components added to the signal by the demodulation.

Bibliography

- Baccigalupi, C.: 2003, *New Astronomy Review* **47**, 1127
- Baccigalupi, C.: 2001, *Astron. and Astrophys.* **372**, 8
- Barkats, D.: 2003, *New Astronomy Review* **47**, 1077
- Becker R. H. et al.: 2001, *Astron. J.* **122**, 2850
- Bennett C. L.: 2003, *Astrophys. J., Suppl. Ser.* **148**, 97
- Benoît, A. : 2004, *Astron. Astrophys.*, *accepted*
- Bhatia, R. S., Chase, S. T., Jones, W. C., Lange, A. E., Mason, P. V., Philhour, B. J., and Sirbi, G.: 2002, *cryogenics* **42(1)**, 113
- Brown, M. L.: 2004, *Level C presentation at QUaD design review*, private communication
- Bruscoli M. et al.: 2002, *New Astronomy* **7**, 171
- Bunn, E. F.: 2002, *Phys. Rev. D* **65(4)**, 043003
- Bunn, E. F., Zaldarriaga, M., Tegmark, M., and de Oliveira-Costa, A.: 2003, *Phys. Rev. D* **67(2)**, 023501
- Cahill G.: 2003, *Zeemax prediction of QUaD focal plane projection*, private communication
- Chamberlin, R. A., Lane, A. P., and Stark, A. A.: 1997, *Astrophys. J.* **476**, 427
- Church, S. E.: 2003, *Sensitivity presentation at QUaD design review*, private communication
- Colless et al., M.: 2001, *Mon. Not. R. Astron. Soc.* **328**, 1039
- Cortiglioni, S. and Spoelstra, T. A. T.: 1995, *Astron. and Astrophys.* **302**, 1
- Couchot, F., Delabrouille, J., Kaplan, J., and Revenu, B.: 1999, *Astron. and Astrophys. Suppl. Ser.* **135**, 579

- de Bernardis, P. et al.: 2000, *Nature* **404**, 955
- de Oliveira-Costa, A., Tegmark, M., O'dell, C., Keating, B., Timbie, P., Efstathiou, G., and Smoot, G.: 2003, *New Astronomy Review* **47**, 1117
- Dodelson, S.: 2003, *Modern Cosmology*, Elsevier Science
- Draine, B. T. and Lazarian, A.: 1999a, *Bulletin of the American Astronomical Society* **31**, 890
- Draine, B. T. and Lazarian, A.: 1999b, in *ASP Conf. Ser. 181: Microwave Foregrounds*, pp 133–+
- Efstathiou, G.: 2002, *Mon. Not. R. Astron. Soc.* **332**, 193
- Efstathiou, G. and Bond, J. R.: 1999, *Mon. Not. R. Astron. Soc.* **304**, 75
- Farese P. C. et al.: 2004, *Astrophys. J.* **610**, 625
- Finkbeiner, D. P.: 2003, *Astrophys. J.*, *accepted*, *astro-ph/0311547*
- Finkbeiner, D. P., Davis, M., and Schlegel, D. J.: 1999, *Astrophys. J.* **524**, 867
- Fosalba, P., Lazarian, A., Prunet, S., and Tauber, J. A.: 2002, in *AIP Conf. Proc. 609: Astrophysical Polarized Backgrounds*, pp 44–50
- Giardino, G., Banday, A. J., Górski, K. M., Bennett, K., Jonas, J. L., and Tauber, J.: 2002, *Astron. and Astrophys.* **387**, 82
- Grainge, K. et al.: 2003, *Mon. Not. R. Astron. Soc.* **341**, L23
- Griffin, M. J., Bock, J. J., and Gear, W. K.: 2002, *Appl. Opt.* **41**, 6543
- Grossman, E.: 1989, *AT – Atmospheric Transmission Software User's Manual*, Airhead Software Co., Boulder, CO
- Guth, A. H.: 1981, *Phys. Rev. D* **23**, 347
- Halverson, N. W et al.: 2002, *Astrophys. J.* **568**, 38
- Hanany, S., Jaffe, A. H., and Scannapieco, E.: 1998, *Mon. Not. R. Astron. Soc.* **299**, 653
- Hanany, S. et al.: 2000, *Astrophys. J., Lett.* **545**, L5
- Haslam, e. a.: 1981, *Astron. and Astrophys.* **100**, 209

- Hinderks, J. R.: 2003, *Electronics presentation at QUaD design review*, private communication
- Hinshaw, G.: 2003, *Astrophys. J., Suppl. Ser.* **148**, 135
- Hobson, M. P. and Magueijo, J.: 1996, *Mon. Not. R. Astron. Soc.* **283**, 1133
- Holland, W., Duncan, W., and Griffin, M.: 2002, in *ASP Conf. Ser. 278: Single-Dish Radio Astronomy: Techniques and Applications*, pp 463–491
- Hu, W.: 2002, *Phys. Rev. D* **65(2)**, 023003
- Hu, W. and Okamoto, T.: 2002, *Astrophys. J.* **574**, 566
- Hu, W. and Sugiyama, N.: 1995, *Astrophys. J.* **444**, 489
- Hu, W. and White, M.: 1997a, *New Astronomy* **2**, 323
- Hu, W. and White, M.: 1997b, *Astrophys. J.* **479**, 568
- Johnson B. R. et al.: 2003, *New Astronomy Review* **47**, 1067
- Jones, W. C., Bhatia, R., Bock, J. J., and Lange, A. E.: 2003, in *Millimeter and Submillimeter Detectors for Astronomy. Edited by Phillips, Thomas G.; Zmuidzinas, Jonas. Proceedings of the SPIE, Volume 4855*, pp 227–238
- Kamionkowski, M., Kosowsky, A., and Stebbins, A.: 1997a, *Physical Review Letters* **78**, 2058
- Kamionkowski, M., Kosowsky, A., and Stebbins, A.: 1997b, *Phys. Rev. D* **55**, 7368
- Kaplinghat, M.: 2003, *New Astronomy Review* **47**, 893
- Kaplinghat, M., Chu, M., Haiman, Z., Holder, G. P., Knox, L., and Skordis, C.: 2003a, *Astrophys. J.* **583**, 24
- Kaplinghat, M., Knox, L., and Song, Y.: 2003b, *Physical Review Letters* **91(24)**, 241301
- Keating, B., Timbie, P., Polnarev, A., and Steinberger, J.: 1998, *Astrophys. J.* **495**, 580
- Keating, B. G., Ade, P. A. R., Bock, J. J., Hivon, E., Holzapfel, W. L., Lange, A. E., Nguyen, H., and Yoon, K.: 2003, in *Polarimetry in Astronomy. Edited by Silvano Fineschi. Proceedings of the SPIE, Volume 4843*, pp 284–295
- Keating, B. G., de Oliveira-Costa, A., O'dell, C. W., Piccirillo, L., Stebor, N. C., Tegmark, M., and Timbie, P. T.: 2002, in *AIP Conf. Proc. 616: Experimental Cosmology at Millimetre Wavelengths*, pp 175–182

- Keating, B. G., O'Dell, C. W., de Oliveira-Costa, A., Klawikowski, S., Stebor, N., Piccirillo, L., Tegmark, M., and Timbie, P. T.: 2001, *Astrophys. J., Lett.* **560**, L1
- Kesden, M., Cooray, A., and Kamionkowski, M.: 2002, *Physical Review Letters* **89**(1), 011304
- Kesden, M., Cooray, A., and Kamionkowski, M.: 2003, *Phys. Rev. D* **67**(12), 123507
- Klein, U., Mack, K.-H., Gregorini, L., and Vigotti, M.: 2003, *aap* **406**, 579
- Knox, L.: 1995, *Phys. Rev. D* **52**, 4307
- Knox, L. and Song, Y.: 2002, *Physical Review Letters* **89**(1), 011303
- Kogut, A. et al.: 2003, *Astrophys. J., Suppl. Ser.* **148**, 161
- Kosowsky, A.: 1999, *New Astronomy Review* **43**, 157
- Kovac, J. M., Leitch, E. M., Pryke, C., Carlstrom, J. E., Halverson, N. W., and Holzapfel, W. L.: 2002, *Nature* **420**, 772
- Kraus, J., D.: 1997, *Radio Astronomy*, McGraw Hill
- Lamarre, J. M.: 1986, *Appl. Opt.* **25**, 870
- Lamarre, J. M. et al.: 2003, *New Astronomy Review* **47**, 1017
- Lawrence, C. R.: 2003, *New Astronomy Review* **47**, 1025
- Lay, O. P. and Halverson, N. W.: 2000, *Astrophys. J.* **543**, 787
- Lazarian, A. and Prunet, S.: 2002, in *AIP Conf. Proc. 609: Astrophysical Polarized Backgrounds*, pp 32–43
- Leach, S. M. and Liddle, A. R.: 2003, *Phys. Rev. D* **68**(12), 123508
- Lewis, A., Challinor, A., and Turok, N.: 2002, *Phys. Rev. D* **65**(2), 023505
- Masi, S. et al: 2003, *Societa Astronomica Italiana Memorie Supplement* **2**, 54
- Mather, J. C.: 1982, *Appl. Opt.* **21**, 1125
- Mather, J. C. et al.: 1994, *Astrophys. J.* **420**, 439
- Mesa, D., Baccigalupi, C., De Zotti, G., Gregorini, L., Mack, K.-H., Vigotti, M., and Klein, U.: 2002, *Astron. and Astrophys.* **396**, 463

- Montroy, T. et al.: 2003, *New Astronomy Review* **47**, 1057
- Pearson T. J. et al.: 2003, *Astrophys. J.* **591**, 556
- Peiris et al.: 2003, *Astrophys. J., Suppl. Ser.* **148**, 213
- Penzias, A. A. and Wilson, R. W.: 1965, *Astrophys. J.* **142**, 419
- Percival, W. J., Sutherland, W., Peacock, J. A., Baugh, C. M., Bland-Hawthorn, J., Bridges, T., Cannon, R., Cole, S., Colless, M., Collins, C., Couch, W., Dalton, G., De Propris, R., Driver, S. P., Efstathiou, G., Ellis, R. S., Frenk, C. S., Glazebrook, K., Jackson, C., Lahav, O., Lewis, I., Lumsden, S., Maddox, S., Moody, S., Norberg, P., Peterson, B. A., and Taylor, K.: 2002, *Mon. Not. R. Astron. Soc.* **337**, 1068
- Perlmutter et al., S.: 1999, *Astrophys. J.* **517**, 565
- Press, W.: 1992, *Numerical recipes in C*, Cambridge University Press
- Prunet, S., Sethi, S. K., Bouchet, F. R., and Miville-Deschenes, M.-A.: 1998, *Astron. and Astrophys.* **339**, 187
- Prunet, S. et al.: 2001, in *Mining the Sky*, pp 421–+
- Readhead et al., S.: 2004, *Science, accepted*, *astro-ph/0409569*
- Rees, M. J.: 1968, *Astrophys. J., Lett.* **153**, L1+
- Riley, K. F., Hobson, M. P., and Bence, S.J.: 1997, *Mathematical Methods for Physics and Engineering*, Cambridge University Press
- Runyan, M. C. et al.: 2003, *Astrophys. J., Suppl. Ser.* **149**, 265
- Rybicki, G. B. and Lightman, A. P.: 1979, *Radiative processes in astrophysics*, New York, Wiley-Interscience
- Sachs, R. K. and Wolfe, A. M.: 1967, *Astrophys. J.* **147**, 73
- Schlegel, D. J., Finkbeiner, D. P., and Davis, M.: 1998, *Astrophys. J.* **500**, 525
- Schutz, B., F.: 1985, *A first course in General Relativity*, Cambridge University Press
- Seljak, U.: 1996, *Astrophys. J.* **463**, 1
- Seljak, U.: 1997, *Astrophys. J.* **482**, 6
- Seljak, U. and Zaldarriaga, M.: 1996, *Astrophys. J.* **469**, 437

- Seljak, U. and Zaldarriaga, M.: 1997, *Physical Review Letters* **78**, 2054
- Silk, J.: 1968, *Astrophys. J.* **151**, 459
- Smoot et al., G. F.: 1992, *Astrophys. J., Lett.* **396**, L1
- Spergel D.N. et al.: 2003, *Astrophys. J., Suppl. Ser.* **148**, 175
- Stompor, R. and Efstathiou, G.: 1999, *Mon. Not. R. Astron. Soc.* **302**, 735
- Taylor, A. C., Challinor, A., Goldie, D., Grainge, K., Jones, M. E., Lasenby, A. N., Withington, S., Yassin, G., Gear, W. K., Piccirillo, L., Ade, P., Mauskopf, P. D., Maffei, B., and Pisano, G.: 2004, *ArXiv Astrophysics e-prints*
- Tegmark, M. and Efstathiou, G.: 1996, *Mon. Not. R. Astron. Soc.* **281**, 1297
- Tegmark, M., Eisenstein, D. J., Hu, W., and de Oliveira-Costa, A.: 2000, *Astrophys. J.* **530**, 133
- Tegmark, M., Taylor, A. N., and Heavens, A. F.: 1997, *Astrophys. J.* **480**, 22
- Tegmark, M. and Zaldarriaga, M.: 2002, *Phys. Rev. D* **66**(10), 103508
- Tinbergen: 1996, *Astronomical Polarimetry*, Cambridge University Press
- Toffolatti, L., Argueso Gomez, F., de Zotti, G., Mazzei, P., Franceschini, A., Danese, L., and Burigana, C.: 1998, *Mon. Not. R. Astron. Soc.* **297**, 117
- Tucci, M., Martínez-González, E., Toffolatti, L., González-Nuevo, J., and De Zotti, G.: 2004, *Mon. Not. R. Astron. Soc.* **349**, 1267
- Tucci M. et al.: 2002, *Astrophys. J.* **579**, 607
- Wandelt, B. D., Hivon, E., and Górski, K. M.: 2001, *Phys. Rev. D* **64**(8), 083003
- Zaldarriaga, M.: 1997, *Phys. Rev. D* **55**, 1822
- Zaldarriaga, M.: 2001, *Phys. Rev. D* **64**(10), 103001
- Zaldarriaga, M.: 2003, *American Astronomical Society Meeting* **202**,
- Zaldarriaga, M. and Seljak, U.: 1997, *Phys. Rev. D* **55**, 1830
- Zaldarriaga, M. and Seljak, U.: 1998, *Phys. Rev. D* **58**(2), 023003
- Zaldarriaga, M., Spergel, D. N., and Seljak, U.: 1997, *Astrophys. J.* **488**, 1
- Zemcov, M.: 2004, *Map making presentation at QUaD design review*, private communication

